Mechanical and Tribological Properties of Aluminium Matrix Syntactic Foams Manufactured with Recycled Aluminium Smelter Waste

Thesis submitted in accordance with the requirements of the University of Liverpool for the Degree of Doctor in Philosophy

By

Bhavik Ajaykumar Mehta

June 2020

Abstract

Aluminium smelter waste (ASW) is a big contributor to landfill. Recycling ASW and forming more useful products has been of great interest. This study explores the feasibility of using ASW particles, which has a porous structure, for manufacturing a lightweight composite material known as a syntactic foam. Metal matrix syntactic foams (MMSFs) have many attractive properties, such as high strength, low wear and high energy absorption, and are suitable for a wide range of applications. However, no study has been conducted on MMSFs with ASW as a filler material.

This thesis investigated the mechanical and tribological properties of Al matrix syntactic foams manufactured by melt infiltration with ASW particles of three particle size groups, designated as Small (125-250 μm), Medium (250-425 μm) and Large (425-1000 μm), and compared the ASW syntactic foam samples with a syntactic foam made with a commercially available ceramic microsphere powder (E-sphere; 250-500 μm).

Compressive strength and energy absorption properties of the syntactic foams were measured by both quasi-static and drop hammer impact tests. Under quasi-static loading, the strength increased as ASW particle size increased. The failure mode was a more ductile deformation in the Large syntactic foam sample and a more catastrophic brittle failure in the Medium and Small syntactic foam samples. Heating the Large ASW particles before melt infiltration showed a transition from ductile to brittle failure, because the strength of the Large particles increased upon heating. Heating the Small and Medium particles before infiltration had no significant effect, because their non-heated counterparts were small enough to be heated during melt

infiltration. T6 treatment of the syntactic foam samples led to an increase in strength and energy absorption capacity, with no change in deformation behaviour. The Large syntactic foam sample showed a transition from ductile to brittle deformation under drop hammer impact, indicating strain rate sensitivity. The ASW syntactic foam samples showed a higher yield strength and energy absorption capacity than the E-sphere syntactic foam under both quasi-static and drop hammer impact loading, mainly because the ASW particles have a lower porosity.

Flexural strength and energy absorption were assessed by three-point bending and Charpy impact tests. In three-point bending, the crack propagation occurred through the interface between the ASW particles and Al matrix and deviated away from the point of loading as particle size decreased. The flexural strength and energy absorption decreased with particle size. T6 treatment led to significant increases in flexural strength and energy absorption because of the increase in hardness of the Al matrix. In Charpy impact tests, all samples showed a brittle failure, with the impact toughness decreasing with decreasing particle size. The crack propagated straight through the Al matrix and particles alike. ASW syntactic foam had inferior flexural strength and energy absorption compared to E-sphere syntactic foam.

Tribological properties were evaluated through dry and lubricated sliding wear tests. Under dry sliding conditions, the coefficient of friction (COF) had an initial sharp increase, followed by a decrease in gradient and finally a steady state as sliding distance increased. The wear surfaces showed presence of adhesive, abrasive and oxidative wear, with some presence of delamination. Small particle sizes led to decrease in average COF, increase in the amount of abrasive wear, decrease in

surface roughness, and decrease in specific wear. Heating the Large ASW particles enhanced overall wear properties of the resultant syntactic foam. T6 treatment enhanced the wear properties due to the hardening of the Al matrix. The average COF of the ASW syntactic foams was higher than that of the E-sphere syntactic foam, which had predominantly abrasive nature of wear. The specific wear of the ASW syntactic foams can be higher or lower than the E-sphere syntactic foam, depending on the ASW particle size. Under lubricated sliding conditions, the wear type changed from predominantly adhesive to predominantly abrasive due to the lubricating effect, which led to an enhancement of wear properties when compared to the dry sliding wear behaviour. The porous particles acted as lubricant reservoirs and provided a constant supply of lubricant. The lubrication had a more significant effect on the wear behaviour than the sample characteristics.

Declaration

I hereby certify that the content of this project work entitled “Mechanical and Tribological Properties of Aluminium Matrix Syntactic Foams Manufactured with Recycled Aluminium Smelter Waste”, submitted for the degree of Doctor in Philosophy in the Faculty of Science and Engineering at the University of Liverpool, is a record of an original work done by me under the supervision of Prof. Yuyuan Zhao of the School of Engineering, University of Liverpool, and this project work has not been used as the basis for the award of any other degree/diploma.

Bhavik Ajaykumar Mehta

15th June, 2020

Acknowledgements

Firstly, I would like to thank my supervisor, Prof. Yuyuan Zhao for his trust and guidance throughout, from streamlining my work and guiding my initial literature search to my lab work and excursions while trying to find a suitable tribometer for my work. The expertise he brought to the table was priceless and it helped me come up with a path I need to follow. His expertise in many fields gave me confidence to pursue my research and I would not be submitting if it were not for him.

I also want to thank the whole team at Ultromex Limited, starting with Mr Michael Glass and Mr Nigel Seddon. They helped me understand their process and guided me in the different ways I could consider using the waste. They also allowed me free reign when it came to the final direction of the project, without which this work would not have been completed. Everyone else at Ultromex was supportive and always willing to help, making my life easier and my work much better.

Next, I want to thank the Low Carbon team on campus that financed part of my project and, as a team, pushed me to be the best version of myself. I made some long-lasting friends from this group and every one of them is responsible for my ability to complete this thesis.

Apart from my supervisors and sponsors, I want to express my gratitude to everyone else who helped me organise labs, book equipment, sort through training, fabricate, machine and polish samples, and supported me mentally at the University: Dr. Liping Zhang, Mr. Dave Atkinson, Mr. Jiji Mathews, Mr. Tony Topping and the entire workshop team, and Dr. Matt Bilton. Their encouragements and insights gave me plenty of new things to consider. I also want to thank Alice Gillett at the University of Chester for allowing me access to the Tribometer at Thornton Science Park.

My fellow lab mates, Kaikan, Edgar, Pengcheng, Xianke, Yue, Chen and Zejun, were particularly helpful in guiding me through and helping me understand my work. All others that supported me in the University, Rodrigo, Josh, Vanessa, Neil, Juhi, Suraj and Manohar, brought in expertise of their own and made me think more deeply about my work. And outside of the University, Gunjan, Mash, Ramis, Trishna, Yeshmita, Fenchi, Priyanka and Brian, all supported me mentally while I worked through the years. I will cherish the memories made with every one of them outside of work and I thank them all for their support through my journey.

Words cannot do justice to the support I have received from my parents back in Kenya, my aunts and uncles and here in the UK. Without their support, I would not be submitting this work today. They allowed me to do whatever I thought was right, never once asking me why or what I've been doing. Their trust motivated me to push for the limits and their faith in my abilities was the backbone to this work. I cannot thank them enough.

Table of Contents

List of Figures

List of Tables

List of Abbreviations

Al	Aluminium
ASF	Aluminium Syntactic Foam
ASW	Aluminium Smelter Waste
COF	Coefficient of Friction
CM	Ceramic Microsphere
IC	Ion-Exchange Chromatography
ICP	Inductively Coupled Plasma
MMC	Metal Matrix Composite
MMSF	Metal Matrix Syntactic Foam
PM	Powder Metallurgy
PMSF	Polymer Matrix Syntactic Foam
SEM	Scanning Electron Microscope
SF	Syntactic Foam
XRD	X-Ray Diffraction
XRF	X-Ray Fluorescence

List of Symbols

A_k	Impact toughness	kj m^{-2}
b	Specimen width (flexural)	mm
D (4,3)	Mass-weighted mean diameter	µm
d	Specimen thickness (flexural)	mm
E_B	Modulus of elasticity (flexural)	GPa
M	Mass of pendulum	kg
m	Slope of force-displacement graph (flexural)	
L	Support span length (flexural)	mm
P	Flexural load	N
R	Radius of pendulum	m
R_a	Mean surface roughness	mm
R_z	Mean roughness depth	mm
S	Surface area	m^2

Greek symbols

α	Initial angle	º
β	Final swing-through angle	º
δ	Deflection of the centre of the beam (flexural)	mm
ε	Strain	
σ	Stress	MPa

Chapter 1 INTRODUCTION

1.1 Background and Motivation

Over the past decade, global warming has taken precedence over many other issues on political agendas for governments and newly elected world leaders. It is a testament to the importance of the issue that the Times Person of The Year 2019 was a teenager who rallied to get things done by calling everyone out to act. Similarly, there has been a lot of news lately regarding the need for doing more to reduce emissions, or to find more ways to increase recycling efforts and reusability of materials by diverting waste away from landfills.

One of the largest contributors to landfills is the metals processing industry, like the aluminium industry. The aluminium industry started growing less than 150 years ago, yet today it is just second to the iron and steel industry sector in size (Schlesinger, 2017). In the last 50 years, aluminium production from recycled sources has grown to more than one-third the size of the entire industry from a point where less than 18% was recycled during the 50s (Menzie *et al.,* 2010; Schlesinger, 2017).

The secondary aluminium process primarily generates three products: the molten aluminium, an off-gas and a semi-solid skim, better known as dross that is scraped off the surface of the molten metal (Schlesinger, 2017). This dross is commonly processed further to extract more metal and remove the salts from it, which leaves behind a non-metallic waste, known as Aluminium Smelter Waste (ASW). The composition of ASW varies, but it mainly contains alumina and other oxides. It may also contain traces of aluminium nitride, carbide and trace aluminium (Tsakiridis, 2012). When ASW is left in open air, a chain reaction occurs with the moisture in the

air which eventually leads to the production of hydrogen and a potential fire and explosion hazard, limiting the potential uses of ASW (Schlesinger, 2017).

With the need to recycle and find ways to limit carbon emissions, an idea was flirted with on ways to reuse ASW, currently being sent to landfill, in ways that may end up reducing carbon emissions either directly, through lightweight applications, or indirectly, via the repurposing of land that would have gone to be used as a landfill site for ASW. With this in mind, the idea was then formed to study ASW in the development of a metal matrix syntactic foam, which is a lightweight composite material with applications in the automotive industry. This was important for reducing waste going into landfill and was the motivation for this study.

As per the definition provided by the American Society for Testing and Materials (ASTM), a syntactic foam is a 'material consisting of hollow sphere fillers in a resin matrix' (Gupta *et al.,* 2001). The ASTM definition limits syntactic foams to a polymer matrix, and this work extends the definition to include a metal matrix. In such a foam, the matrix is combined with hollow spherical particles which have a methodical arrangement in the matrix (John and Nair, 2010). Hollow particles will have a lower density compared to the matrix, therefore their incorporation allows for the manufacture of lightweight products whose density finally depends on the ratio of filler material to matrix (Wouterson *et al.,* 2005; C. Karthikeyan, Sankaran and Kumar, 2001; Maharsia, 2005). Because the density can be controlled by controlling the ratio of hollow spheres to matrix, syntactic foams can be fabricated to tailor for the needs of a specific application, hence making them very useful products (Gupta *et al.,* 1999).

Most foams are two-phase systems with a dispersed gaseous phase and a continuous solid phase. What makes syntactic foams unique is their ability to capture air pockets within two solid phases, making them three-phase systems. The properties of the final fabricated product depends on the properties of the constituent materials as well as on the manufacturing process used to make the foams as well as on the desired properties. Since their introduction in the 1960s, there has been plenty of research conducted on syntactic foams, with metal matrix syntactic foams (MMSFs) being studied and applied industrially for their exceptional mechanical properties.

In previous studies, MMSFs have been manufactured using several different processes, including pressure infiltration (Luong *et al.,* 2013; Gupta, Luong and Cho, 2012; Tao and Zhao, 2012; L. P. Zhang and Zhao, 2007) and powder metallurgy (X. Xue and Zhao, 2011; Mondal, Datta Majumder *et al.,* 2012; Xie, Zhao and Dunkley, 2013; Neville and Rabiei, 2008; Vogiatzis *et al.,* 2015). For pressure infiltration process, a molten metal is forced through a packed bed of ceramic particles. Using this process, a syntactic foam with a high volume fraction of filler materials can be fabricated where the fillers are uniformly distributed in the matrix.

The properties of MMSFs depend on various factors, including the choice of metal matrix and the volume fraction of microspheres. When compared to polymer matrix syntactic foams and metal foams, MMSFs have superior properties that make them more suitable for lightweight, high strength and high temperature applications (Gupta, Pinisetty and Shunmugasamy, 2013; Gupta and Rohatgi, 2015; Ashby, 2000; Kiser, He and Zok, 1999).

Based on a review of the existing literature on the mechanical and tribological properties of MMSFs, very little work has been done to understand the use of irregular filler materials in MMSFS. Even less so is the research which looks at incorporating a waste stream coming from the metals processing industry as a filler material. Some work exists in studies related to the incorporation of fly-ash or pumice as a filler material. However these are confined to compressive and dynamic strength properties, with little work pertaining to the friction and wear characteristics of the resultant MMSFs (Ahmaruzzaman, 2010; P. K. Rohatgi, Weiss and Gupta, 2006; P. K. Rohatgi *et al.,* 2006; Mondal, Goel and Das, 2009). One study looked at the development of fly ash based composites for wear applications, where the authors incorporated various materials to form the mix of the composite, including phenolic resin, aramid pulp, glass fibre, potassium titanate, graphite, aluminium fibre and copper powder (Mohanty and Chugh, 2007). The authors were able to form composites with 50wt% fly ash which showed consistent coefficients of friction of between 0.35-0.4 with a reduction in weight compared to commercially available brake linings. However, the reproducibility of this study was highlighted by the author as the fly ash was specific to their supplier and would vary with region. Furthermore, the focus of the study was to demonstrate that brake linings with greater than 25wt% of fly ash could be fabricated, and very little work was done to characterise the wear profile and surface properties of the samples.

1.2 Aim and Objectives of the Study

The aim of this study is to investigate the mechanical and tribological properties of Al-matrix syntactic foams manufactured with ASW by pressure infiltration casting.

The objectives of this study are:

- To study the composition, morphology and mechanical properties of ASW provided by Ultromex Limited, UK.
- To fabricate different types of Al/ASW syntactic foams using pressure infiltration, along with a MMSF with one other commercially available ceramic microsphere (CM).
- To explore the compressive and energy absorption properties of the syntactic foams under quasi-static and dynamic (drop hammer impact) loading conditions.
- To investigate the flexural properties of the as-manufactured syntactic foams under static (three-point bending) and impact loading (Charpy test) conditions.
- To investigate the tribological properties of the Al/ASW and Al/CM syntactic foams under dry and lubricated conditions.
- To understand the friction and wear behaviour of syntactic foams.

1.3 Outline of the Thesis

Chapter 2 of this thesis looks at the literature relevant to this body of work, which includes a review of the aluminium processing industry, the difficulties of working with ASW, the manufacturing processes, mechanical properties and applications of cellular solids, metal matrix composites, polymer matrix and metal matrix syntactic foams. A closer look at the tribological properties of composites is also provided in this section.

Chapter 3 provides a detailed report on the experimental procedures used in this work. This includes the properties of the commercially available ceramic microspheres and the Al alloy used in this study, the procedures for characterising the ASW, the fabrication process of the various syntactic foams, the methods for conducting the density measurements, microstructural images and observations, quasi-static compressive tests, drop hammer impact tests, three-point bending tests, Charpy tests, friction and wear tests and surface characterisation.

Chapter 4 presents the results obtained from the experiments conducted for this study, including ASW characteristics, the density, microstructure, compressive, flexural and impact behaviours of the ASW/Al syntactic foams, with a more detailed description provided for the friction and wear properties and surface characteristics. The results of the ASW/Al syntactic foam samples are compared to the Al/CM syntactic foams wherever applicable. The effect of heat treatment of the syntactic foams as well as the effect of heating the ASW is also described in this section, with a look at the changes in compressive, energy absorbing, impact, flexural, Charpy, friction and wear and surface properties.

Chapter 5 provides a conclusion for this body of work, with a summary of the relevant results and findings of this study. Recommendations are also provided for future work.

Chapter 2 LITERATURE REVIEW

Metal matrix syntactic foams (MMSFs) are a type of composite material that have unique mechanical properties. Mechanical behaviours of several similar materials, including closed-cell metal foams, metal matrix composites, reinforced foams and polymer matrix syntactic foams, have been studied in the past. All these materials have characteristics that separate them from one another, yet they have certain similarities that allow us to compare them where necessary. This chapter begins by evaluating the other types of composite materials and foams, followed by an overview of the characteristics of hollow particles and filler materials, and onto a critical evaluation of the MMSFs. A focus is provided on the properties of all classes of materials discussed in this chapter, with a bigger focus on MMSFs.

2.1 Porous Metals and Composite Foams

2.1.1 Closed-cell metal foams

Closed-cell metal foams are a class of lightweight cellular material with tailorable and desirable properties for lightweight, energy absorbing and thermal management structures (Ashby, 2000). There are currently several metal foams available in industry made using a range of different metals, including zinc, copper, lead, bronze, titanium, steel, gold, aluminium, magnesium, and nickel (Ashby, 2000; Diao, Xiao and Zhao, 2015; Capek and Vojtech, 2011; Degischer and Kriszt, 2002). Al-alloy foams have been explored heavily for commercial applications due to their low cost, low density and desirable properties (Duarte, 2012). The properties of closed-cell foams can be altered by changing the pore size, pore shape and porosity (Gupta and Rohatgi, 2015).

Figure 2-1 displays the microstructure of a closed-cell metal foam. The “closed-cell” naming is because the pores within the structure are not interconnected and are therefore encapsulated by the metal matrix. One of the challenges during fabrication is controlling the shape of the pores, which can lead to directional properties that may not be desirable (Ashby, 2000).

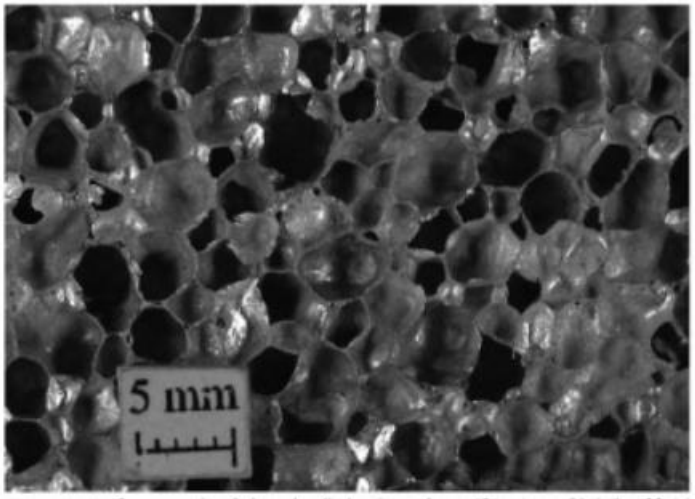

Figure 2-1: Micrograph of a closed-cell Al foam (Gupta and Rohatgi, 2015)

2.1.1.1 *Fabrication processes*

Fabrication processes can be generally classed into two groups: direct and indirect foaming (Banhart, 2001). The direct foaming, or melt, methods start with the molten metal with evenly distributed ceramic particles, and the pores are generated either chemically (blowing agent decomposition), direct gas injection, or gas precipitation. The indirect foaming, or powder metallurgy (PM), methods involve more pre-fabrication preparations where the precursors are formed first before being heated to create a foam. The pre-foaming particles consist of dense powders in which the blowing agent is uniformly dispersed in the metal matrix (Duarte, 2012).

Several commercially available Al foams exist today. The Cymat Aluminium Corporation (Canada) use the direct gas injection method to manufacture “stabilised aluminium foams” on a large-scale (Duarte, 2012). Liquid melts are generally difficult to foam by introducing bubbling air into them. Therefore, ceramic particles, such as SiC, Al_2O_3 and MgO, are used to alter the foaming properties of the melt by increasing its viscosity, leading to a more stable foam produced because of the ceramic particle presence (Duarte, 2012). This process is the most cost-effective way of producing a foam with high throughput volumes and low densities. The biggest disadvantage however is the control of cell size and quality of foam produced, where the foam is produced with irregular cell sizes and density gradients. The process also requires secondary operations, such as machining and cutting larger foam samples after foaming, which can be difficult owing to the high ceramic content present in the foams (10-30vol%) (Duarte, 2012). Hütte Klein-Reichenbach G.m.b.H company (Austria) produces and commercialises foams using a similar technique with uniform cell sizes called MetComb (Duarte, 2012). The gas injection process is shown in Figure 2-2.

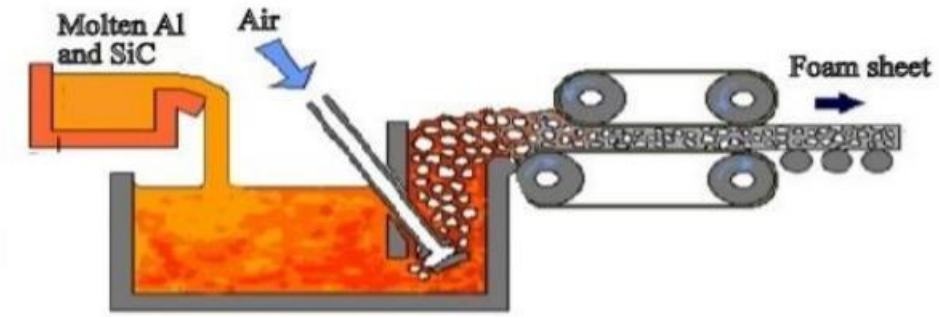

Figure 2-2: Gas injection fabrication process (Mahajan and Jadhav, 2015)

Another direct method for foaming melts is by adding a blowing agent to the liquid melt, which decomposes upon heating to release gases that speed up the foaming process (Duarte, 2012). One such batch casting commercial process is utilised to produce “Alporas” foams in volumes reported of up to 1000kg per day by Shinko Wire Company (Japan) (Miyoshi *et al.,* 2000). In the Alporas process, 1.5wt% calcium metal is added to the molten Al melt at 680^{o}C and stirred continuously until the required viscosity is reached through the oxidation of calcium. Next, titanium hydride is added (typically 1.6wt%) as the blowing agent, which releases hydrogen and causes the foam to expand, gradually filling the vessel. The pressure typically used is in the range of 20-50 atms. After the setup cools and depressurises, the mould is removed and the foam is sliced to various thicknesses (Duarte, 2012). The final structure is more uniform when compared to the gas injection process product but is more expensive and requires more complex processing equipment (Duarte, 2012). Figure 2-3 displays the schematic for this process.

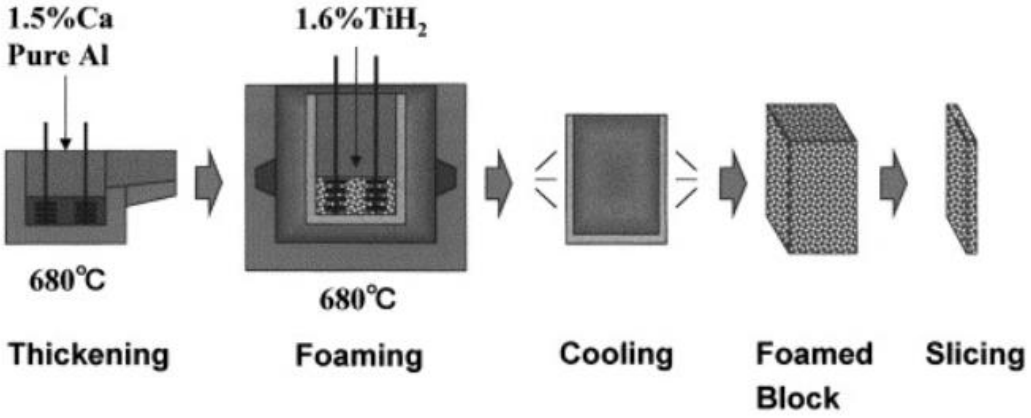

Figure 2-3: Liquid melt foaming method (Banhart, 2001)

For the powder metallurgy route, alloy or metal powders are mixed with powdered blowing agents to produce a uniformly distributed precursor material, which is then hot compacted to produce the resultant foam. The heat allows for the metal to expand while developing an internal closed-cell porous structure owing to the concurrent decomposition of the blowing agent. The resultant liquid foam is cooled in air, which produces a solid foam with superior mechanical properties and foam porosities of up to 90% (Duarte, 2012). The materials in this process are combined without any other chemical additives with good surface finishes, however it is costly to produce foams using this method due to the powder prices and it is difficult to control the pore structure (Duarte, 2012). Figure 2-4 shows the foam production process via the PM route.

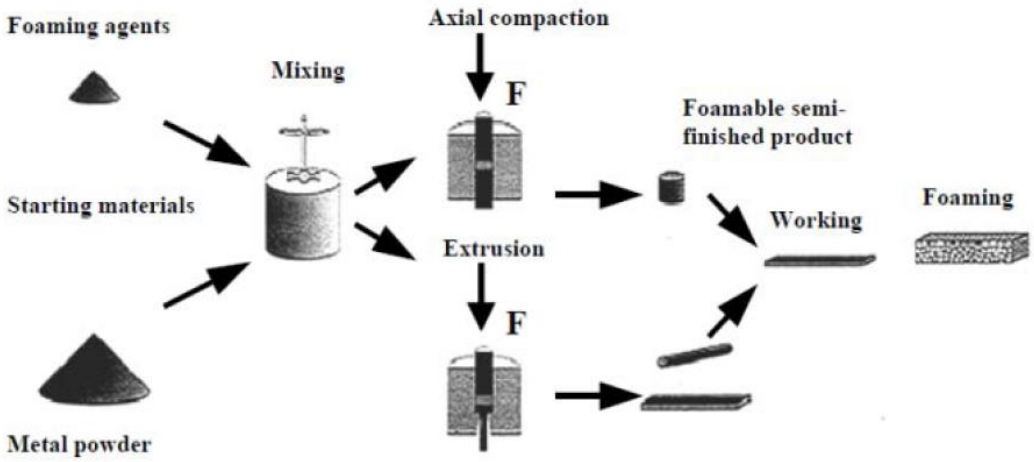

Figure 2-4: Foam production via PM route (Mahadev, Sreenivasa and Shivakumar, 2018)

2.1.1.2 *Applications*

Metal foams are strong, stiff and lightweight structures with enhanced energy absorbing capabilities that make them useful within the automotive and aerospace industries (Mahadev, Sreenivasa and Shivakumar, 2018). Even though there are various methods for manufacturing metal foams, metal foams find applications find use in less demanding markets due to concerns related to final product quality (Duarte, 2012). Figure 2-5 shows examples of structures made using metal foams. These structures are further enhanced by special casting techniques to produce sandwich structures with desirable properties. The small amount of metal present (<40%) reduces thermal conductivity but can retain sufficient electrical conductivity. Due to the foamed nature, the products also show resistance to damage and high energy-absorbing capabilities (Ashby, 2000).

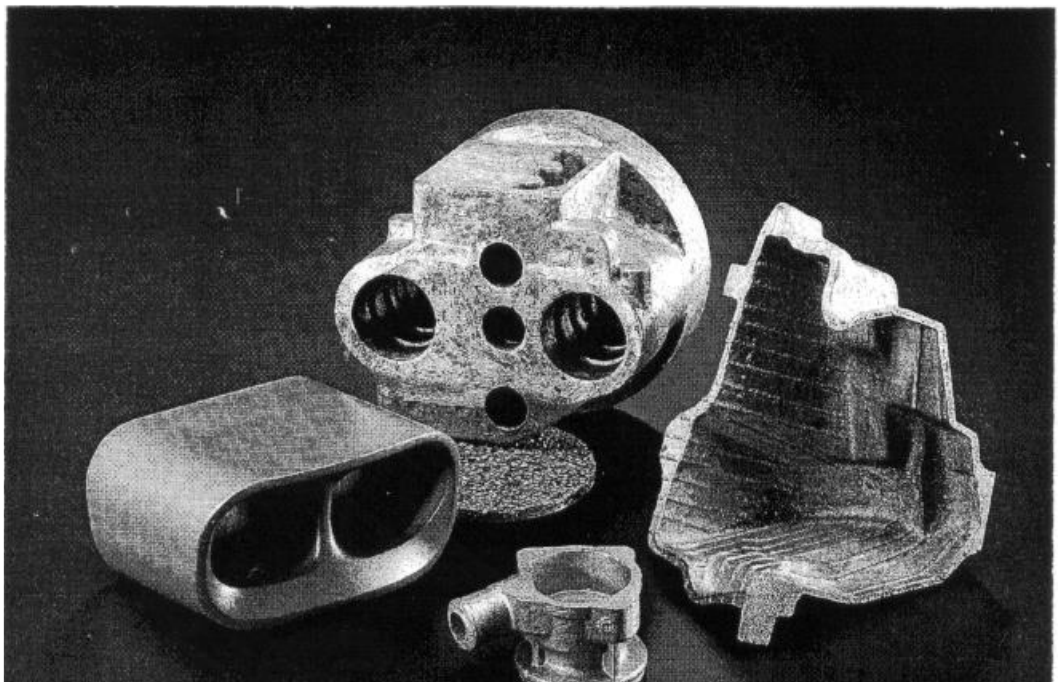

Figure 2-5: Foamed Al components with integral skins for car parts (Ashby, 2000)

2.1.2 **Metal matrix composites**

Metal matrix composites (MMCs) are a class of material that consists of two phases where one phase is distributed in another continuous phase. In the case of MMCs, the continuous phase is the metal matrix and the distributed phase can be particles, short fibres or sheet laminates/monofilaments (Chawla and Chawla, 2013), as described in Figure 2-6 . The combination of two phases with different properties and shapes allows for MMCs to have properties that the individual phases do not have (Nishida, 2013).

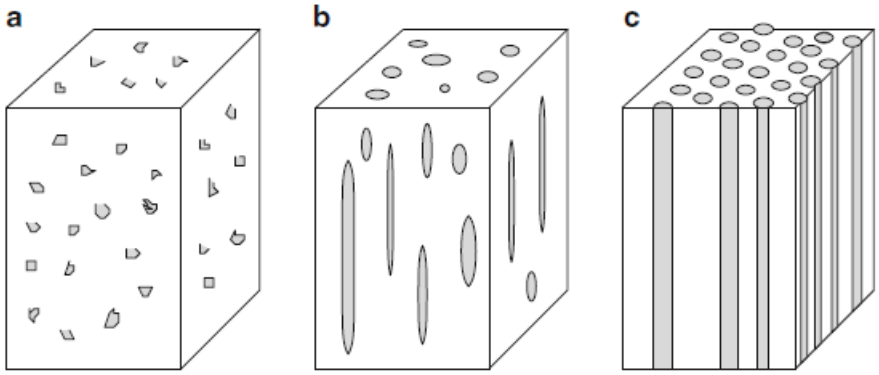

Figure 2-6: Classification of composites as (a) particular reinforced, (b) discontinuous/short fibre reinforced and (c) continuous fibre/sheet laminate reinforced MMCs (Nishida, 2013)

Most reinforcements for MMCs are made up of either alumina, SiC or carbon, depending on the type of reinforcement and the fabrication method used (Nturanabo, Masu and Kirabira,2020; Yue, 2019).

2.1.2.1 *Fabrication*

Fabrication methods for incorporating fibres or particles into metals can be split into 4 categories: solid-state fabrication (powder metallurgy and metal foils), liquid-state fabrication (molten metal mixes), gas-state fabrication (chemical or physical vapour deposition) and in-situ fabrication (external treatments) (Nishida, 2013).

For the PM method, particle or fibre reinforcements are evenly dispersed in a metal powder or foil and the mixture is sintered to form a composite. There are two ways to fabricate MMCs using the PM method: the wet method and the dry method. The wet method uses a solvent with low surface tension and latent heat of evaporation, which allows for the mix to dry easily, such as industrial ethanol. The fibre and metal powders are mixed into the solvent, allowed to settle and then decanted to remove the solvent. The resultant mix is then dried in a water bath. The dry method, where a solvent is not required, has the advantage of avoiding these initial steps. A ball mill is instead used to mix the powders and obtain a uniformly distributed powder. From here, the final mixture is degassed, canned and sintered to produce the composite (Nishida, 2013). The schematic of the process is show in Figure 2-7.

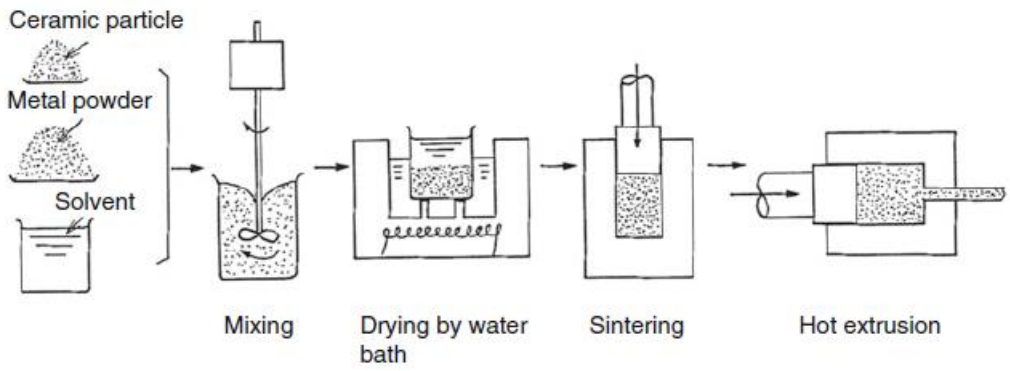

Figure 2-7: Fabrication of particulate MMCs via PM route (Nishida, 2013)

The advantage of using the PM method is that the wettability of particles is not an issue, so relatively good distribution of fibres in the metal is obtained. However, it is still challenging to disperse ceramic particles into metal particles and the ideal way to obtain uniform distribution is by using comparable particle sizes of both (Nishida, 2013).

Another solid-state fabrication method is known as diffusion bonding, where continuous fibres are placed on a metal foil sheet with a second sheet placed on top of the fibres. This is continued until a composite stack is formed, after which the contents are degassed and sintered under high pressure to produce a composite (Figure 2-8). The sintering in this process is important to remove all voids from the stack (Nishida, 2013). The process is useful to fabricate directional MMCs.

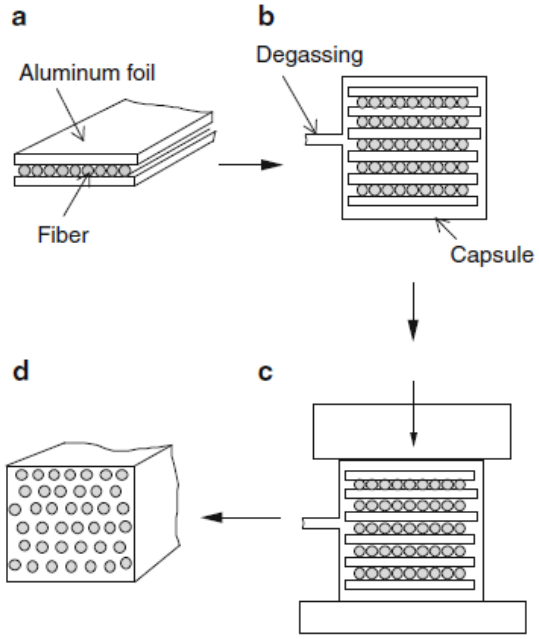

Figure 2-8: Diffusion bonding process by using metal foil (a) units of fibres and foils, (b) fibre stack in a capsule for degassing, (c) sintering under high pressure, (d) continuous fibre reinforced composite (Nishida, 2013)

The liquid state fabrication methods involve mixing reinforcements, usually ceramic particles, into a molten metal in an inert gas atmosphere. Ceramics tend to have poor wettability in many molten metals, one notable exception being magnesium (Nishida, 2013), so the wettability is improved by either adding a chemical coating, such as nickel or copper, on the surface of the ceramic particles or by using a sufficient amount of energy to overcome the resistance. When using chemical coatings, the molten metal is strongly agitated to generate a vortex which is maintained until the ceramic particles are well dispersed in the molten mix. The wettability of the molten metal has been found to improve by the addition of metals such as Ca, Mg or Li to the mix (Nishida, 2013). The vortex technique is not energy efficient, but it does allow for the wetting to be improved in the mix. Figure 2-9 shows a schematic of this process.

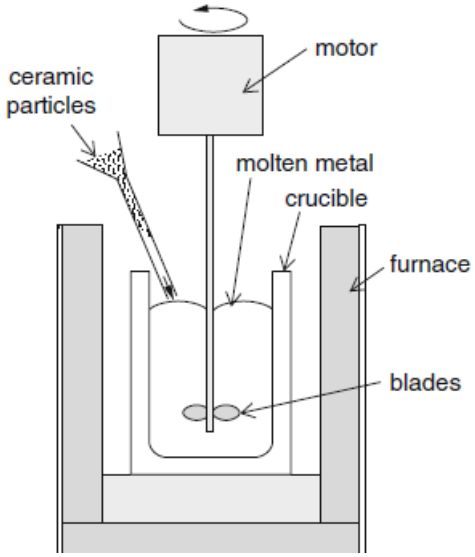

Figure 2-9: Composite production by vortex addition technique (Nishida, 2013)

The mechanical liquid state fabrication method that has been used commercially is "squeeze casting". In this process, the molten metal is added to a preform of particles or short fibres in a mould and high pressure is used to force the mixing to occur with the aid of a mechanical punch. The infiltration pressure needs to be well controlled to avoid the fibres or particles being deformed but also to occupy the voids and interstices between them. In some cases, where the fibres are compacted before infiltration, some voids are left because the required pressure cannot be achieved to infiltrate the smaller gaps. Figure 2-10 shows the general squeeze casting process.

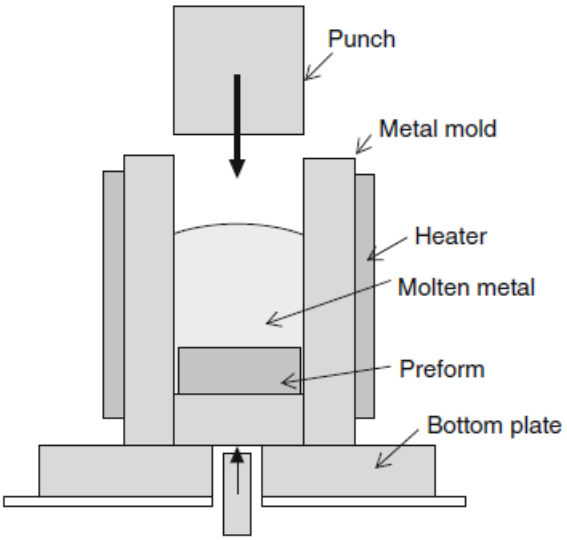

Figure 2-10: Squeeze casting process (Nishida, 2013)

Gaseous state fabrication methods are suitable for generating thin film composites. They work by depositing a substance in the gaseous state on the surface of a substrate. The methods are classed into Chemical Vapour Deposition (CVD) and Physical Vapour Deposition (PVD) processes.

In the CVD process, materials in the gaseous phase react on the surface of a hot substrate, resulting in a solid deposition on the substrate. There are three ways to make this reaction occur: using hydrogen in the gaseous phase as a catalyst to reduce metal halides, gaseous phase thermal decomposition and substrate reactions with the gaseous phases (Nishida, 2013). The process is temperature dependent and Figure 2-11 displays an example of one apparatus that has been used to produce thin film coatings of composites.

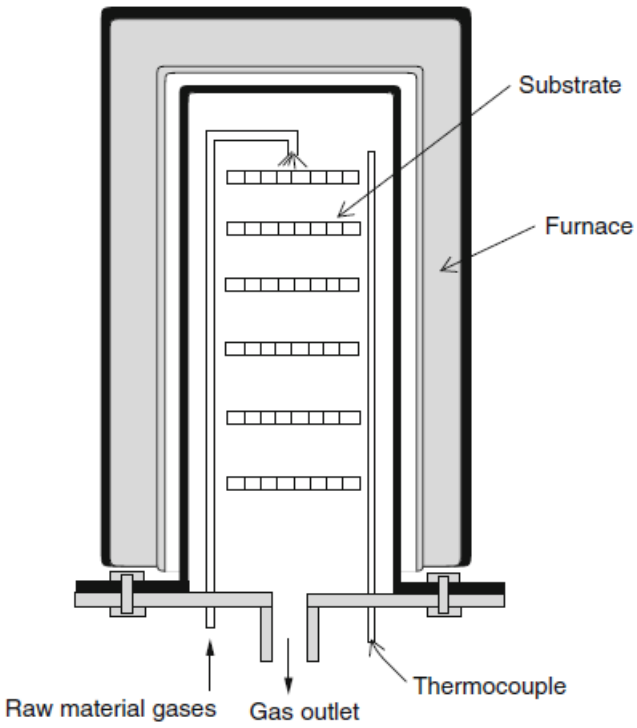

Figure 2-11: Hot wall type apparatus for CVD method (Nishida, 2013)

In the PVD process, either electrical resistive or electron beam heating is used to evaporate a material in a vacuum before it is deposited onto the substrate. One of the PVD methods developed, known as sputtering, involves using ion bombardment to release atoms and/or clusters from a material and depositing it onto the substrate. Atoms or ions are generated from either elements in plasma, such as argon, oxygen, or nitrogen, or by using an ion beam from an ion source chamber (Nishida, 2013). The former leads to a significant rise in temperature of the substrate, whereas the latter uses a lower pressure and allows for more control of the substrate surface conditions (Nishida, 2013).

2.1.2.2 *Applications*

Al Alloy MMCs have found uses in various industries due to the improved properties, as opposed to the native metal, and can replace heavier materials such as ferrous, aluminium and titanium alloys. They are also used as a replacement for polymer composites due to their improved mechanical properties (Nturanabo, Masu and Kirabira,2020).

Al MMCs produced using both solid and liquid-state fabrication methods have been manufactured with reinforcements including SiC, Al_2O_3, TiC, TiB_2 and B_4C for applications in the automotive and aerospace industries. Al MMCs have found specific uses in braking systems, valves, crankshafts, gear parts and suspension arms for automobiles, as well as flight control hydraulic manifolds, ventral fins, fuel access cover doors and rotating blade sleeves for aircrafts and helicopters (Nturanabo, Masu and Kirabira,2020). Short fibre-reinforced Al MMCs have found use in track shoes in military tanks as well as in pistons and cylinder liners (Nturanabo, Masu and

Kirabira,2020). Continuous fibre-reinforced Al MMCs have been used to make antenna waveguides for the Hubble Space Telescope due to their high thermal and electrical conductivity, superior dimensional accuracy and resistance to oxidation (Nturanabo, Masu and Kirabira,2020). Figures 2-12, 2-13, and 2-14 show various components made from Al MMCs.

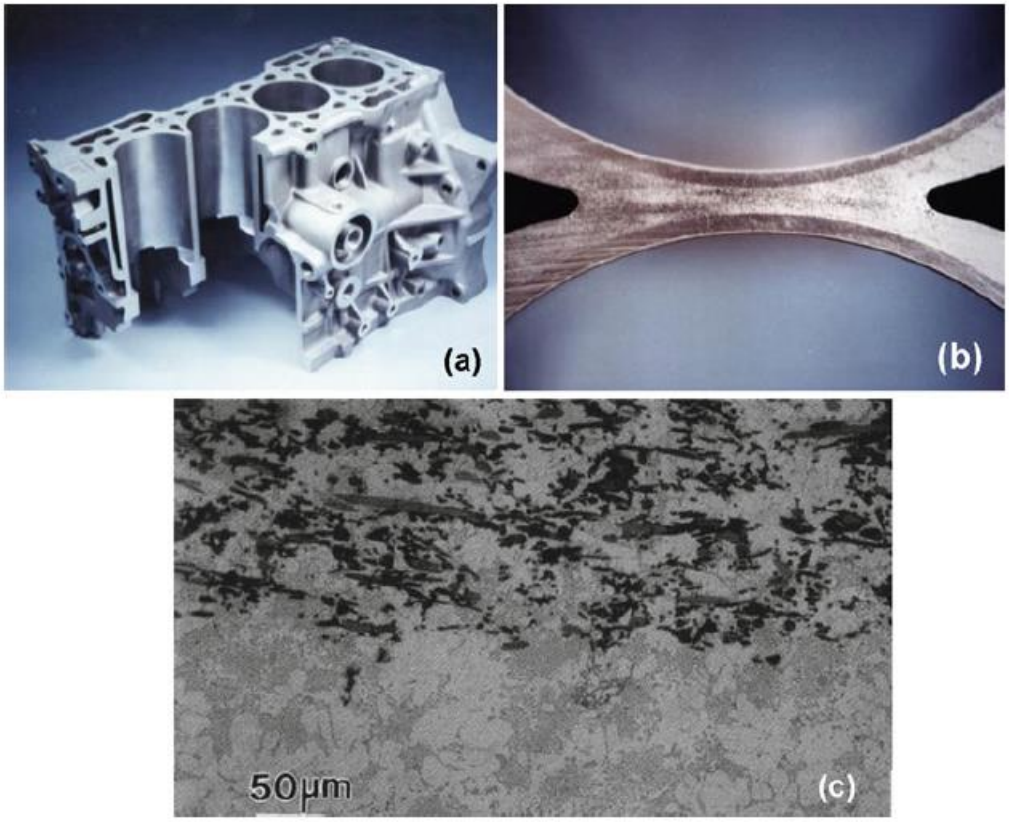

Figure 2-12: Hybrid particulate reinforced Al-MMCs used as a cylinder liner in the Honda Prelude (parts (a) and (b)), and (c) microstructure of composite showing carbon (black) and alumina (dark grey) fibres (Chawla and Chawla, 2013)

Figure 2-13: Particulate MMCs for use in brake drums and brake rotors, as a replacement for cast iron (Chawla and Chawla, 2013)

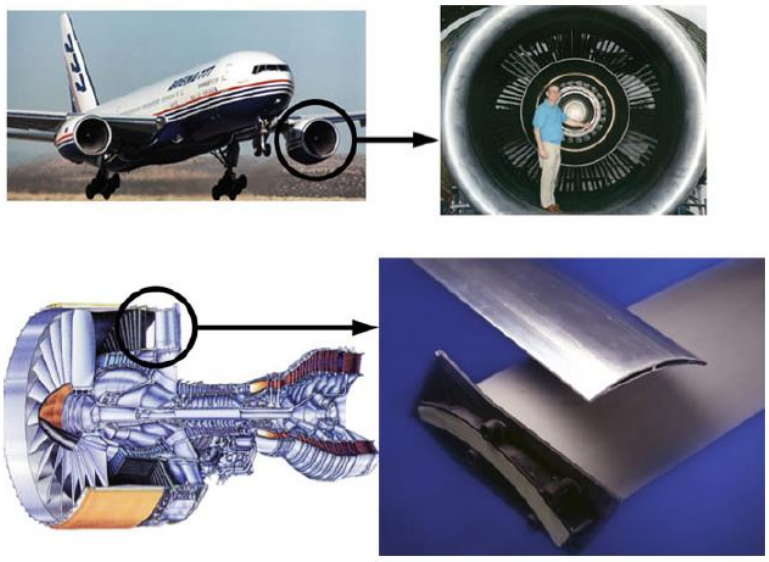

Figure 2-14: Application of a SiC particle reinforced Al MMC in the fan-exit guide vane of a Pratt & Whitney engine on a Boeing 777 (Chawla and Chawla, 2013)

2.1.3 **Polymer matrix syntactic foams**

Several industries look for lightweight materials with high specific strength that can be tailored for structural applications. A syntactic foam is a type of composite foam where hollow or porous particles, often called microspheres, are incorporated into a continuous phase, known as the matrix. In polymer matrix syntactic foams (PMSFs), the continuous phase is polymeric in nature, such as epoxies, phenolics, cyanate, esters, bismaleimides, unsaturated polyesters, and polyurethanes (John and Nair, 2010). In some cases, a binder material is also incorporated to either harden or lower the viscosity of the matrix (C. Karthikeyan, Sankaran and Kumar, 2001). The main limitation for not using polymer matrices is their relatively lower strength compared to metal matrices. Figure 2-15 shows the microstructure of a PMSF.

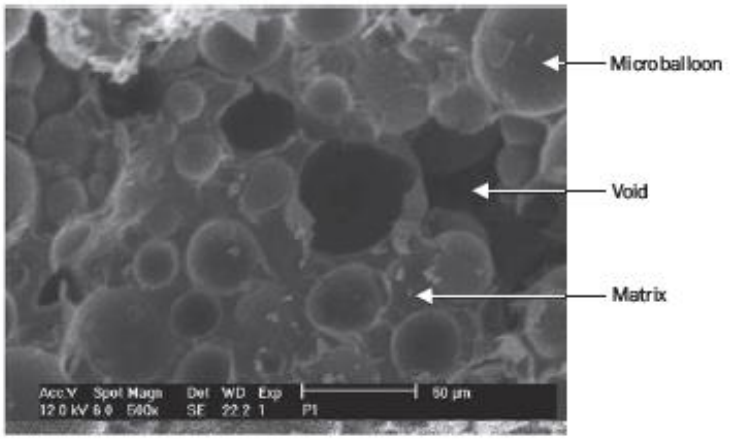

Figure 2-15: Microstructure of PMSF (John and Nair, 2010)

2.1.3.1 *Fabrication processes*

The manufacturing conditions, such as the composition and concentration of the matrix and microspheres respectively, the temperature, mixing time and addition sequence dictate the method used to fabricate PMSFs. Methods range from simple

mixing to coating methods (Klempner and Sendijarevic, 2004). In all cases in which a binder is used, the material must have desirable properties that enhance the fabrication of the foam (Klempner and Sendijarevic, 2004).

One way of fabricating PMSFs is by the infiltration method described for MMCs above. The difference here is that the penetration of the polymer can be achieved without high pressures and in a vacuum. The binder material is added to the mixture to allow for the contents to harden. This method is less energy intensive, but has several disadvantages. For instance, the process can bring about several defects and non-uniformities in the structure (John and Nair, 2010). Solid-state fabrication is also possible with PMSFs when the resin is available as a powder. In this case, the two powders are mixed with a binder material, pressed, and cured. Alternatively, microspheres can be added to a thermoplastic melt and extruded or kneaded. The main drawbacks of this method come from the small size of the microspheres, which causes environmental concerns. The microspheres may also break during the pressing stage or due to rough handling. This method is particularly useful for preparing relatively higher density PMSFs (John and Nair, 2010).

A coating method has been used to fabricate PMSFs to achieve a uniform resin coating and distribution in the final product. First, the polymer solution is adsorbed onto the surface of the sphere to obtain a slurry. This is then vacuum-filtered and rinsed with liquids to simultaneously precipitate the polymer and remove the solvent. Finally, vacuum-drying the contents delivers a moulding powder of distinct particles (John and Nair, 2010).

2.1.3.2 *Applications*

PMSFs have found a significant use in deep submergence buoyancy due to their low water absorption and compressive properties. Glass-microsphere syntactic foams have been successfully employed in this application because of their desirable strength properties. The ability to control the volume fraction of microspheres in the syntactic foams allows for the control of buoyancy (John and Nair, 2010). Figure 2-16 shows a syntactic foam being used in this manner.

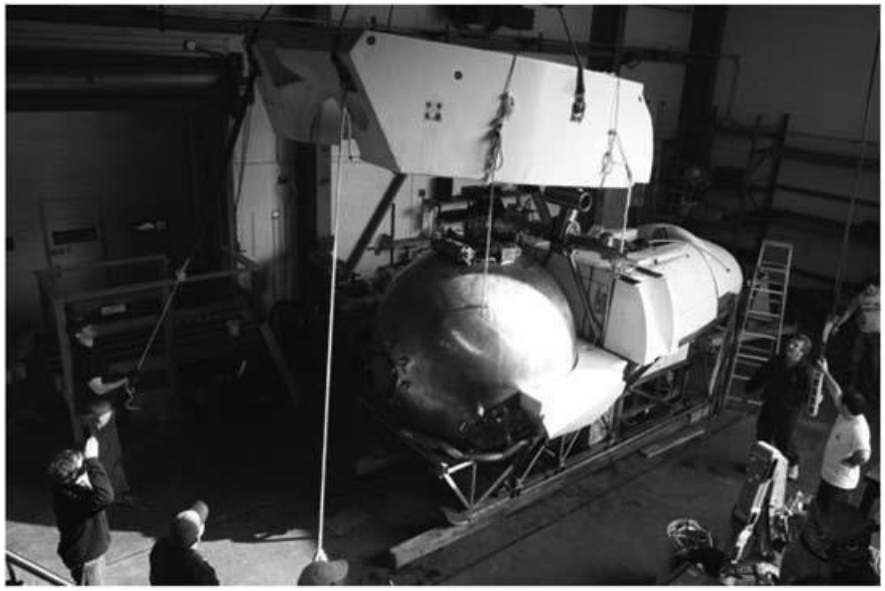

Figure 2-16: A 2,218 pound piece of syntactic foam used in Alvin. Alvin Overhaul, Oceanus, Woods Hole, MA, USA, 2005 (John and Nair, 2010)

PMSFs have also found use as thermal insulators for deep-water subsea components, such as pipelines, valves, jumpers, and manifolds. Demand for PMSFs in the aerospace industry exists due to their low dielectric constants and enhanced transition temperatures, depending on the resin material used (John and Nair, 2010). PMSFs have found great use as lightweight, high-specific strength materials in the sports industry. Bayer and Adidas produced high-tech soccer balls for the UEFA Euro

2004 Championships, known as ‘Fevernova’ (A to Z of Materials, 2004; McClusky, 2005). Figure 2-17 shows a schematic of ‘Fevernova’, where all layers are made of Bayer’s Impranil® Polyurethane (PU).

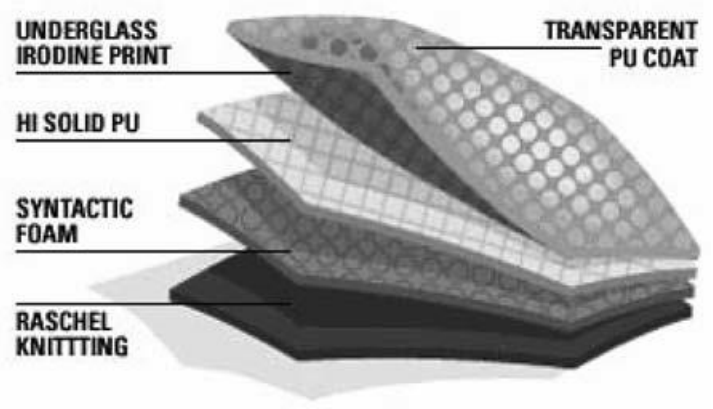

Figure 2-17: Different layers present in ‘Fevernova’ (John and Nair, 2010)

2.2 Hollow Particles and Filler Materials

Hollow particles and filler materials are used to fabricate syntactic foams, whether with a polymer or metal matrix. These can be engineered particles made of ceramic, metal or glass, or can be processed by-product materials such as fly-ash cenospheres. MMSFs generally use hollow spheres of alumina, mullite, fly ash, nickel, or steel. Figure 2-18 shows an image of hollow particles manufactured by Deep Springs Technology (DST) (Gupta and Rohatgi, 2015).

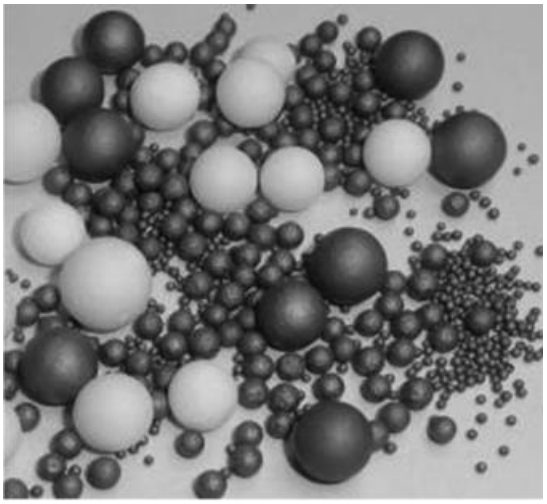

Figure 2-18: Commercially available hollow particles (Gupta and Rohatgi, 2015)

Hollow spheres can be made by injecting slurries and a gas through a coaxial nozzle, from a template or can simply be obtained as a by-product of a different process.

The coaxial nozzle method utilises powders with diameters of 1-10 µm in a slurry, which are injected via an inlet of a coaxial nozzle and simultaneously encounter a gas flow through an inner jet forming bubbles. The slurry leaves the nozzle as a cylinder which eventually forms into a sphere. Production rates of up to 15,000 spheres/min have been reported (Gupta and Rohatgi, 2015).

The template method makes use of a “core”, which is coated with the required material. The structure is then pyrolyzed to leave behind a hollow particle with the coating, which is eventually sintered for hardening and used as a hollow microsphere (Gupta and Rohatgi, 2015).

Cenospheres can be obtained from coal-fired boilers as by-products as molten silica encapsulates bubbles of gas as it solidifies. Fly ash is a by-product of coal combustion and contains between 0.01-1% cenospheres, which are used as fillers in a variety of materials, such as low-density concrete, plastics and composites for bowling balls, kayaks, surfboards and automotive components (Gupta and Rohatgi, 2015). The biggest drawback is separating the cenospheres from the impurities found in other accompanying particles from coal combustion. This separation adds an additional cost to it for what would have been a free material (P. Rohatgi *et al.,* 2011). Furthermore, the specifications of fly ash cenospheres are dependent on the conditions they are created from. Typically, colour ranges from white to grey, diameters are between 5-500 micron, true density is between 0.35-0.90 g/cc (CenoStar, 2020) and they mostly contain silica, alumina and iron oxide (Fe_2O_3) (Gupta and Rohatgi, 2015). Figure 2-19 displays an image of cenospheres obtained from Tolsa, USA.

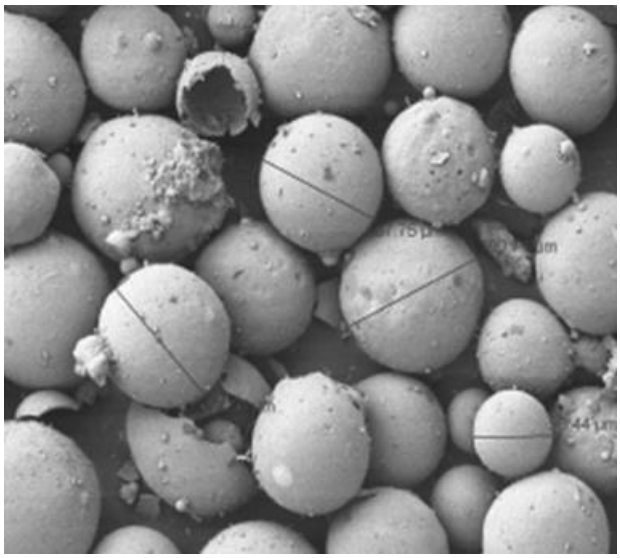

Figure 2-19: Fly ash cenospheres from Tolsa, USA (Gupta and Rohatgi, 2015)

2.3 Introduction to Metal Matrix Syntactic Foams

Like PMSFs, MMSFs are a class of syntactic foam where hollow or porous particles are dispersed in a continuous phase. Unlike PMSFs, the continuous phase in the MMSFs is metallic in nature. Several metal matrices have been studied, including titanium (X. B. Xue *et al.,* 2010; Mondal, Datta Majumder *et al.,* 2012) and magnesium (Newsome *et al.,* 2015). However, most MMSFs tend to incorporate an aluminium alloy as the metal matrix due to its relatively low melting point and lightweight nature. Figure 2-20 displays a micrograph of an Al alloy syntactic foam.

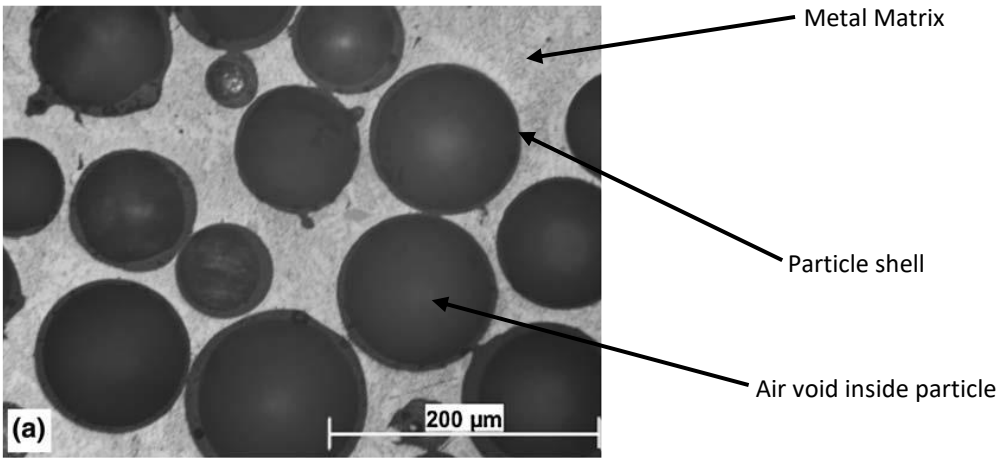

Figure 2-20: Micrograph of Al alloy syntactic foam with hollow microspheres (Orbulov, Dobranszky and Nemeth, 2009)

MMSFs have generated more interest over the past decade because of the ability to control the volume fractions of matrix and filler material in the final product as that can bring about useful properties with cost-cutting real-world applications. Choice and control of characteristics of filler materials such as particle size, volume fraction,

porosity, morphology, density and wall thickness can lead to important changes in different foam properties (Gupta and Rohatgi, 2015).

2.3.1 **Fabrication processes**

The fabrication of MMSFs is very similar to the techniques used to manufacture MMCs. The two major classes of production are solidification processing and powder metallurgy processing. Solidification processing techniques can be split into two specific methods – melt infiltration and stir casting.

For the melt infiltration technique, a set volume of particles are placed in a mould and loosely packed to allow for infiltration to take place. The molten metal is then infiltrated into the mould by applying an external high pressure, a vacuum, or both. The pressure allows for the melt to infiltrate the interstices of the particles before solidifying and forming the syntactic foam (L. P. Zhang and Zhao, 2007). This process is particularly useful for generating syntactic foams with high volume fractions of filler materials. However, the infiltration pressure can cause rupture of the particles, which can degrade the quality of the final syntactic foam. Furthermore, it is necessary to closely control the operation parameters. For instance, the infiltration pressure and temperature of the mould cannot be too low, otherwise the infiltration will be incomplete and the melt will solidify too soon, or too high, or else the particles will rupture and the melt will infiltrate the pores or air pockets within the particles (Gupta and Rohatgi, 2015). Figure 2-21 shows two setups for the melt infiltration process.

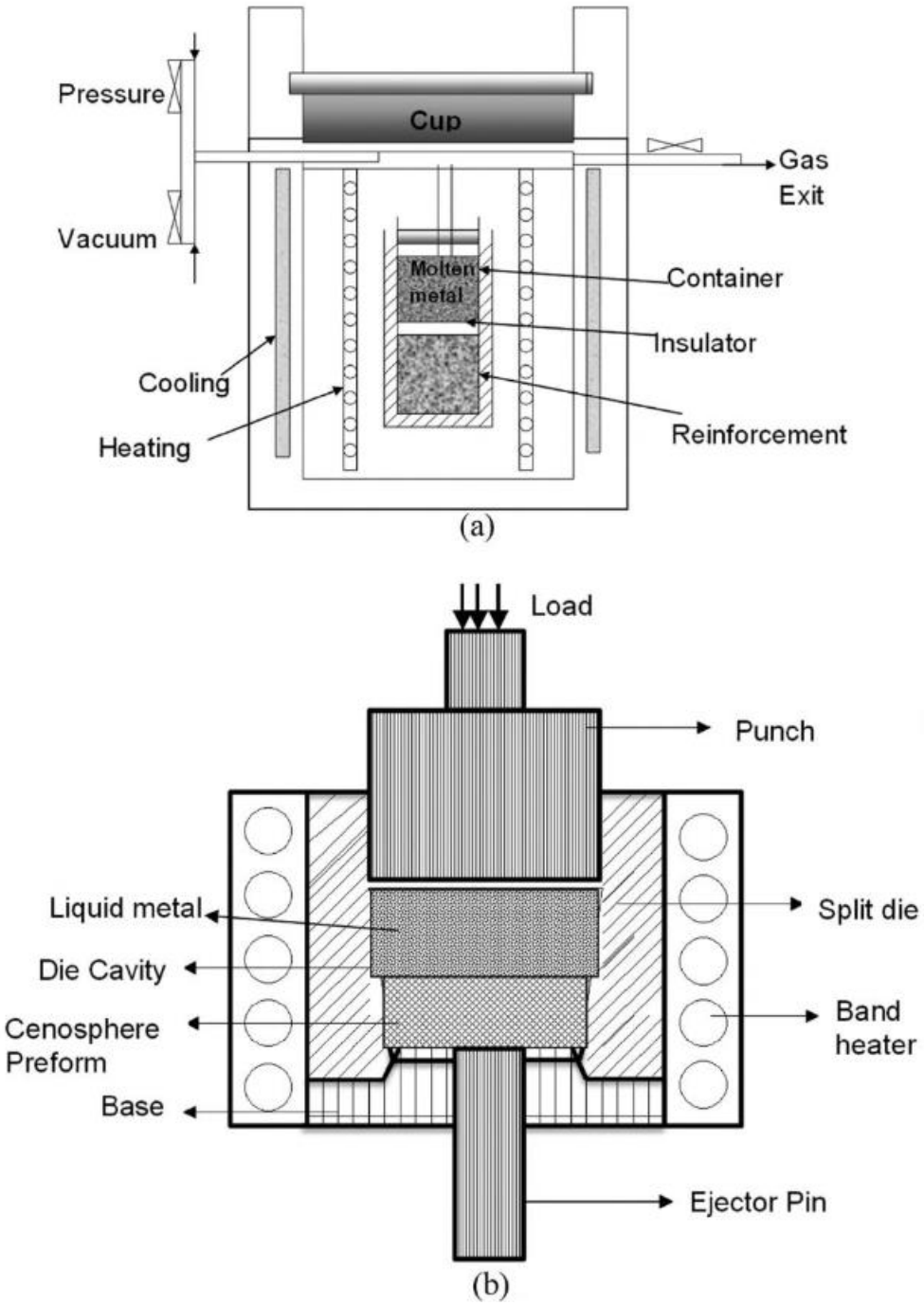

Figure 2-21: Infiltration setup (a) through direct application of pressure over the melt and (b) through gas pressure (Gupta and Rohatgi, 2015)

The stir casting technique involves adding the required amount of filler material to the molten metal which is maintained at a constant temperature. The mix is stirred

continuously, creating a vortex which forces the particles into the melt (Rajan *et al.,* 2007). The resultant mix is placed in a pre-heated mould and left to solidify. This process is easy to implement due to its low costs and can be used to fabricate syntactic foams with varying particle volume fractions. The downside is that low-density particles will float to the top of the melt and form a layer, especially at low volume fractions. At higher particle volume fractions, the mixing can cause particle rupture. Wettability is also a concern, since no external pressures are applied to force the wetting of particles (Gupta and Rohatgi, 2015). Figure 2-22 displays a schematic for the stir-casting process.

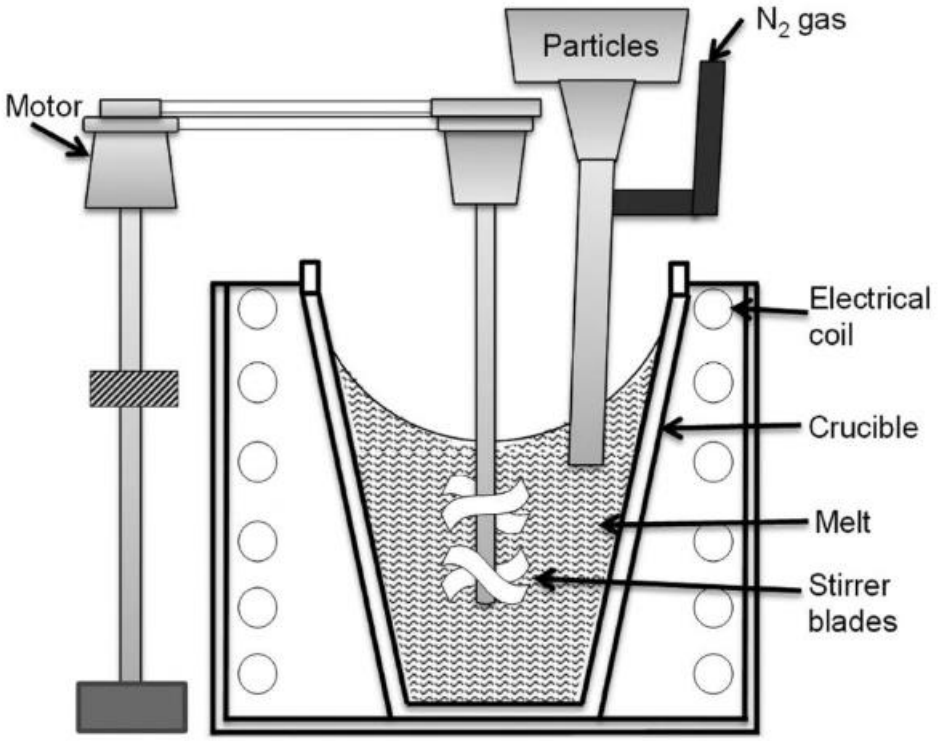

Figure 2-22: Stir-casting process schematic (Gupta and Rohatgi, 2015)

In the PM process, the matrix metal is combined in the form of a powder with the required filler material and, if required, an agent to improve the mixing. Once the mixture is made, it is pressed, outgassed and sintered to obtain a final syntactic foam. The compaction stage can also be done via forging, extrusion or rolling (Gupta and Rohatgi, 2015). The PM process can be used to fabricate MMSFs with reactive metals that cannot be used in their molten state, however the fracture of the particles can be significant in the compaction stage (Gupta and Rohatgi, 2015).

2.3.2 **Applications**

MMSFs are relatively new materials and therefore find many potential applications still in the research phase. For instance, the superior damping capacity of Al-6061 alloy syntactic foams with fly-ash cenospheres compared to the matrix alloy is found to be beneficial in automotive applications (Wu *et al.,* 2006). Al matrix syntactic foams have also been studied for fabricating automotive brake rotors (P. K. Rohatgi, Weiss and Gupta, 2006). The A356/fly-ash (Sudarshan and Surappa, 2008) and Al-6061/fly-ash (P. R. S. Kumar *et al.,* 2010) cenosphere syntactic foam composites have also been found to have better wear resistance when compared to the matrix alloy, which can also be used for similar automotive brake system applications.

2.4 Compressive Properties

There is a current need to fabricate materials that can provide protection from possible terrorist attacks. Lightweight, strong and ductile materials with good compressive and impact resistance properties can be used in manufacturing military vehicles. The most important attributes of structures undergoing plastic deformation after being subjected to a blast or impact are the deformation mechanism and failure mode, the energy absorption capability and the shock wave transfer (Hanssen, Enstock and Langseth, 2002). This section will look at the compressive properties of the materials described above.

2.4.1 Porous metals and composite foams

2.4.1.1 *Closed-cell metal foams*

Several studies have revealed that metal foams perform well under static and dynamic loading conditions, especially when considering their energy absorption capabilities. There has been an increased focus on the impact response of metal foams in the recent years. Liu et al. (2013) investigated the mechanical response and deformation behaviour of Al foams under impact loading and discovered the energy absorption capability of Al alloy foams to be supervisor to that of pure Al foams.

Xia et al. (2014) studied the compressive properties of closed-cell Al foams with different CM content as reinforcements (up to 20%) and found that the addition of CMs to the Al foam significantly improved the yield strength, meal plateau stress, densification strain and energy absorption capacity of the original foams. They also found that the CM content should be limited if energy absorption capacity is to be kept at optimal levels. Peroni, Solomos and Pizzinato (2013) evaluated the impact

behaviour of Al foams using the Split-Hopkinsons Pressure Bar (SHPB) test in the strain range of 100-300 s^{-1} and showed that the foams showed significant dependency on density, with no real effect of strain-rate observed. Ramachandra, Kumar and Ramamurthy (2003) studied the impact response of Al foams with velocities ranging from 3-30 ms^{-1} and found that the energy absorbed increased marginally below velocities up to 10 ms^{-1}, but increased more significantly at higher velocities, suggesting that energy absorption is velocity dependent.

Jang et al. (2015) investigated the mechanical properties of the commercially available ALPORAS closed-cell aluminium foam. The as-received foam blocks were 600 mm x 600 mm x 150 mm. Crushing experiments were conducted using the MTS 810, where two rigid plates were controlled to compress the foam at a quasi-static strain rate of 7.5 x 10^{-4} s^{-1}. Figure 2-23 shows the compressive response of the ALPORAS foam specimen. The curve showed three regions: a linearly elastic region, followed by a plateau and a final densification region.

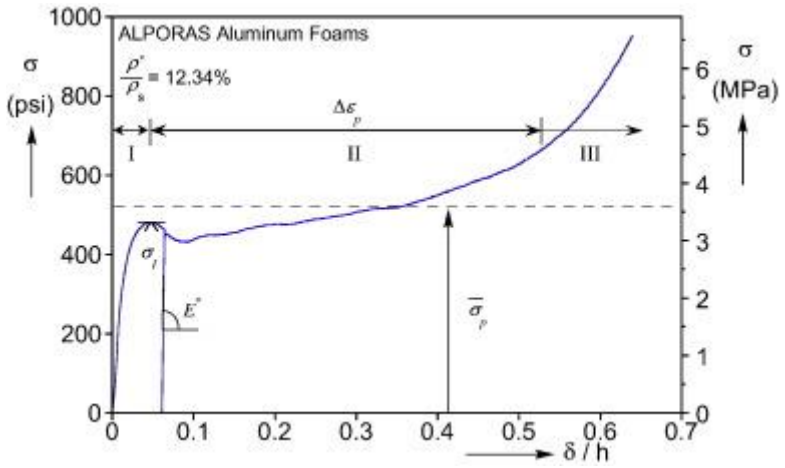

Figure 2-23: Compressive stress-strain response of ALPORAS closed-cell foam (Jang *et al.,* 2015)

In the linear region, deformation was observed to be relatively minimal and many sections remained elastic. As stress increased, the deformation was more evident due to the internal irregularities of the foam structure, until the maximum stress of 482 psi (3.3 MPa) was reached (at 0.0478 strain). After this point, the stress dropped to a plateau and remained near-unchanged for a long period. The deformation was localised and the plateau region is the reason for the foam's energy absorption capabilities (Jang *et al.,* 2015).

2.4.1.2 *Metal matrix composites*

Al and Al-alloy MMCs have been studied extensively to show their suitability in many applications due to their high specific strength, stiffness, stability, and wear resistance. Purohit, Rana and Verma (2012) found compressive strength of Al/SiCp MMCs increased with increasing wt.% of reinforcements. Similar observations were made for Al 2618 alloy and SiC particle reinforcements (Fadhil and Ravikiran, 2016). Lokesh et al. (2018) found that Al 7075 alloy reinforced with 0.5wt% graphene nano-particles demonstrated superior resistance to compressive loads, with a breaking load of 222 kN at 0.60025 strain.

Das et al. (2019) fabricated Al 7075 MMCs with SiC particles using liquid state fabrication route and studied the effect of T6 treatment on their compressive properties. Figure 2-24 shows the fractured MMC specimens after compressive tests. Table 2-1 shows the sample composition of fabricated MMCs. Figure 2-25 shows the effect of thermal treatment, SiC mean particle size and wt.% on the compressive strength of the MMCs. Results showed that the compressive strength increased as the wt.% of SiC particles increased and as particle size decreased. The incorporation

of smaller particles causes an increase of particle count in MMCs, causing the improvement in compressive strength. T6 treatment of samples showed an increase in compressive strength when compared to the non-T6 treated samples.

Figure 2-24: Fractured MMC specimens after compression (Das *et al.,* 2019)

Table 2-1: Sample composition of fabricated MMCs

Sample Number	Mean particle size (µm)	Wt% of SiCp
A1	30.65	5
A2	30.65	15
A3	30.65	25
B1	8.18	5
B2	8.18	15
B3	8.18	25
C1	6.18	5
C2	6.18	15
C3	6.18	25

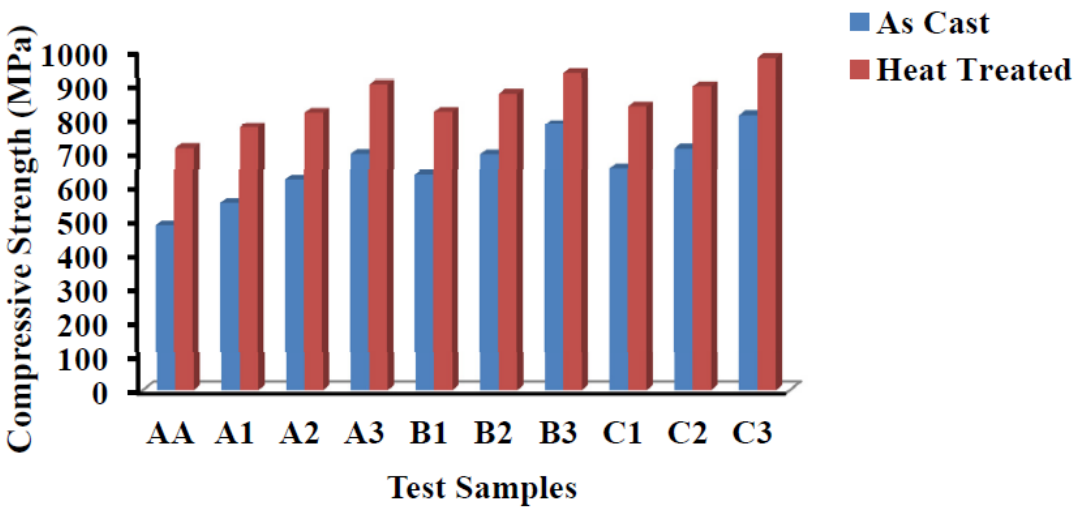

Figure 2-25: Effect of thermal treatment, SiCp wt.% and mean particle size on compressive strength (Das *et al.*, 2019)

2.4.1.3 *Polymer matrix syntactic foams*

The compressive response of PMSFs has been thoroughly studied due to their superior compressive strength, energy absorption and damage tolerance. Swetha and Ravikumar (2011) investigated the compressive behaviour of epoxy syntactic foams with hollow glass microspheres and found that the compressive strength and elastic modulus decreased as wall thickness of the microspheres increased. Ahmadi et al. (2015) studied the compressive behaviour of epoxy syntactic foams with ceramic microspheres at strain rates ranging from quasi-static to high-strain rates. They found that as the microsphere volume fraction increased, the compressive strength, compressive modulus, failure strain and plateau stress decreased for all samples at all strain rates. Studies have also shown that mechanical properties such as toughness and damage resistance are affected by interfacial bonding strength as well as particle size (Lin *et al.,* 2016; Lin *et al.,* 2017). Song et al. (2005) found that lateral confinements subside crack propagation, increasing the compressive strength and energy absorption capacity.

Fan et al. (2019). Studied the effect of particle size and internal constraints on the compressive behaviour of fly-ash/polyurethane syntactic foams. Syntactic foams with two different size groups (LT: diameter 450 ± 200 µm and wall thickness 30 ± 10 µm; LG: diameter 950 ± 200 µm and wall thickness 50 ± 10 µm) of fly-ash cenospheres were fabricated using the pressure infiltration method at room temperature. Al honeycombs with hexagonal cells were used as reinforcements with side length of 4.0mm and thickness of 60 µm (RLT and RLG respectively). The quasi-static tests were conducted at ambient temperature at strain rates of 10^{-3} s^{-1}, while

the dynamic tests were performed using a modified Split-Hopkinson's Pressure Bar (SHPB) testing system.

Figure 2-26 shows the quasi-static response of the syntactic foam samples with a density of 0.6 gcm^{-3}. All samples display three regions: a linear elastic region referring to the flexible deformation stage, a plateau region indicating the collapse of the polyurethane cells and the microspheres, and a densification region. The LT specimen exhibits a higher compressive strength and plateau stress than the LG specimen. The Al honeycomb reinforcements significantly improve the mechanical properties of the syntactic foams (Fan *et al.,* 2019).

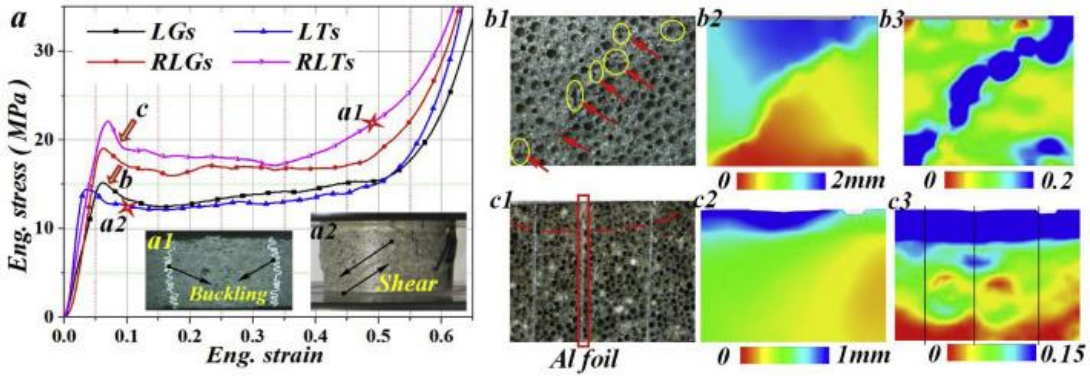

Figure 2-26: Typical compressive response of fly-ash polyurethane SFs under quasi-static loading: (a) stress-strain curves, axial displacement and strain fields of (b) LTs and (c) RLTs specimens (Fan et al., 2019)

The sectional view of an RLT specimen compressed to 50% strain is shown in Figure 2-26(a1). The syntactic foam within the honeycomb cells is fully compressed and the Al foil shows buckling deformation behaviour. More heavily deformed Al foils act as

stronger lateral constraints to the syntactic foam during compression as they better restrict the lateral expansion of the materials. Furthermore, all samples show a stress drop immediately after the yield strength, which is due to the accumulation of the microscopic damage in the samples (Fan *et al.,* 2019). Figure 2-26 (b) and (c) show displacement and axial strain fields obtained by digital image correlation (DIC) technique. The deformation field displays several sub-regions which indicates localised deformation patterns, but generally the failure mode of the non-reinforced samples is controlled by shear cracking.

Consequently, the initial failure of reinforced syntactic foam samples is dictated by buckling of Al foils. Figure 2-26.c1 shows the Al foils dividing the syntactic foam sample into longitudinal columns that share the load and experience lateral confinement, therefore displaying stress values higher than non-reinforced samples. The deformation mode changed from shear cracking to gradual compression (Fan *et al.,* 2019).

Figures 2-27 and 2-28 show the stress-strain curves for the syntactic foam samples at varying strain rates. The shape of the curves is similar to that under quasi-static loading conditions, with the dynamic compressive strength being higher than the quasi-static strength. The larger stress drop after initial loading indicates that syntactic foam samples have superior damage resistance to fracture under dynamic loading (Fan *et al.,* 2019). Engineering stress and strain are different from true values as true stress and strain take into account the changing size of the tested sample with time as it is being tested.

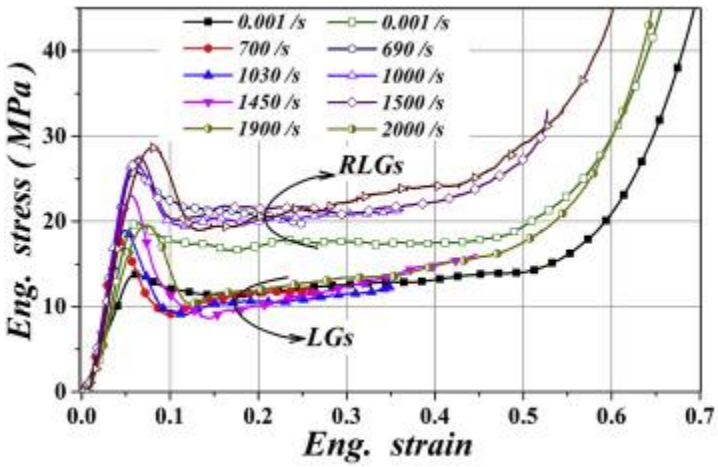

Figure 2-27: Dynamic compressive stress-strain curves of polyurethane SFs containing large size cenospheres (Fan *et al.,* 2019)

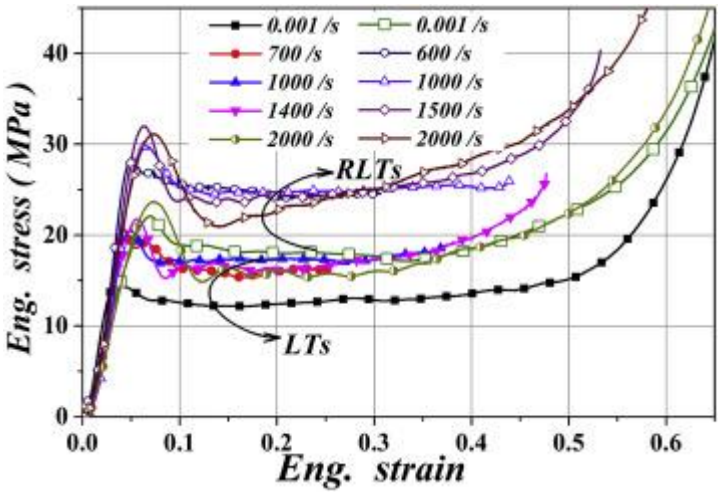

Figure 2-28: Dynamic compressive stress-strain curves of polyurethane SFs containing small size cenospheres (Fan *et al.,* 2019)

All samples show strain rate sensitivity. Distinct strain rate dependence was observed in the LG samples. The compressive strength increased up to a strain rate of 1500 s^{-1}, and then decreased until a strain of 2000 s^{-1}, due to the change in deformation behaviour at high strain rates.

The difference in strain rate dependence between LT and LG samples is due to the increased distance between the microspheres in the LG samples, which can accommodate more polymer. The polyurethane polymer is brittle and highly strain rate sensitive, which results in the change in deformation behaviour of the LG samples (Fan *et al.,* 2019).

2.4.2 **Metal matrix syntactic foams**

MMSFs have characteristics similar to both metal foams and PMSFs. Therefore different deformation behaviours and failure profiles have been observed. Both ductile failure, owing to the crushing of embedded particles and collapse of the matrix, and brittle failure are common (Tao and Zhao, 2009; L. P. Zhang and Zhao, 2007; Wu *et al.,* 2007). Furthermore, the available literature provides conflicting information on strain-rate sensitivity of MMSFs.

Dou et al. (2007) studied the high strain rate compressive response of cenosphere/pure Al syntactic foam samples and found the compressive strength increased from 45-75 MPa to 65-120 MPa and energy absorption capacity increased by 50-70% as loading conditions changed from quasi-static to high strain rate. Goel et al. (2012) investigated the strain-rate sensitivity of cenosphere/Al-2014 syntactic foams using the SHPB setup. They found that the compressive strength and energy absorption increased up to a strain rate of 750 s^{-1} and then decreased with further increases in strain rate. They also found that the coarser cenospheres were more sensitive to strain rate. On the other hand, several groups reported that plateau stress and densification strain are insensitive to strain rate under static and quasi-

static conditions, but become marginally strain rate sensitive at dynamic conditions (Mondal, Goel and Das, 2009; Mondal, Jha *et al.,* 2012).

Gupta and Rohatgi (2015) examined the compressive behaviour of AA2014/cenosphere syntactic foam samples. The stress-strain curves presented in Figure 2-29 show five regions: the initial linear elastic region, a short flat region immediately after yielding, a sharp drop in stress followed by a marginal increase in stress, a stress plateau region, and finally a densification region. The plateau region corresponds to the plastic deformation and foam compaction stage. The extent of stress reduction after yield stress is achieved is attributed to the strength of the cenospheres. The plateau region shows continuous oscillations due to the shearing of the matrix around the cells, collapse of cells, and compaction of pores. Similar regions were observed during the compressive deformation of LM13-30 vol% cenosphere syntactic foams in Figure 2-30, which also shows that plateau stress of aluminium matrix syntactic foams (AMSFs) is insensitive to strain rate. The plateau stress of AMSFs was noted to decrease with increasing cenosphere fraction (Gupta and Rohatgi, 2015).

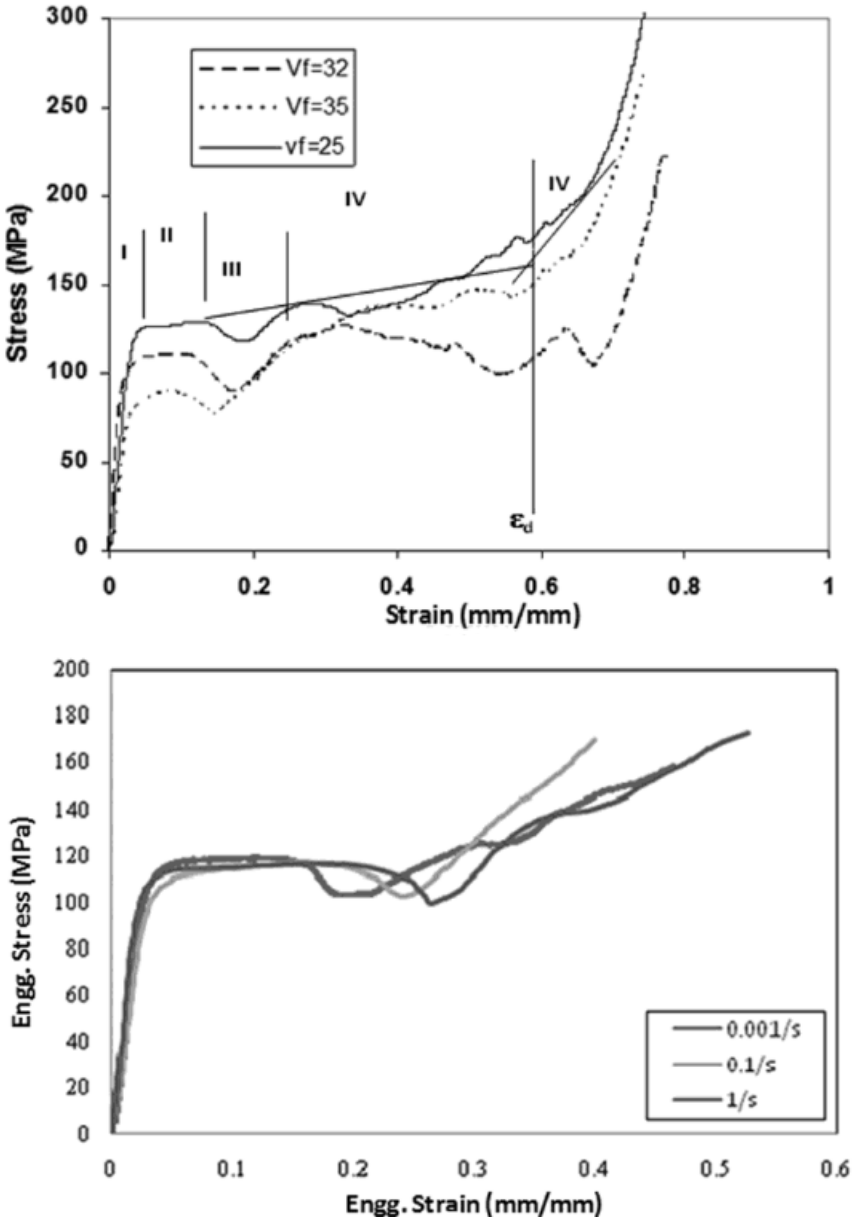

Figure 2-29: Stress-strain curve of AA2014-cenosphere syntactic foams (a) containing different cenosphere volume fraction and (b) tested at different strain rates (Gupta and Rohatgi, 2015)

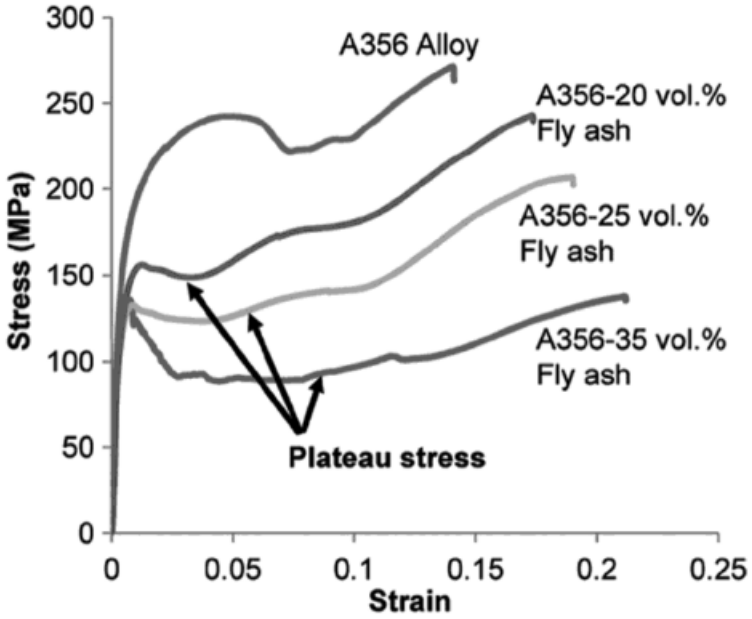

Figure 2-30: Stress-strain curve of A356 cenosphere syntactic foam (Gupta and Rohatgi, 2015)

The deformation behaviour of MMSFs was observed to be similar to that of dense materials. Under compression, the deformation initiates from the corners and propagate 45^{o} towards the centre of the specimen (L. P. Zhang and Zhao, 2007; Gupta and Rohatgi, 2015). Sheer deformation plays a significant role in the compressive deformation of syntactic foams. It was noted that the sheer deformation initiates earlier and is more evident for syntactic foams with coarser cenospheres. The rate of cenosphere fracture or shearing increased with increasing strain rate in the quasi-static conditions. However they showed minimal variations during dynamic conditions (Gupta and Rohatgi, 2015).

2.5 Flexural Properties

Polymer and metal foams have previously been studied in sandwich structures for applications where they require significant strength in bending. By extension, several studies have also been conducted to understand the flexural properties of SFs and MMCs to understand their behaviour and deformation mechanisms under bending. This section elaborates and describes these behaviours for the materials described above.

2.5.1 Porous metals and composite foams

2.5.1.1 *Closed-cell metal foams*

The various fabrication methods of closed-cell Al foams produces a high porosity material at the end, which limits its mechanical properties. One of the challenges with this is that Al foams show no plateau stage after yield stress is achieved under bending (Duarte, Vesenjak and Krstulović-Opara, 2014). To improve this, metal plates and metal tubes are introduced to produce Al foam sandwiches and foam-filled tubes respectively. Enhanced foams have shown load-deflection curves with a wider plateau amplitude when compared to traditional Al foams (T-AF) (Taherishargh *et al.,* 2016; Duarte *et al.,* 2015).

An et al. (2017) compared the bending behaviour of T-AFs to that of Al foams reinforced with an Al metal grid structure (Al-MGS). The T-AFs were fabricated using the direct melt foaming method. The MGS, made of stainless steel (304SS), was obtained by bending 2D metal mesh and welding them together. The MGS skin was then immersed in HCl solution first for 30 minutes and then in NaOH solution for 30 minutes to prevent formation of an oxide layer. The MGS was then placed in a casting

mould preheated to 720°C and the foamable Al melt was poured into the same mould, where the temperature was maintained at 710°C for 3 min and then left to cool. Three-point bending tests were conducted using a universal testing machine, shown in Figure 2-31, to analyse the mechanical properties of the samples. The speed and diameter of the pressure head was constant at 2 mm/min and 10 mm, respectively. The samples were machined to 140 mm x 50 mm x 25 mm and were placed on two fixed cylindrical supports with diameters of 30 mm and a span of 80 mm (An *et al.,* 2017).

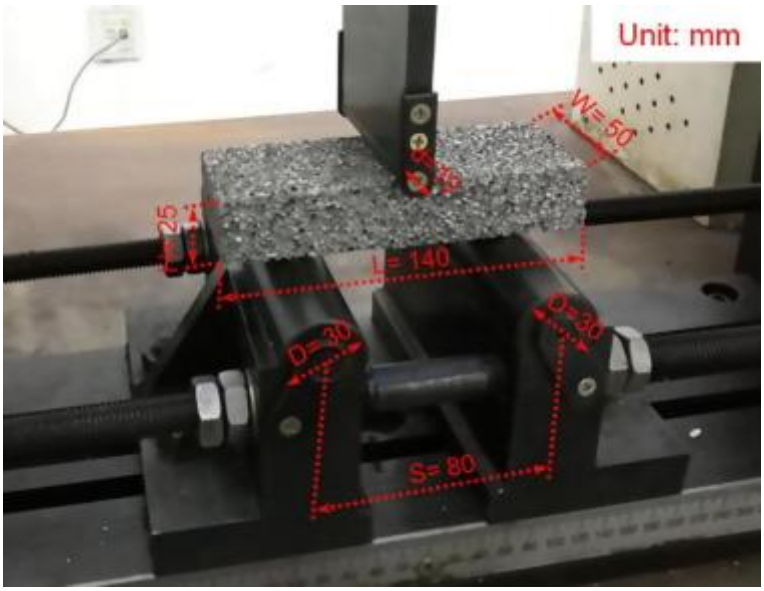

Figure 2-31: Experimental setup of the quasi-static three-point bending test (An *et al.,* 2017)

Figure 2-32 shows optical photographs and the load deflection curve of T-AF with a density of 0.18 g/cc during three-point bending test. The sample presented a single elastic deformation that resulted in a sharp increase in bending load. This then triggered local plastic deformation as critical load was exceeded. The top and bottom surfaces were subjected to compressive and tensile stress respectively. Local indentation at the top of the surface by the pressure head resulted in a change in gradient of the load-deflection curve, from point A to point B on Figure 2-32, and degraded the bending performance of the sample. From Point B, initial cracks were observed at the bottom surface due to the tensile strength of the pore wall being exceeded. The bending load from here on was released from cracks rather than from any indentation and the top surface indentation therefore remained largely unchanged. The cracks propagated along the weakest pore walls until the T-AF failed, indicating that the deformation process was governed by the tensile strength of the pore walls (An *et al.,* 2017).

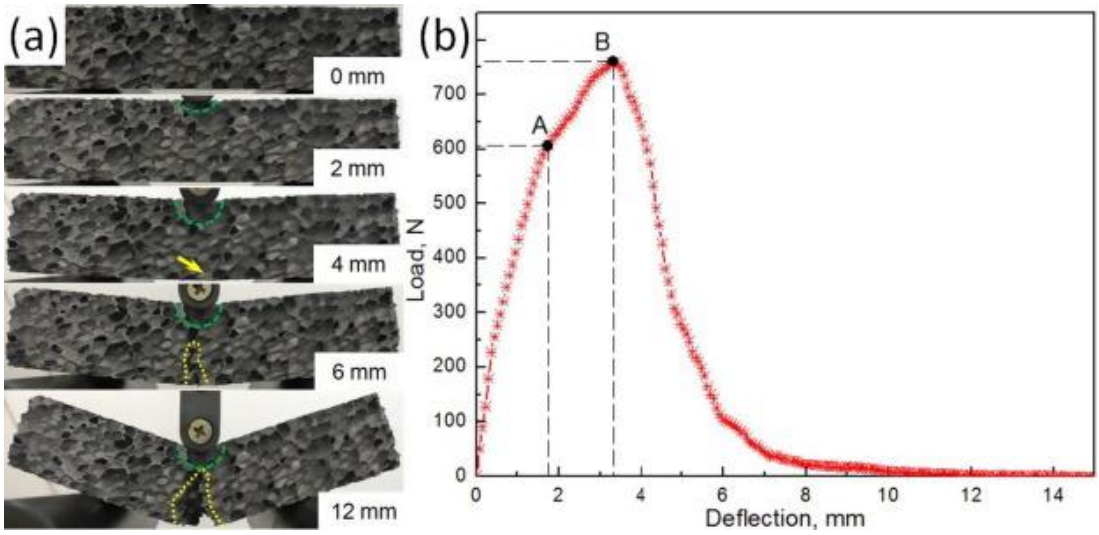

Figure 2-32: Deformation sequences (a) and load-deflection curve (b) during quasi-static three-point bending tests of T-AF (An *et al.,* 2017)

Figure 2-33 shows the deformation sequence and the load-displacement curve for the MGS-AF sample under three-point bending. At low deflection, the deformation was similar to what was observed for the T-AF sample to point A, with smaller drops observed and a steeper gradient recorded after this point due to local indentation. The presence of the MGS enhanced the stress condition and delayed the deflection due to plastic deformation. The yield load was higher for the MGS-AFs (1710-2180 N) than for the T-AFs (750-980 N) (An *et al.,* 2017).

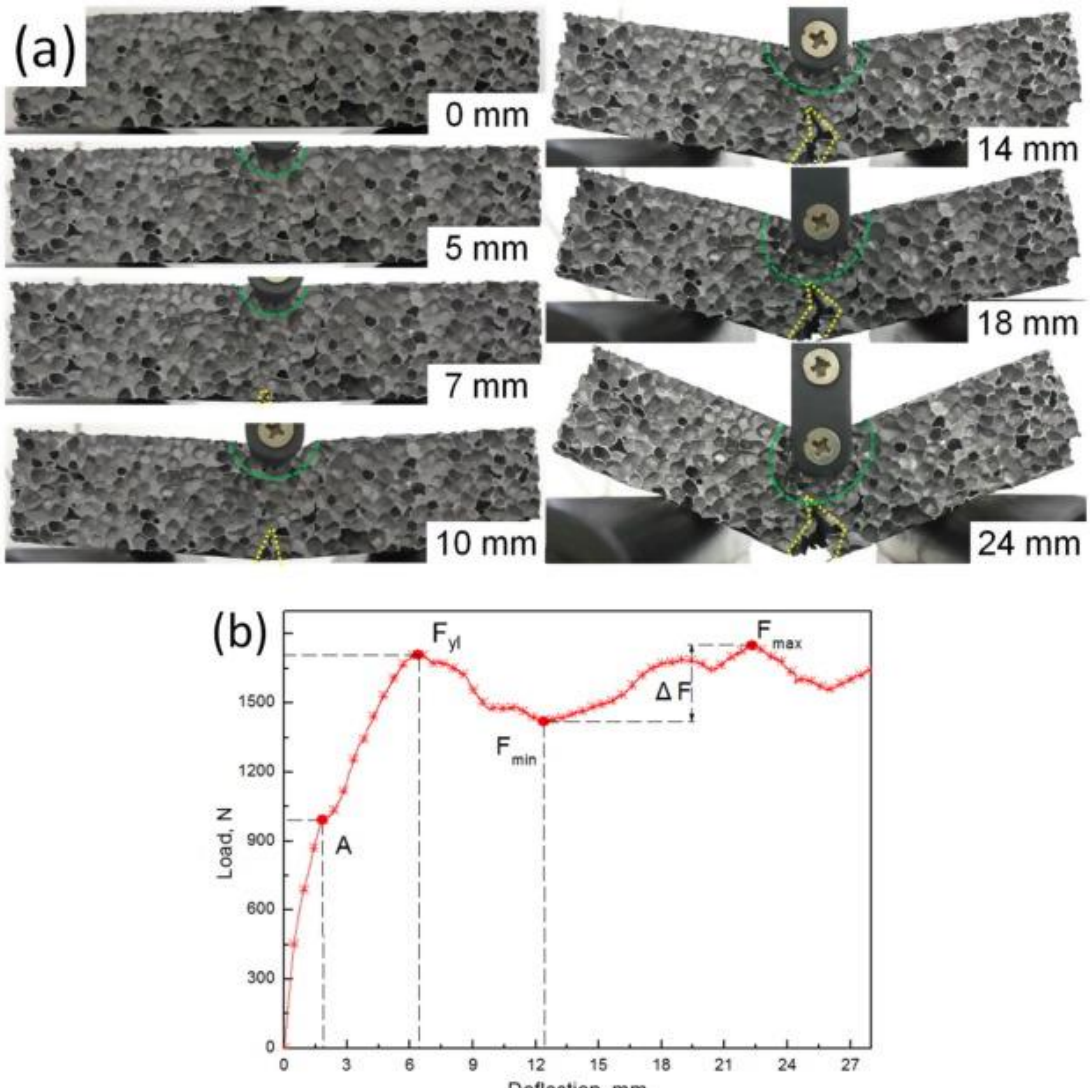

Figure 2-33: (a) Deformation sequences of MGS-AF and (b) its load-deflection curve (An *et al.,* 2017)

2.5.1.2 *Metal matrix composites*

Al MMCs have been studied to understand their behaviour under bending conditions as well as to understand their impact response under similar conditions. Demir and Altinkok (2004) found that the bending strength of Al MMCs reinforced with SiCp and alumina increased with increased reinforcement fraction up to 13 vol%, after which it decreased. Kalkanli and Yilmaz (2008) discovered the flexural strength of Al 7075/SiCp MMCs increased with increasing SiCp fraction, until 10 wt.%, and decreased beyond that point. Kumar et al. (2018) noted that the impact strength increased with increasing cenosphere content in cenosphere reinforced Al 7075 MMCs up to 7.5 wt.% reinforcement, and decreased thereafter.

Zhang et al. (2016) studied the bending behaviour of Al MMCs with pre-woven carbon fibres fabricated using the electromagnetic casting method. Figure 2-34 displays the load-displacement curves for the composite and that for pure Al metal. Both curves kept their respective shapes, with no sudden breakages observed. The addition of the fibres resulted in a 33.6% increase in bending strength compared to the metal (149 MPa to 199 MPa), with minimal differences in ductility. The increase in strength is due to the higher specific strength of the carbon fibres, the exceptional interfacial bond, and the effective stress transfer (J. Zhang *et al.,* 2016).

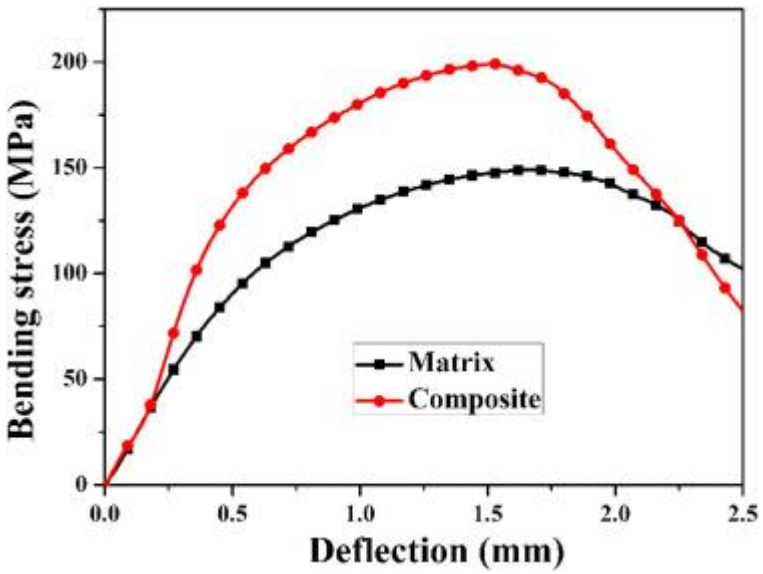

Figure 2-34: Results of the three-point bending tests on Al MMCs with pre-woven carbon fibres (J. Zhang *et al.,* 2016)

Das et al. (2019) fabricated Al 7075 MMCs with SiC particles using liquid state fabrication route and studied the effect of T6 treatment on their flexural properties. Table 2-1 above described the composition of the fabricated samples. Figure 2-35 shows the fractured MMC samples after impact and three-point bending tests. Subsequently, Figures 2-36 and 2-37 show the effects of heat treatment, wt.% and mean particle size of SiCp on the impact strength and flexural strength of the samples respectively.

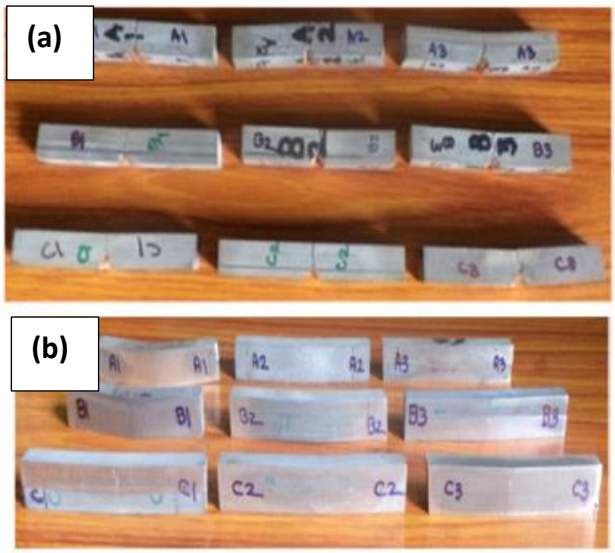

Figure 2-35: Fractured MMC specimens after (a) impact test; and (b) three point bend test (Das *et al.,* 2019)

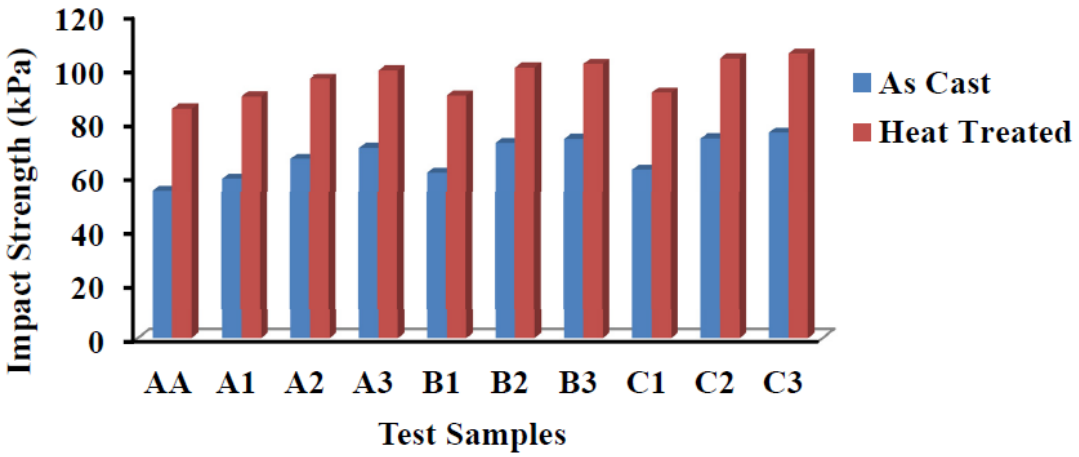

Figure 2-36: Effect of thermal treatment, SiCp wt.% and mean particle size on impact strength (Das *et al.,* 2019)

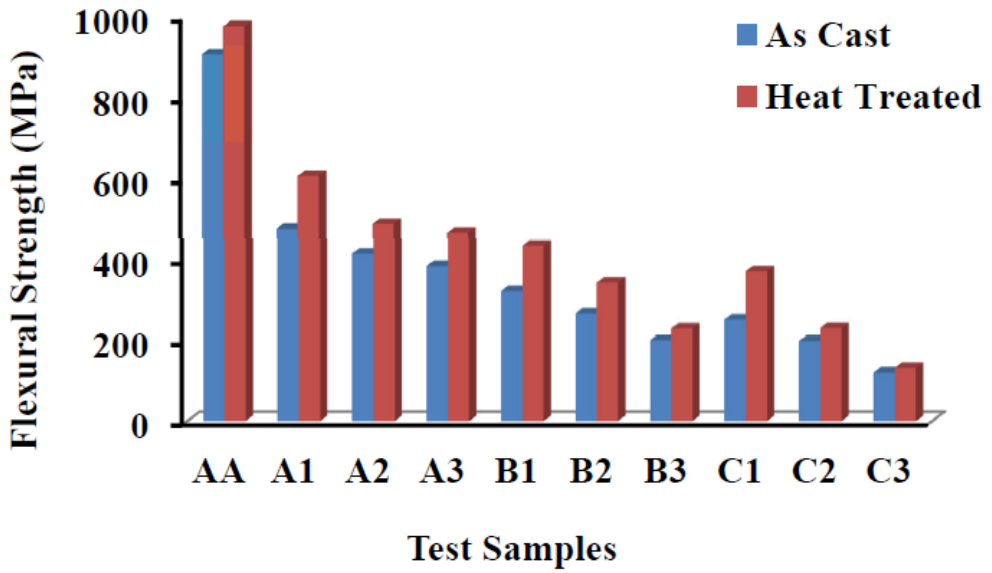

Figure 2-37: Effect of thermal treatment, SiCp wt.% and mean particle size on flexural strength (Das *et al.,* 2019)

Impact strength increased with increasing SiCp content, decreasing particle size and after T6 treatment. This is due to the homogenous dispersion of SiCp and strong interfacial bonds and the distribution of SiCp in smaller particle sizes. The highest impact strength of 105.8 kPa was obtained for T6 treated MMCs containing 25 wt.% SiCp with a particle size of 6.18 µm. On the other hand, flexural strength decreased when particle content and particle size were decreased and increased, respectively. However, T6 treatment increased the flexural strength of the MMCs. The highest flexural strength of 978 MPa was noted for T6 treated MMCs with 5 wt.% SiCp with a particle size of 30.65 µm.

2.5.1.3 *Polymer matrix syntactic foams*

Several studies have been reported in literature to understand the behaviour of PMSFs under flexural conditions. It has been found that reinforcing PMSFs is a good way to increase their strength and stiffness, especially when using short fibres as reinforcements (Huang *et al.,* 2010; Ferreira, Capela and Costa, 2010). However, adding higher volume fractions can lead to a lowering of strength for the syntactic foams (Tagliavia, Porfiri and Gupta, 2010; Antunes, Ferreira and Capela, 2011). Karthikeyan, Sankaran and Kishore (2000) noted a 21% increase in flexural strength in syntactic foams reinforced with 3.64 vol% short glass fibres. Blackman et al. (2007) fabricated epoxy syntactic foams with nano-SiO_2 particles and found that the initial toughness and fracture toughness increase. Colloca, Gupta and Porfiri (2013) found the tensile properties of syntactic foams with hollow particles to be enhanced by adding 0.25 wt.% carbon nanofibre reinforcements because sample failure is dependent more on the matrix fracture under tensile loading conditions when compared to the compressive loading conditions.

Wang et al (2014) investigated the flexural properties of epoxy syntactic foams with 15 wt.% hollow glass microspheres (true density 0.25 g/cc; diameter 55 µm) with and without reinforced fibreglass mesh (4mm x 4mm epoxy resin grid) and/or short glass fibres (length 3mm). A polyamide hardener 651 at 25 wt.% was also used in the fabrication stage. Flexural tests were conducted using a universal testing machine according to ISO 178 standard. Figure 2-38 shows the three-point bending test setup. Specimens were fabricated to 80 mm x 10 mm x 5 mm and a load rate of 2mm/min was maintained for testing. The location of the fibreglass mesh was expressed as *x/h*.

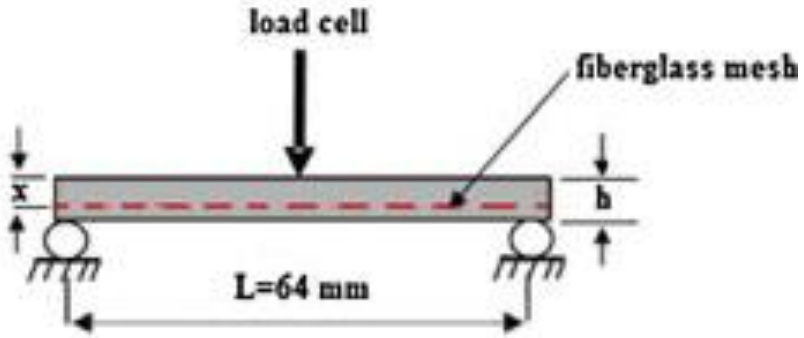

Figure 2-38: Schemes of three-point bending test (L. Wang *et al.,* 2014)

Figure 2-39 displays the flexural strength and modulus vs location of the mesh. The location of the mesh had a significant effect on the flexural properties of the syntactic foam. When *x/h* was less than 0.5, the flexural strength was the same as that of the unreinforced syntactic foam, which was 31.08 MPa. As *x/h* increased from 0.5 to 1, the flexural strength almost tripled. However, flexural modulus was at a minimum when *x/h* was 0.5, which was the same as the unreinforced syntactic foam sample (2.02 GPa) (L. Wang *et al.,* 2014).

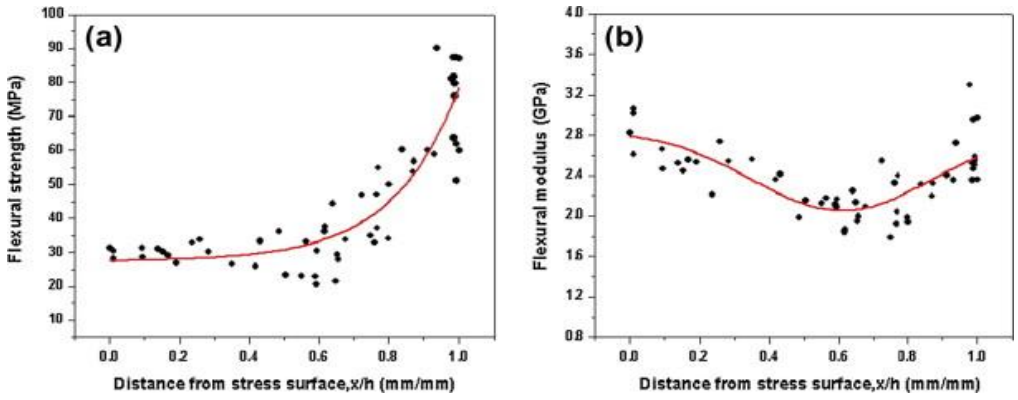

Figure 2-39: The effect of the location of one-layer fibreglass mesh on (a) flexural strength and (b) flexural modulus (L. Wang *et al.,* 2014)

Stress-displacement curves for syntactic foams with reinforced fibreglass mesh at different positions and number of layers (*N*) are shown in Figure 2-40(a). The failure shows two different modes. For reinforcements closer to the loading surface, the initial linear curve is followed by a sharp drop in stress and ultimate failure. A step-failure is observed for reinforcements further away from the loading surface. This is also seen in three-layer fibreglass mesh foams, where the reinforced foams exhibit higher strength as the middle mesh is further away from the stress surface. Figure 2-40(b) shows the stress-displacement curves for unreinforced syntactic foams as well as samples with different reinforcements. Brittle failure is seen in short glass fibre reinforced syntactic foams, with step-failure noted for the other reinforced samples. The first crack strength is affected by the fibreglass mesh and the short glass fibre, however the deflection of the first-step failure is only affected by the short glass fibre reinforcements (L. Wang *et al.,* 2014).

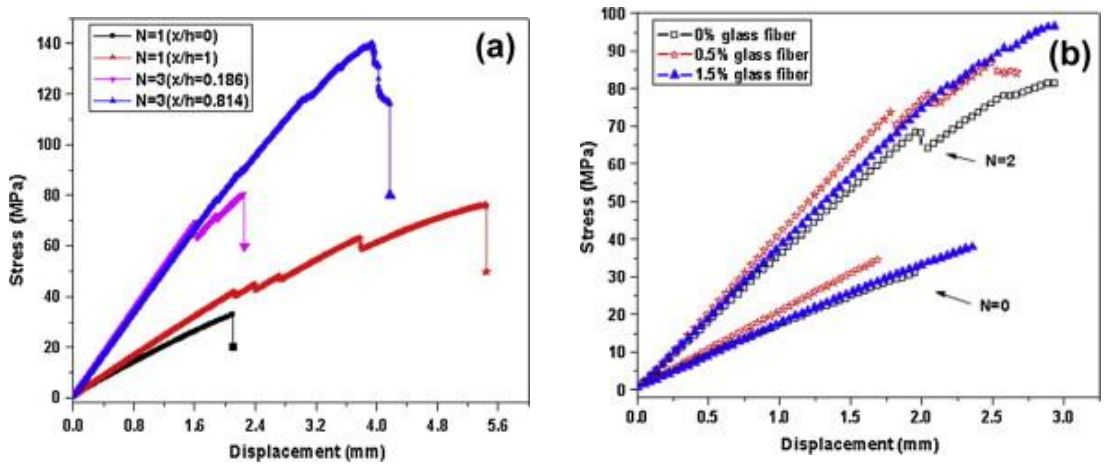

Figure 2-40: (a) Typical bending stress–displacement curves of (a) fiberglass mesh reinforced and (b) different reinforcements syntactic foams (L. Wang *et al.,* 2014)

It was suggested that the microspheres under the loading nose underwent local crushing, whereas those on the tensile side fractured and de-bonded due to the low strength of the microspheres (5.17 MPa). The fracture regions will then act as local stress-concentration sites, leading to matrix cracking and eventual failure (L. Wang *et al.,* 2014).

2.5.2 **Metal matrix syntactic foams**

There is limited work done on the flexural properties of MMSFs. Omar et al. (2015) investigated the flexural properties of A356 matrix syntactic foam core sandwich structures under three-point bending. They observed that cracks initiated on the tensile side, causing failure of the matrix, followed by rapid failure of the core in the direction of the load. Lin et al. (2016) studied the mechanical behaviour of pure Al and Al-Mg (5A06) syntactic foams with glass cenospheres fabricated by pressure infiltration under three-point bending and found that the flexural strength of the Al alloy syntactic foam was higher than the pure Al syntactic foam regardless of the stress state.

Altenaiji (2014) investigated and characterised the flexural properties of Al7075/CM and Al-6082/CM syntactic foam samples under three-point bending. The samples were cut to 10mm x 80 mm x 10 mm and were tested using the INSTRON 4045 with cylindrical supports (diameter 10 mm). Table 2-2 displays the composition of the syntactic foam samples, Figure 2-41 shows the three-point bending response of the samples and Table 2-3 provides a quantitative analyses of the samples with different particle sizes (Altenaiji, 2014).

Table 2-2: Composition of AMSFs (Altenaiji, 2014)

Sample ID No.	Al alloy	Size of ceramic micro-spheres
CM (I)	7075-T6	250-500μm
CM (II)	7075-T6	100-250μm
CM(III)	7075-T6	25-75μm
CM (IV)	6082-T6	250-500μm
CM (V)	6082-T6	100-250μm
CM (VI)	6082-T6	25-75μm

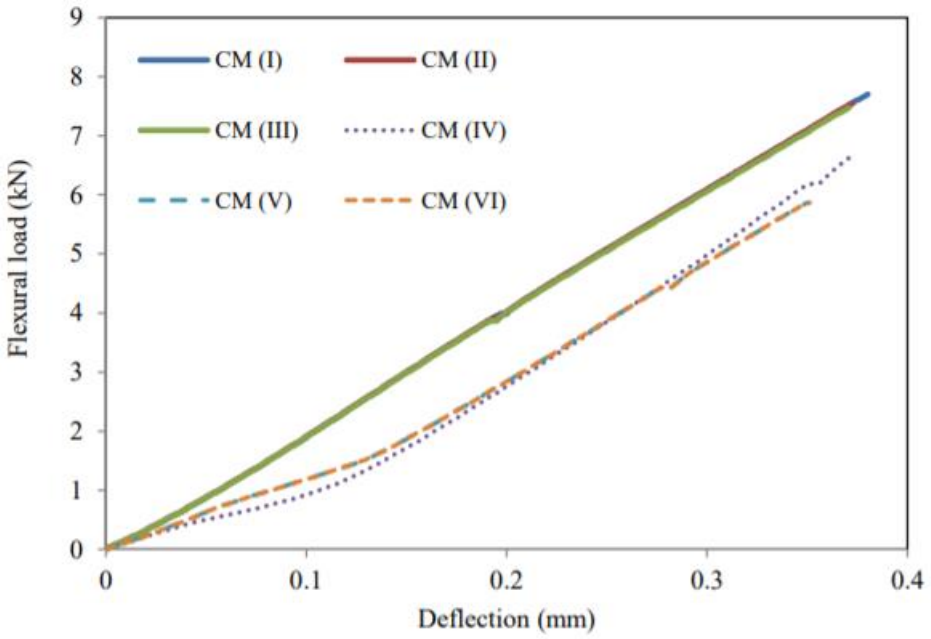

Figure 2-41: Three-point bending response of AMSFs (Altenaiji, 2014)

Table 2-3: Average flexural properties of AMSFs (Altenaiji, 2014)

Foam	Density (kg/m^3)	Maximum deflection (mm)	Peak load (kN)	Stiffness (kN/mm)	Flexural modulus (GPa)	Flexural strength (MPa)	Flexural strain (bottom)	Specific energy (kJ/kg)
CM(I)	2388	0.385	7.70	21.91	2.07	462.23	0.00641	1.469
CM(II)	2321	0.377	7.55	20.46	2.06	452.98	0.00628	1.412
CM(III)	2250	0.375	7.47	19.77	2.03	448.40	0.00625	1.390
CM(IV)	1790	0.373	6.66	19.43	2.02	399.50	0.00621	1.033
CM(V)	1630	0.359	6.16	17.10	2.00	369.75	0.00598	0.982
CM(VI)	1616	0.352	5.87	16.05	1.98	352.15	0.00586	0.920

The results showed that all samples showed the same elastic region in the load-displacement curves with similar responses to applied load and failed in a brittle fracture mode. It was also noted that cracks started forming on the tensile side of the sample as deflection increased and that an increase in density resulted in an increase in stiffness, specific energy absorption and flexural strain (Altenaiji, 2014). The CM particle size was observed to play a significant role in the flexural properties of the syntactic foam sample, where an increase in particle size led to an increase in the peak load and a resultant increase in the energy absorbed (Altenaiji, 2014).

2.6 Tribological Properties

There are many articles in literature today that discuss the wear properties of different lightweight structures with several different reinforcements. Some of these are discussed below by highlighting the important characteristics and behaviours observed for the materials described above.

2.6.1 Porous metals and composite foams

2.6.1.1 *Closed-cell metal foams*

Closed-cell metal foams have previously been studied to understand their ability to be filled with different materials, like oil, and be used for respective applications. For instance, Du et al. (2010) studied copper foams with elongated cylindrical pores and found that they were able to hold a good amount of oil regardless of pore structure so that a constant oil layer and supply is maintained on the surface of the sample. However, there is not much work done to study the friction and wear properties of closed-cell metal foams and a comprehensive study on the wear behaviour of highly porous materials is missing.

Du et al. (2012) studied the friction behaviour of as-fabricated porous copper with elongated cylindrical pores. Two types of porous copper were tested – one as-fabricated porous copper rings and the other impregnated rings with the lubricating oil. The results were also compared with those for non-porous copper. Ball-on-disc tests were conducted using a vertical universal friction-abrasion testing machine. The sliding partner was a WC-Co ball with a diameter of 6.35 mm and a hardness of HV1750 and the ball was revolved around the copper rings for 1.8 x 10^3 s with a sliding speed of 1 rps under a load of 50 N and a track radius of 24 mm.

Table 2-4 shows the average coefficient of friction (COF) values for the wear tests. This average COF decreased with oil impregnation, indicating the formation of an oil layer on the surface that prevents direct contact to decrease the frictional force between the surfaces. It was also observed that the increasing porosity, that led to a decrease in strength, contributed to an increase in contact area between the partners (Du *et al.,* 2012).

Table 2-4: Average COF and porosity values for the wear tests. FC1: COF for as-fabricated rings, FC2: COF of the impregnated rings (Du *et al.,* 2012)

Specimen	1	2	3	4	5	6	7
FC1	0.258	0.234	0.238	0.229	0.262	0.237	0.292
FC2	0.172	0.161	0.166	0.152	0.187	0.165	0.261
Porosity	32.6	30.2	37.1	29.8	26.2	47.1	0

Figure 2-42 shows the development of COF vs sliding time for porous copper rings impregnated with oil. The COF is observed to be stable over time for the porous copper rings with lower porosity, and fluctuations are observed for samples with the highest porosity and that with no porosity as well (Du *et al.,* 2012).

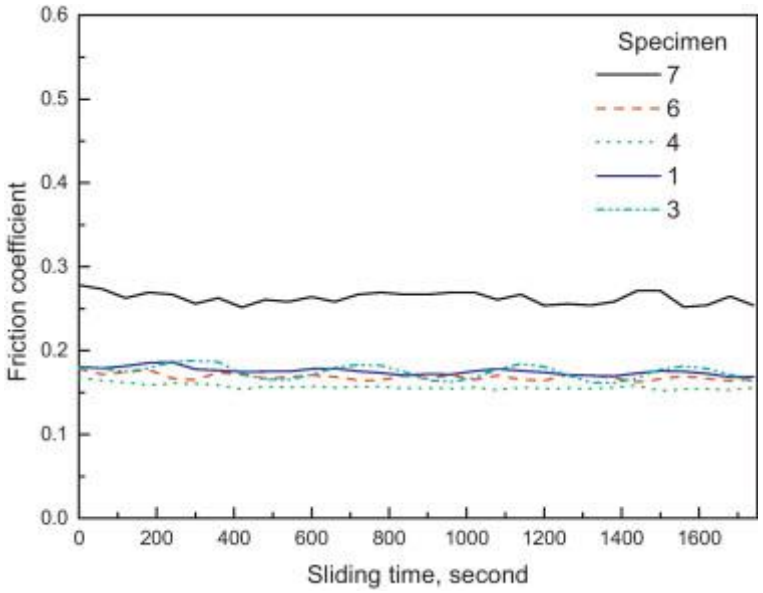

Figure 2-42: Variation of the friction coefficient with the sliding time of the porous copper rings (Du *et al.,* 2012)

2.6.1.2 *Metal matrix composites*

Several studies have been published to study the wear behaviour of Al MMCs under dry and lubricated conditions. MMCs generally have better wear and seizure resistance when compared to the virgin alloy, but the COF is slightly higher comparatively. This is because the hard ceramic phase protects the matrix from severe contact wear and locks debris on the wear surface for longer periods, forming a mechanically mixed layer and reducing the actual contact between the two surfaces (Gupta and Rohatgi, 2015).

Deuis, Subramnian and Yellup (1996) found Al MMCs containing hard particles to have enhanced resistance to wear when compared with Al-Si alloys. Kwok and Lim (1999) observed that the size of the particle reinforcements in Al MMCs with SiCp affected the high-speed wear resistance, where particles smaller than a threshold

value would result in extensive wear and these MMCs were suggested to be more suitable for lower-speed applications. The threshold value was a factor of the fracture toughness, indentation hardness and Young's modulus of the wearing material. Sharma, Nanda and Pandey (2019) concluded that the T6 treatment of LM30/sillimanite reinforced composites showed superior wear resistance and a lower COF than the as-fabricated composite.

Ramachandra and Radhakrishna (2007) investigated the effect of fly-ash particulate reinforcements MMCs on the sliding wear behaviour of Al-12% Si alloy MMCs fabricated using the stir casting method. A computerised pin-on-disc wear test machine was used to conduct the sliding wear tests. Tests were conducted at three different loads (4.9, 9.8 and 14.7 N) at a sliding speed of 95 m min^{-1} for 2hr 20min. The pins were made of three different MMCs and the disc was made of carbon steel (diameter 50mm and hardness 64 HRC).

The wear resistance increased with increasing fly-ash content due to the increase in hardness contributing to the overall bulk hardness of the material. The particles carry the load and prevent plastic deformation in the initial wear regime. In the later stages of the wear regime, the worn particles are dislodged and get mixed with wear debris, which get pushed into the formed craters and continue acting as load bearers. The COF decreased with increasing fly-ash content. Figure 2-43 shows the development of COF vs sliding time for samples tested under a load of 14.7 N and a sliding velocity of 95 m min^{-1} (M. Ramachandra and Radhakrishna, 2007).

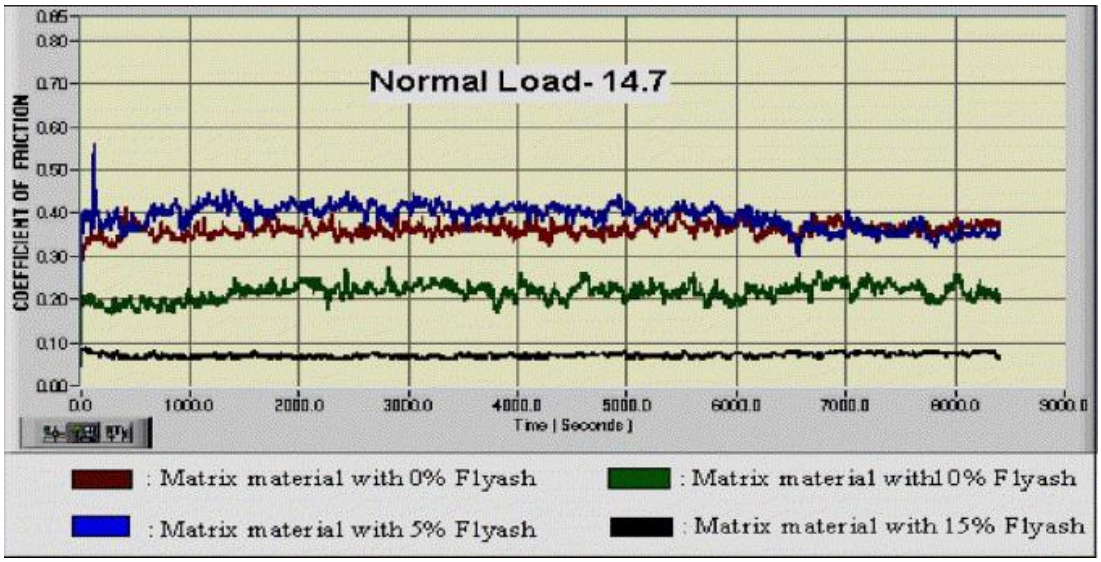

Figure 2-43: COF variation with fly ash content (M. Ramachandra and Radhakrishna, 2007)

Optical microscopic images showed various types of wear mechanisms, either alone or in combination, under the different sliding conditions (M. Ramachandra and Radhakrishna, 2007):

1. Abrasive wear was observed as grooves and scratches were formed on the sample surface.
2. Oxidative wear was noted as dark surfaces were significantly covered by thin layers of fine particles and large quantities of fine powders were present in the wear debris.
3. Fatigue-related wear, known as delamination, was characterised by subsurface cracks that gradually grow and shear to the surface, forming long thin wear sheets.

4. Adhesive wear was observed as material was transferred onto the surface of the pin, with some signs of plastic deformation.

Figure 2-44 displays micrographs of the various wear mechanisms.

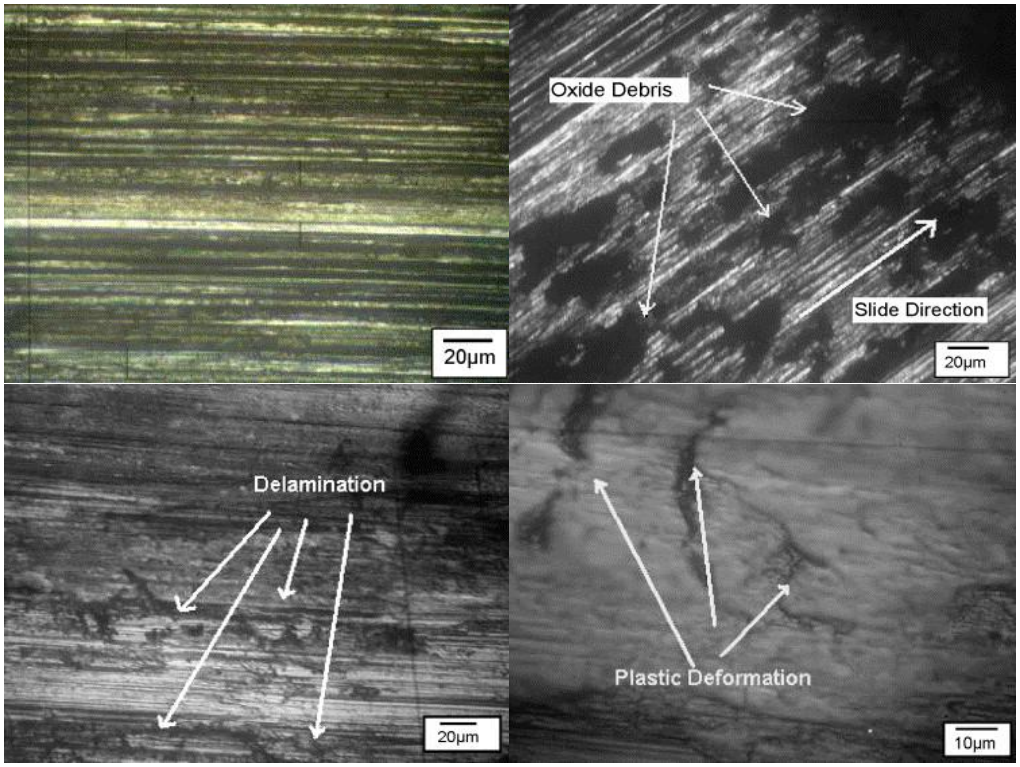

Figure 2-44: Sample surface features indicative of (a) abrasive wear, (b) oxidative wear, (c) delamination of wear surface, and (d) adhesive wear (M. Ramachandra and Radhakrishna, 2007)

2.6.1.3 *Polymer matrix syntactic foams*

PMSFs containing hollow particles have been investigated to understand their tribological behaviour. The sliding wear behaviour is significantly different from composites reinforced with solid particles. Manakari et al. (2015) found that void spaces within the hollow particles act as accumulators for wear debris and provide a smoother surfaces, which results in superior wear resistance. Singh and Siddhartha

(2015) found that the wear resistance of 10 wt.% cenosphere-polyester syntactic foams increased as particle size decreased. Chauhan and Thakur (2013) reported similar properties for vinyl ester syntactic foams with cenospheres.

Chaitanya and Narasimha (2019) investigated the effect of fly-ash volume fraction on the tribological properties of epoxy syntactic foams. The samples were fabricated with 10-40 vol.% fly-ash with epoxy resin and hardener used as the matrix material. Pin-on-disc tests were conducted by using an EN31 steel material disc as the counter surface. Experiments were conducted at a sliding speed of 1 ms^{-1} at a load of 50 N and a sliding distance of 2000m. The wear rate and COF vs sliding distance curves are shown in Figure 2-45 and 2-46 respectively. The wear rate of the samples decreased with increasing fly-ash volume fraction because the increase in volume fraction increases the porosity and reduces the contact area (Chaitanya and Rao, 2019).

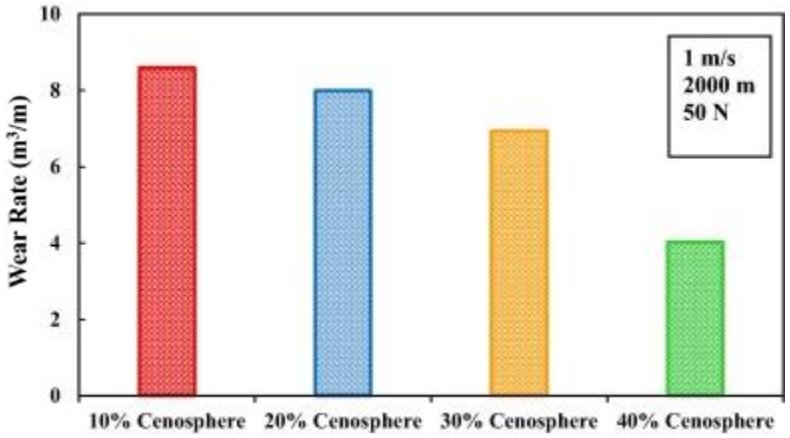

Figure 2-45: Relationship between wear rate and reinforcement volume fraction (Chaitanya and Rao, 2019)

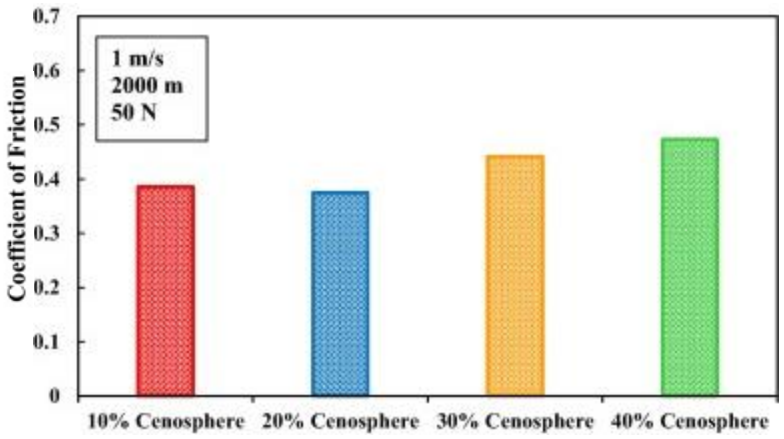

Figure 2-46: Relationship between COF and reinforcement volume fraction in the foam (Chaitanya and Rao, 2019)

Micrographs of worn surfaces for 20 and 40 vol.% fly-ash syntactic foam samples are shown in Figure 2-47. The absence of wear grooves on the worn surface indicates adhesive wear (Chaitanya and Rao, 2019).

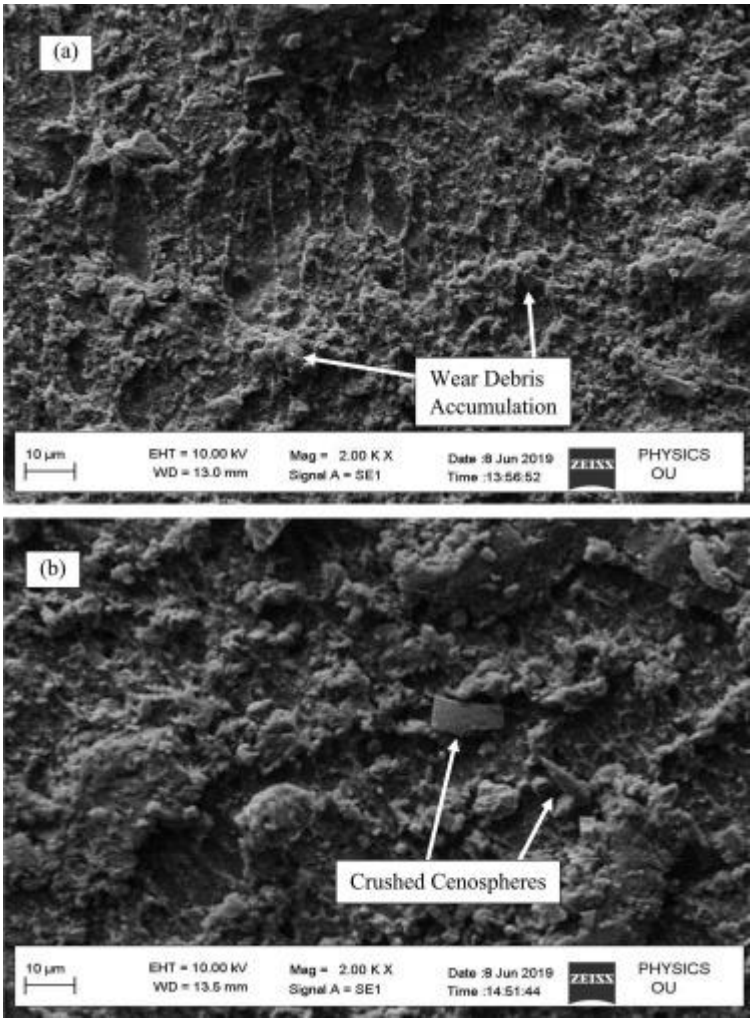

Figure 2-47: Worn surface micrographs of (a) 20% cenosphere syntactic foam and (b) 40% cenosphere syntactic foam (Chaitanya and Rao, 2019)

2.6.2 **Metal matrix syntactic foams**

Detailed studies have been conducted to study the friction and wear behaviour of Al-matrix syntactic foams under dry and lubricated conditions. When porous or hollow ceramic particles get mixed on the wear surface, the strength and wear resistance of the syntactic foam are improved. Under lubricated conditions, the exposed pores on the surface of the foam will hold lubricants for a longer time, which can provide sustained lubrication on the sliding surface. Further, the porous structure of the particles in the syntactic foam will provide a "cushioning effect" on the wear surface (Gupta and Rohatgi, 2015).

Mondal, Das and Jha (2009) studied and compared the dry sliding wear behaviour of cenosphere reinforced Al syntactic foams to 10 wt.% SiC reinforced Al-MMCs. They found that the syntactic foam samples had significantly lower COF values compared to the Al-SiC composites due to the increased abrasive action seen on the surface of the composite. The wear rate was observed to be similar at low applied loads, however at higher loads, the syntactic foam sample had a higher wear rate than the Al-SiC composites due to the lower cenosphere strength and significant adhesive wear.

Májlinger et al. (2016) studied the tribological behaviour of hybrid Al syntactic foam samples under dry and lubricated conditions. Hollow spheres and reinforcements used were ceramic hollow spheres, iron hollow spheres and E-spheres. The tests were conducted over a sliding distance of 500 m with a load of 98 N (corresponding to a nominal pressure of 0.64 MPa). Lubricated sliding tests used 10W40 mineral oil, where 5x20 µl was added at the start of each experiment. They found that the COF,

overall height loss and specific wear increased with increasing ceramic ratio due to an increase in abrasive wear. Under lubricated conditions, the COF values were very similar, though they slightly decreased with increasing ceramic content. The specific wear and height loss were much lower compared to dry sliding conditions, with no significant wear track observed on the worn discs. The open hollow spheres acted as lubricant reservoirs.

Jha et al. (2011) similarly compared the sliding wear behaviour of 10 wt.% SiC reinforced LM13 Al-MMCs to cenosphere filled LM13 AMSFs. Both types of samples were fabricated using the stir casting technique. Sliding wear tests were conducted on a pin-on-disc machine by sliding a cylindrical pin sample (length 28 mm, diameter 8 mm) against the surface of hardened EN24 steel (hardness 600HV). Both dry and lubricated tests were carried out at a normal load of 30 N for a sliding distance of 2000 m. The sliding speed was changed between 2, 3 and 4 ms^{-1}. For lubricated tests, commercial synthetic oil (SAE 40 of Indian Oil Ltd.) was added at 20 drops per minute to maintain a thin lubricating layer.

Figure 2-48 shows the development of COF vs sliding distance for Al MMCs and AMSF samples under dry sliding conditions at varying sliding speeds (Jha *et al.,* 2011). The COF for Al MMCs (>0.5) was observed to be much higher than that for the AMSFs (<0.1) regardless of sliding speed. This is due to the increase in contact surface area between the sample and the steel disc and the higher strength of the angular SiC particles in the Al MMCs, which provide significant resistance to sliding (Jha *et al.,* 2011).

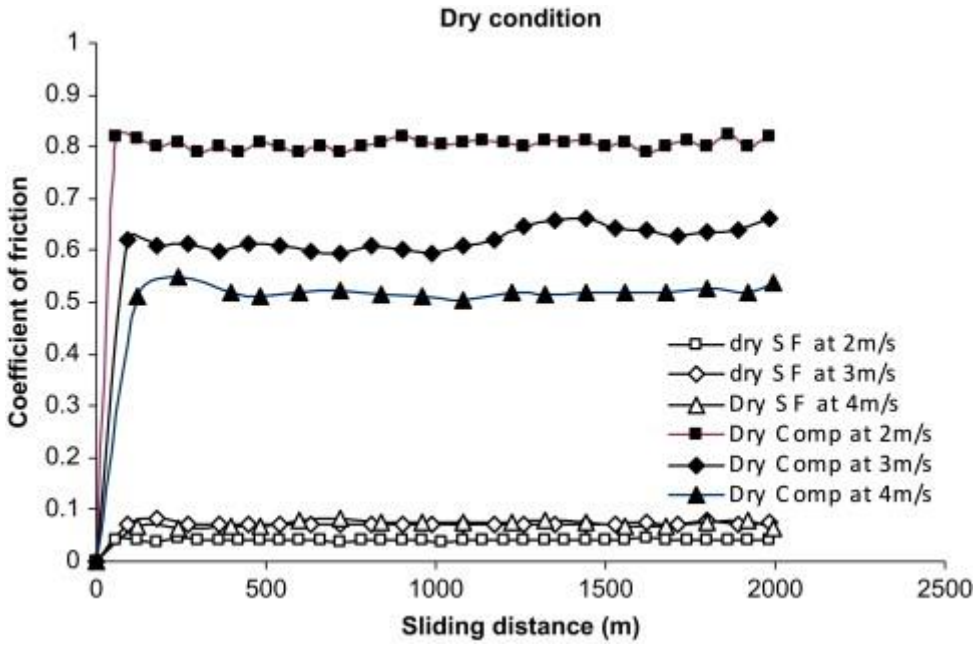

Figure 2-48: Development of COF vs sliding distance under dry sliding conditions (Jha *et al.,* 2011)

Figure 2-49 shows the development of COF vs sliding distance for samples under lubricated conditions (Jha *et al.,* 2011). The COF for both materials is significantly less under lubricated conditions than under dry conditions, with the difference in COF between AMSF and Al MMCs being insignificant. The presence of the lubricant causes a slipping action, which leads to the significantly lower COF (Jha *et al.,* 2011).

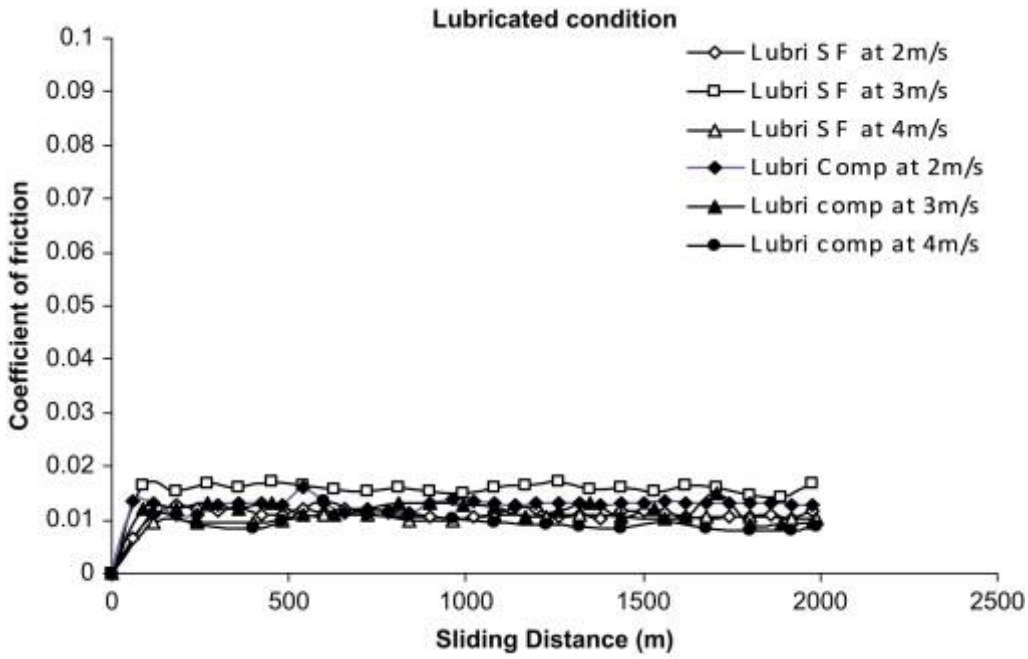

Figure 2-49: Development of COF vs sliding distance under lubricated sliding conditions (Jha *et al.,* 2011)

Figure 2-50 shows the worn surfaces of the Al-SF samples when tested under dry sliding conditions at different sliding speeds. There are several phenomena observed by the study on these surfaces (Jha *et al.,* 2011):

1. Fine and shallow abrasive grooves and craters at the site of cenospheres at a sliding speed of 2 ms^{-1}, marked 'C' in Figure 2-50(a), which get sheared and elongated along the sliding distance.
2. Matrix material being spread over the broken cenospheres and getting accumulated at a sliding speed of 2 ms^{-1}, marked 'A' in Figure 2-50(b).

3. An increase in sliding speed to 3 ms^{-1} leads to more significant shearing, with wear debris getting accumulated at craters, marked ‘A’ on Figure 2-50(c). Some craters also get elongated, which are marked ‘E’ on Figure 2-50(c).
4. At a speed of 4 ms^{-1}, several serration marks are noted, indicating greater extent of material flow over the worn surface. This is marked as ‘S’ on Figure 2-50(d).
5. Large wear debris (marked ‘D’ on Figure 2.50(e)) was trapped in the matrix at a sliding speed of 4ms^{-1}, with minor cracks evident on the worn surface, as indicated by arrows on Figure 2.50(e).

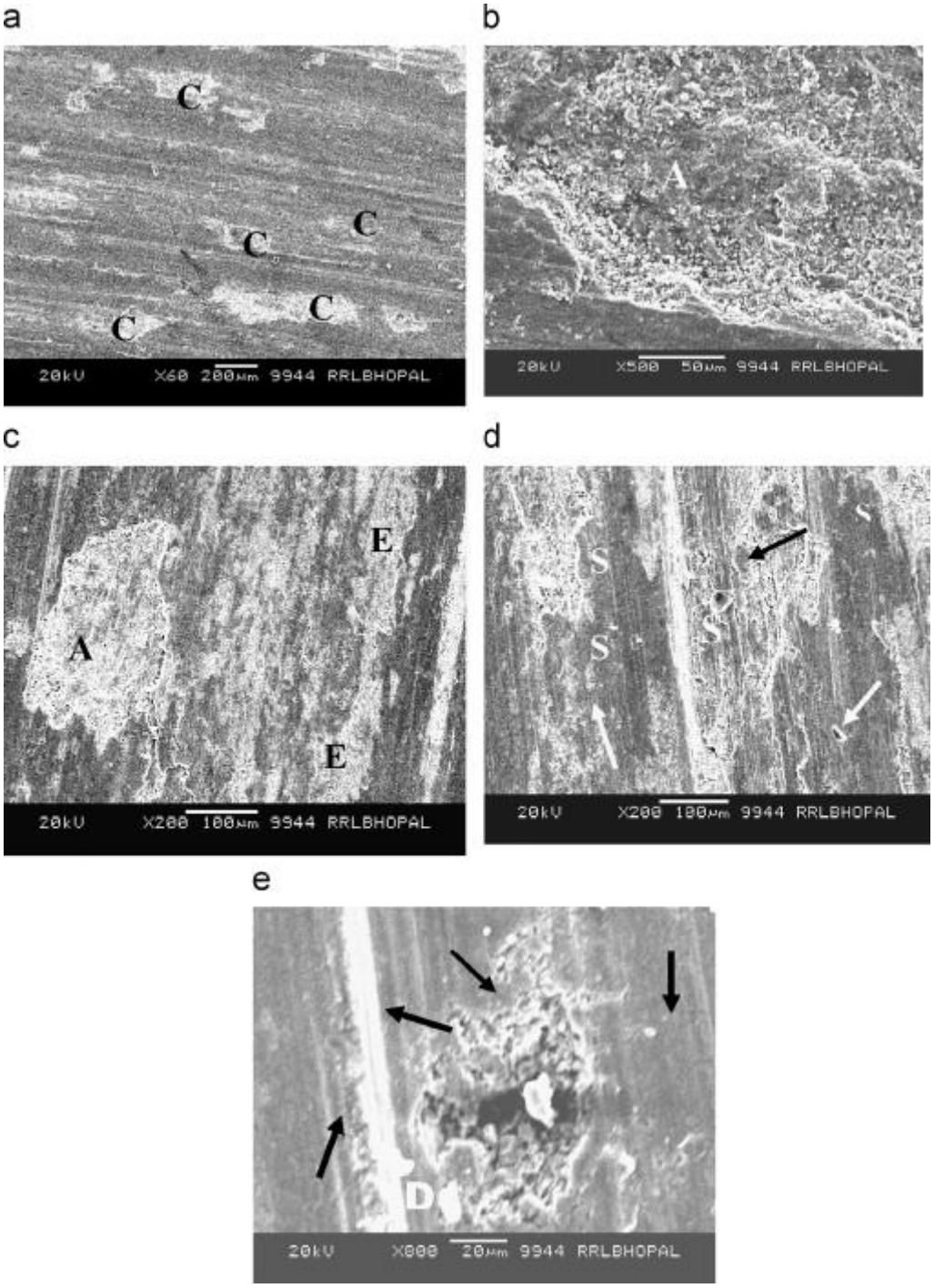

Figure 2-50: Worn surface of aluminium syntactic foam at sliding speeds of (a) and (b) 2 ms^{-1}, (c) and (d) 3 ms^{-1}, and (e) 4 ms^{-1} (Jha *et al.,* 2011)

2.7 **Summary**

This chapter summarises the literature available on several different materials and their respective properties. A lot of work has been done previously to understand the mechanical and tribological properties of porous materials, composites, and syntactic foams. The fabrication method has been seen to have a significant impact on the final properties of these materials, with internal structures and ratio of materials defining the properties of these materials.

One major limitation of the current literature is that very little work has been done to understand the properties of syntactic foams made with recycled filler materials that have impurities and are irregular in shape.

Chapter 3 EXPERIMENTAL PROCEDURE

This chapter presents a detailed description of the characterization process, fabrication process, the mechanical and tribological testing procedures and the micro- and macro-structural observations for the aluminium syntactic foam samples.

3.1 Raw Materials

The aluminium smelter waste (ASW) was provided by Ultromex Limited, UK. The bulk material was sieved into three particle size groups: Small (125-250 μm), Medium (250-425 μm) and Large (425-1000 μm). The three sizes were treated as three different powders and were used separately to characterize their properties as well as to fabricate syntactic foams and to evaluate the effect of particle size on the properties of syntactic foams. Each particle size sample was split into two portions, where one portion was heated to a temperature of 450^{o}C and left to cool in air and the second was used as is, to make a total of six different powder samples and respective syntactic foams (SFs). The heated ASW powder samples were labelled with a -H suffix.

A second, commercially available ceramic powder filler material was used to fabricate syntactic for comparison purposes. The ceramic microsphere (CM) powder was provided by Envirospheres Pty Ltd (Linfield, Australia). The chemical composition of the CM powder is shown in Table 3-1. The CM powder was separated into three size groups: 75-125 μm, 125-250 μm and 250-500 μm. Based on the morphology and characteristics of the CM powder, only the large size group (250-500 μm) was used to fabricate syntactic foams as a comparison to ASW-SFs.

There are two distinct inner structures of the CM powders – hollow or porous. The hollow spheres have a solid shell and a thickness-to-radius ratio of 1:10 and a smooth surface texture. The porous CM spheres, on the other hand, have a coarser surface texture and a spongy inner structure with various pore morphologies ranging from perfect spheres to irregular pores of differing size. Table 3-2 below summarises the properties of the large CM powder.

Table 3-1: Chemical composition of CMs (Envirospheres Pty Ltd, 2018)

Chemical Element	**Weight %**
Silica (SiO_2)	55-65
Alumina (Al_2O_3)	30-36
Iron Oxide (Fe_2O_3)	1-2
Titanium Dioxide (TiO_2)	0.5-1

Table 3-2: Properties of large CM particles (Envirospheres Pty Ltd, 2018)

Property	**Value**
Particle Size range (µm)	250-500
Mean Diameter (µm)	326
Morphology	Spherical, porous particles, very coarse surface structure, spongy inner structure
Pore morphology	Spherical, nearly spherical or irregular
Pore percentage	78%
Bulk Density (g/cc)	0.66
Hardness (Mohs Scale/GPa)	6/7

Aluminium 6082 alloy was used in block form to manufacture the syntactic foams. Table 3-3 shows the composition of Al-6082 alloy in weight percentages (BSI, 2019). The alloy was specifically chosen for its high Si content, which allows for better fluidity, and a relatively high Mg content, which adds to the strength of the alloy (Kalhapure and Dighe, 2015). Cylindrical Al-blocks, either 50 mm or 70 mm in diameter, were used to manufacture syntactic foams of these two sizes. The two different sample sizes allowed for a wider range of mechanical property tests to be carried out given that certain equipment required larger samples for the test to be conducted.

Table 3-3: Chemical composition of Al-6082 alloy

Element	**wt%**
Aluminium	Balance
Silicon	0.7-1.3
Magnesium	0.6-1.2
Manganese	0.4-1.0
Iron	<0.5
Chromium	<0.25
Zinc	<0.2
Copper	<0.1
Titanium	<0.1
Others (Each)	<0.05
Others (Total)	<0.15

3.2 Characteristics of ASW

There is not enough information available that describe the characteristics of the ASW. Experiments were therefore conducted to determine all the necessary properties of the ASW particles.

3.2.1 Composition

The composition of the ASW powder was unknown at the beginning of this study, so experiments were conducted to estimate the composition and to better understand the mechanical behaviour of the samples.

The ASW particles were suspended in a clear epoxy resin and, after solidification, the samples were polished to provide a 1 µm finish. These samples were examined using a SEM JEOL-7001 to observe the morphology of the particles. An Energy-Dispersive X-Ray (EDX) spectrum was also generated using the microscope to roughly estimate the elemental composition of the particles.

X-Ray Diffraction (XRD) Spectroscopy was performed using a Rigaku Miniflex XRD (3rd Generation) with a Cu k-α X-Ray source. A small sample of each particle size was placed into separate sample holders and examined at angles between 10^{o} – 80^{o}. The XRD spectra was then analysed and filtered to find the peaks, which were compared to existing spectra so that the compounds present in the particles could be identified.

Several other compositional analysis tests, including X-Ray Fluorescence Spectroscopy (XRF), Inductively Coupled Plasma (ICP) and Ion-Exchange Chromatography (IC), were conducted by Ultromex Limited to understand the constituents of the powder and these were used to complement the findings from the EDX, XRD and SEM analyses.

3.2.2 **Particle morphology**

Optical and electron microscopy techniques were used to observe the particle size and morphology of ASW. Optical images of the ASW particles were taken to observe the size and shape of the particles and to estimate their particle size distribution. Individual particles were measured, and a particle size distribution curve was generated for the individual particle size groups. Since the particles are irregular in shape, the shorter diameter of the particles was used to generate the distribution curves. A mass-weighted mean diameter (D (4,3)) was calculated to estimate the average diameter of the particles in each particle range by:

$$\mathrm{D}\ (4,3) = \frac{\sum_{i=1}^{k} n_i D_i^4}{\sum_{i=1}^{k} n_i D_i^3} \tag{3.1}$$

Where *k* refers to the number of size ranges found in the sample. D(4,3) was chosen to estimate the mean diameter of the particles because of their irregular shape and size and therefore a mass-weighted estimate would be more accurate estimation of the mean diameter in this case. A Scanning Electron Microscope (SEM) (JEOL-7001) was used to obtain higher resolution images and examine the surface characteristics of individual particles.

3.2.3 **Density and porosity**

The actual density of the ASW particles was measured using the Archimedes method, with water being used as the working medium. Wax was used to encapsulate and seal the ASW particles so that an accurate density measurement can be taken. A set amount of wax was melted, cooled and solidified in a steel container attached to a wire and the total volume of the setup was measured using the Archimedes method.

The wax was then re-melted at a relatively low temperature of 80^{o}C to ensure no evaporation took place. A pre-weighed amount of ASW was stirred into the wax in the steel container and the entire setup was left to cool and solidify. The subsequent total volume of the setup was measured, and simple subtraction was used to get the total volume of the ASW powder. This was then used to calculate the effective density of the ASW powder. This experiment was repeated at least three times to ensure a high level of accuracy in the data collected.

The bulk density of the ASW powder was determined using a cylindrical steel container closed at one end and with a known diameter. A set amount of ASW powder was weighed and carefully poured into the steel container. The volume occupied by the ASW powder was then calculated using the known diameter and the height of the ASW powder. The bulk density was finally calculated. These measurements were made for every particle size group and repeated at least three times.

The porosity of the ASW particles was estimated using micrographs obtained using the SEM JEOL-7001. The diameter of the pores was measured and the percentage of porosity in the powder was calculated.

3.2.4 **Mechanical properties**

Bulk and individual particle property tests were conducted to characterise the ASW samples. To measure the mechanical properties of individual particles, particles were suspended in an epoxy resin and were examined by a KLA-Tencor Nanoindenter G200 with a Berkovich XP head. Here, the XP tip was set to a maximum load of 500 mN and an indent of 2000 nm was made in several particles in different regions. At least 15

indents were made for each powder sample. The hardness and Young's modulus of the particles were obtained from the data.

Bulk property tests were conducted using an Instron 4045. In these experiments, a cylindrical steel tube capped at one end was filled with the ASW powder up to a height of 20 mm and compressed at a strain-rate of 10^{-3} s^{-1} to a maximum load of 100 kN. The load-displacement data was collected using the Bluehill 2.0 software and subsequently analysed using Microsoft Excel. The results were represented as load-displacement curves.

3.3 Fabrication of Al-Matrix Syntactic Foams

All the Al-matrix syntactic foams used to produce this body of work were fabricated using the pressure infiltration casting process. In this process, a steel tube with a height of 55 mm and a diameter of either 50 mm or 70 mm was used as a mould. The tube was closed off on one end with a steel disc, with slight incisions on its edges to allow for air to escape during infiltration.

Once the mould was set, a pre-measured amount of ASW powder was poured and packed into the mould. An ultrathin Kaowool filter paper was placed on top to prevent direct contact between the ASW powder and the Al melt before infiltration and to partially filter the aluminium oxide layer during infiltration. An Al block was then placed on top of the filter paper. The volume of the Al block was kept relatively higher than 50% of that of the ASW powder to ensure complete infiltration. Finally, a steel disc whose diameter is very slightly smaller than the inner diameter of the mould was placed on top of the Al block.

The entire mould with its contents was placed in an electric furnace, heated and maintained at 715°C for 30 minutes to ensure that the Al block melts completely. The setup was then carefully moved to a hydraulic press and the melted Al was pressed rapidly to infiltrate into the ASW powder, occupying the interstices within the packed powder bed. It was left to cool before the syntactic foam sample was carefully extracted.

The syntactic foam samples were ground and cut into the required shapes and sizes for mechanical testing. Several ASW-SF samples were taken and subjected to T6 heat treatment (ASM, 1991) and investigated for the effect of heat treatment on the properties of ASW-SFs. The heat treatment, as shown in Figure 3-1, involved an initial heating of the syntactic foam samples up to 540°C for 100 minutes, followed by quenching in water and finally age-hardened for 10 hours at 180°C.

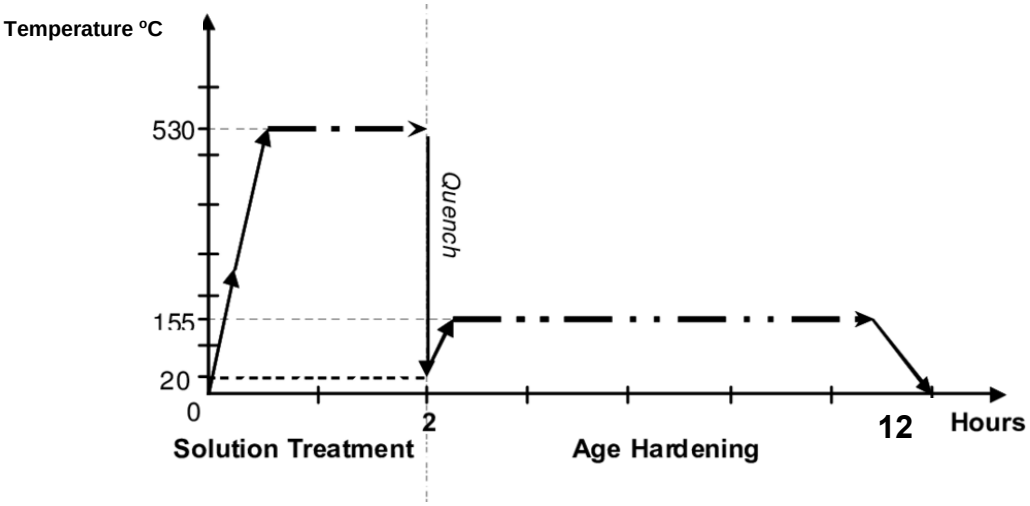

Figure 3-1: T6 heat treatment process (Yue, 2019)

Density measurements of the syntactic foams were completed using the Archimedes method described in section 3.2.2, with water being used as the working medium. The weight of the syntactic foam sample was measured first. The sample, tied with a

string, was then carefully put into water and its weight in water was recorded. The density of the foam was subsequently calculated from the measured weight and volume of the sample.

Table 3-4 describes the types of powders in the syntactic foam samples manufactured for this body of work. Samples denoted with a -H were manufactured using the heated ASW powder. Samples subjected to T6 heat treatment are denoted with a -T6 suffix.

Table 3-4: Properties and treatment conditions of the syntactic foam samples

Sample ID	**Powder Type**
S-ASF	Small ASW powder 125-250 µm
SH-ASF	Small ASW powder 125-250 µm, heated
S-ASF-T6	As S-ASF with T6 heat treatment
M-ASF	Medium ASW powder 250-425 µm
MH-ASF	Medium ASW powder 250-425 µm, heated
M-ASF-T6	As M-ASF with T6 heat treatment
L-ASF	Large ASW powder 425-1000 µm
LH-ASF	Large ASW powder 425-1000 µm, heated
L-ASF-T6	As L-ASF with T6 heat treatment
E-Sphere	CM powder 250-500 µm

3.4 Mechanical Properties of ASW-SFs

Several experiments were carried out to investigate the mechanical properties of the different fabricated ASW-SFs. The results from these tests were compared to the CM powder syntactic foams either by directly carrying out the experiments or from literature. All the tests were completed several times to obtain repeatable results.

3.4.1 Quasi-static compressive tests

Quasi-static compression tests were conducted to study the mechanical properties of the ASW-SFs. All the samples were cut into 10 mm x 10 mm x 15 mm and polished with their surfaces lightly lubricated to keep the effects of friction against the loading plates to a minimum. All the quasi-static loading tests were conducted at room temperature using an Instron 4045 machine supplied by Instron Corporation, Canton, USA, with a 50kN load cell and at a strain rate of 10^{-3} s^{-1} to ensure quasi-static condition. The raw data was collected using the Bluehill 2.0 software and subsequently analysed using Microsoft Excel to provide final stress-strain curves for all experiments.

3.4.2 Confined compression tests

In certain applications, the ASW-SFs will be confined in certain regions, primarily by itself. To understand their performance in these situations, confined compression tests were conducted. In the confined test, a sample of the same size as in Section 3.4.1 was machined, ground, polished, surface lubricated and placed in a mould designed to hold it without adding any strength to the setup. The mould was closed on all sides except the top so that the sample did not expand outwards to allow for a compression load to be applied as in the previous section. Apart from the addition of

the mould, the setup and data analysis method were identical to those described in section 3.4.1.

3.4.3 **Three-point bending tests**

Three-point bending tests were used to measure the flexural properties and the elastic modulus of the syntactic foam samples. Figure 3-2 shows the experimental setup to carry out the tests and Figure 3-3 (ASTM, 2018a) shows the setup for the test sample. The samples were machined to 60 mm length, 10 mm width and 4 mm thickness. These dimensions were chosen based on ASTM C1341 (2018) (ASTM, 2018a).

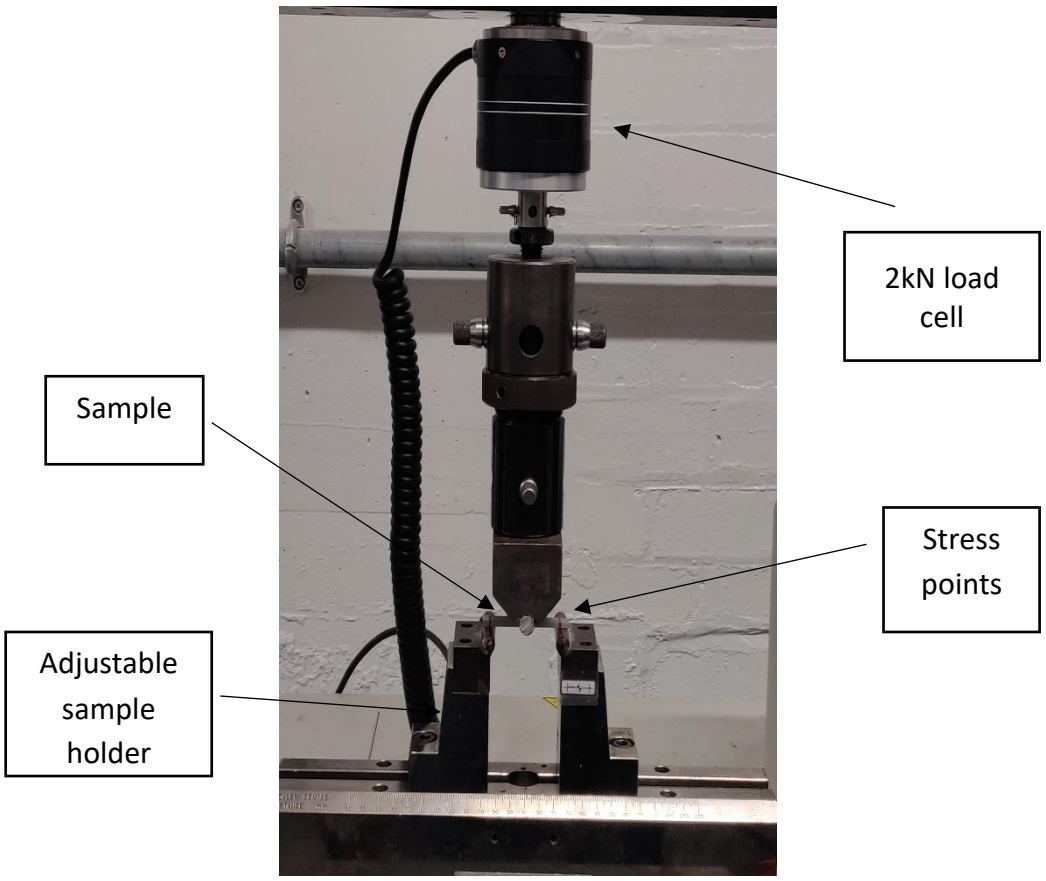

Figure 3-2: Experimental setup for three-point bending tests

.

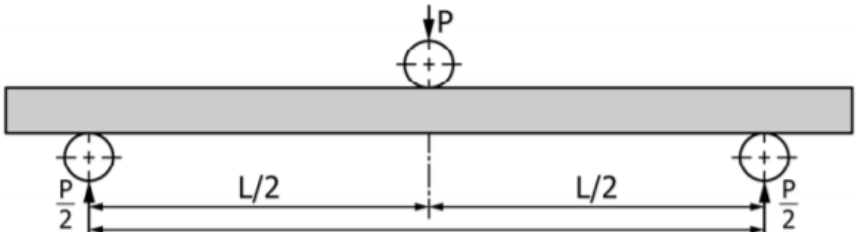

Figure 3-3: Setup of test sample [taken from (ASTM, 2018a)]

The Instron 4505 machine used in section 3.4.1 was used here in three-point bending mode and a similar start-up procedure as for the compression tests was used. The subsequent load-displacement data was collated into a Microsoft Excel sheet from the Bluehill 2.0 software and the following equations were used to calculate the flexure stress (σ), flexure strain (ε) and the modulus of elasticity (E_B):

$$\sigma = \frac{3PL}{2bd^2} \tag{3.2}$$

$$\varepsilon = \frac{6\delta d}{L^2} \tag{3.3}$$

$$E_B = \frac{L^3 m}{4bd^3} \tag{3.4}$$

where *P* is the load (N), *b* is the specimen width (mm), *d* is the specimen thickness (mm), *L* is the support span length (mm), *m* is the initial slope of the force-displacement graph and *δ* is the deflection of the centre of the beam (mm).

3.4.4 **Drop hammer impact tests**

Drop weight tests were conducted to characterise the performance of ASW-SFs under dynamic loading conditions and to obtain dynamic properties of the syntactic foams, such as energy absorption, strength reduction and failure mechanism (L. P. Zhang and Zhao, 2007). A drop weight tower rig was set up as shown in Figure 3-4.

The rig consists of the following components: a drop weight carriage consisting of a 15 kg hammer held 1.5 m above the sample and two vertical steel guiding bars, a cylindrical block holding the sample, a piezoelectric load cell (Kistler 9061, maximum load of 200 kN) and a high-speed camera (MotionPro-X4 with 50mm lens). The setup allowed for a maximum impact velocity of 5.42 ms^{-1} and impact energies of up to 221 J. The piezoelectric load cell was used to collect force-time data that was recorded using the Data Flow Plus software package. The high-speed camera was used to observe the deformation behaviour of the sample. The Pro Analyst software package was used to identify the motion of the drop weight impactor, to auto-track the deformation of the sample using the high-resolution images taken by the camera,

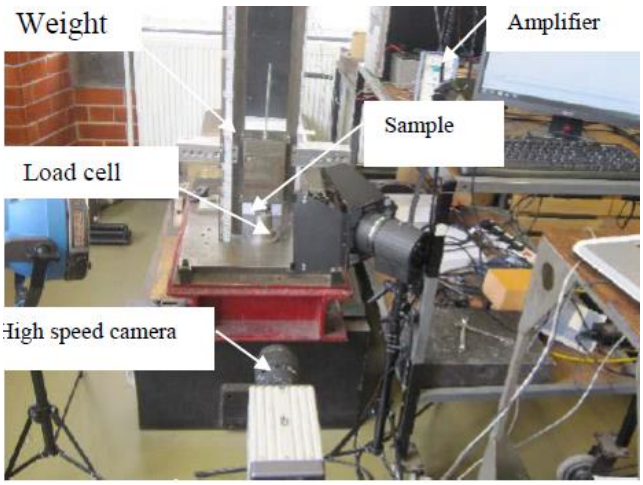

Figure 3-4: Drop weight hammer setup

and to generate velocity-time data and curves. The results were combined and analysed to generate stress-strain curves under dynamic loading conditions.

3.4.5 Charpy V-notch impact tests

The Charpy V-notch impact tests were conducted as per ASTM E23 (ASTM, 2018b) that described the standardised process for notched bar impact testing of metallic materials. The purpose of the V-notch is to locally concentrate the stress such that the specimen fractures on impact. Figure 3-5 shows the setup for the experiment along with a description of the hammer position relative to the specimen and the notch. This experiment was used to determine the toughness of syntactic foam samples by measuring the energy absorbed by the samples as the hammer swung through. Specimens were machined and carefully notched to dimensions that guaranteed failure. These dimensions are visually represented in Figure 3-6.

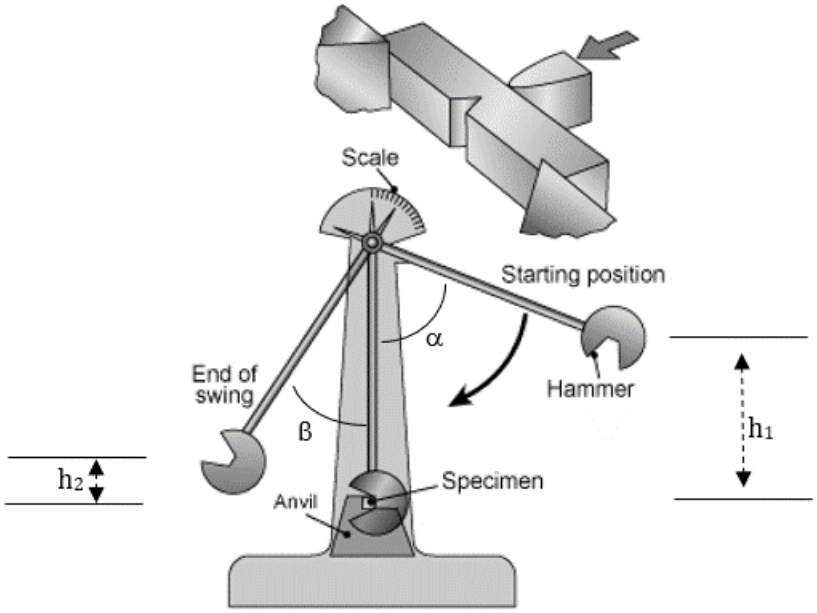

Figure 3-5: Standardised testing procedure for notched bar impact tests [Adapted from (ASTM, 2018b)]

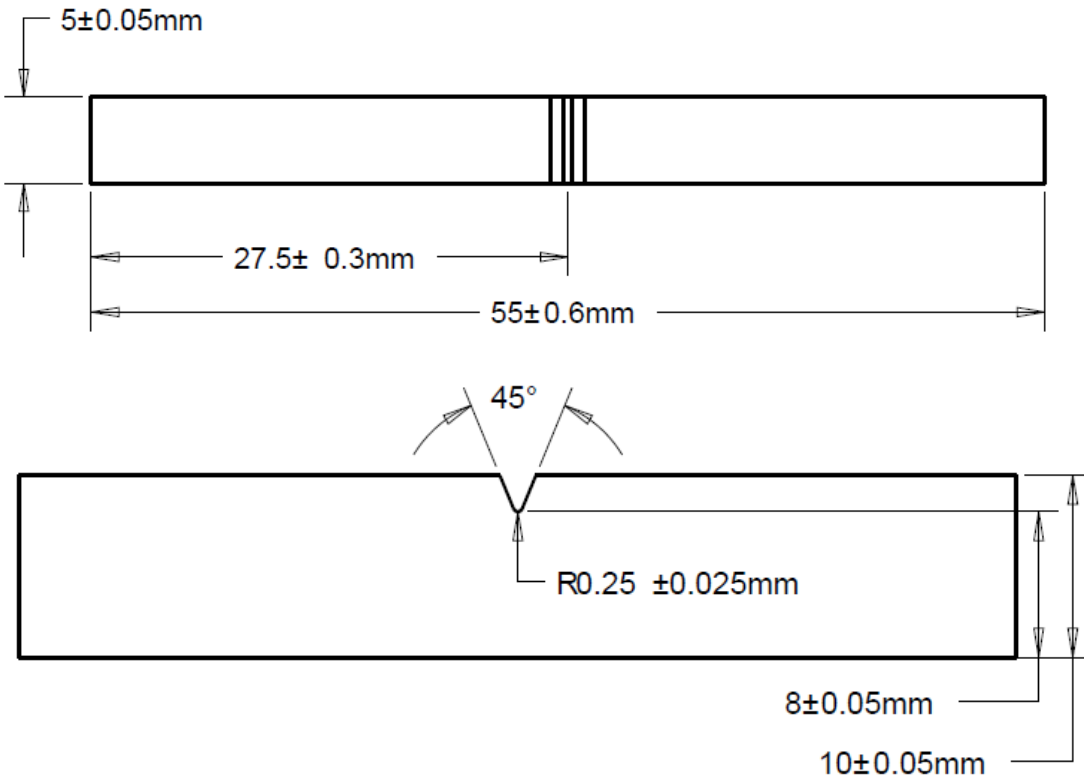

Figure 3-6: Dimensions of the samples for notched bar impact tests (Yue, 2019)

To start the experiment, the specimen and anvil were lined up so that the anvil was parallel to and against the notch. The anvil was then lifted to a height h_1 that corresponded to a potential energy of mgh_1. The hammer was released and allowed to swing through the specimen, converting potential energy to kinetic energy, to a final height h_2 corresponding to a final potential energy of mgh_2. Angles α and β were recorded to allow for the calculation of energy absorbed by the sample using the formula:

$$E_a = Mg \times R(cos\beta - cos\alpha) \tag{3.5}$$

$$A_k = \frac{E_a}{S} \tag{3.6}$$

where M is the mass of the hammer (3.7 kg), g is the gravitational acceleration constant (9.81 ms^{-2}), R is the radius of the pendulum (0.347 m), α is the initial angle (150^{o}) and β is the final swing-through angle and A_k is the impact toughness.

3.5 Tribological Tests of ASW-SFs and CM-SFs

3.5.1 Introduction to wear parameters

Tribology is the study of friction, wear and lubrication, which are important for materials with applications in the transport industry with a focus on lubrication, energy consumption and efficiency (Stachowiak, 2017). Some important properties studied during tribological testing include frictional force, coefficient of friction, specific wear and surface roughness.

Frictional force is the force generated when two bodies slide against each other. The magnitude of the force is governed mainly by the surface properties of both bodies and the magnitude of any external forces acting on either body. The frictional force can be reduced or increased by adding surfactants onto either body, effectively adding a layer which acts as an intermediary that increases or decreases the frictional force.

Another way of representing the frictional force is through the coefficient of friction (COF), which is a dimensionless scalar quantity allowing for a simpler comparison between materials, symbolised by the Greek character μ. This is a ratio of the frictional force between two bodies and the external force pressing them together and is dependent on the materials used. COF can be as little as zero or as high as greater than one. COF is normally lower when two bodies of different materials rub

against each other. For instance, steel on steel has a high COF, but is lower when the partner material changes to brass or aluminium (The Air Brake Association, 1924).

When two bodies continuously slide against each other for a certain distance, known as the sliding distance, one or both materials will show signs of damage. This damage is known as wear and occurs due to the friction force between the two bodies. The specific wear is described by the volume lost per unit distance and is a measure of the material's resistance to wear. The lower the specific wear, the more resistant it is to wear and the longer it will run before it will need to be replaced.

When looking at friction and wear, a material's surface texture is an important characteristic in its overall performance. The property studied for tribological behaviour is surface roughness, which is a measure of the micro-irregularities in the surface texture and the roughness value can be an indicator of the suitability of the material in certain applications. For instance, rough surfaces tend to wear more and be more prone to corrosion and cracks when compared to smoother surfaces (PCE Instruments, 2020). Two parameters are generally measured for quantifying the surface roughness of materials: R_a and R_z. R_a is the mean surface roughness and R_z is the difference between the highest and lowest points of the studied surface.

These properties altogether give a better understanding of the material's tribological behaviour and its suitability for various applications.

3.5.2 **Sliding wear tests**

Tribological property tests were conducted at the University of Chester's Tribology Lab using a tribometer (TRB Tribometer supplied by Anton Parr) and surface wear images were taken using a Stereomicroscope (Leica M135 microscope with a Leica

M120 HD Camera). For the sliding wear tests, ball-on-disc tests were carried out where the static partner used was a steel ball with a diameter of 3 mm. The ASW-SFs and CM-SFs were manufactured to discs of a height of 15 mm and a diameter of 45 mm. The surfaces of all syntactic foam discs were ground to provide an even surface finish.

In the ball-on-disc tests, the track radius was set at 10 mm, the applied load was 10 N, which corresponded to 0.36 MPa nominal surface pressure, the linear speed was 5.0 ms^{-1} and the sliding distance was 2000 m for each test. The data on the coefficient of friction and frictional force vs sliding distance was collected by the tribometer software. A stereomicroscope was used to capture surface images of the static partner and the syntactic foam samples once the experiment was completed.

Both dry and lubricated tests were conducted under the same parameters as described above, except the latter were with the addition of 5 drops of Comma DOT4 Brake and Clutch Fluid (20 µl per drop) every 500 m of sliding distance.

3.5.3 **Wear surface characterisation**

The specific wear of the syntactic foam was estimated by measuring the weight difference before and after the tests.

After the wear tests, the syntactic foam samples were analysed using an Interferometer (Veeko Wyko NT1100). Here, the sample was placed under the interferometer lens and the surface was scanned to reveal the change in surface properties. The data and images obtained were fed to a computer software (Vision 3.60) and analysed to obtain data on surface roughness (R_a and R_z) and track depth.

Chapter 4 RESULTS AND DISCUSSION

4.1 Characteristics of Aluminium Smelter Waste

The characteristics of the ASW particles are important for understanding the properties of the resultant syntactic foams. These characteristics include the composition, morphology, density, and porosity and mechanical properties of the ASW particle size groups, which are presented and discussed in this section. The physical characteristics of the ASW particles are then compared to those of the commercially available E-spheres.

4.1.1 Composition of ASW particles

Figure 4-1 shows the difference in colour between the heated and non-heated ASW particles. What can be seen from the figure is that the Large sample showed a change in colour from dark grey to off-white when heated, whereas the other samples did not show a noticeable change in colour. To understand this change, a compositional analysis was conducted. Table 4-1 shows the EDX elemental analysis obtained for each particle size.

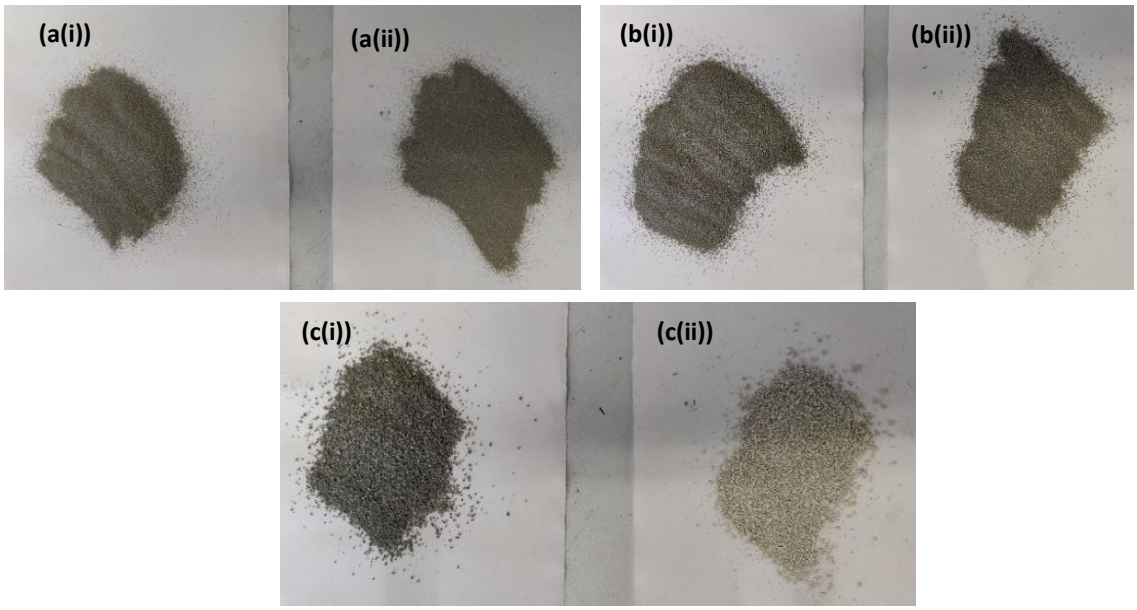

Figure 4-1: Colour change from (i) heated and (ii) non-heated samples of (a) Small, (b) Medium and (c) Large ASW powders

Table 4-1: EDX elemental composition of ASW particles

ASW Size Group	Composition (wt%)							
	O	F	Na	Mg	Al	Si	Ca	Fe
Small	21	8	1	14	43	2	-	11
Medium	21	2	-	4	40	9	4	20
Large	21	-	-	4	44	17	-	13
Small-H	21	8	2	14	42	2	-	11
Medium-H	22	1	-	5	43	8	2	19
Large-H	31	-	-	3	44	13	-	9

Although the EDX results cannot be used on their own to determine the composition of the ASW particles, the results do show that the different particle size groups samples have different elemental compositions. Furthermore, the heated Large sample shows a higher weight percentage of oxygen in the particles when compared to Large, yet the other two particle sizes did not show as significant a difference in oxygen concentration. The colour change therefore can be attributed to a change in oxidation state of elements present in the mix. For example, the grey colour can be attributed to aluminium metal and the off-white colour can be due to the colour of alumina.

Following on from the EDX results, the graphs from the XRD analyses are presented in Figure 4-2. The graphical outputs were compared to existing XRD analyses of compounds and elements present in ASW particles, including iron and iron oxides (Suresh, Karthikeyan and Jayamoorthy, 2016; Manohar *et al.,* 2012), aluminium and alumina (Murali *et al.,* 2017; Kishi and Toraya, 2004), magnesium and magnesium oxide (Dercz *et al.,* 2009), calcium oxide and calcium fluoride (Linggawati, 2016; Jing-hong Song *et al.,* 2011), silicon (Hossain, Johra and Jung, 2018) and sodium (Senden, Geitenbeek and Meijerink, 2017). A summary of the compounds present in the different ASW samples is found in Table 4-2. The composition of E-spheres is included for comparison.

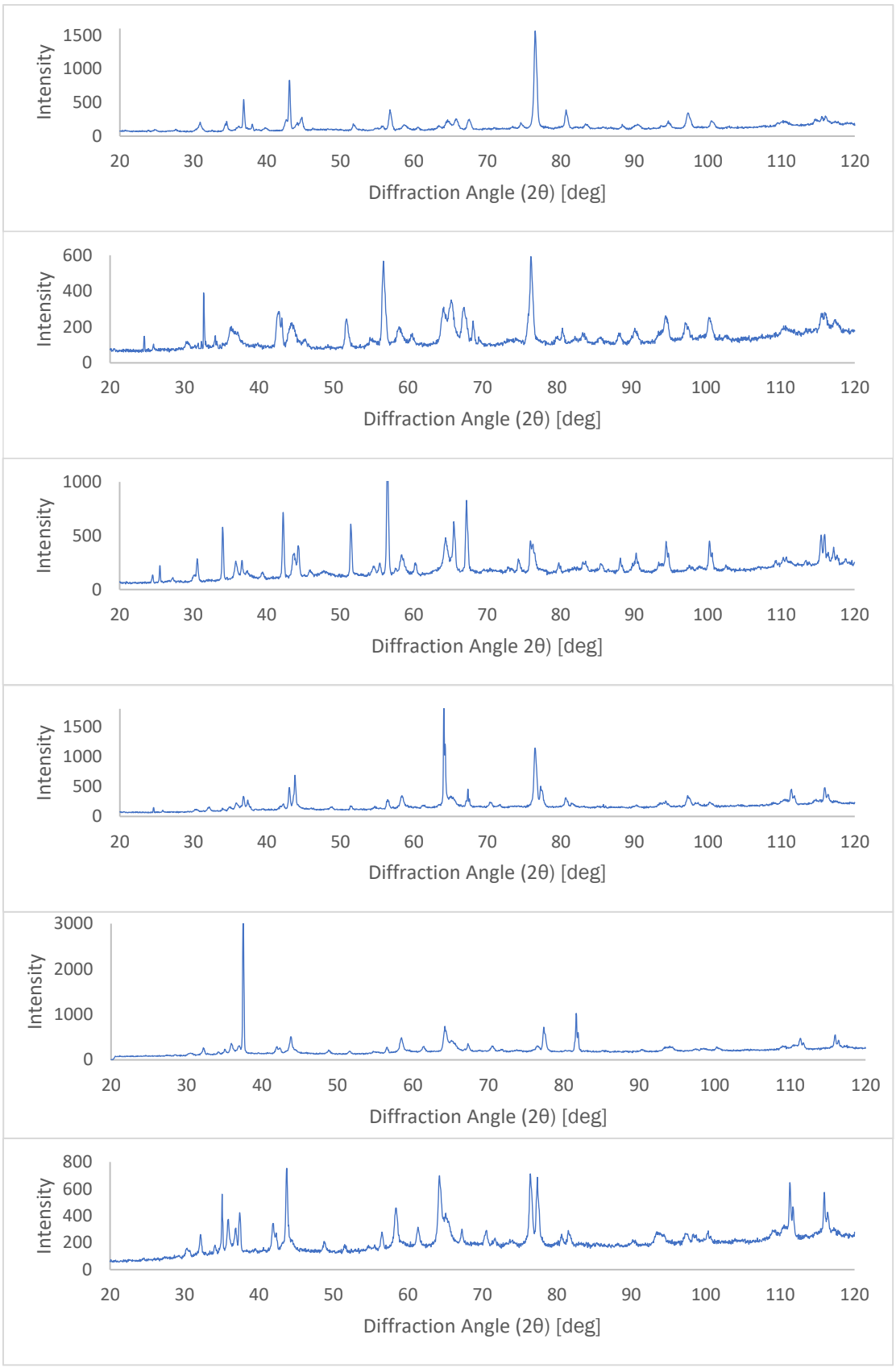

Figure 4-2: XRD peaks for (from top to bottom) Large, Large-H, Medium, Medium-H, Small and Small-H samples

Table 4-2: Summary of compositional analysis

ASW Size Group	XRD Results (Compounds Present)
Small	Fe_2O_3, Al_2O_3, MgO, Al, SiO_2, **Na_3AlF_6**
Medium	Al_2O_3, Fe_2O_3, MgO, Al, SiO_2, **CaF_2**, **CaO**
Large	Al_2O_3, Fe_2O_3, MgO, Al, SiO_2
Small-H	Fe_2O_3, Al_2O_3, MgO, Al, SiO_2, **Na_3AlF_6**
Medium-H	Al_2O_3, Fe_2O_3, MgO, Al, SiO_2, **CaF_2**, **CaO**
Large-H	Al_2O_3, Fe_2O_3, MgO, Al, SiO_2
E-Sphere	Al_2O_3, SiO_2, Fe_2O_3, TiO_2

Table 4-2 shows that most of the compounds present in the ASW particles are the same across the different particle sizes, which is to be expected given that they come as a bulk powder. The difference in composition is in the Small and Medium sizes, which have one or two additional compounds present in the form of cryolite, and calcium fluoride and calcium oxide, respectively.

The cryolite impurity present in the Small sample can be explained by looking at the secondary aluminium smelting process (Schlesinger, 2017). Many smelters add salts in their mix to lower the temperature of the melt down to between 1000-1100^{o}C. The addition of salts, such as sodium fluoride (NaF) forms a composite structure with aluminium to form cryolite, which has a lower melting point than alumina. Similarly, the presence of other metal oxides in all the particle sizes is mostly due to the nature of the secondary smelting process, where the recycled aluminium can come with various trace elements. The calcium fluoride present in the Medium sample is mainly

due to the reaction between calcium and the sodium salts in the mix. The effect of these impurities on the various samples is investigated later in this section through nanoindentation and quasi-static loading tests.

XRF and IC tests were conducted by Ultromex Limited to estimate the percentage of oxides present in the particle size groups. The findings are summarized in Table 4-3. These results complement the XRD analysis and show that ASW particles are made up of mostly oxides, with trace impurities that decrease as particle size increases.

Table 4-3: Summary of IC and XRF analyses

ASW Size Group	Oxides (includes Al_2O_3, MgO, Fe_2O_3, SiO_2) (wt%)	Loose Al Metal (wt%)	Impurities (includes CaO, CaF_2 and Na_3AlF_6) (wt%)
Small	83.82	7.16	9.02
Medium	89.61	7.10	3.82
Large	87.00	9.06	2.94
Small-H	83.86	6.51	9.04
Medium-H	89.94	7.01	3.05
Large-H	96.10	3.42	1.48

When compared to commercially available filler materials, like the E-spheres, the ASW particles have significantly higher amounts of impurities and compounds that are not oxides. The impurities present may influence the overall properties of the manufactured SFs, which will be discussed later in this chapter.

It was noticed during powder handling that simple bulk powder separation using a sieve can get rid of most impurities in the powders. However, it may not be complete separation and there may still be trace impurities in all samples that were not detected in the EDX and XRD analyses, because of the comparatively small sample sizes used. Nevertheless, it is possible to reduce the level of impurities down to a minimum by bulk separation.

4.1.2 **Physical Characteristics**

The ASW particles are observed to have an irregular shape with a porous structure. All the particle sizes display the same irregular morphology. Figure 4-3 shows micrographs for the three particle sizes and the subsequent Figure 4-4 shows the presence of pores in the particles. The particle size distributions of the powders are shown in Figure 4-5 and Table 4-4 shows the mass-weighted mean diameters,

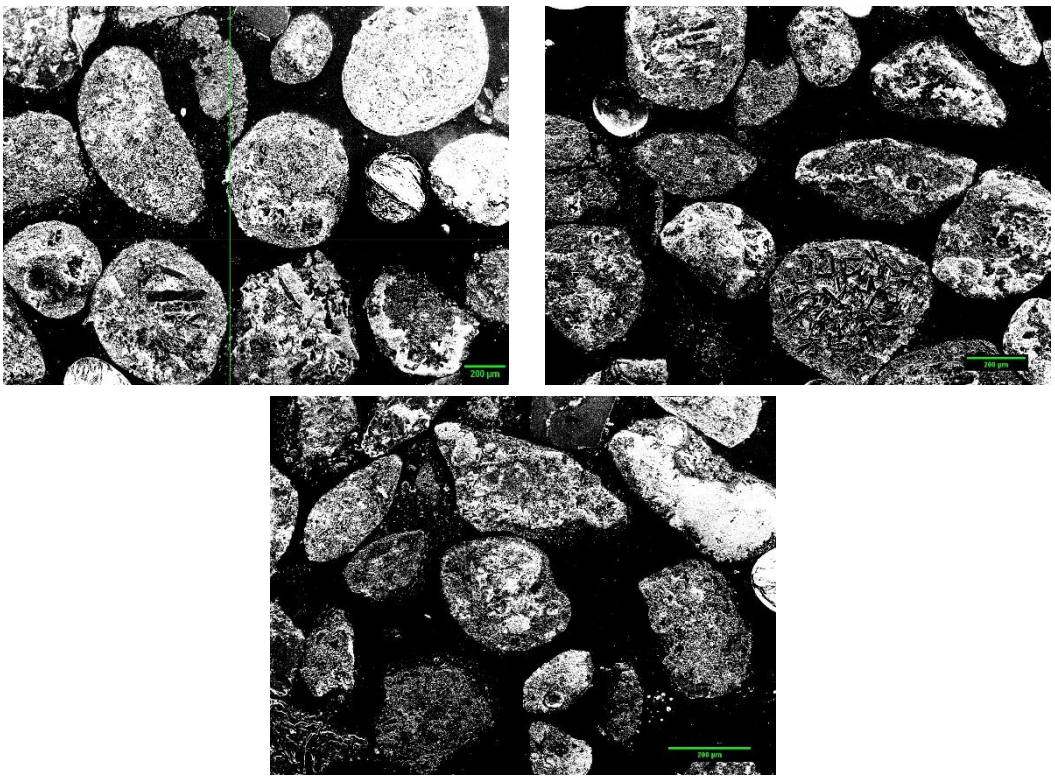

Figure 4-3: SEM micrographs of (top left) Large , (top right) Medium and (centre) Small ASW samples

calculated using Equation 3.1. Table 4-5 shows the measured porosity and density values for all ASW samples. Table 4-6 lists the weight changes after heating the ASW powders. From the above figures at tables in this section, it is evident that the ASW particles are irregular in shape and size, with a variable range of particle sizes in the size groups. They have an irregular pore structure, with an increase in porosity as particle size increases and a resultant decrease in density. The various impurities present also have an effect on the densities, with the Large particle size group having a lower density due both to the higher Al content compared to oxide content and also to the porosity.

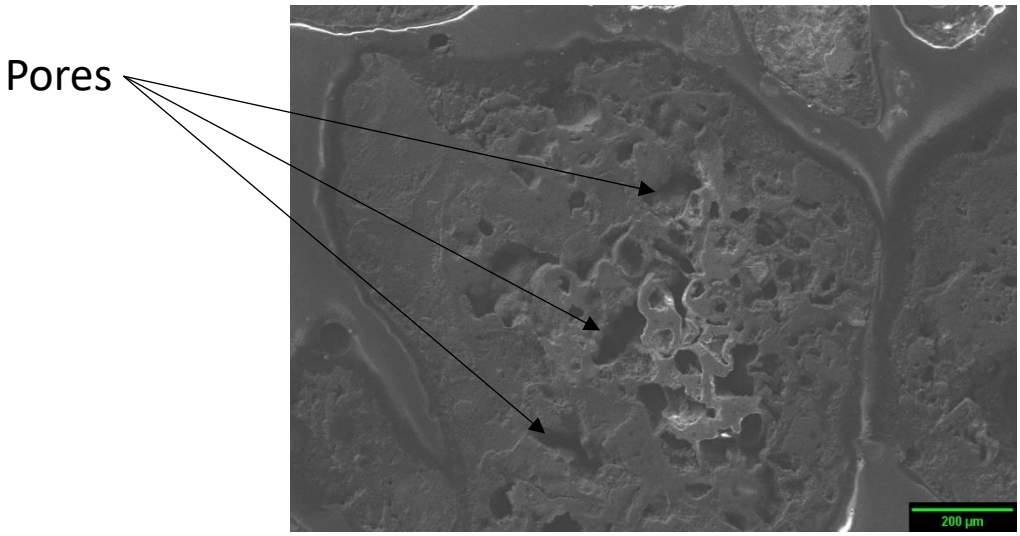

Figure 4-4: SEM micrograph showing the presence of pores in a Large ASW particle

Table 4-4: Mass-weighted mean diameters of the three ASW particle size groups

ASW Size Group	D [4,3]
Small (125-250 µm)	207 µm
Medium (250-425 µm)	358 µm
Large (425-1000 µm)	805 µm

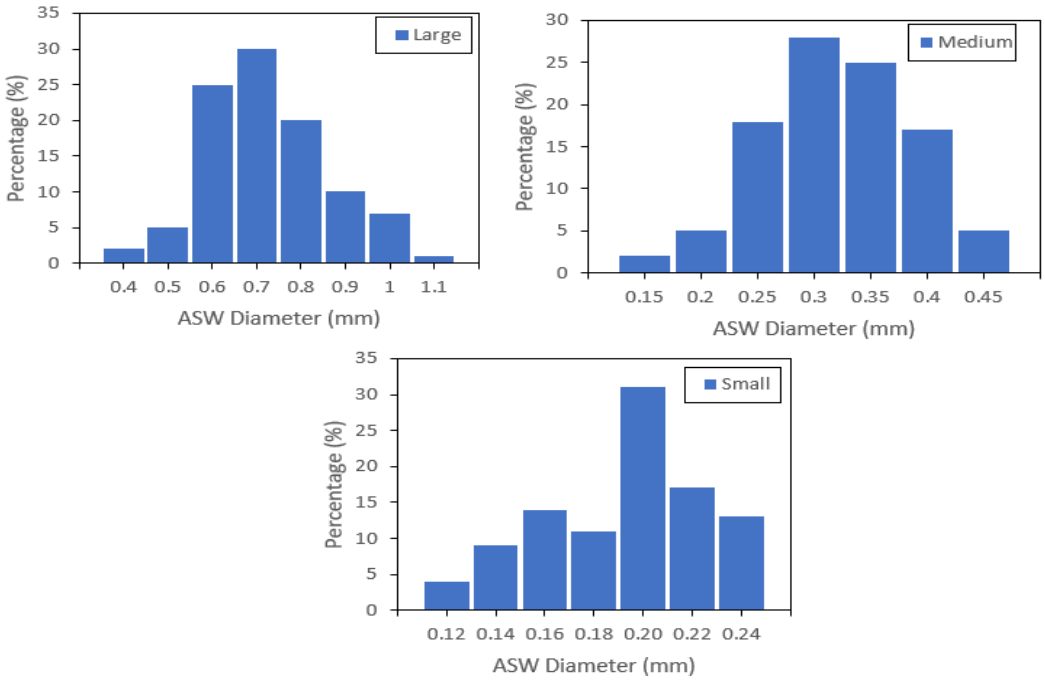

Figure 4-5: Particle size distributions of the ASW particles

Table 4-5: Densities and porosities of the ASW and E-sphere powders

ASW Size Group	Density (gcm^{-3})	Porosity (%)
Small	1.40	15
Medium	1.20	21
Large	1.15	30
Small-H	1.40	16
Medium-H	1.20	20
Large-H	1.05	36
E-sphere	0.66	78

Table 4-6: Weight change after heating ASW powders

ASW Size Group	Weight change after heating (%)
Small	+1%
Medium	0
Large	-8%

4.1.3 **Mechanical Properties**

The compressive behaviour of the ASW powders in their respective size ranges in confined compression is shown in the load-displacement curves in Figure 4-6. All the graphs show two distinct phases during compression: crushing and densification. The first phase starts with a short period of packing or particle rearrangement. The particles are then gradually collapsed during the crushing phase due to the porosity in the particles. This is seen in the graph as a relatively steady increase in displacement as the load is increased. Once most of the particles have been crushed, the curve enters the densification phase where the fragmented bits of the particles densify to display a rapid increase in load as displacement is increased. Table 4-7 displays the load at a set displacement equivalent to 35% strain and the displacement at the maximum load of 100 kN so that the properties of the samples can be compared.

Table 4-7: Comparisons of critical load and displacement for the ASW powders

ASW Size Group	Load at 35% Strain (kN)	Displacement at 100 kN Load (mm)
Small	31.78	12.25
Medium	55.58	10.25
Large	31.28	11.50
Small-H	43.72	10.75
Medium-H	33.78	11.75
Large-H	26.20	13.00

For the non-heat treated samples, the Large sample has a higher strength than the Medium and Small samples and reach the 100 kN load at a higher displacement. This means that the large particles are stronger and have more porosity than the small or medium particles. This can be due to the magnitude of impurities present in the particles as well as the difference in porosity.

The heat treated Large sample shows a sharp decrease in strength after heat treatment. Table 4-6 shows that there is a weight loss of 8% and Table 4-5 shows that there is a reduction in density, from 1.15 gcm^{-3} to 1.05 gcm^{-3}, in the large ASW powder after heating, which indicates an increase in porosity in the particles. It is the presence of additional pores that introduces a weakness in the particles.

The heat treatment of the ASW particles results in an overall increase in strength for the Small and Medium samples. There is minimal change in density or porosity for these samples. The cryolite present in the Small sample prevents oxidation from

occurring within the sample, so there are minimal changes in colour, density, or porosity. Calcium fluoride present in the Medium sample acts in a similar way to cryolite (Tressaud, 2019), preventing reactions occurring in the mix.

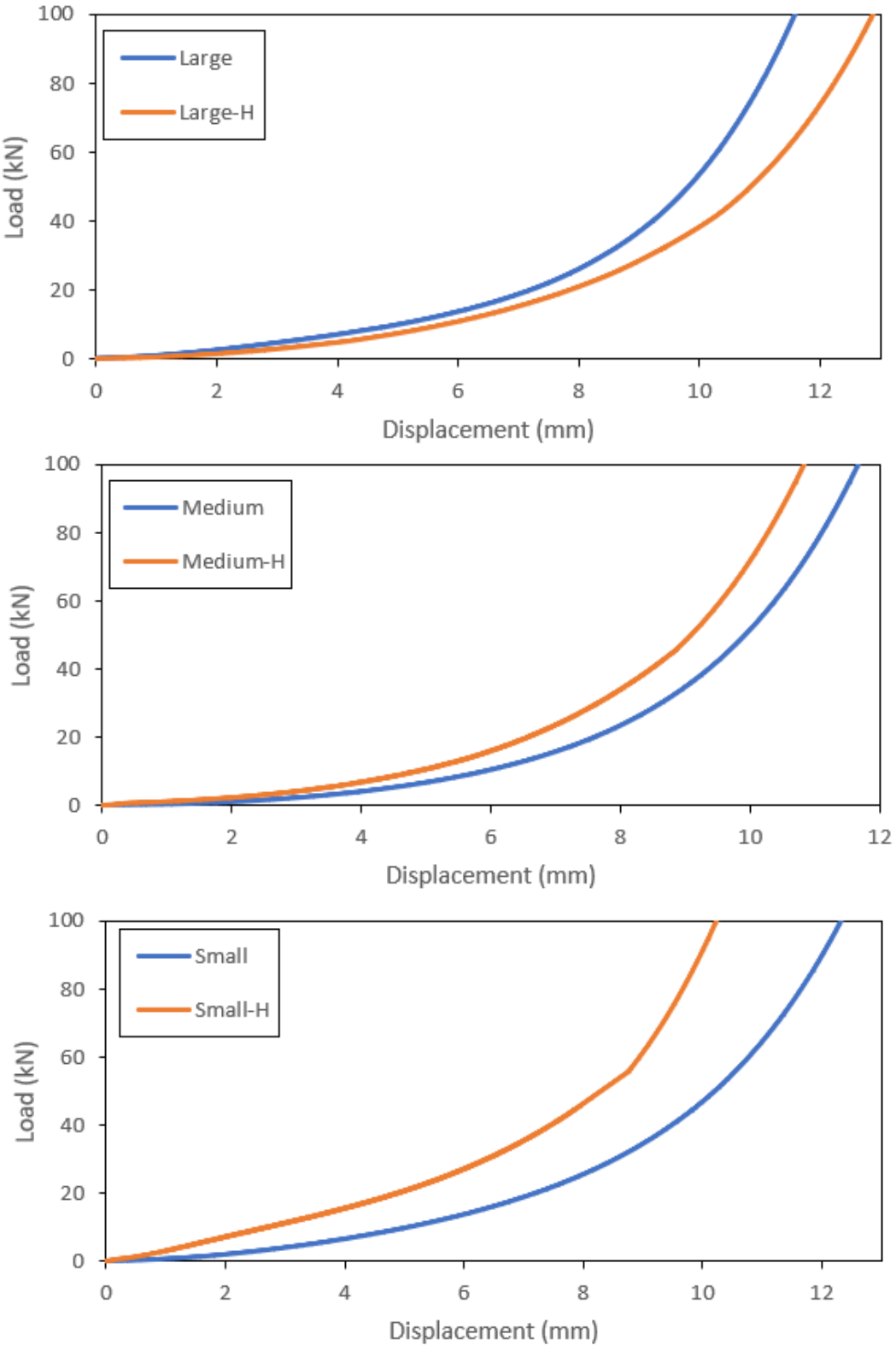

Figure 4-6: Compressive behaviour of ASW samples

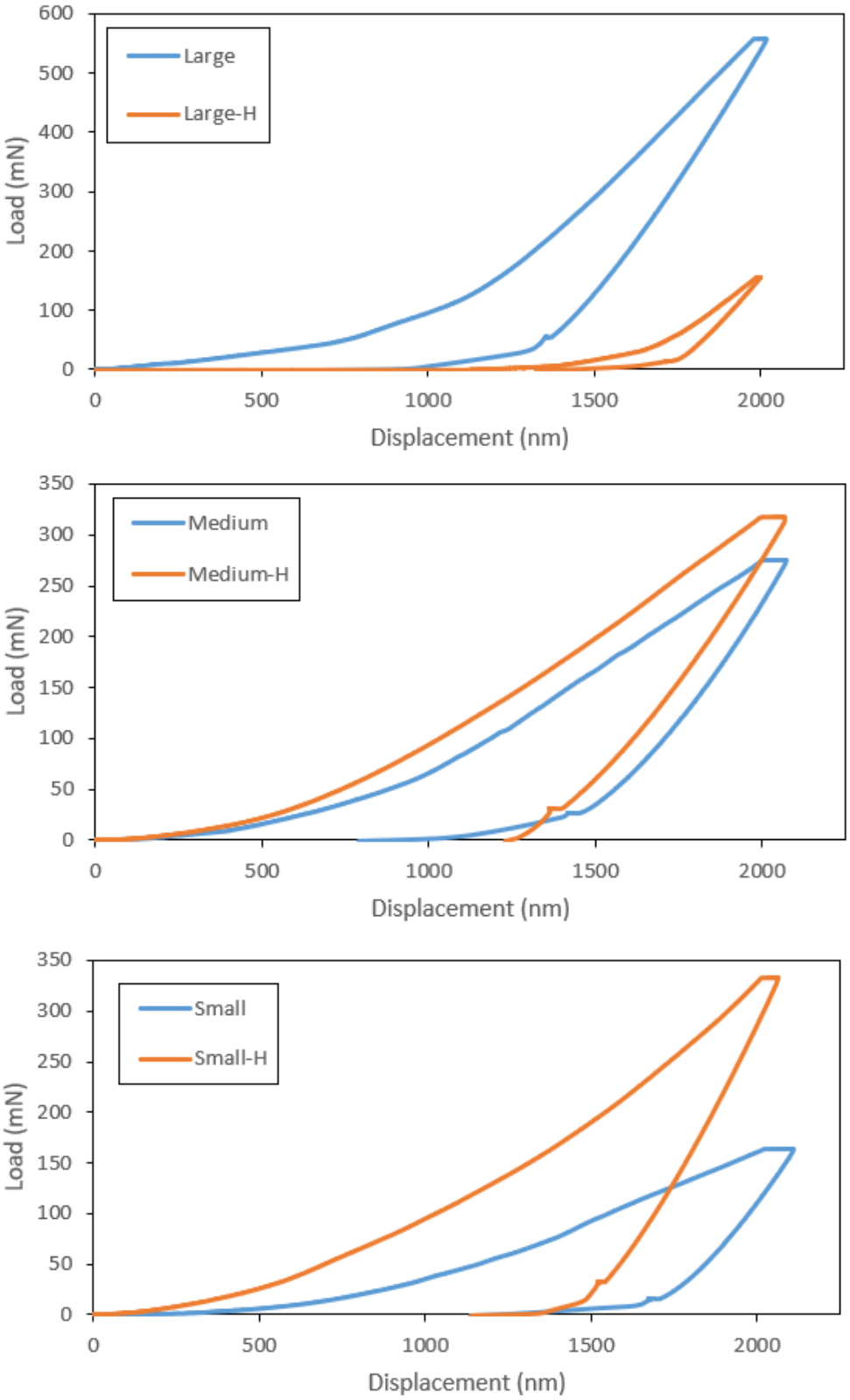

Figure 4-7: Loading-unloading curves for the ASW samples

Table 4-8: Elastic modulus and hardness of ASW particles

ASW Size Group	Elastic Modulus (GPa)	Hardness (GPa)
Small	48.09	1.93
Medium	60.53	2.57
Large	113.98	9.32
Small-H	77.02	4.68
Medium-H	61.55	4.91
Large-H	67.34	1.93
E-Sphere	37.2	7.00

Figure 4-7 shows the loading-unloading curves obtained from the nanoindentation experiments that examined the individual particle properties. Table 4-7 summarize the elastic modulus and hardness results. The nanoindentation curves show a similar trend to that summarised in Table 4-6, where the heating of the particles leads to an increase in strength for small and medium particles and a decrease in strength for the large particles.

Table 4-7 summarizes the elastic modulus and hardness results. Upon heating, the small particles show a sharp increase in elastic modulus and hardness. The Medium particles tend to show an increase in hardness and a much smaller increase in the elastic modulus. This is similar to what was observed in Figure 4-6. The results indicate that the heating of the Small and Medium ASW particles leads to hardening of the individual particles, which in turn leads to an increase in overall strength and stiffness (Richerson, 1992; Kirchner, 1979; Carton, 2016). The opposite is observed in

the large particles where heating leads to a decrease in hardness, strength and stiffness. The increase in porosity during heating of the particles seems to have a significant effect on the mechanical properties of the large ASW particles.

4.1.4 **Comparison with E-Spheres**

Commercially available E-spheres are selected as a comparator to the ASW particles to understand the suitability of ASW particles as a filler material in a syntactic foam. The selected E-spheres have both hollow and porous inner structures, with most of the particles being porous, and are near-spherical in shape, which allows for good packing in a contained space. They have a porosity of greater than 80% and a density of 0.60 gcm^{-3}. They have a relatively fixed composition and have no recorded impurities. The surface hardness of the E-spheres is 7.00 GPa, with an elastic modulus of 37.2 GPa and a mean diameter of 326 µm (Envirospheres Pty Ltd, 2018).

The ASW particles are porous, with a lower porosity of 15-36% and a higher density of 1.05-1.40 gcm^{-3} compared to the E-spheres. They are also irregular in shape and have several impurities. The imperfections present may introduce localised mechanical stresses when used as filler materials for syntactic foams. Furthermore, the hardness and elastic modulus values vary, and increase in magnitude as particle size increases.

4.1.5 **Summary**

All ASW particles have an irregular shape with a porous structure. When the Large ASW particles are heated, they show a change in colour from dark grey to off-white, while the other particle size groups show no change in colour. The compositional analysis shows that this colour change can be due to the formation of alumina from the oxidation of loose Al. Furthermore, the composition of the ASW particles shows a change as the particle size changes, where the particles in the Small sample has more impurities present. The compressive behaviours of the particles under confined compression and nanoindentation both show that the heating strengthens and hardens the small and medium particles, but has the opposite effect for large particles. For large particles, the increase in porosity leads to the decrease in strength. In comparison, E-spheres are more stable, with fewer impurities and a regular structure, which allows for better packing for infiltration.

4.2 Structural Properties of Syntactic Foams

The microstructure of the as-manufactured syntactic foams has a great effect on their mechanical properties, as explored in Chapter 2. Furthermore, any defects generated during the infiltration step will also contribute to the properties of the syntactic foam. For instance, a significant number of air pockets or voids within the syntactic foam samples can bring about microstructural weaknesses and therefore result in a potential reduction of strength. The possible defects that can be present in the syntactic foams, and those that can affect their properties, are first presented in this section, followed by an analysis of the microstructure and density of the syntactic foams. Optical images and micrographs of the polished cross-sections are presented.

4.2.1 Defects

Figure 4-8 shows the cross-section of a syntactic foam sample with a crack running across it. When molten Al is forced through the packed bed of ASW particles in a steel tube, it tends to flow preferentially along the gaps between the particles and the steel tube wall because of the low resistance on the inner surface of the steel tube. Once the molten Al reaches the bottom of the tube, it flows back up through the ASW particles as well. Premature solidification of the molten Al, due to a temperature gradient between the press and the steel tube, can lead to air pockets being present in the foam and minimal or no infiltration in that region.

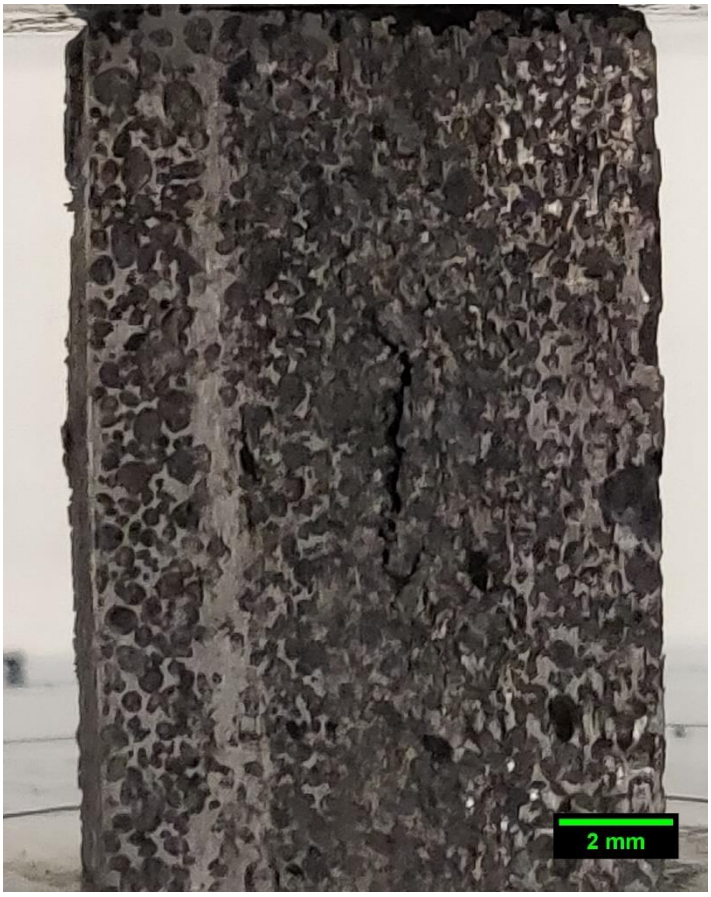

Figure 4-8: SF sample with a defect: Crack running down the interior of the sample

Figure 4-9 shows the cross-section of a syntactic foam sample as a result of broken ASW particles floating in the metallic phase of the foam. There is debris floating in the metal matrix, which indicates that some of the surrounding ASW particles were indeed crushed. Given that a mechanical process is used to obtain the ASW particles, there are defects present in some particles. These defective particles can be infiltrated with Al when molten Al is forced through a packed bed of particles during fabrication of the syntactic foam sample. Some defects can occur during infiltration when the infiltration pressure is higher than the strength of the ASW particles. In theory, it is possible to control the infiltration pressure in a way that it is high enough to force molten Al through the interstices of the ASW particles, yet not so high to

break the ASW particles. Under the experimental conditions used to fabricate these syntactic foams, however, it is difficult to control the pressure and estimate when complete infiltration of the molten Al is achieved. Therefore, applying continuous pressure after complete infiltration can lead to the crushing of some ASW particles, resulting in some of these particles being infiltrated with Al too.

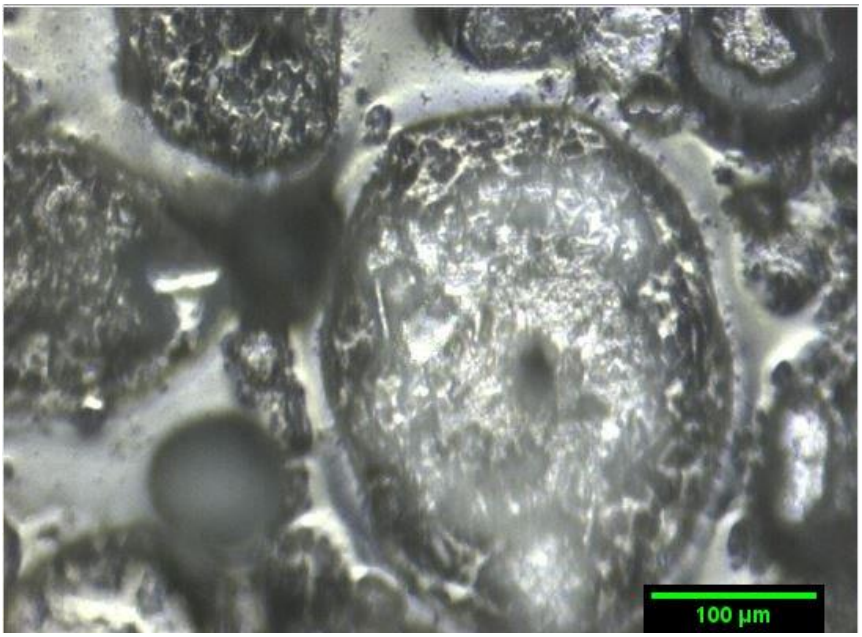

Figure 4-9: Cracked ASW particles infiltrated with molten Al

One thing to note is that some loose Al is already present within the ASW particles, as shown in the compositional analysis from Section 4.1. It transforms to its molten state during the infiltration process and may occupy more space in the said particles once it solidifies.

4.2.2 **Microstructure**

Figures 4-10 shows the surface of a fractured syntactic foam sample where there is further evidence of voids or air pockets present within the syntactic foam. Figure 4-11 shows the microstructure of a typical syntactic foam samples manufactured with ASW particles. All the ASW particles are similar in shape, so the overall

microstructure of the resultant foams is not different from one to the other. In general, the molten Al fills the interstices between the particles well, even though the ASW particles are irregular in shape. There are some observed defects, for instance there are some air pockets present due to incomplete infiltration, which are circled in Figure 4-11. The percentage of defects, including broken particles and air pockets, was estimated by examining 1000 ASW particles among 200 syntactic foam samples for each particle size group. The amount of air pockets in all samples was found to be less than 1% and so was insignificant to the overall properties of the foam.

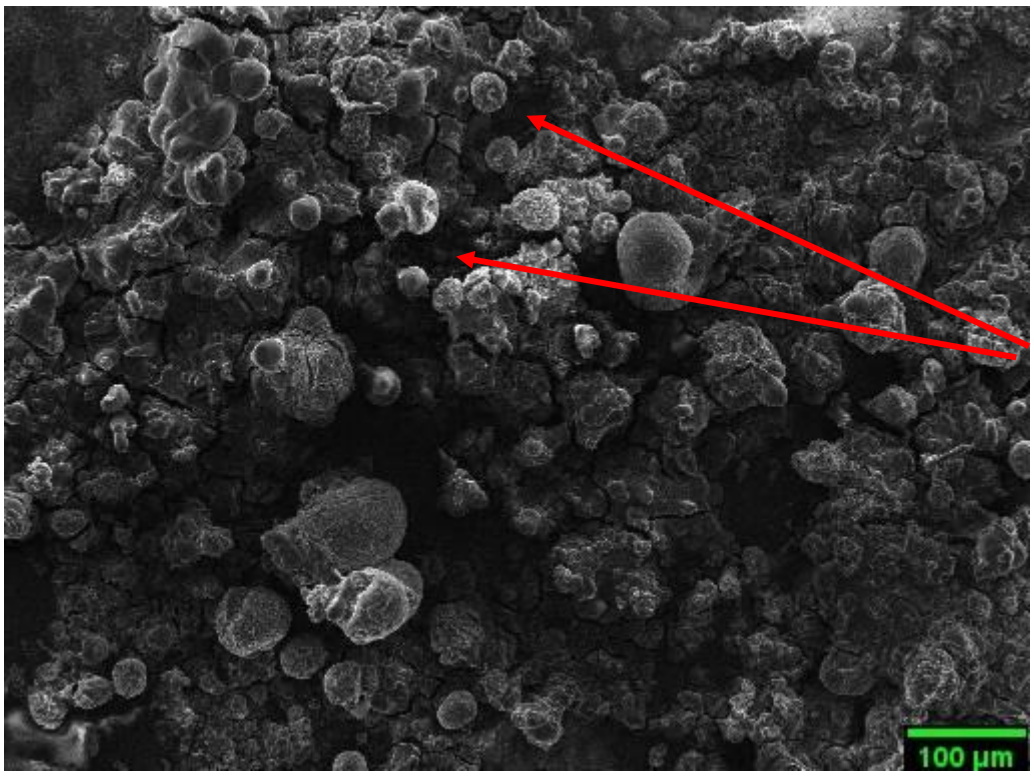

Figure 4-10: Micrograph of a fractured surface of a syntactic foam sample

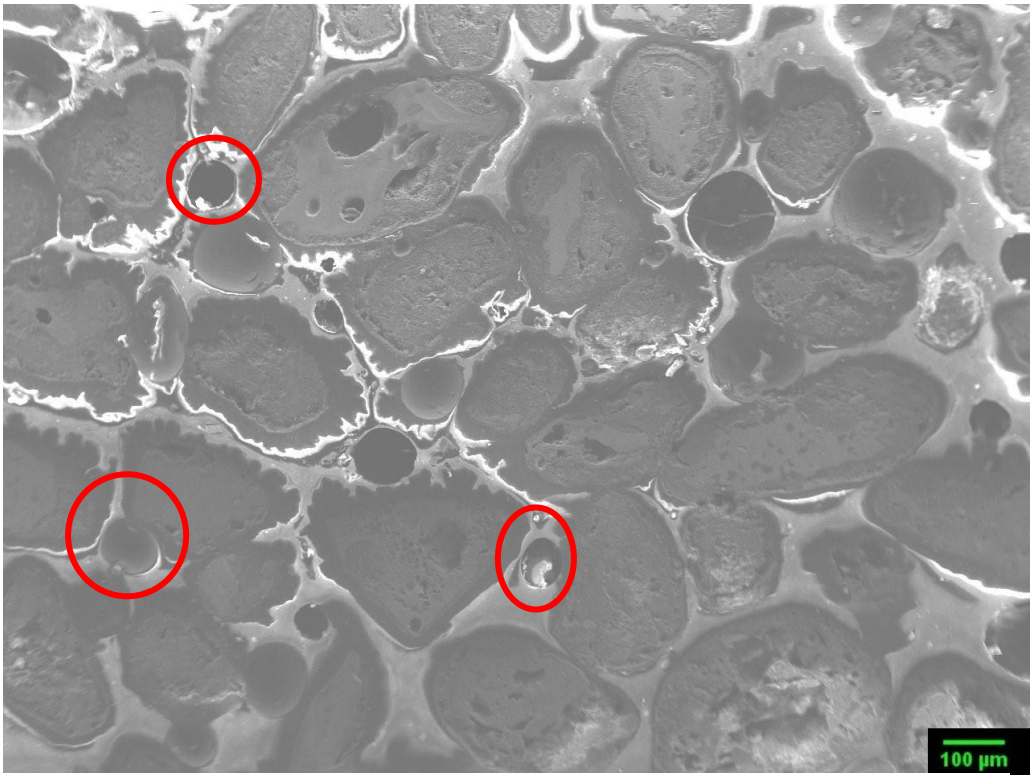

Figure 4-11: Micrograph of SF sample displaying air pockets within

4.2.3 **Density**

Table 4-9 summarizes the measured densities of the SF samples with different ASW particle size groups. Theoretical density values calculated by assuming a fraction of 63% ASW particles in the syntactic foam (Hartmann *et al.,* 1999) are also included for comparison. The measured density of the samples decreases as the particle size increases.

Table 4-9: Measured and theoretical density values for SF samples

Sample ID	Measured Density (g/cm^3)	Theoretical Density (g/cm^3)
S-ASF	1.90±0.02	1.88
SH-ASF	1.92±0.05	1.88
M-ASF	1.78±0.01	1.76
MH-ASF	1.75±0.02	1.76
L-ASF	1.57±0.03	1.45
LH-ASF	1.45±0.01	1.39

Most of the measured values are close to the theoretical values, showing that the defects present do not have a significant effect on the foam. The largest difference is seen in the L-ASF and LH-ASF samples. This is because the samples may have a lower percentage of Al than what is estimated in the theoretical calculations, given the particles are larger and irregular in shape and have a smaller interstitial space for the molten Al to occupy.

4.2.4 **Summary**

The syntactic foam samples manufactured with ASW particles exhibit small amounts of defects, such as ASW particles infiltrated with molten Al and incomplete infiltration leaving cracks in the interior, or air pockets within the foam. These defects are due to the low controllability of manufacturing conditions, such as the temperature gradient within the particle bed in the steel tube mould and a high infiltration pressure. The number of defects in the final samples is relatively low, less than 1% of the samples observed. The measured density of the samples decreases as the particle size increases, and is close to the calculated theoretical density. The densities of the ASW syntactic foam with the large particle size group are slightly out of range, which may be an effect of the decreased infiltration by molten Al in the interstices of the samples.

4.3 Quasi-Static Compressive Behaviour of ASW Syntactic Foams

This section presents and discusses the quasi-static compressive behaviour of ASW syntactic foam samples. More results are provided in Appendix A.

4.3.1 Syntactic foams with non-heated ASW particles

4.3.1.1 *Unconfined compression*

Figure 4-12 shows the stress-strain curves of the syntactic foams with non-heated ASW particles under quasi-static compressive loading. The curves show two different behaviours. The Large sample shows behaviour observed in typical cellular solids, with an initial linear region, a plateau region and a densification region. In the initial linear or elastic region, stress increases proportionally with strain, until peak stress is reached. Following on from this is the plateau region, so named because the stress is relatively unchanged over a large strain range. Finally, once the pores have largely collapsed within the ASW particles, the particles start to densify, which leads to their crushing and a steep increase in the stress until the syntactic foam becomes fully dense.

The Medium and Small samples display behaviour that is similar to that of brittle metal matrix composites, where the material fails catastrophically after reaching the yield stress. By definition, the manufactured sample is still a syntactic foam due to the presence of pores within the filler material, in this case the ASW particles, however its compressive behaviour indicates that the final foam is brittle in nature.

The yield and plateau strengths of the samples decrease as the size of the ASW particles increases, which is linked to the reduction in porosity and increase in brittle components, i.e. more oxides and impurities as particle size decreases. The ASW

particle size groups however were observed to have an increase in strength as the particle size increases. One of the reasons for the change in the syntactic foams may be the different volume fractions of the particles. The smaller the particles, the higher the volume fraction of the particles in the syntactic foam, therefore the stronger, harder and more brittle the sample will be. Another factor is that the large ASW particles have a higher porosity than the small and medium particles, therefore decreasing the overall strength of the foam.

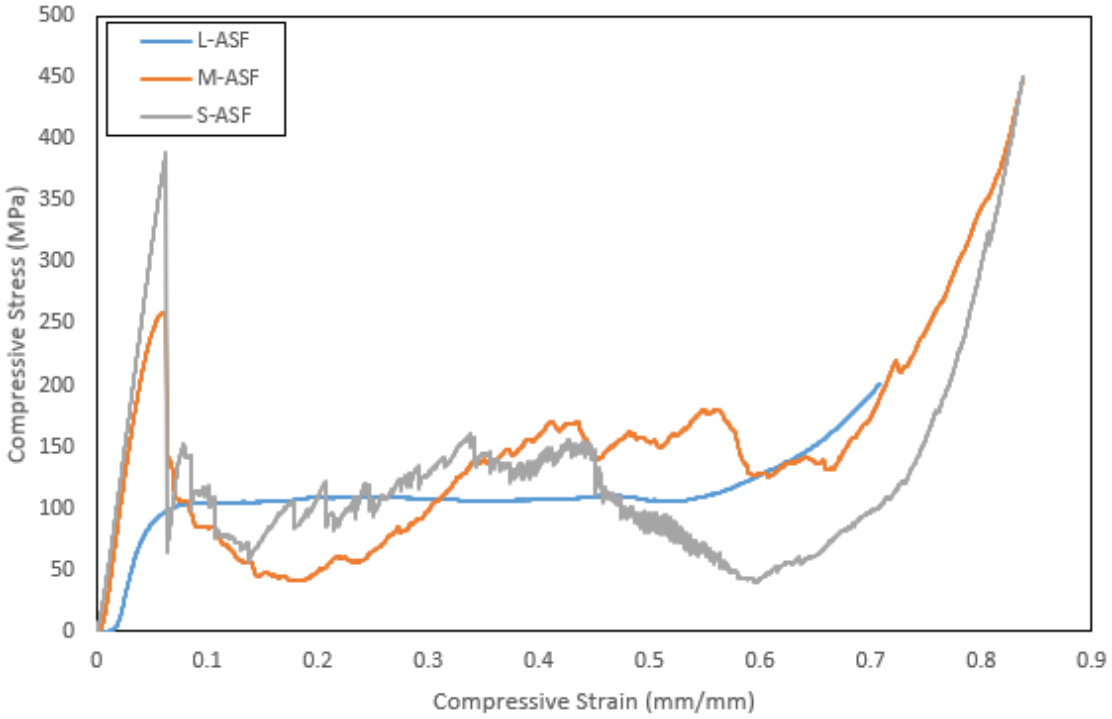

Figure 4-12: Stress-strain curves for ASW particle syntactic foams under quasi-static loading

Table 4-10 displays the characteristics of the three particle size group samples, including energy absorption, which is obtained by calculating the area under the stress-strain curves. The L-ASF sample displayed three distinct regions in its stress-strain curve, suggesting good energy absorption capabilities. Since M-ASF and S-ASF samples failed catastrophically, the energy absorption values are less useful because

energy absorbed after failure is not particularly meaningful. From these results, the L-ASF sample has superior energy absorption capabilities to M-ASF and S-ASF samples, even though the yield and plateau strengths are both lower. The presence of more pores in the Large ASW particle size group than the other two groups is likely the reason for the stable plastic deformation.

Table 4-10 : Compressive properties of the ASW particle syntactic foams

Sample ID	Yield Strength (MPa)	Plateau Strength (MPa)	Densification Strain	Specific Energy Absorbed (MJ m^{-3})	Modulus in Compression (GPa)
L-ASF	111.09	111.09	0.47	53.49	4.67
M-ASF	259.27	113.91	0.40	34.29	5.56
S-ASF	388.51	118.83	0.50	44.31	6.91

The micrographs of the syntactic foams with non-heated ASW particles after compression are shown in Figure 4-13. Each sample shows a different deformation behaviour and failure mode. The L-ASF sample bulged from its sides, giving rise to multiple small cracks in the middle and pushing outwards so the sample is wider than its initial width. This effect is known as the barrelling effect due to plastic deformation and this effect shows that the failure of the foam sample is ductile in nature, where the ASW particles are compressed and crushed as stress is increased. This can also be seen from Figure 4-12 where there is a clear plateau region, defined by the crushing of particles before complete collapse follows.

The M-ASF sample developed a large crack across the sample, which started at an angle of 45^{o} to the direction of the force. Some smaller cracks are also observed through the middle of the sample, indicating minimal barrelling. During quasi-static loading, a loud sound was heard that corresponded to the drop in stress and the formation of the large crack. After this, the sample was practically split into two pieces and moved slowly away from each other as more load was applied. The sample failed catastrophically and was brittle in nature. The stress-strain readings from this point onwards were not really meaningful.

The S-ASF sample also displayed deformation behaviour characteristics of brittle catastrophic failure. A loud noise was also heard when the sample reached the fracture strength, when the signs of the large crack were first observed. This crack developed parallel to the direction of the force and ran down the centre of the sample. The sample did split as well, but into more than two pieces after the large crack was observed, and these pieces of the syntactic foam began to fall off the sample. Stress-strain readings for the S-ASF sample were also not informative after the large crack developed.

The transition from ductile to brittle failure as particle size decreases can be due to a number of factors: decrease in porosity, increase in impurities, decrease in Al present and the irregular shape of the particles. As observed in Section 4.1, the percentage of pores present decreases as particle size decreases. When these ASW powders are used to make syntactic foams, the syntactic foam with a smaller particle size group has a lower porosity. This means that there is a smaller amount of porosity that needs to collapse before the sample is fully densified, hence leading to a decrease in plastic

deformation. Furthermore, the Small and Medium ASW particle size groups have more impurities present, in the form of cryolite and calcium fluoride respectively. This, coupled with the relatively lower Al present, leads to a higher percentage of brittle compounds in the final syntactic foam, further decreasing the ductility of the sample. Finally, the irregularity of the particles present adds further mechanical stresses within the syntactic foam samples. These will be more significant in the Small and Medium size groups because there will be more particles present in a syntactic foam for these particle size groups than for the Large particle size group, hence leading to a more brittle failure. All these factors combine to develop a brittle syntactic foam that fails catastrophically.

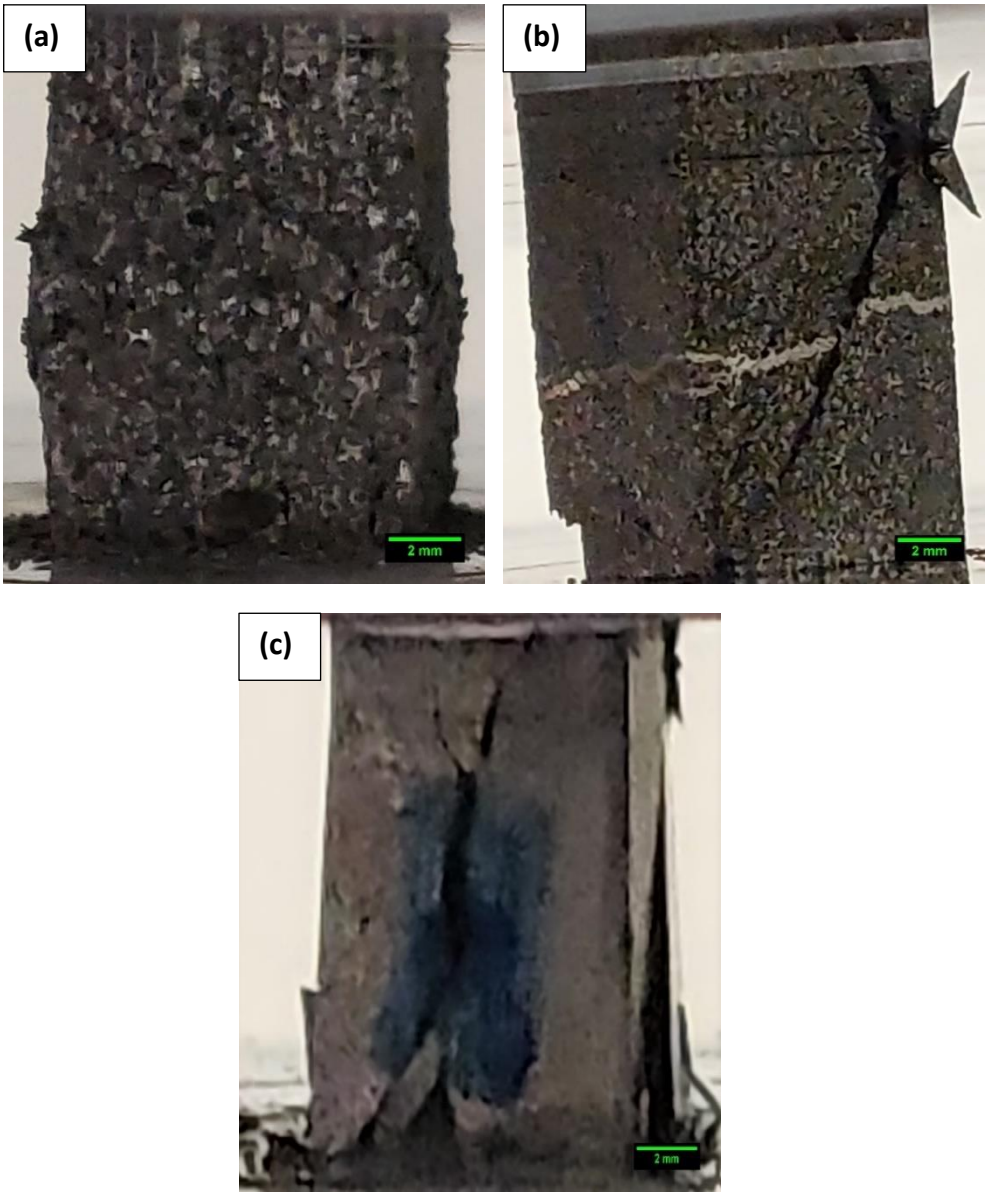

Figure 4-13: Micrographs of (a) L-ASF, (b) M-ASF and (c) S-ASF samples

4.3.1.2 *Confined compression*

The manufactured syntactic foams were observed to either fail catastrophically, or bulge outwards, or both in confined compression. Studying their behaviour in spaces where the samples cannot bulge or fall apart, i.e. in situations where they are confined by boundaries to restrict their movement, will help in understanding the full deformation process.

Figure 4-14 compares the stress-strain curves of the samples under unconfined and confined compression. The confinement of the samples allows for continuous loading with an induced plateau region for brittle samples, where the curves display minimal changes in stress as strain increases, which was not observed in the curves obtained unconfined curves. All samples were also observed to show an average of 10% increase in yield strength because of the confinement, which allows for the stress to spread evenly through the sample and generates plastic deformation in more regions in the sample.

For the L-ASF sample that displayed a barrelling effect under the unconfined condition, the densification of the sample started sooner, at a strain of 0.39 under confined conditions, which is sooner than the unconfined data, where the densification occurred at a strain of 0.47. This is because the sample was not allowed to push outwards from the sides to disperse stress, so all the applied stress was going through the particles present, which were crushed faster, and the sample densified sooner as well.

The M-ASF and L-ASF samples showed the presence of an induced plateau region, with large drops in stress observed at intervals, under the confined conditions. As the samples are not allowed to slide away from each other or disintegrate, these sharp drops are a result of additional cracks developing within the confined space. The densification strain observed in these curves is a more accurate representation of the real densification strain because the entire sample is compressed in a confined space as opposed to two halves or multiple fragments of the same sample.

Table 4-11 summarizes the findings from the stress-strain curves and provides the energy absorption figures in a confined environment. It is evident now that in a confined space, the S-ASF shows a superior energy absorption capability compared to the M-ASF and L-ASF. As previously explained, the confined space does not allow for a disbursement of stress across multiple pieces of the sample, therefore resulting in a higher plateau stress, which allows for more absorption of energy. This property can be useful in applications where the syntactic foam is enclosed or is big enough to confine itself.

Table 4-11: Quasi-static compressive properties of confined ASW particle syntactic foams under confined conditions

Confined Sample ID	Yield Strength (MPa)	Plateau Strength (MPa)	Densification Strain	Specific Energy Absorbed (MJ m^{-3})	Modulus in Compression (GPa)
L-ASF	119.19	119.19	0.39	39.54	1.33
M-ASF	291.75	112.28	0.31	36.42	5.53
S-ASF	402.59	155.40	0.27	44.03	6.47

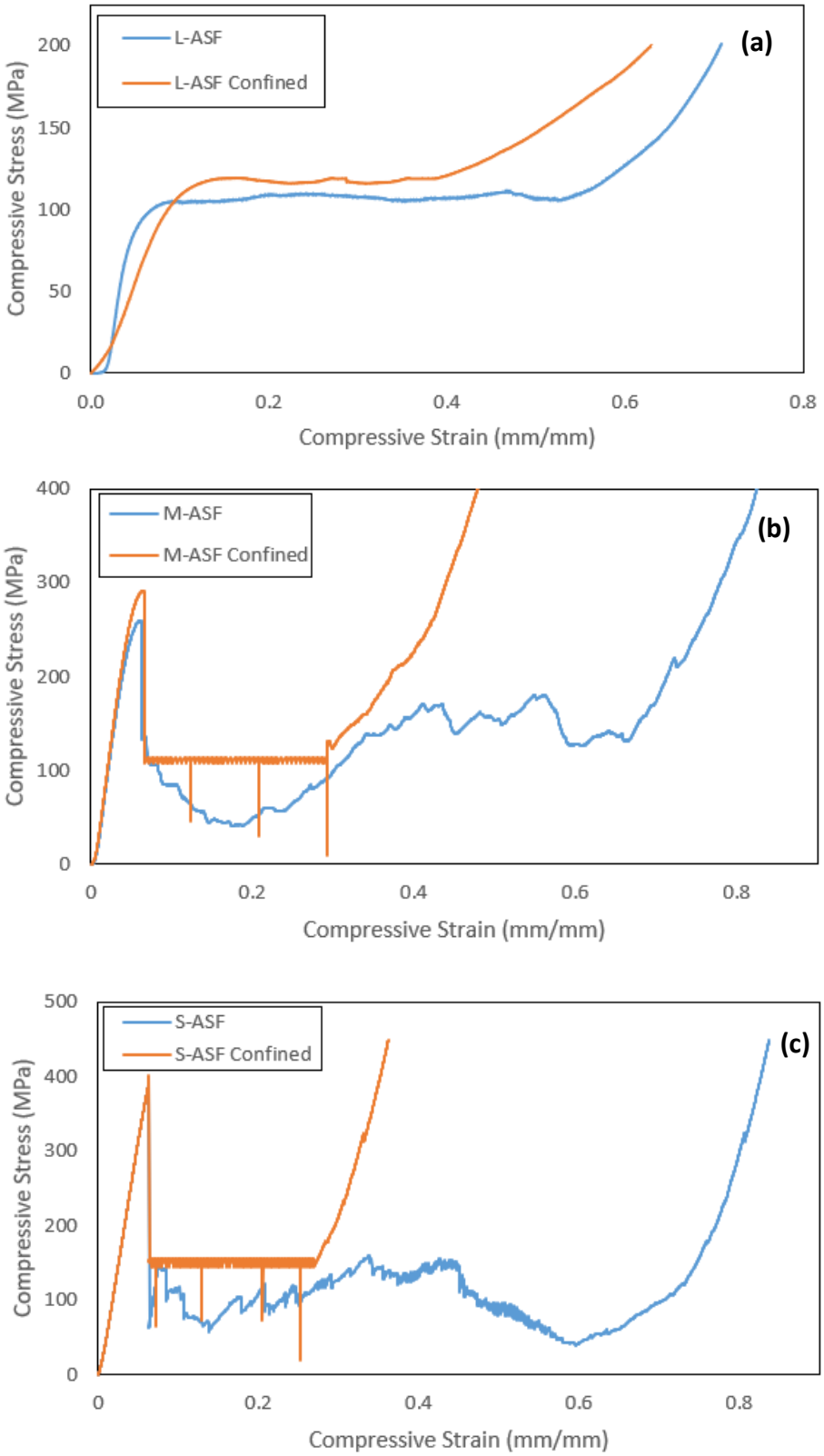

Figure 4-14: Comparison of stress-strain curves of (a) Large, (b) Medium and (c) Small ASW particle syntactic foams under confined and unconfined compression

4.3.2 **Syntactic foams with heated ASW particles**

Section 4.1 described the change in properties of the ASW powders upon heating. The properties of the syntactic foams manufactured with heated ASW powders are studied in this section. Figure 4-15 shows the stress-strain curves of the syntactic foams with heated ASW particles under quasi-static loading, compared to their respective syntactic foams with non-heated ASW particles.

The LH-ASF sample shows a transition in behaviour from ductile to brittle failure when compared to the L-ASF sample. There is a large crack formed, leading to a sharp drop in stress. There is no evident plateau region from the graph, as the sample has split up into smaller pieces which are unable to support the stress. The LH-ASF sample does however have a higher yield strength than the L-ASF sample. As seen in Section 4.1, the heating of Large ASW powder leads to a decrease in density and an increase in porosity. It seems that the change from ductile to brittle failure is due to the hardened ASW particles.

The SH-ASF and MH-ASF samples show similar behaviour to their respective counterparts with non-heated powders, with a large crack forming, indicated by the sharp drop in stress, and catastrophic failure typical of brittle fractures. The heated particles are harder and would be expected to increase the strength of the resultant syntactic foam. However, this did not happen. This is probably because the unheated particles are heated by the molten Al during the infiltration process and hardened. The result is that both foams contain the same heated and hardened particles, regardless of whether the particles are heated or not before infiltration.

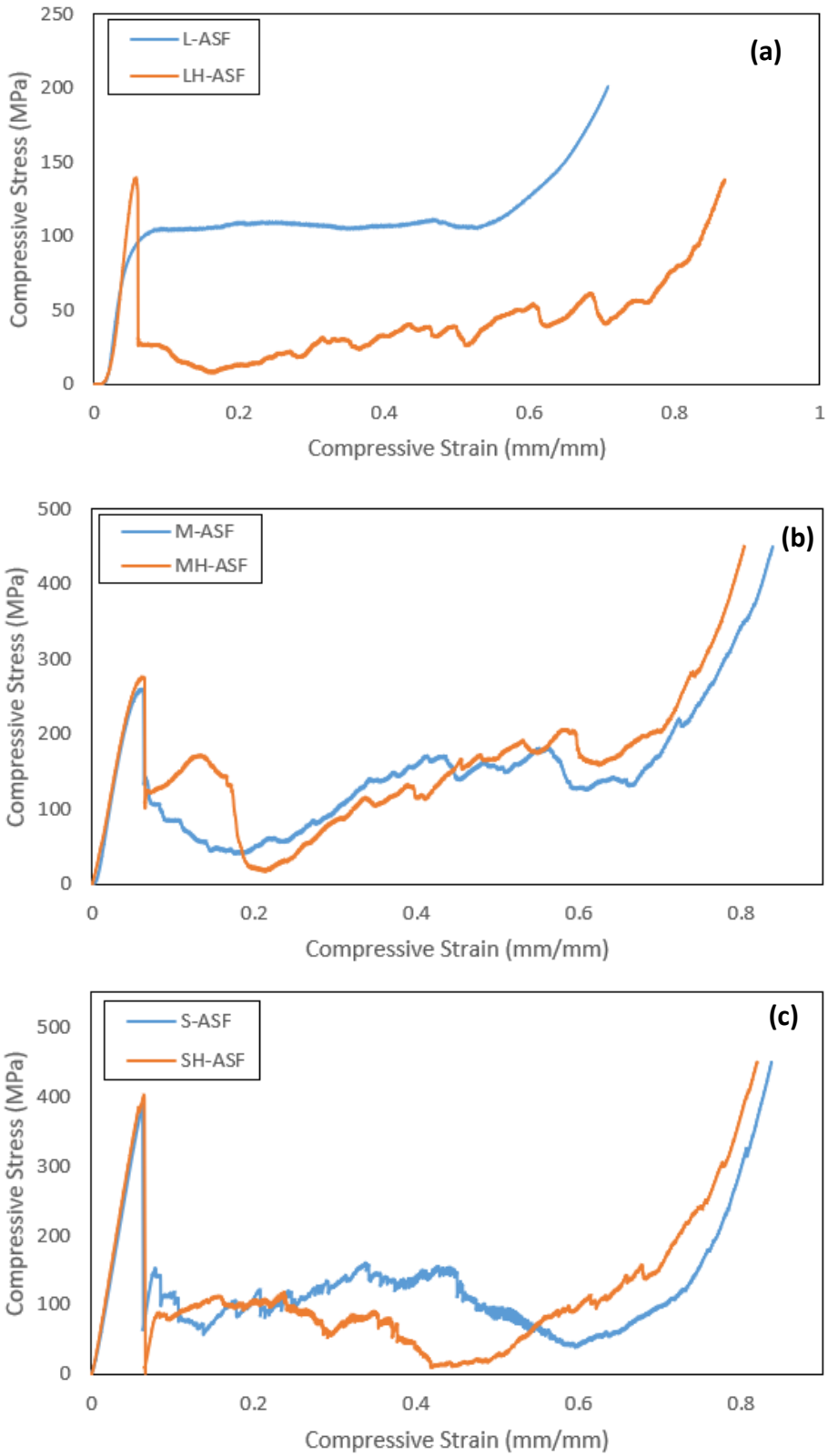

Figure 4-15: Comparison of stress-strain curves of syntactic foams with heated and non-heated (a) Large, (b) Medium and (c) Small ASW particles under quasi-static loading

Table 4-12: Quasi-static compressive properties of syntactic foams with heated ASW particles

Sample ID	Yield Strength (MPa)	Plateau Strength (MPa)	Densification Strain	Specific Energy Absorbed (MJ m^{-3})	Modulus in Compression (GPa)
LH-ASF	139.34	32.64	0.63	18.29	3.99
MH-ASF	275.76	112.31	0.41	33.84	5.69
SH-ASF	395.51	122.38	0.52	45.73	6.88

Table 4-12 summarizes the findings from the stress-strain curves. Once again, the readings for SH- and MH-ASF are similar to those for S- and M-ASF, respectively, with minimal changes for strength or strain values. This is due to the hardening of the ASW powders during infiltration, as previously described.

The LH-ASF sample shows a significant difference in energy absorbed when compared to the L-ASF sample. This is due to the formation of the large crack, which reduces it into smaller pieces, reducing its energy absorption capabilities. Practically, the sample will not be able to absorb any substantial amount energy after a large crack is formed and runs through the sample.

Figure 4-16 shows the micrographs of the syntactic foams with the heated ASW powders. The deformation behaviour of all samples is different from one another. However, the MH-ASF and SH-ASF behaved similarly to M-ASF and S-ASF respectively.

The LH-ASF sample showed multiple cracks running along and through the sample, the largest crack being slightly off-centre and running right down the sample, forcing a part of the sample to lean outwards and away from the rest. Many smaller cracks are also observed running through or along the surface of the sample, splitting the sample up into small pieces and leading to lower stress values recorded. The sample disintegrated almost entirely after the first large crack was formed, leading to debris falling off it and eventual catastrophic failure.

The MH- and SH-ASF samples both showed the same behaviour as the M- and S-ASF samples respectively. The MH-ASF sample had one large crack running at 45^{o} to the direction of the force, with smaller cracks in the middle indicating some barrelling tendency. The SH-ASF sample had multiple cracks running across the sample, splitting the sample into smaller pieces and decreasing the load bearing ability.

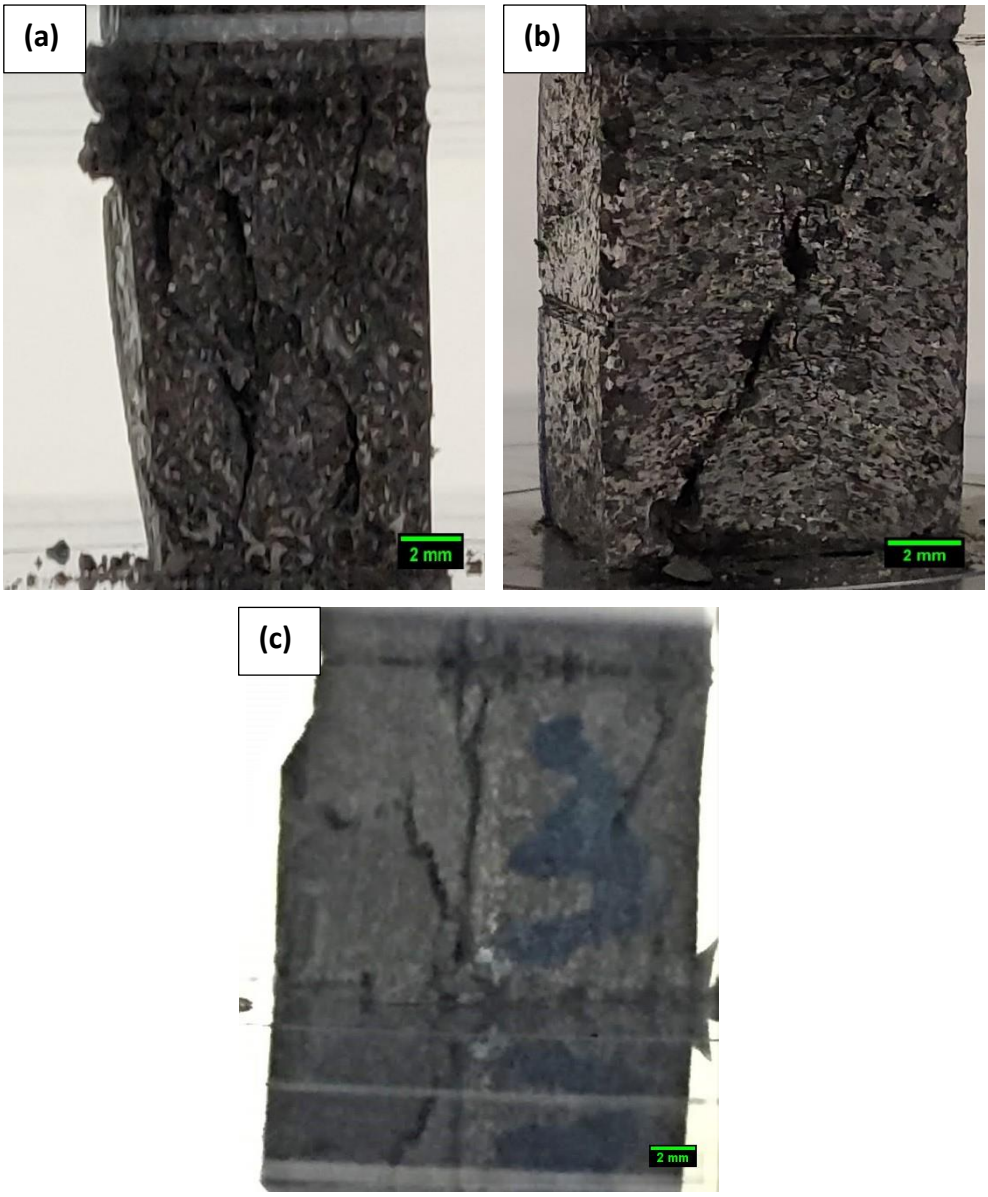

Figure 4-16: Micrographs of (a) LH-ASF, (b) MH-ASF and (c) SH-ASF after compression

4.3.3 T6 treated ASW syntactic foams

Figure 4-17 shows the compressive stress-strain curves for the T6 treated syntactic foam samples under quasi-static loading compared to the samples that are not T6 treated. The samples show similar behaviour to the non-T6 heat treated syntactic foam samples. The yield strength of the samples decreases with increasing particle size. The L-ASF-T6 sample has an indicative densification region and the M-ASF-T6 and S-ASF-T6 samples show a large drop in stress after reaching the fracture strength, indicating the development of a large crack.

Table 4-13 summarizes the findings from the stress-strain curves. The L-ASF-T6 sample showed a significantly increased strength, with an increase of 55% and 17% in the yield strength and the plateau strength respectively. There is also an increase in the densification strain, which leads to an increase in energy absorption capacity by almost 33%. The M-ASF-T6 and S-ASF-T6 samples do not show as significant changes in the yield strength values, which are 17% and 2.5% respectively. However they do show an increase in the densification strain, which results in a 26% and 28% increase in energy absorption capacity respectively. The T6 treatment results in a hardening of the Al matrix, which in turn increases the overall strength and energy absorption capacity of the resultant syntactic foam samples.

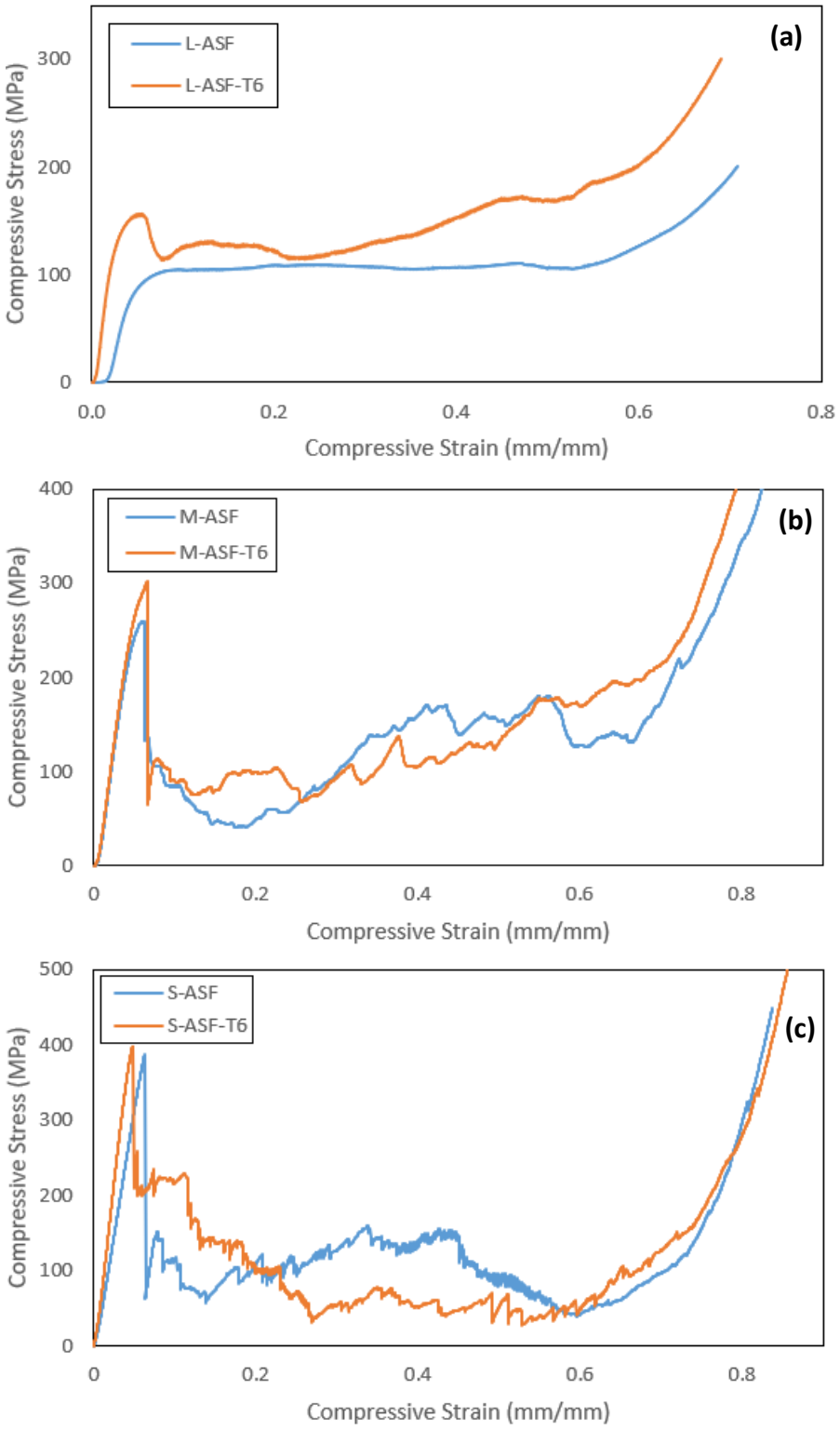

Figure 4-17: Comparison of stress-strain curves for T6 heat treated and non-T6 treated (a) Large, (b) Medium and (c) Small ASW particle syntactic foams under quasi-static loading

Table 4-13: Quasi-static compressive properties of T6 heat treated syntactic foams

Sample ID	Yield Strength (MPa)	Plateau Strength (MPa)	Densification Strain	Specific Energy Absorbed (MJ m^{-3})	Modulus in Compression (GPa)
L-ASF-T6	171.98	130.05	0.53	70.97	5.92
M-ASF-T6	302.91	107.62	0.41	43.48	5.95
S-ASF-T6	397.99	145.05	0.53	56.74	9.41

Figure 4-18 shows the micrographs of T6 treated ASW syntactic foams after compression. The deformation behaviour of the L-ASF-T6 and M-ASF-T6 samples is similar to the non-T6 treated samples. The S-ASF-T6 sample shows the development of X-shaped cracks that start at 45^{o} from the direction of the force and meet close to the centre of the sample. There are smaller cracks visible in the middle of the sample, which indicates a barrelling effect to a small extent. Debris and pieces of the syntactic foam sample are seen to fall off and onto the base, leading to regular stress drops until densification.

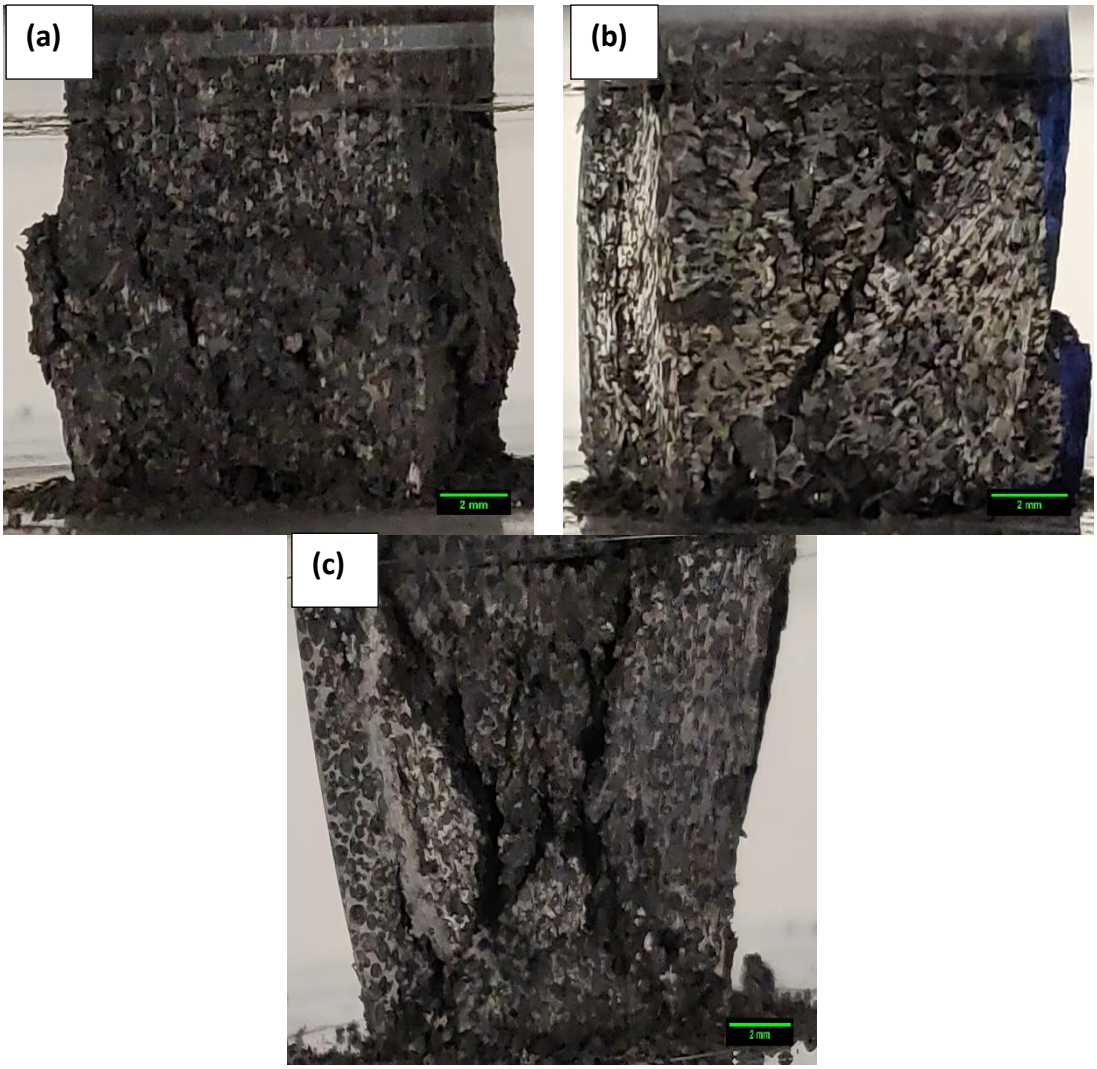

Figure 4-18: Micrographs of (a) L-ASF-T6, (b) M-ASF-T6 and (c) S-ASF-T6 after compression

4.3.4 **Comparison with E-Sphere syntactic foams**

Figure 4-19 shows the stress-strain curves of the ASW particle syntactic foams compared to the E-sphere syntactic foam. The curve of the E-sphere syntactic foam shows three clear phases during compression, which are similar to those observed in the L-ASF sample. After the initial phase where stress increases proportionally to strain, there is a small drop in stress that signals the start of the plateau region. The crushing of particles occurs gradually with minimal increases in stress as strain is increased. Finally, after all the particles are crushed, the densification region begins where the stress increases exponentially with strain.

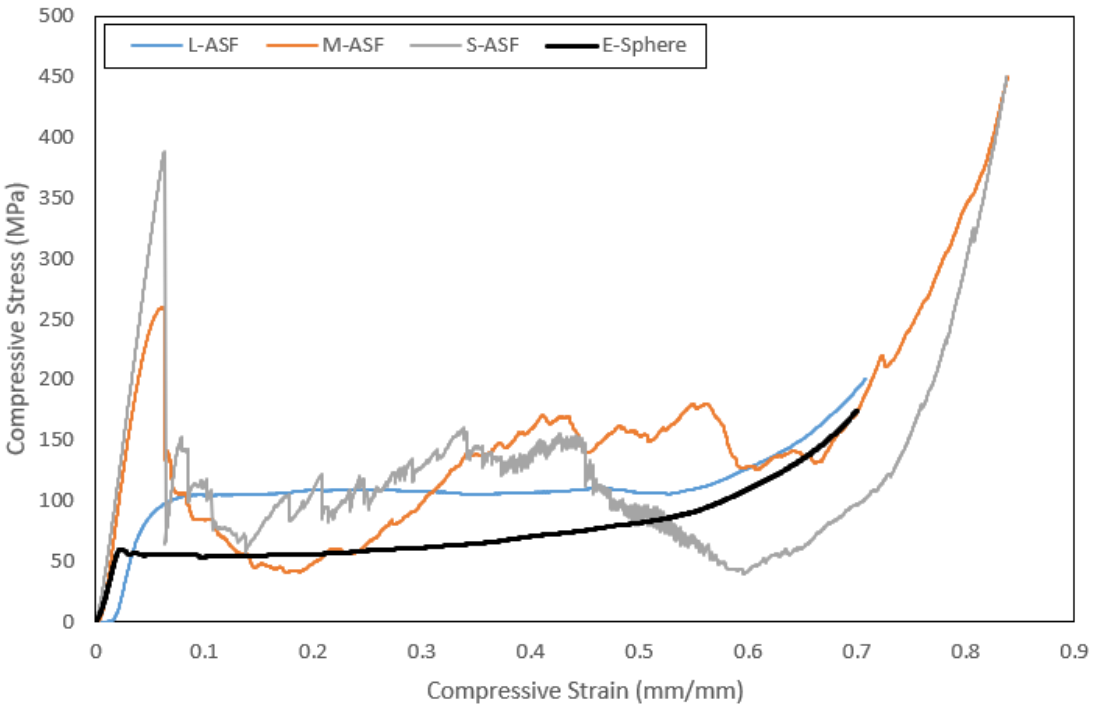

Figure 4-19: Comparison of stress-strain curves between ASW particle and E-sphere syntactic foams

Table 4-14 summarizes the compressive properties obtained from the stress-strain curves. Overall, the E-sphere syntactic foam has a lower yield strength, plateau strength and energy absorption capacity compared to any of the ASW syntactic foams. However, since the E-sphere particles have a higher porosity than the ASW particles, as seen in Section 4.1, the E-sphere syntactic foam densifies later than the ASW syntactic foams.

Table 4-14: Quasi-static compressive properties of ASW particle and E-sphere syntactic foams

Sample ID	Yield Strength (MPa)	Plateau Strength (MPa)	Densification Strain	Specific Energy Absorbed (MJ m^{-3})	Modulus in Compression (GPa)
L-ASF	111.09	111.09	0.47	53.49	4.67
M-ASF	259.27	113.91	0.40	34.29	5.56
S-ASF	388.51	118.83	0.50	44.31	6.91
E-Sphere	41.90	35.70	0.59	19.6	3.27

Figure 4-20 shows micrograph of the E-sphere syntactic foam after compression. It shows the development of a large crack running across the sample at 45^{o} to the direction of the force. The sample does not split into multiple fragments and does not show noticeable barrelling regions in the middle of the sample. This deformation behaviour is similar to that of the M-ASF sample, which splits into two pieces and shows a large drop in stress.

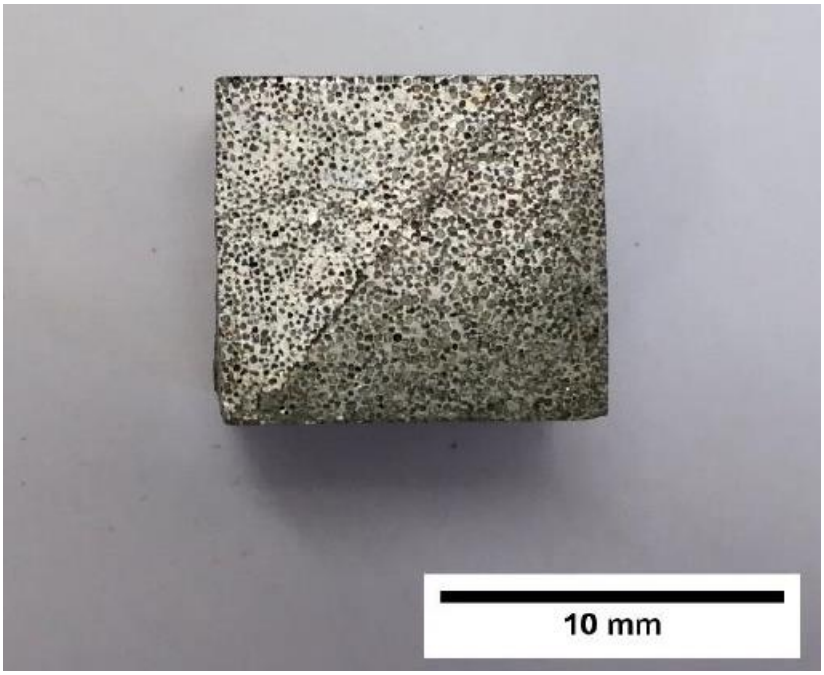

Figure 4-20: Micrograph of E-sphere syntactic foam after compression

4.3.5 **Summary**

The ASW particle syntactic foams show varying quasi-static compressive behaviour and different deformation mechanisms. The L-ASF sample shows a linear elastic region, a plateau region and a densification region with a superior energy absorption capacity than the M-ASF and S-ASF samples. The latter develop large cracks through the samples, leading to catastrophic failure, which means minimal amounts of energy can be absorbed by the samples. The L-ASF sample showed the development of small cracks, with the sample pushing outwards on the sides leading to a barrelling effect. The M-ASF and S-ASF samples developed larger cracks that split the sample into multiple fragments, lowering the strength of the samples. Under confined loading conditions, where barrelling and fragmentation were both limited, all samples showed a small increase in strength and a decrease in densification strain.

The syntactic foam with the heated Large ASW powder, compared to that with unheated powder, showed a transition from ductile to brittle behaviour, where the sample developed a large crack and broke into multiple fragments. The MH-ASF and SH-ASF samples do not show significant differences in compressive or deformation behaviour to their unheated counterparts, implying that the ASW particles are heated and hardened during infiltration. T6 heat treatment of the syntactic foam samples leads to an overall increase in strength and energy absorption capacity with minimal changes in deformation behaviour. ASW particle syntactic foams have a significantly higher strength and energy absorption capacity than the E-sphere syntactic foam, which densifies later than the ASW samples due to the higher porosity of the E-sphere particles.

4.4 Drop Weight Impact Behaviour of ASW Syntactic Foams

This section presents and discusses the drop weight impact behaviour of ASW syntactic foam samples. More results are provided in Appendix A.

4.4.1 Syntactic foams with non-heated ASW particles

Figure 4-21 shows the stress-strain curves for the syntactic foams with non-heated ASW particles under drop weight impact loading. The curves all show a similar shape and are split into two regions. There is an initial region where the stress increases rapidly with strain, followed by an oscillating plateau region. There is a large stress drop after the initial region between 0.1-0.2 strain, followed by continuous oscillations in stress to varying degrees. For all samples with different particle sizes, the drop in stress is accompanied by the formation of a large crack in the sample, indicating failure of the samples.

The curves of the M-ASF and S-ASF samples during impact loading show similar behaviour as during quasi-static loading, where the sample fails catastrophically upon reaching peak strength. The strength is seen to increase as particle size decreases, which is also observed during quasi-static loading.

The curve of the L-ASF sample shows a sharp drop in stress after peak strength is reached, followed by a minimal plateau strength, indicating catastrophic failure. This is different from the quasi-static behaviour of the L-ASF sample described in Section 4.3, where the onset of failure is characterised by the increase in stress after densification. The initial regions of the curves for the M-ASF and S-ASF samples however are similar to both quasi-static and impact loading, where there are sharp drops in stress after initial loading. The change in behaviour may be due more

pronounced stress concentrations present in the sample for Large ASW particles. The effect of the stress concentrations during impact loading is more significant because the strain rate is higher, leading to multiple regions of the syntactic foam being crushed simultaneously, leading to catastrophic failure. When comparing quasi-static loading to drop weight impact loading, all other aspects of the sample are the same except for the strain-rate, which is increased. The increase in strain-rate results in a change in deformation behaviour from ductile failure to brittle failure, which potentially indicates strain-rate sensitivity.

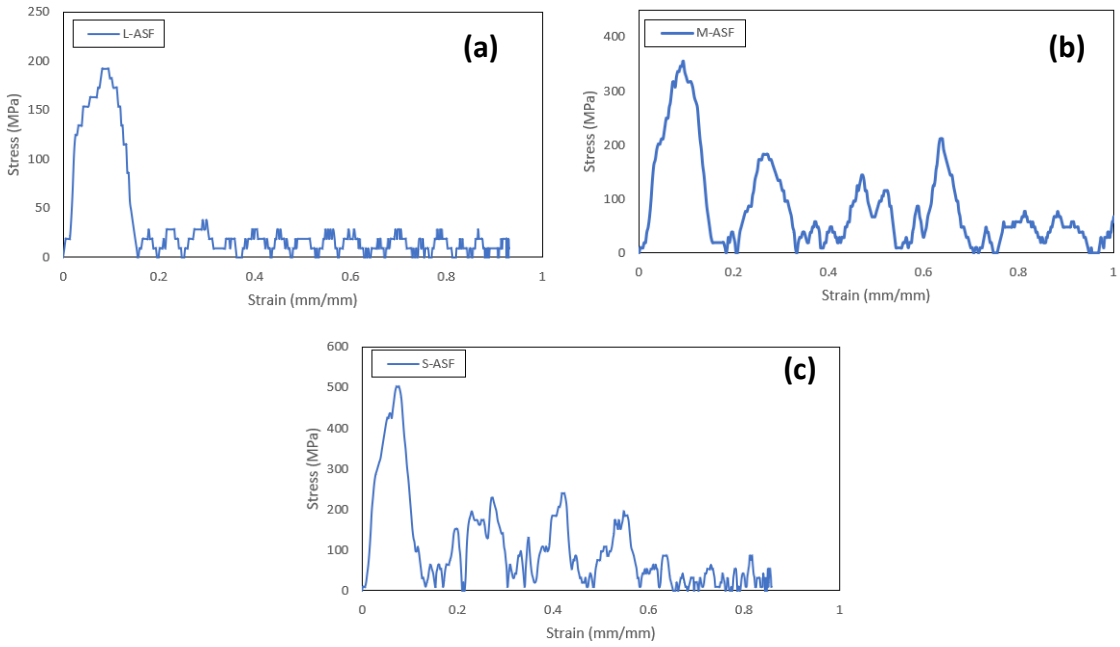

Figure 4-21: Stress strain curves of (a) L-ASF, (b) M-ASF and (c) S-ASF samples under drop weight impact loading

Table 4-15 displays the characteristic properties of the three samples with different particle sizes under drop weight impact. There is a significant increase in the peak strength during impact loading when compared to quasi-static loading results in Section 4.3. Increases in peak strength have been previously reported (Broxtermann *et al.,* 2018; Abd El-Aty *et al.,* 2019; B. Zhang *et al.,* 2016; Goel *et al.,* 2012) and

indicate strain rate sensitivity. The energy absorption capability is presented, however should be used with care given the catastrophic failure of the samples. The results do show a decrease in energy absorption capability as particle size decreases, which is similar to what was observed under quasi-static loading.

Table 4-15: Drop weight impact properties of syntactic foam samples with non-heated ASW particles

Sample ID	Peak impact strength (MPa)	Impact energy (J)	% increase in max strength compared to quasi-static loading
L-ASF	192.00	24.75	73
M-ASF	355.20	23.17	37
S-ASF	501.82	18.00	29

The micrographs of the syntactic foams with non-heated ASW particles at an instant of impact loading are shown in Figure 4-22. All the micrographs show the start of a crack in different regions of the syntactic foam samples, propagating through the sample and splitting the sample into two pieces. A similar deformation behaviour is observed under quasi-static loading for M-ASF and S-ASF samples. The L-ASF sample under quasi-static loading showed smaller cracks forming in the middle of the sample and a bulge that indicated barrelling effect. However, under impact loading, the sample develops a large crack, which results in a decrease in stress. This is further evidence of the strain-rate sensitivity of the L-ASF sample.

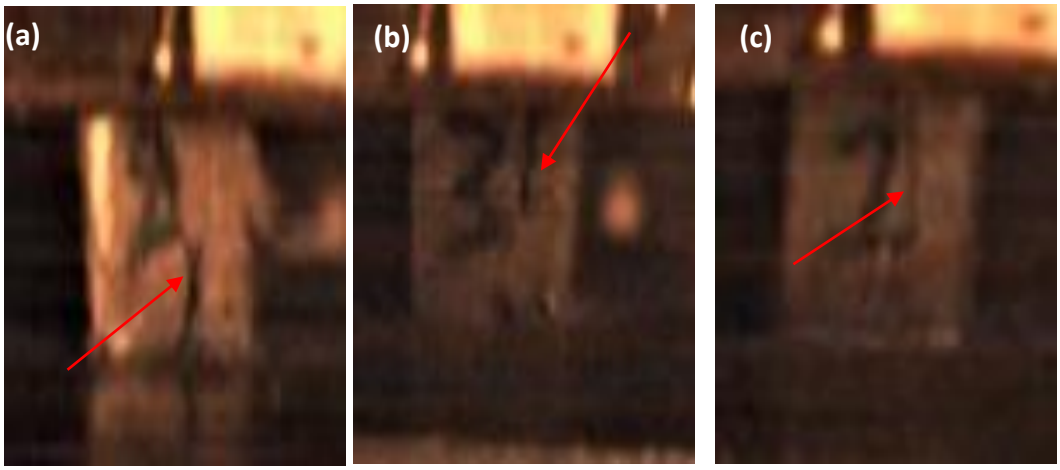

Figure 4-22: Micrographs of (a) L-ASF, (b) M-ASF and (c) S-ASF under drop weight impact loading indicating crack location

4.4.2 **Syntactic foams with heated ASW particles**

Figure 4-23 shows the stress-strain curves for the syntactic foams with heated ASW particles under drop weight impact loading. The curves are similar to those of the syntactic foams with non-heated ASW particles, with two visible regions in the curves: the initial steep region followed by the oscillating plateau region. The behaviour observed in the initial region is also similar to the quasi-static loading behaviour discussed in Section 4.3, where all the samples fail catastrophically after the initial loading.

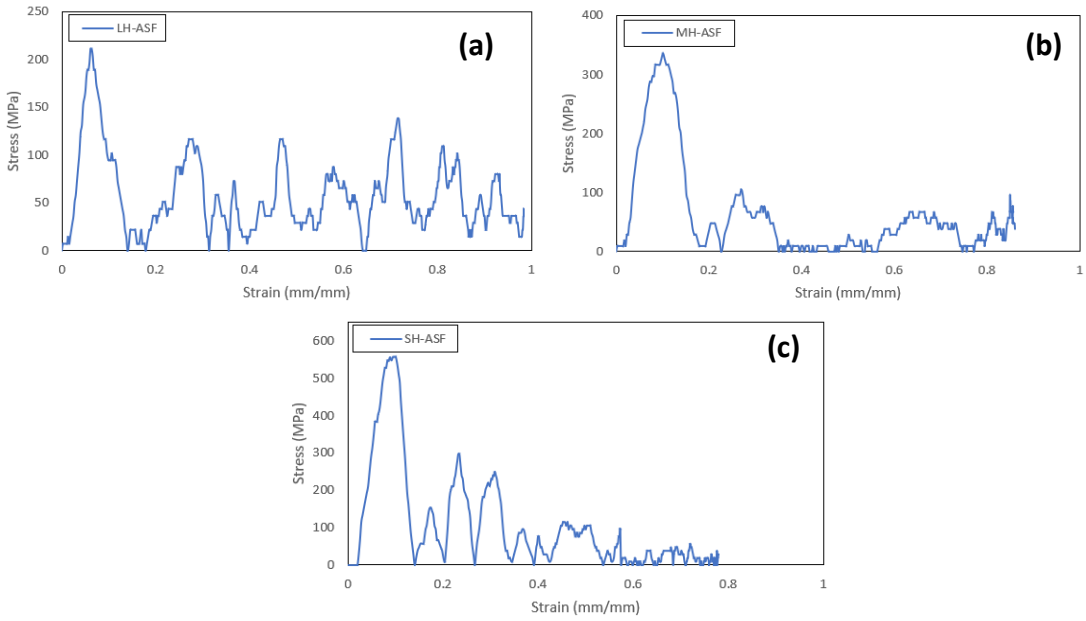

Figure 4-23: Stress strain curves of (a) LH-ASF, (b) MH-ASF and (c) SH-ASF samples under drop weight impact loading

Table 4-16 summarizes the findings from the stress-strain curves of the syntactic foams with heated ASW particles under drop weight impact loading. Similar to what was observed for the syntactic foams with non-heated ASW particles, there is a significant increase in strength during impact loading due to the increase in strain rate when compared to the yield strength under quasi-static loading.

The heating of ASW particles yields minimal change in properties during impact loading for the Small and Medium ASW particle size groups, however there is a reduction in energy absorption capabilities for the Large ASW particle size group. This is similar to what was observed during quasi-static loading.

Table 4-16: Drop weight impact properties of syntactic foams samples with heated ASW particles

Sample ID	Peak impact strength (MPa)	Impact energy (J)	% increase in max strength compared to quasi-static loading
LH-ASF	203.64	16.3	46
MH-ASF	336.00	25.2	22
SH-ASF	506.88	18.68	28

Figure 4-24 shows the micrographs of the syntactic foams with heated ASW particles at an instant of impact loading. The LH-ASF sample develops a large crack 45^{o} to the direction of the force, splitting the sample into two pieces and reducing the stress. This is comparatively different from the crack location observed for the L-ASF sample, however it does result in catastrophic failure. This is also comparatively different from the sample's behaviour under quasi-static loading, where several large cracks

developed through the sample, but the result was the same, with the sample failing catastrophically.

The MH-ASF and SH-ASF samples show some debris flying off the specimen as the test continues. There are very small cracks observed on the sample surface, but the sample is eventually reduced to multiple fragments. This is similar to what is observed under quasi-static loading, with all samples failing catastrophically.

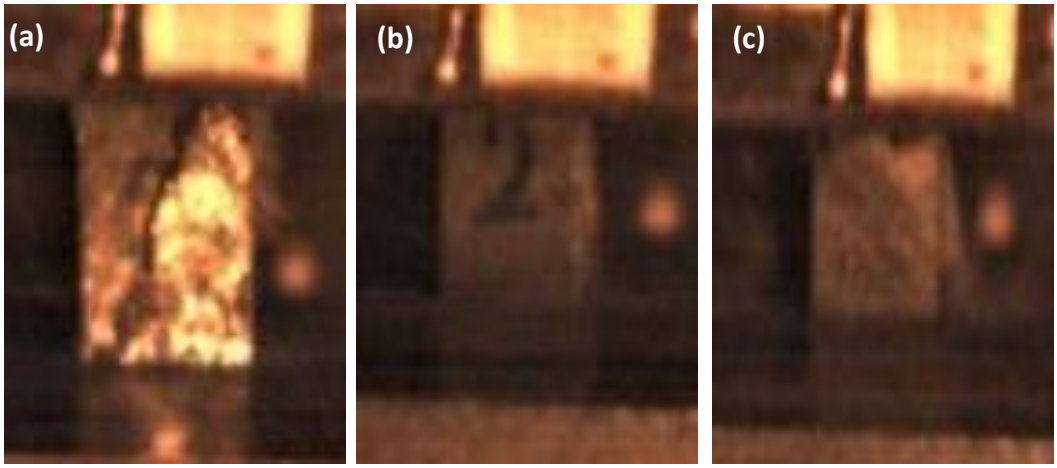

Figure 4-24: Micrographs of (a) LH-ASF, (b) MH-ASF and (c) SH-ASF under drop weight impact loading

4.4.3 T6 treated ASW syntactic foams

Figure 4-25 shows the stress strain curves for the T6 treated ASW syntactic foams under drop weight impact loading. The behaviour is similar to the non-T6 treated samples discussed in this section, displaying an initial steep region followed by an oscillating plateau region. The main difference is that the oscillating plateau region displays more gradual stress drops compared to the non-T6 treated samples, which can be attributed to the hardening of the Al matrix during the T6 treatment. All samples show a clear point of failure after the first large stress drop, indicating catastrophic failure.

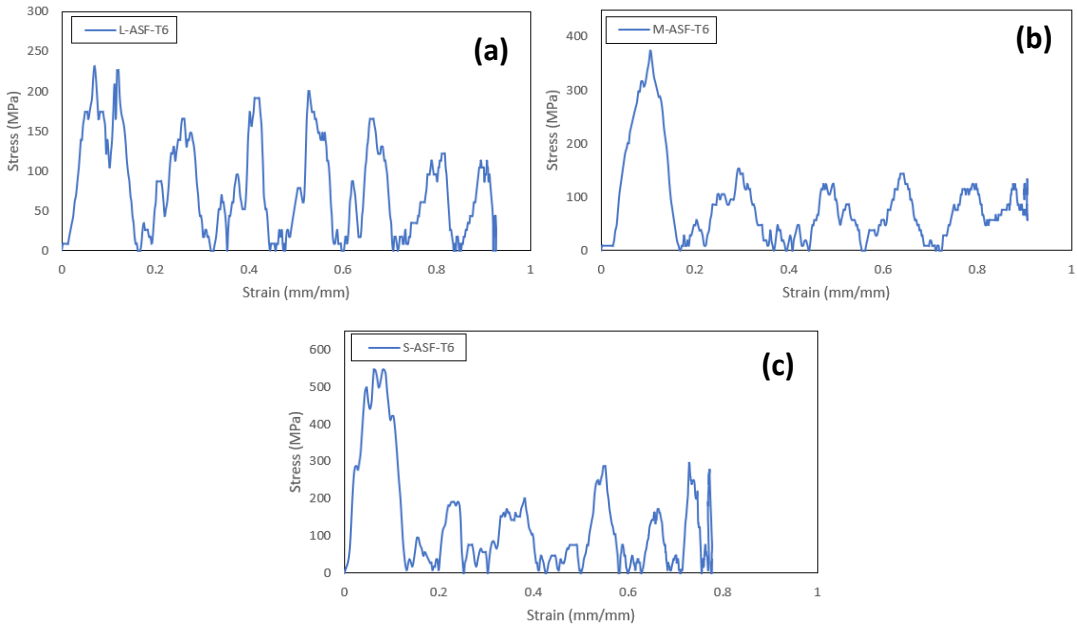

Figure 4-25: Stress strain curves of (a) L-ASF-T6, (b) M-ASF-T6 and (c) S-ASF-T6 samples under drop weight impact loading

Table 4-17 summarizes the findings from the stress-strain curves of the T6 treated ASW syntactic foams. T6 heat treatment results in an increase in overall strength and energy absorption capacity of the syntactic foam samples. There is also an increase in strength when compared to the T6 treated samples under quasi static loading. As previously described, the absorbed energy may not be particularly useful in this instance due to the catastrophic failure of the samples.

Table 4-17: Drop weight impact properties of T6 treated ASW syntactic foam samples

Sample ID	Peak impact strength (MPa)	Impact energy (J)	% increase in strength compared to non-T6 treated samples	% increase in max strength compared to quasi-static loading
L-ASF-T6	232.15	29.22	21	35
M-ASF-T6	374.40	26.84	5	24
S-ASF-T6	547.20	20.62	9	37

The micrographs of the T6 treated syntactic foams under drop weight impact loading are shown in Figure 4-26. All the samples show fragmentation and cracks developing on the surface. The L-ASF-T6 sample shows some barrelling occurring in the middle of the sample, with fragments falling off as well. The T6 treatment therefore made the sample more ductile, but did not prevent large cracks splitting the sample up eventually. M-ASF-T6 and S-ASF-T6 samples both developed large cracks and were reduced to debris at the end of the experiment, indicating strain-rate sensitivity.

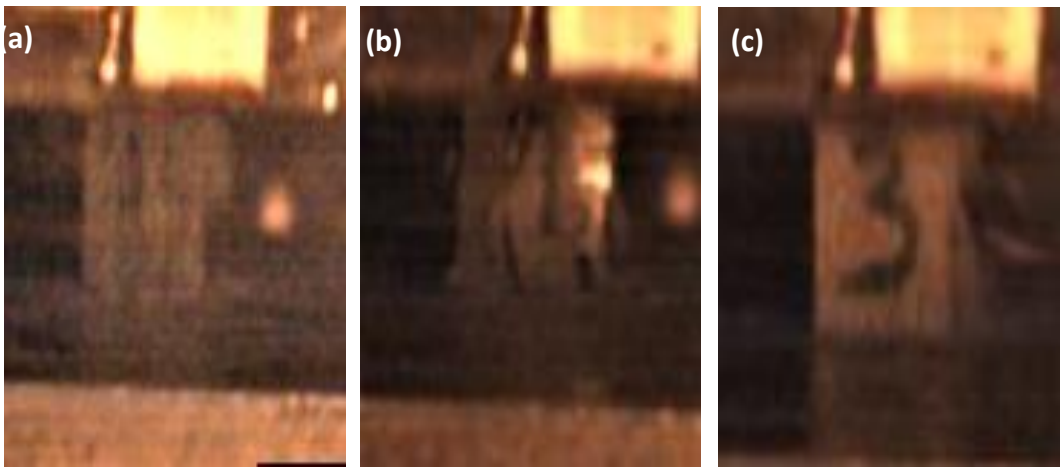

Figure 4-26: Micrographs of (a) L-ASF-T6, (b) M-ASF-T6 and (c) S-ASF-T6 under drop hammer impact loading

4.4.4 Comparison with the E-sphere syntactic foam

Figure 4-27 shows the stress-strain curve for the E-sphere syntactic foam under drop weight impact loading. The curve displays a similar behaviour to that observed in the ASW syntactic foams, with an elastic region followed by an oscillating plateau region. The difference here is that there is a clear densification region at the end as well, indicating that all the particles were crushed and densified. As strain increases, the sample shows an upward trend in the minimum stress after each stress drop, indicating continuous crushing of particles and an increase in overall strength of the densifying foam.

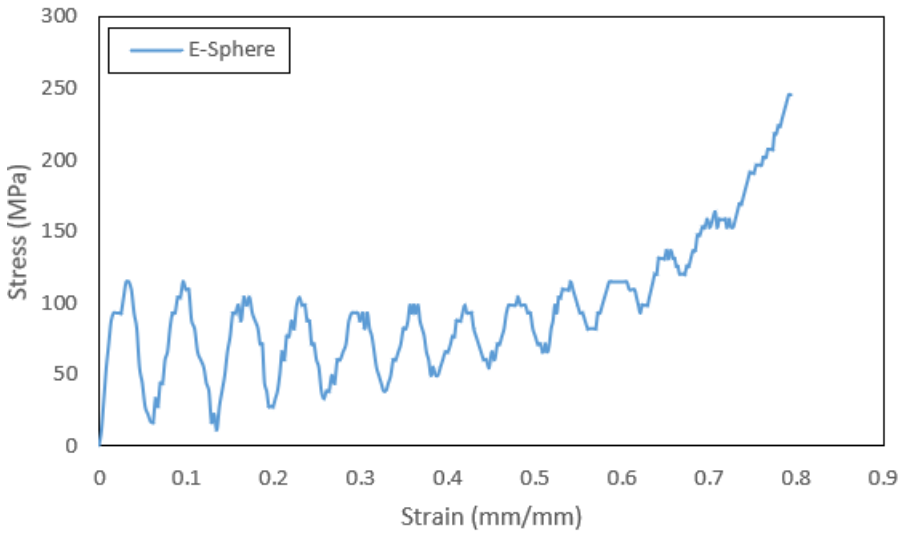

Figure 4-27: Stress strain curve of an E-sphere syntactic foam sample under drop weight impact loading

Table 4-18 compares the findings of the ASW syntactic foams under drop weight impact loading to those of the E-sphere syntactic foams. The ASW syntactic foams have a lower energy absorption capacity and display a smaller increase in strength from quasi-static to impact loading, when compared to the E-sphere syntactic foam, although they are stronger than the E-sphere syntactic foam. The latter has an energy absorption capacity of 36.62 Jg^{-1} and displays a strength increase of 160%.

Table 4-18: Comparison of drop weight impact properties of ASW and E-sphere syntactic foam samples

Sample ID	Peak impact strength (MPa)	Impact energy (J)	% increase in max strength compared to quasi-static loading
L-ASF	192.00	21.75	73
M-ASF	355.20	23.17	37
S-ASF	501.82	18.00	29
E-Sphere	109.08	36.62	160

A micrograph of the E-sphere syntactic foam under drop weight impact loading is shown in Figure 4-28. The sample displays significant barrelling in the middle, with smaller cracks dominating the deformation behaviour. The large stress drops seen in Figure 4-27 can be indicative of cracks being formed, however the sample does not disintegrate or split into multiple samples, indicating a good energy absorption capability. This is different from what is observed for the ASW syntactic foams, all of which develop large cracks and eventual catastrophic failure.

Figure 4-28: Micrograph of E-sphere syntactic foam sample under drop weight impact loading

4.4.5 **Summary**

The properties of ASW and E-sphere syntactic foams under drop weight impact are presented and discussed in this section. The stress-strain curves of the ASW syntactic foam samples are characterised by a significant increase in strength when compared to quasi-static loading. However, they also develop cracks on the surface, indicated by large stress drops on the stress-strain curves, resulting in catastrophic failure. The energy absorption values presented are not useful in this case given that the sample disintegrates into several pieces. The L-ASF sample also fails catastrophically under impact, which is different from what is observed under quasi-static loading, indicating strain-rate sensitivity.

The heating of the ASW powders has an insignificant effect on the behaviour of the samples. T6 treatment shows an increase in strength and energy absorption, but the samples also develop large cracks and, particularly in the case of S-ASF-T6 and M-ASF-T6, are reduced to debris. The L-ASF-T6 displays some barrelling in the middle section, which can be attributed to the hardening of the Al matrix.

The ASW syntactic foam samples show a similar stress-strain relationship to the E-sphere syntactic foam sample, but without an evident densification region. The ASW syntactic foam samples are stronger than the E-sphere syntactic foam sample under similar conditions. However, the ASW syntactic foam samples have less energy absorption capacity than the E-sphere syntactic foam sample. The latter shows significant barrelling in the middle of the sample, with minimal debris or fragments falling off, and also has significantly better performance under drop weight impact compared to quasi-static loading.

4.5 Three-Point Bending Behaviour of ASW Syntactic Foams

This section presents and discusses the flexural three-point bending behaviour of ASW syntactic foam samples. More results are provided in Appendix B.

4.5.1 Syntactic foams with non-heated ASW particles

Figure 4-29 shows the load-displacement curves of syntactic foams with non-heated ASW particles under three-point bending. All three samples show three regions present during the experiment. In the initial region, the displacement increased linearly with load due to the initial elastic deformation of the sample. A decrease in the gradient of the curve occurred afterwards due to localised plastic deformation. After the critical load was reached, extensive localised plastic deformation and crack propagation resulted in a gradual decline in the bending load. This behaviour is typically observed in metal foams (An *et al.,* 2017; N. Wang *et al.,* 2016).

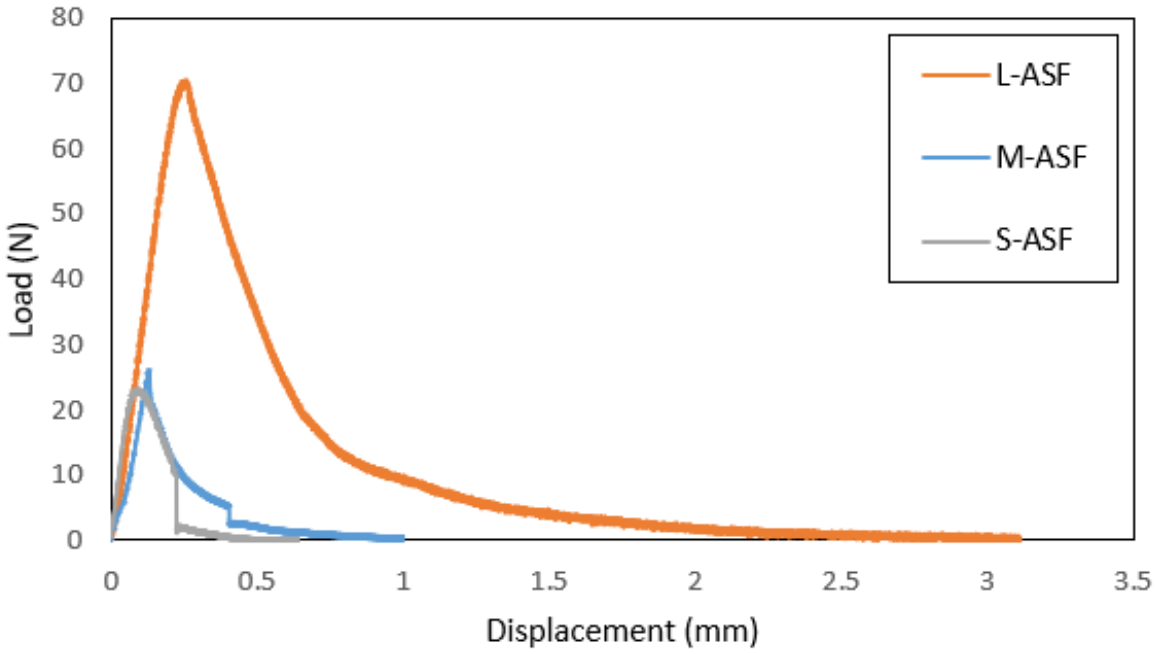

Figure 4-29: Load-displacement curves for syntactic foams with non-heated ASW particles under three-point bending

The L-ASF sample had a gradual decrease in bending load in the third stage before complete failure. The M-and S-ASF samples display a relatively large drop in bending load before reverting to the gradual decrease, which is indicative of a large crack developing within the samples. The ASW particles have a significant effect on the overall flexural properties of the syntactic foams. The L-ASF sample has the highest critical bending load before fracture occurs, while the S-ASF has the lowest. The S-ASF sample failed sooner than the M-ASF sample, which failed considerably earlier than the L-ASF sample, due to the decreasing ductility and porosity with decreasing particle size.

Table 4-19 provides a quantitative analysis of the curves to give the flexural properties of the samples. It is clear that the ASW particle size has a significant impact on the flexural properties of the syntactic foam, where the larger the particle, the stronger and more ductile it is and the more energy it can absorb. All samples have similar flexural moduli.

Table 4-19: Flexural properties of the syntactic foams with non-heated ASW particles

Sample ID	Flexural Strength (MPa)	Flexural Strain	Flexural Modulus (GPa)	Flexural Energy (J g^{-1})
L-ASF	35.23	0.0025	14.82	36.45
M-ASF	26.05	0.0012	14.65	10.94
S-ASF	10.79	0.0009	14.63	3.94

Figure 4-30 provides images displaying the locations of the cracks in the three samples. Each sample cracked at a different location relative to the centre of the sample, which would have affected the calculated results. The L-ASF sample developed a crack very close to the centre of the sample, which suggests that the flexural properties calculated in Table 4-19 are close to the real values for this syntactic foam sample. The M-ASF and S-ASF samples fractured further away from the centre and closer to the end. When a load is applied in the centre of the sample, it is distributed along the sample towards the ends. As the load is increased, smaller cracks may develop first off-centre on the sample due to local microstructural defects or weaknesses, reducing the local strength of the sample. If the local stress around

the small crack becomes significantly higher than the local strength, the crack propagates to form a larger crack and runs through the sample. This is what is observed in the M-ASF and S-ASF samples. This also means that the flexural property results for these two samples are less accurate than those for the L-ASF sample.

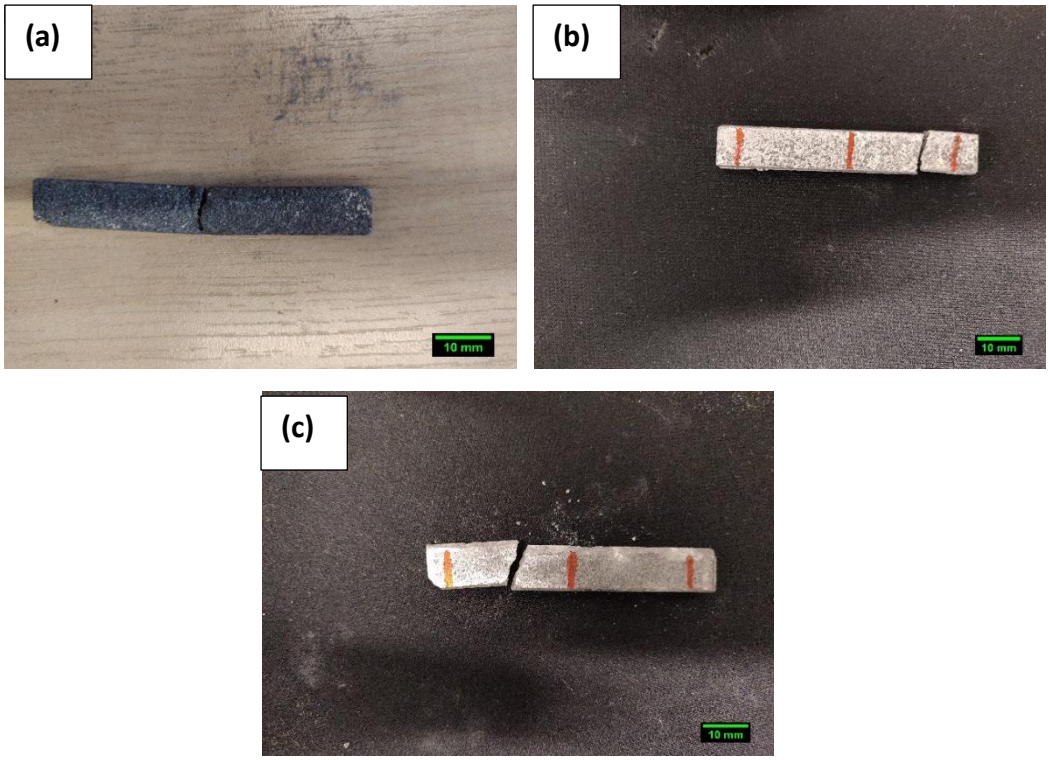

Figure 4-30: Images showing locations of cracks for (a) L-ASF, (b) M-ASF and (c) S-ASF samples

Figure 4-31 shows micrographs of the fracture surfaces of samples. It is shown that the crack tends to run through the Al matrix and goes around the ASW particles. It seems the Al-particle interface is relatively weak and is easily torn apart under tension.

In all samples, the crack deviates away from a perpendicular direction to the sample length, as seen in the uneven fracture surfaces in Figure 4-31. This is due to the difference in elastic modulus of the ASW particles and the Al alloy, as well as the weaker particle-matrix interface (J. Zhang *et al.,* 2016).

The failure mode of the syntactic foam samples fabricated with ASW particles can be explained in stages. In the initial stage, as load increases, the ASW particles provide sufficient reinforcement and resistance to deformation and deflection. This leads to the rapid increase in load. As the load is further increased, the deflection of the sample increases, generating initial cracks at the bottom of the sample. As deflection keeps increasing, the crack propagates along the loading direction. When the crack path is obstructed by ASW particles, it tends to deviate and propagate through the metal-particle interface due to the weak interfacial bonds.

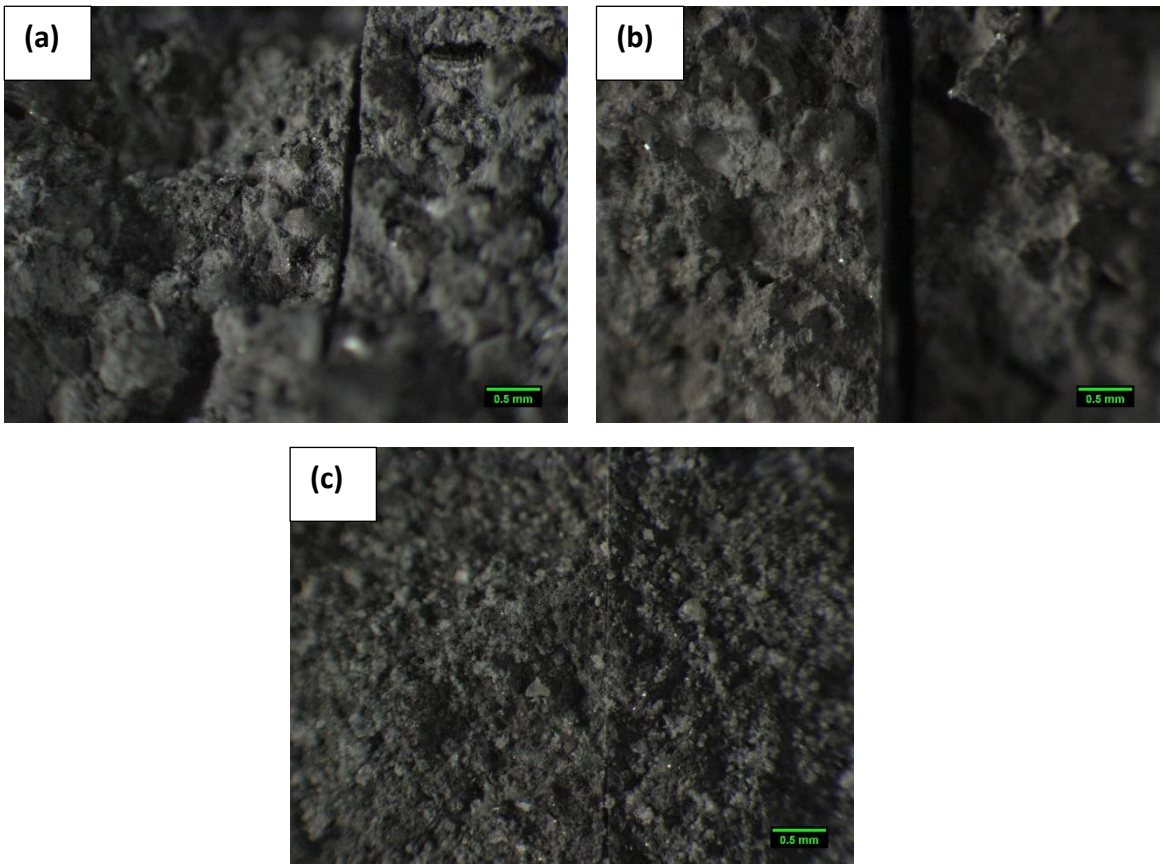

Figure 4-31: Micrographs of fracture surfaces of (a) L-ASF, (b) M-ASF and (c) S-ASF samples

Section 4.3 showed that the compressive strength of the ASW/Al syntactic foam samples increased with decreasing particle size, however the opposite is observed for flexural strength, where the strength decreases with decreasing particle size. The different effects of particle size are due to the different roles played by the particles in compression and in bending. In compression, the particles strengthen the Al matrix, and usually the smaller the particles the greater the strengthening effect. In bending, the crack initiation and propagation are due to tension and the local strength is dictated by the Al-particle interface or the Al matrix in this case. The larger the particles, the less interface and the thicker the Al network, hence the higher the flexural strength.

4.5.2 Syntactic foams with heated ASW particles

Figure 4-32 compares the three-point bending load-displacement curves of the syntactic foams manufactured with heated ASW particles to those manufactured with non-heated ASW particles. There is a change in the loading behaviour for all the samples.

The LH-ASF curve has a lower critical load, with a more gradual decline and a sharp drop in load before behaving similarly to the L-ASF sample towards the end. The critical load is lowered, because the ASW particles are weakened and softened by the heating of the large ASW particles. The sharp drop in load is associated with the sudden propagation of the crack, which eventually splits the sample. Since the LH-ASF and L-ASF samples have the same Al matrix, there is no difference in the extended region before complete failure.

The MH-ASF sample has a higher critical load and longer gradual decline region than the M-ASF sample. This is primarily due to the different locations of the cracks for the MH-ASF sample (Figure 4-33) and the M-ASF sample (Figure 4-30) samples. The crack was more centralised in the MH-ASF sample, its load-displacement curve is a better representation of the loading behaviour of the syntactic foam Medium ASW particles under three-point bending conditions.

The SH-ASF sample has a lower critical load and a larger displacement than the S-ASF sample. The fact that the difference in critical load between the SH-ASF and S-ASF samples is not large can be attributed to the heating effect in the S-ASF sample during the infiltration process, where the Small ASW particles are heated by the Al matrix.

The small change is because the particles may not have been fully heated in this scenario.

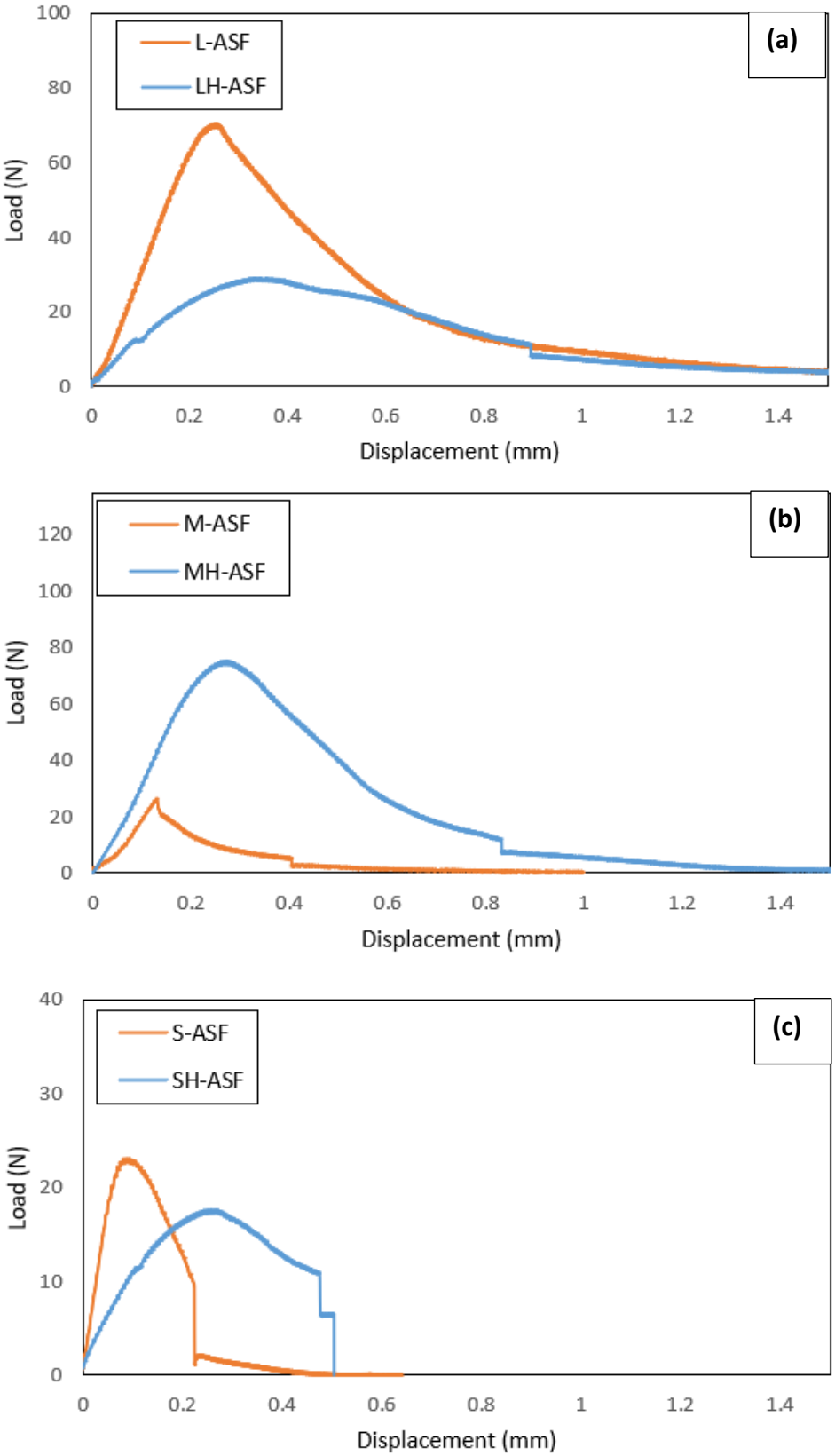

Figure 4-32: Comparison of load-displacement curves of syntactic foams with heated and non-heated (a) Large, (b) Medium and (c) Small ASW particles

Figure 4-33 displays the location of the crack relative to the sample. All the samples have cracks propagating away from the centre, with only the MH-ASF sample displaying a crack propagation that is nearly perpendicular to the sample length.

Table 4-20 summarises the flexural properties of the syntactic foams with heated ASW particles obtained from the three-point bending tests. The SH-ASF sample has similar flexural properties to the S-ASF sample, while there are some differences between LH-ASF and L-ASF samples and between the MH-ASF and M-ASF samples.

The LH-ASF sample has a reduced modulus, flexural strength and energy absorption when compared to the L-ASF sample. This is because the heating of the particles causes changes in strength and hardness, as described in Section 4.1. Furthermore, the LH-ASF sample has a crack deviating away from the loading nose. The crack propagates on an inclined direction halfway through before breaking the sample. The crack is also not perpendicular to the sample length, indicating that the crack propagates towards points of localised stress concentrations and away from the ASW particles.

The MH-ASF sample has enhanced flexural properties when compared to the M-ASF sample. The image of the MH-ASF sample shows the initial crack starting closer to the centre of the sample and the propagation occurring almost perpendicular to the sample length. This is different from the M-ASF sample (Figure 4-30) and may be the reason for the recorded enhanced flexural properties. It was established earlier in Section 4.3 that the conditions during infiltration are sufficient to heat the ASW particles. The recorded flexural properties of the MH-ASF are therefore a more

accurate representation of the overall flexural properties of the Medium ASW particle size group syntactic foam.

Table 4-20 : Flexural properties of the syntactic foams with heated ASW particles

Sample ID	Flexural Strength (MPa)	Flexural Strain	Flexural Modulus (GPa)	Flexural Energy ($J\ g^{-1}$)
LH-ASF	13.54	0.0014	14.24	25.15
MH-ASF	35.17	0.0022	13.27	53.72
SH-ASF	8.23	0.0011	13.49	5.18

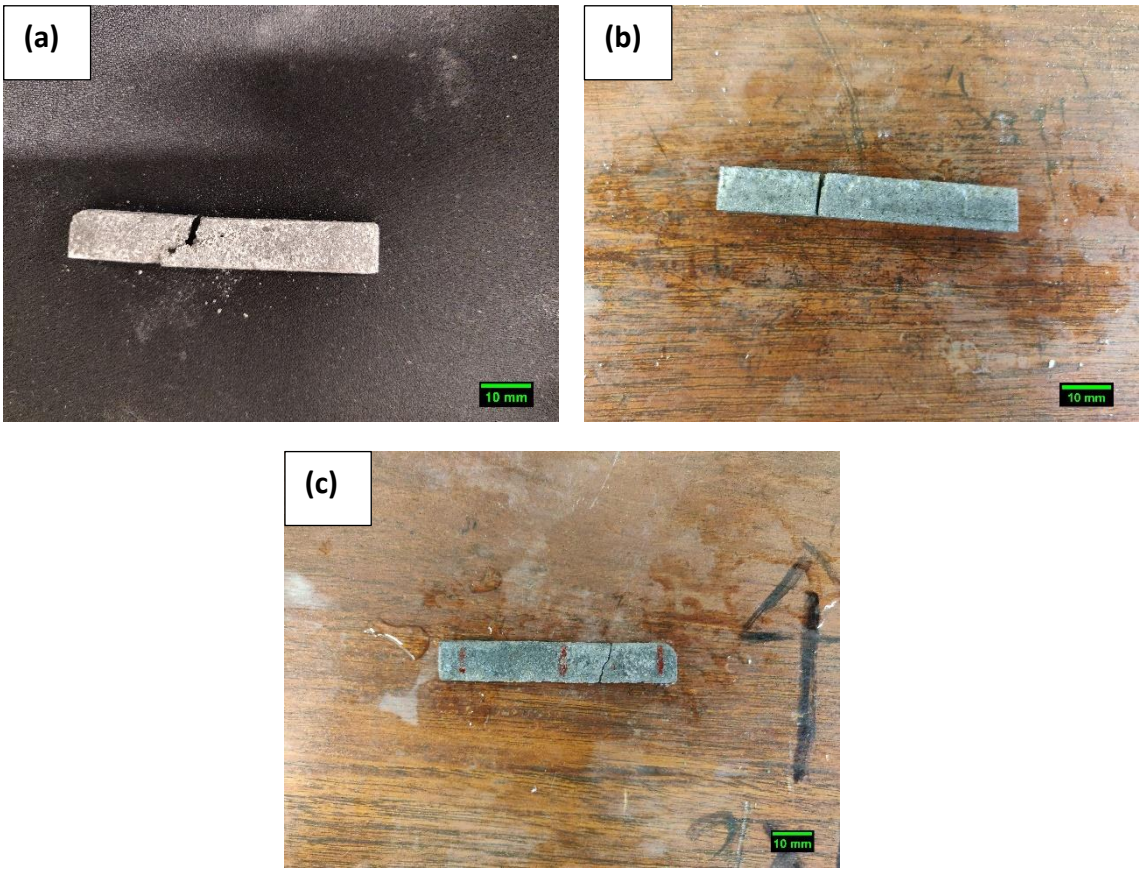

Figure 4-33: Images showing locations of cracks for (a) LH-ASF, (b) MH-ASF and (c) SH-ASF samples

Figure 4-34 shows micrographs of the fracture surfaces of the syntactic foam samples with heated ASW particles. The micrographs suggest that the crack propagation and failure mode is similar to the syntactic foams with non-heated ASW particle in all cases, regardless of the change in flexural properties. The crack seems to go through the Al matrix and around the particles due to the higher strength of the particles.

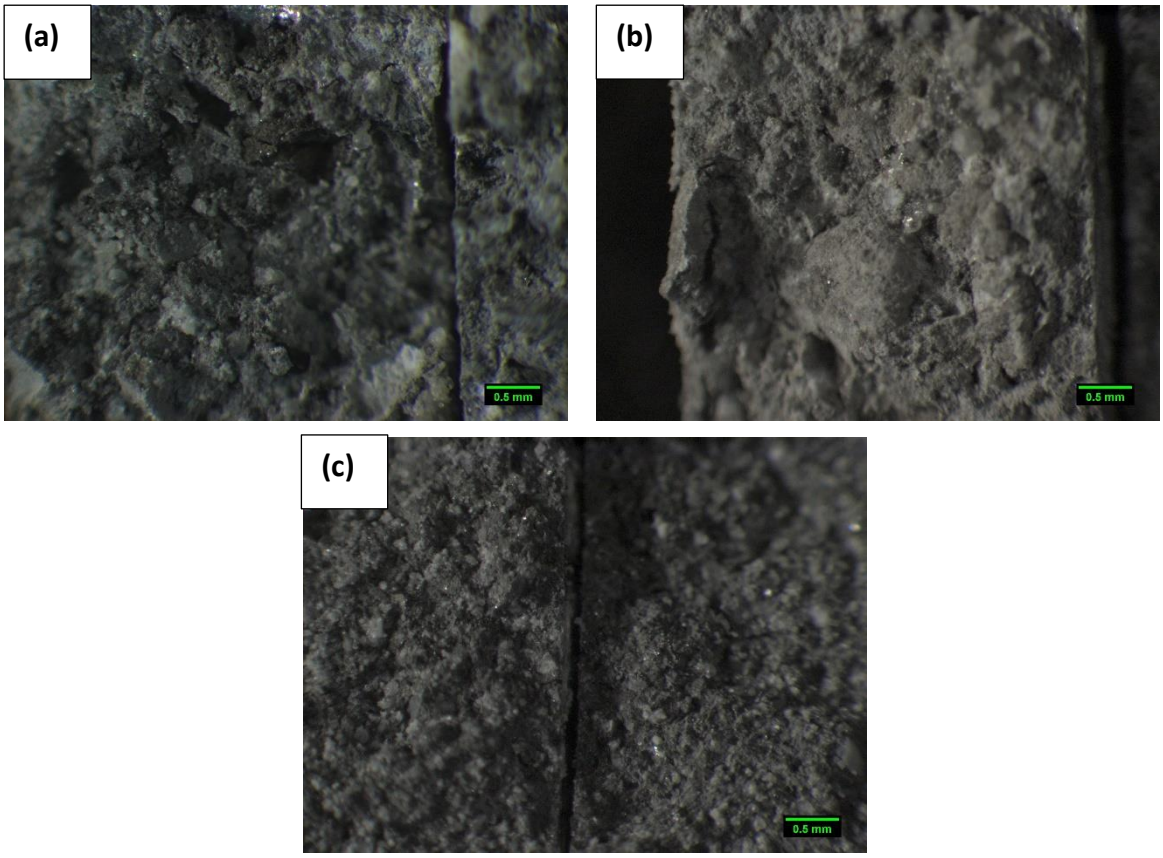

Figure 4-34: Micrographs of fracture surfaces for (a) LH-ASF, (b) MH-ASF and (c) SH-ASF samples

4.5.3 T6 treated ASW syntactic foams

Figure 4-35 compares the three-point bending behaviour of the T6-treated ASW syntactic foams to the non-T6 treated ASW syntactic foams. The T6 treatment greatly affects the shape of the curve when compared to the non-T6 treated syntactic foam samples.

The T6 treated samples all show distinct regions in the load-displacement curves. The initial elastic phase shows a sharp, linear increase in the load as the displacement is increased. A small, gradual decrease in gradient is observed until the critical load is reached, followed by a sharp drop and a gradual decline in stress to the point of ultimate failure. These regions are not as distinct for the non-T6 treated sample curves. The T6 treatment hardens the Al matrix, increasing the strength and hardness of the entire foam as well, leading to the higher critical load. The hardened Al matrix then governs the properties of the samples in the final decline region, which is more gradual and extended than for the non-T6 treated syntactic foam samples.

The sharp drop in stress on the load-displacement curves for the T6 treated syntactic foams is associated with initial crack formation and rapid propagation. The continuous decline region is attributed to slow crack propagation through the Al matrix. In all cases, the extended decline region is at a higher load for the T6 treated samples than for the non-T6 treated samples. This shows that the T6 treatment is effective in strengthening and hardening the Al matrix of the syntactic foam. It is further evidence that the extended plateau region is governed by the properties of the Al matrix.

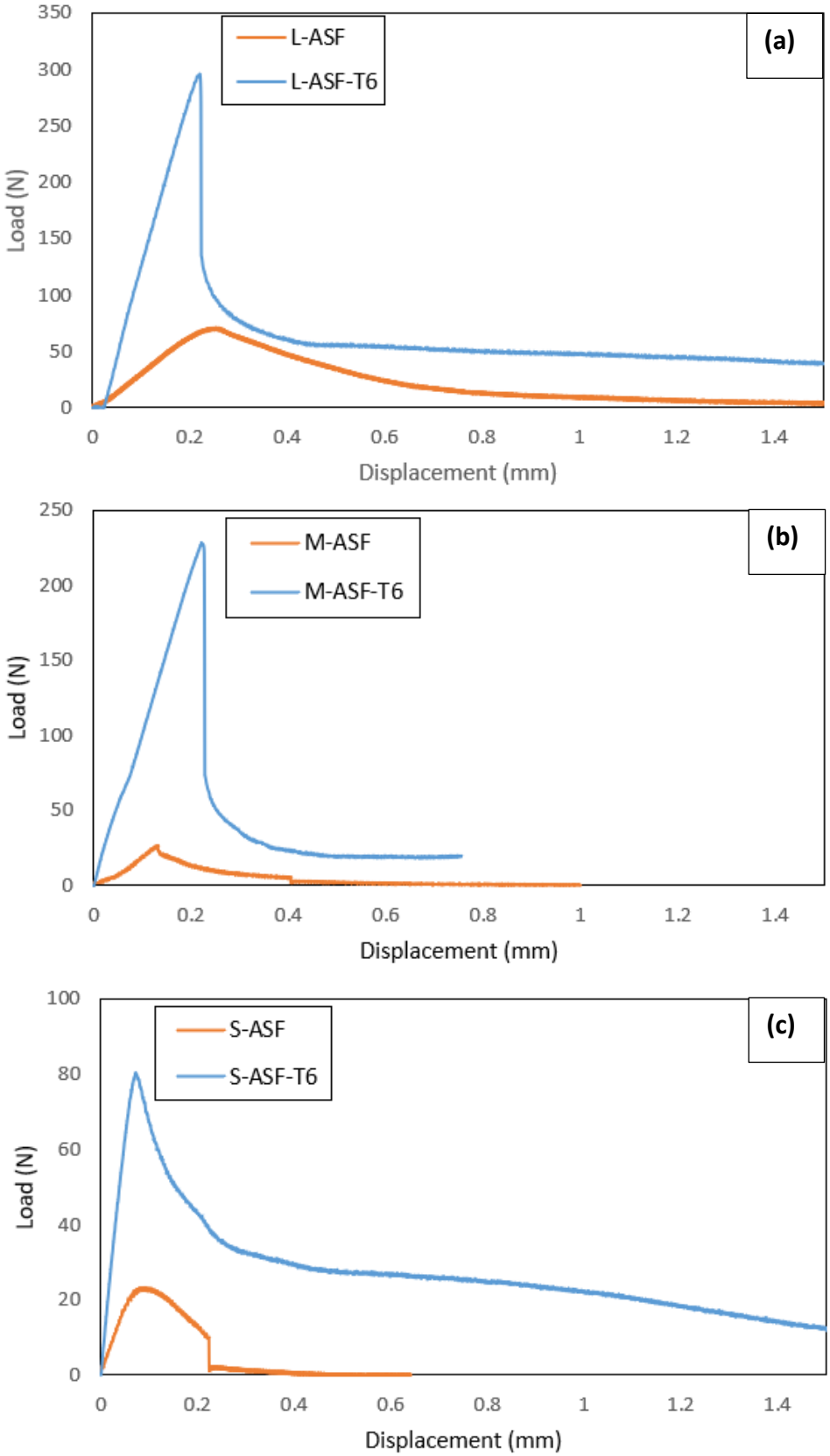

Figure 4-35: Comparison of load-displacement curves of T6 treated and non-T6 treated syntactic foam samples with (a) Large, (b) Medium and (c) Small ASW particles

Table 4-21 summarises the flexural properties of the T6-treated ASW particle syntactic foams obtained from the three-point bending tests.

The results show a significant increase in flexural strength, modulus and energy absorption for all samples after T6 treatment. The T6 treated samples for all particle size groups have a flexural strength and energy absorption that is nearly four times or more than that of the non-T6 treated samples. The highest increase is in the flexural energy for the Small ASW particle size group, which is about 11 times higher than non-T6 treated samples. The S-ASF-T6 samples have the lowest flexural strength, which is the trend observed for non-T6 treated samples as well as heated powder samples, and is primarily due to the brittle nature of the impurities present in the small particle size groups that are not present in the other size groups as well as the weaker Al-particle interface.

Table 4-21: Flexural properties of the T6 treated ASW syntactic foams

Sample ID	Flexural Strength (MPa)	Flexural Strain	Flexural Modulus (GPa)	Flexural Energy ($J\ g^{-1}$)
L-ASF-T6	138.49	0.0021	71.90	141.90
M-ASF-T6	107.45	0.0021	50.67	40.21
S-ASF-T6	37.69	0.0007	45.04	46.27

Figure 4-36 shows the locations of the crack formed after the three point bending tests. The location of the crack is either at (L-ASF-T6) or close to (M-ASF-T6 and S-ASF-T6) the middle of the samples, so the flexural properties recorded from these

tests are an accurate representation of the real flexural properties of the T6 treated ASW syntactic foam samples. The cracks in the M-ASF-T6 and S-ASF-T6 samples have small deflections from the centre and are not perpendicular to the sample length. This is again due to local microstructural defects of weaknesses.

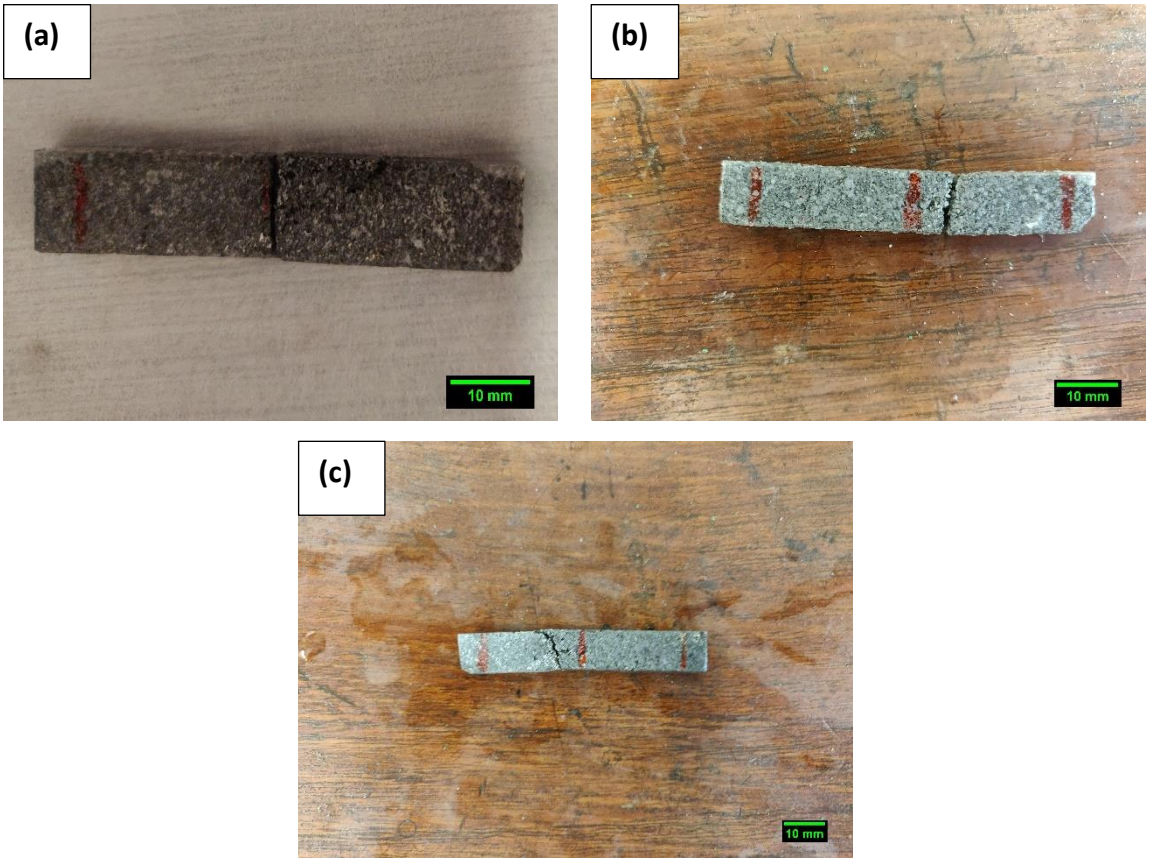

Figure 4-36: Images showing locations of cracks for (a) L-ASF-T6, (b) M-ASF-T6 and (c) S-ASF-T6 samples

Figure 4-37 shows micrographs of the fracture surfaces of the T6-treated ASW syntactic foam samples. Crack propagation mainly occurs through the interface between the Al matrix and the ASW particles, leaving the particles intact. The

micrographs also show the presence of fresh Al on the fracture surfaces, indicating that crack propagation also occurs through the Al matrix.

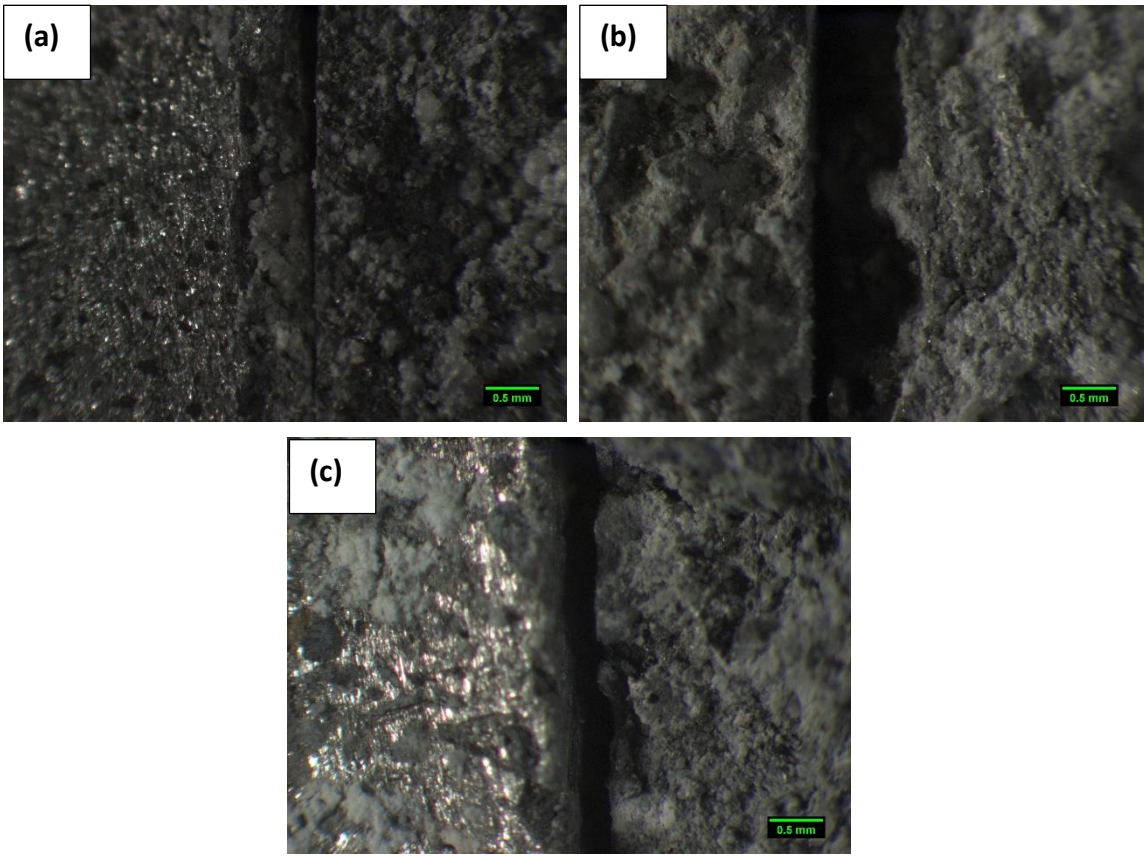

Figure 4-37: Micrographs of fracture surfaces for (a) L-ASF-T6, (b) M-ASF-T6 and (c) S-ASF-T6 samples

4.5.4 **Comparison with the E-sphere syntactic foam**

Figure 4-38 compares the three-point bending load-displacement curves for the syntactic foams with ASW particles to that of the E-sphere syntactic foam. The curve of the E-sphere syntactic foam sample shows similar regions to those of the ASW particle syntactic foam samples, i.e. an initial linear elastic region, an elastic-plastic region with a decreasing gradient before critical load is reached, and an eventual decline. The syntactic foams with ASW particles have lower critical loads than that for the E-sphere syntactic foam sample. This is because the E-sphere particles, being a mixture of hollow and porous particles, have a high shell hardness and are stronger, which increases the critical load.

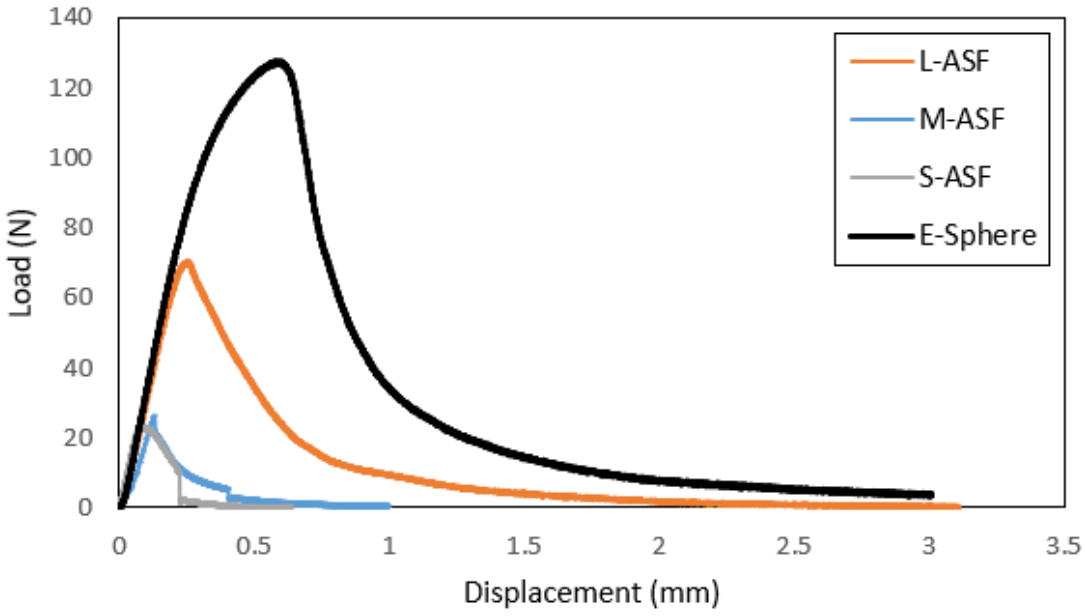

Figure 4-38: Comparison of load-displacement curves between ASW particle and E-sphere syntactic foams

Table 4-22 summarises and compares the flexural properties of the four syntactic foam samples. Compared to the syntactic foams with ASW particles, the E-sphere

syntactic foam sample generally has enhanced flexural properties, with a higher flexural strength, strain, and energy absorption. The lower flexural modulus of the E-sphere syntactic foam sample is attributed to the higher porosity of the E-sphere particles, which allows some of the particles to be or compressed more. This is also seen in Figure 4-38 where the load-displacement curve gradually flattens before reaching critical load and entering the decline region.

Table 4-22: Comparison of flexural properties of the E-sphere and ASW particle syntactic foams

Sample ID	Flexural Strength (MPa)	Flexural Strain	Flexural Modulus (GPa)	Flexural Energy (J g^{-1})
L-ASF	35.23	0.0025	14.82	36.45
M-ASF	26.05	0.0012	14.65	10.94
S-ASF	10.79	0.0009	14.63	3.94
E-sphere	59.80	0.0052	11.62	89.89

Figure 4-39 shows an image of the E-sphere syntactic foam sample after three-point bending along with a micrograph of the fracture surfaces. It is shown that the crack occurs close to the centre of the sample and propagates slightly inclined away from the centre.

The fracture surfaces show a few broken E-sphere particles and many more full particles intact. The broken particles are the ones compressed during loading, leading to the decrease in the gradient of the load-displacement curve as seen in Figure 4-

38. The intact particles are more common and are evidence of the crack propagating primarily through the interface between the Al matrix and the particles, which is similar to what is observed in the ASW particle syntactic foam.

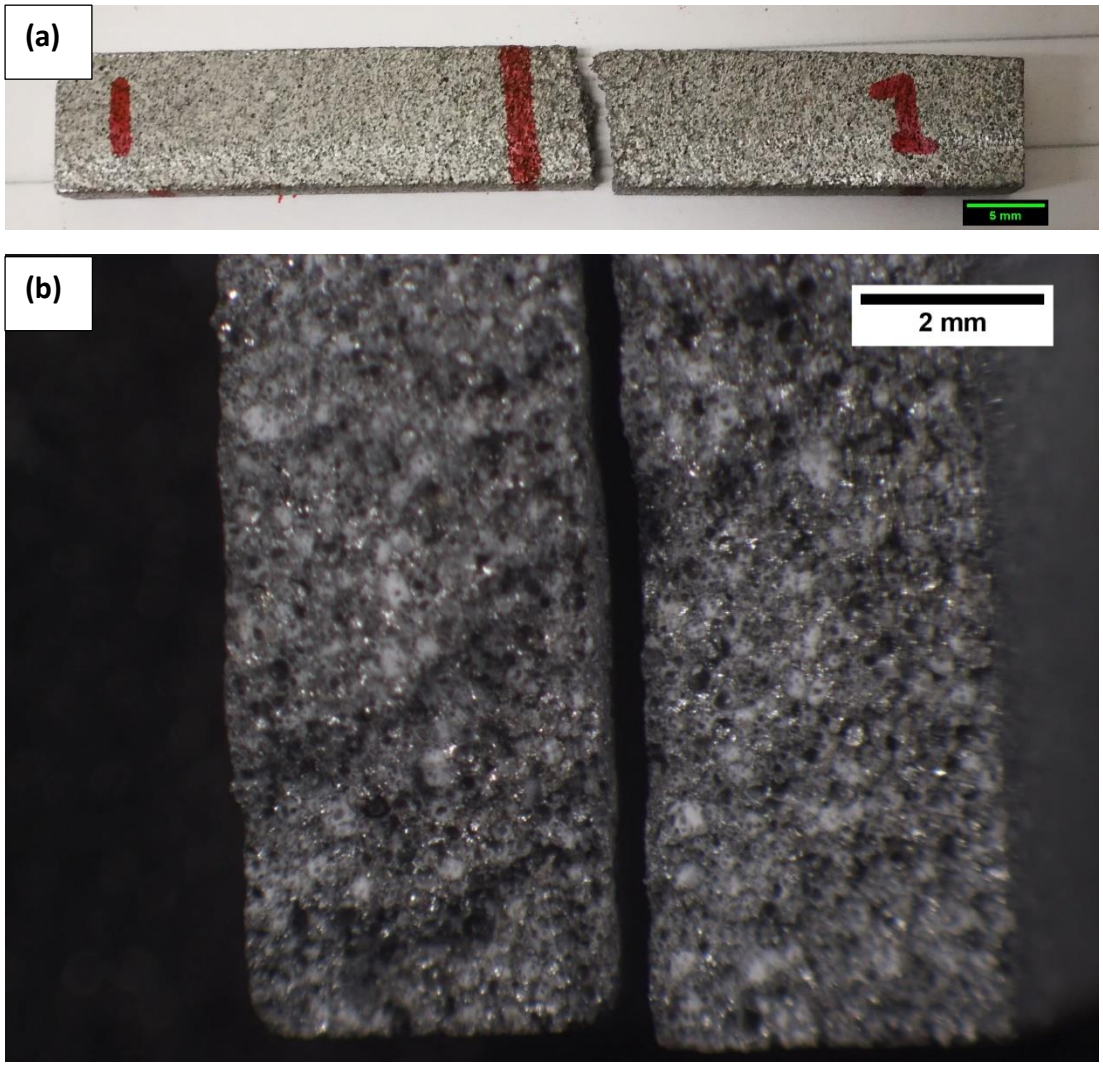

Figure 4-39: (a) Image of the cross-sectional surface showing the location of crack and (b) micrograph of fractured sample surface of the E-sphere syntactic foam sample

4.5.5 **Summary**

This section investigates the flexural properties of the syntactic foams with ASW particles under three-point bending conditions and compares them to the E-sphere syntactic foam. The load-displacement curves of the ASW syntactic foams generally show three distinct regions: the initial elastic region with a sharp linear increase in load, the elastic-plastic region with a decrease in the gradient of the curve until critical load is reached, and the gradual decline region until ultimate failure. The M-ASF and S-ASF samples tend to have sudden drops in applied load in the gradual decline region, indicating fast crack propagation. The crack initiated close to the centre for the L-ASF sample and further away for the M-ASF and S-ASF samples, which may cause inaccuracies in the calculated flexural properties. The flexural properties of the ASW syntactic foam samples show that the flexural strength and energy absorption decreases with decreasing particle size. The initial elastic region is mainly governed by the ASW particles up to the critical load and extended decline region is dependent upon the Al matrix.

Heating the ASW particles has little effect on the Medium and Small particle size group samples, whereas the LH-ASF sample has a significant reduction in flexural strength and energy absorption. This is attributed to the reduction in strength and hardness of the Large ASW particles upon heating. Although heating the Medium and Small particles has little influence on the properties of the syntactic foam samples, the different locations of crack initiation can result in inaccurate calculated flexural property results.

T6 treatment of the syntactic foam samples shows significant increase in the flexural properties, due to the increased hardness and strength of the Al matrix. Compared to the E-sphere syntactic foam sample, the ASW syntactic foam samples have lower critical loads and inferior flexural properties. The load-displacement curve of the E-sphere syntactic foam sample has a decreased gradient before critical load is reached and the extended decline region begins, due to the compression of some E-sphere particles that absorb more energy before complete failure.

4.6 Charpy Impact Behaviour of ASW Syntactic Foams

4.6.1 Syntactic foams with non-heated ASW particles

Charpy impact tests were conducted to study the impact toughness of the syntactic foams with non-heated ASW particles. Figure 4-40 shows images of the samples after the test and Table 4-23 evaluates the impact energy and impact toughness of the syntactic foam samples.

It is evident that the samples all have cracks propagating from the point of impact to the notch, perpendicular to the length of the sample. M-ASF and S-ASF Samples tend to have debris lost on impact in specific regions, as indicated by arrows in the images. The energy absorbed and toughness values show that the smaller the particle size, the lower the impact energy and toughness. This is due to the increase in impurities for the Small and Medium particle size groups and the decrease in porosity as particle size decreases.

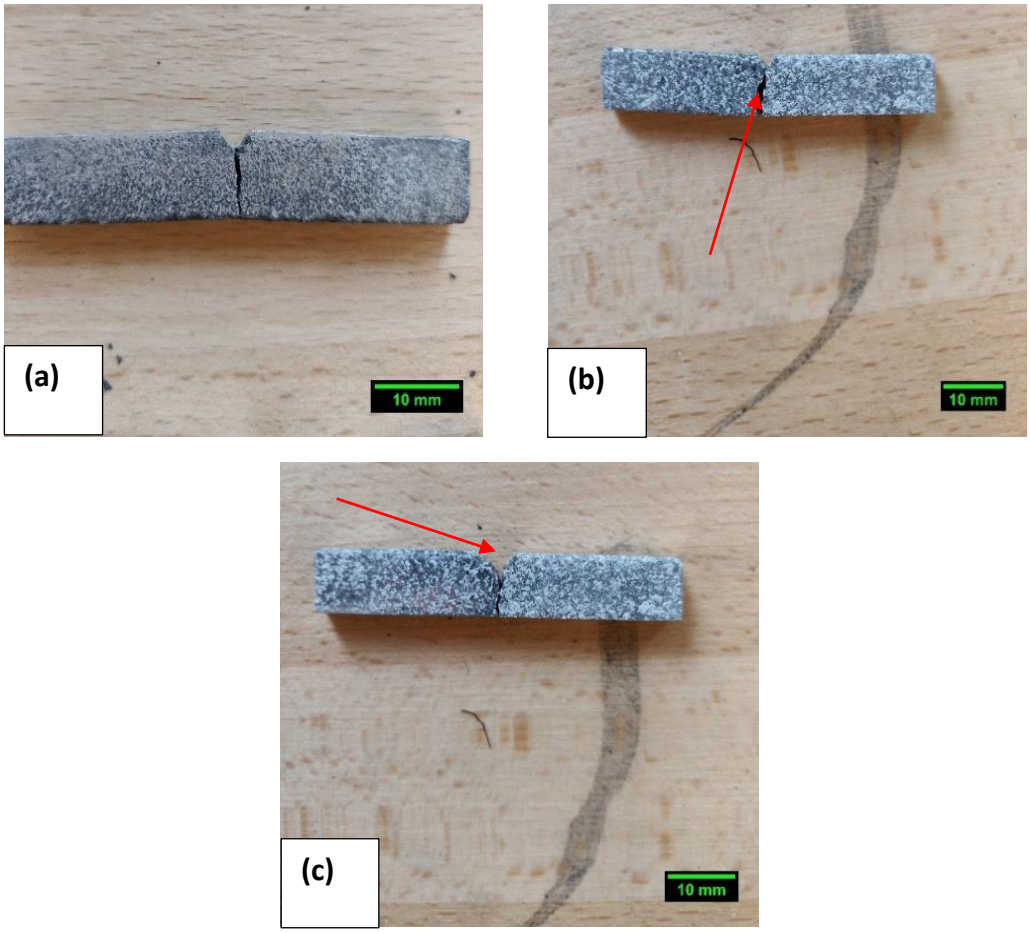

Figure 4-40: Images showing locations of cracks for (a) L-ASF, (b) M-ASF and (c) S-ASF samples

Table 4-23: Charpy impact properties of the syntactic foams with non-heated ASW particles

Sample ID	Charpy Angle (°)	Energy Absorbed (J)	Toughness A^k (kJ m^{-2})
L-ASF	132	2.48	9.02
M-ASF	135	2.00	7.28
S-ASF	136	1.85	6.72

Figure 4-41 displays the micrographs of the fracture surfaces of the syntactic foam samples with non-heated ASW particles. From the micrographs, it seems like the ASW particles have a significant impact on the fracture mechanism of the syntactic foam.

The L-ASF sample has a relatively rough crack surface. The porous nature of the Large ASW particles makes them less brittle and easier to break through, leading to the crack propagating rapidly and off-centre. This leads to a relatively longer crack, resulting in a higher impact energy and toughness.

The M-ASF and S-ASF samples also have flatter crack surfaces. The Medium and Small particles have a lower porosity, which makes them more brittle, leading to a lower energy absorbed and toughness. There are large craters on the fracture surface of the S-ASF sample, indicating loss of material upon impact and crack formation. This confirms the brittle nature of the foam. The energy absorbed decreased with decreasing particle size, because the least-resistant path for the crack to propagate through, i.e. the weak metal-particle interface, is decreased.

Compared to the quasi-static nature of the three-point bending tests, the dynamic loading in the Charpy test does not lead to a significant change in deformation behaviour. However, the samples are more brittle during impact than for quasi-static conditions, as the samples lose debris on impact and demonstrate lower energy absorption.

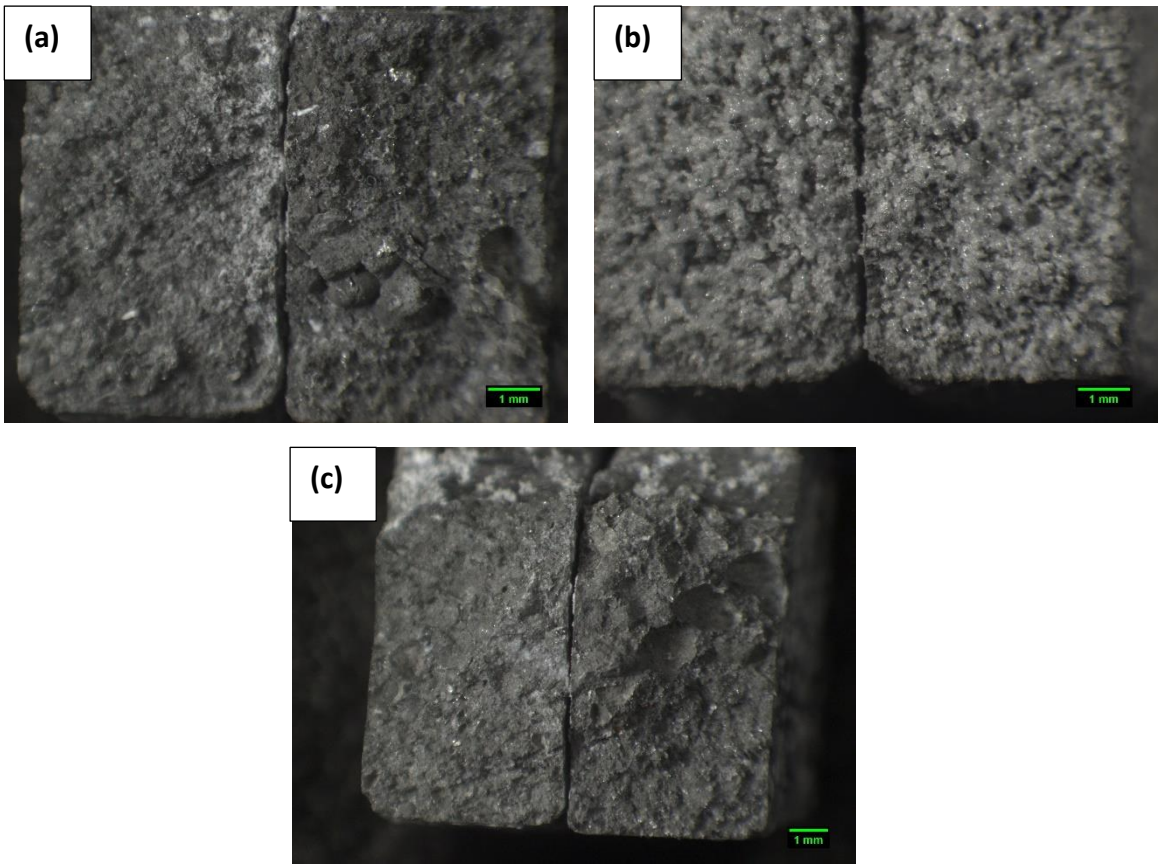

Figure 4-41: Micrographs of fracture surfaces of (a) L-ASF, (b) M-ASF and (c) S-ASF samples

4.6.2 **Syntactic foams with heated ASW particles**

Figure 4-42 shows images of the syntactic foams with heated ASW particles after the Charpy impact test. Like the syntactic foam samples with non-heated ASW particles, the MH-ASF and SH-ASF samples have cracks propagating perpendicular to the sample length. The LH-ASF sample, however, cracks in two places with both cracks deviating from a straight line in the middle of the section. The deviation may be due to the inhomogeneous microstructure. Cracks tend to propagate along the interface between the particles and the Al matrix. Large, heated particles result in a more tortuous crack path. The second crack formed is closer to the edge of the sample i.e. closer to the anvil in the setup described in Figure 3-5. This is because weak Large particles may result in some local defects, which can act as crack initiation sites under impact force. These small cracks may develop into large ones if the local stress condition is favourable.

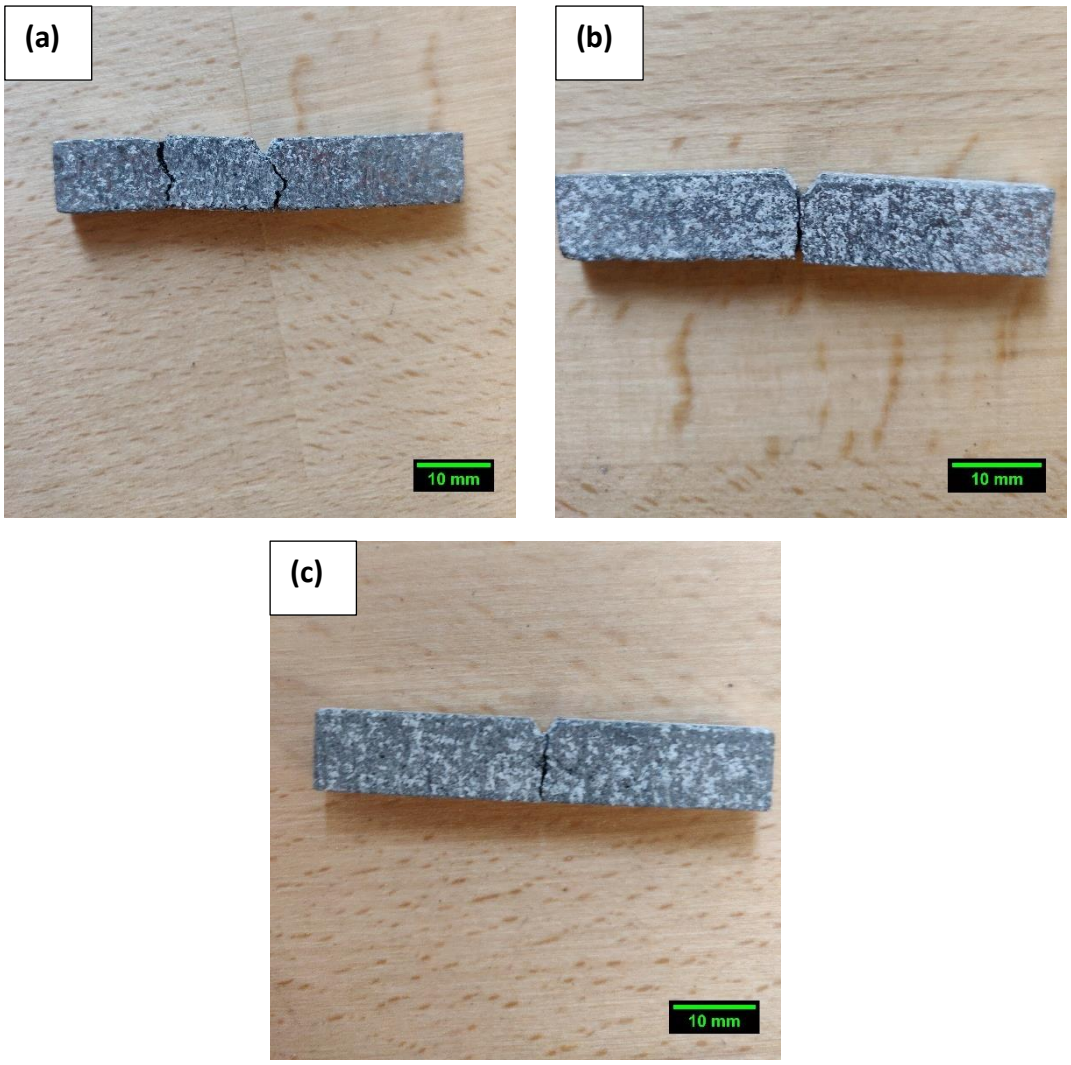

Figure 4-42: Images showing locations of cracks for (a) LH-ASF, (b) MH-ASF and (c) SH-ASF samples

Table 4-24 summarises the results of the quantitative analyses of the impact tests. Section 4.1 earlier described the changes observed after heating the Large ASW particles, where the strength and hardness were reduced. This explains the observed difference in the energy absorbed and toughness between the L-ASF and LH-ASF samples. The difference between the samples with heated and non-heated Medium and Small particles is small, which is because the conditions during infiltration are sufficient to heat the particles, as described in Section 4.3.

Table 4-24: Charpy impact properties of the syntactic foams with heated ASW particles

Sample ID	Charpy Angle (°)	Energy Absorbed (J)	Toughness A^k (kJ m^{-2})
LH-ASF	140	1.26	4.58
MH-ASF	134	2.16	7.85
SH-ASF	137	1.70	6.17

Figure 4-43 shows the micrographs of the fracture surfaces, with two images provided for the LH-ASF sample as it cracked in two regions. The LH-ASF sample has two types of crack propagation. The crack near the notch propagates through particles, as highlighted in the magnified image in Figure 4-44(a). On the fracture surface of the crack closer to the anvil, as highlighted by the magnified image in Figure 4-44(b), the particles are mostly untouched, or lost as debris, and there is increased metal content. This indicates that the crack goes around the particles and propagates through the matrix due to the weaker interfacial bonds. The crack propagation in the MH-ASF and SH-ASF samples is similar to the M-ASF and S-ASF samples, where the crack propagates through the interface between the matrix and the particles.

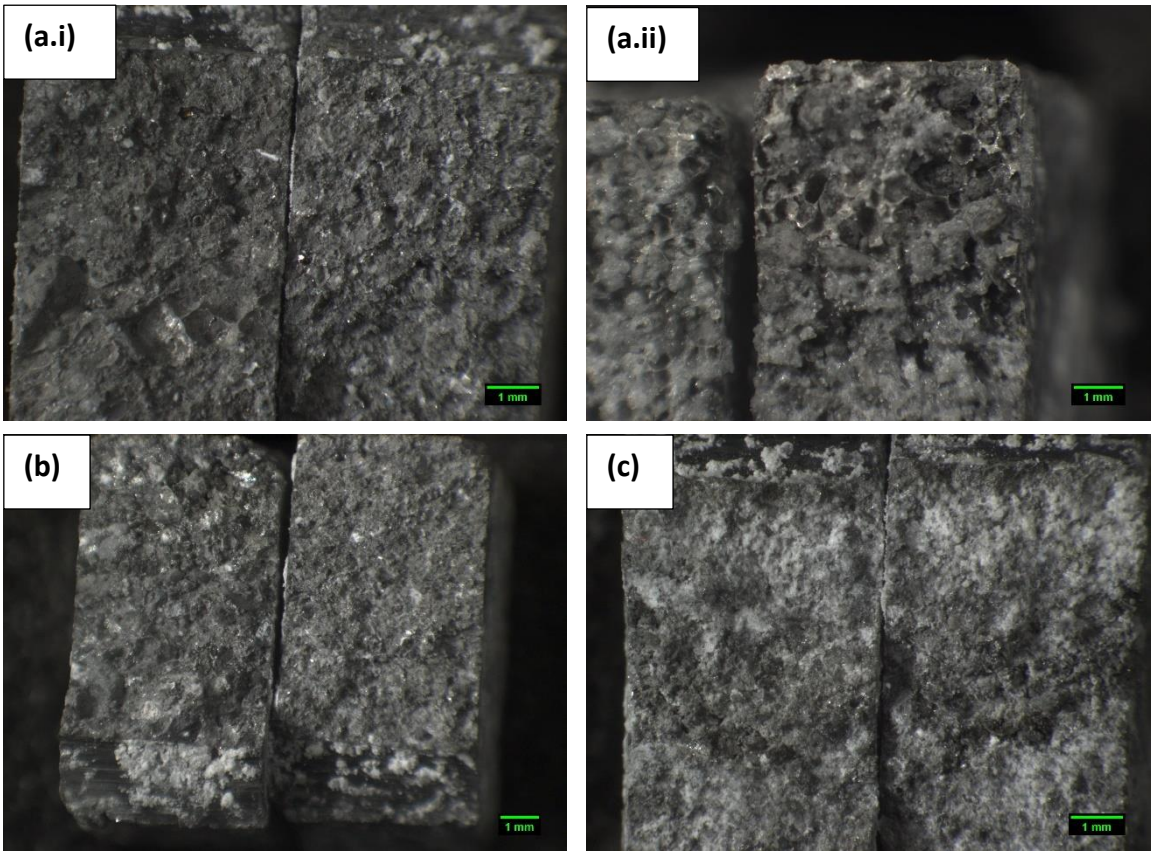

Figure 4-43: Micrographs of fracture surfaces for (a)i) LH-ASF near centre, (a)ii) LH-ASF near anvil, (b) MH-ASF and (c) SH-ASF samples

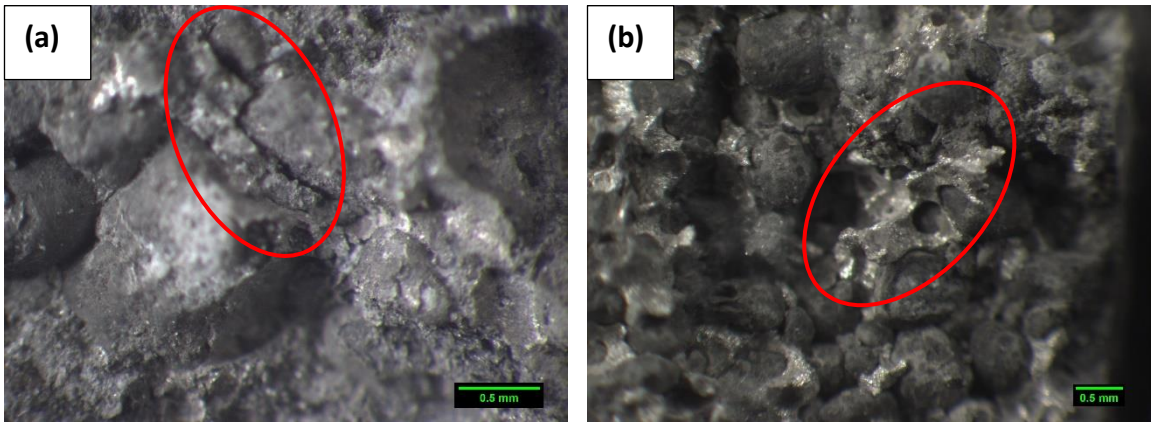

Figure 4-44: Magnified fracture surfaces of LH-ASF sample (a) near centre and (b) near anvil

4.6.3 **T6 treated ASW syntactic foams**

Figure 4-45 shows images of the T6 treated ASW particle syntactic foam samples after the Charpy impact test and Figure 4-46 shows the micrographs of the cracked surfaces. Table 4-25 summarises the results of the quantitative analyses of the tests.

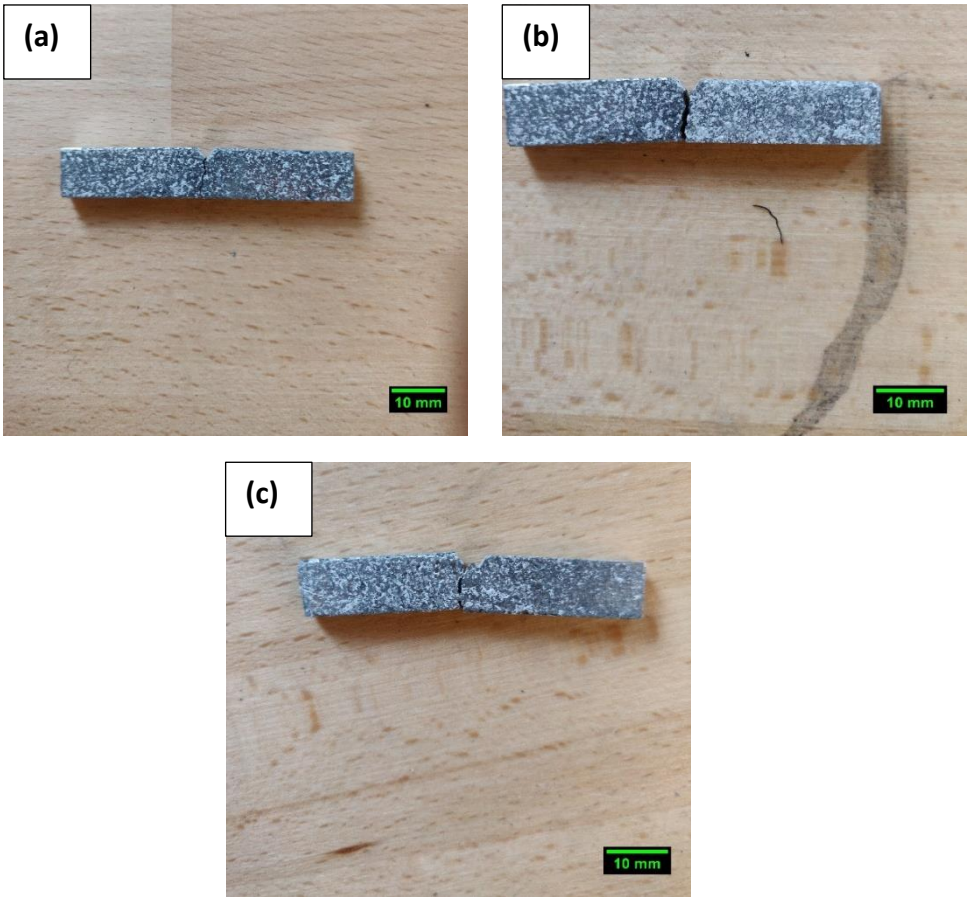

Figure 4-45: Images showing locations of cracks for (a) L-ASF-T6, (b) M-ASF-T6 and (c) S-ASF-T6 samples

T6 treatment does not affect the failure mode of the samples. However, it leads to an overall increase in impact toughness and energy absorbed as shown in Table 4-25. The images displaying the crack propagation show a straight crack from the notch and is perpendicular to the sample length. Slight deviations within the sample are attributed to the lower local strength, with the cracks moving through a path of least resistance. Micrographs in Figure 4-46 clearly show craters on the fracture surface of the sample, indicating loss of particles upon impact and the crack running through the interface between the particles and the matrix.

Table 4-25: Charpy impact properties of the T6 treated ASW syntactic foams

Sample ID	Charpy Angle (^{o})	Energy Absorbed (J)	Toughness A^k (kJ m^{-2})
L-ASF-T6	125	3.68	13.39
M-ASF-T6	128	3.15	11.47
S-ASFT6	134	2.16	7.85

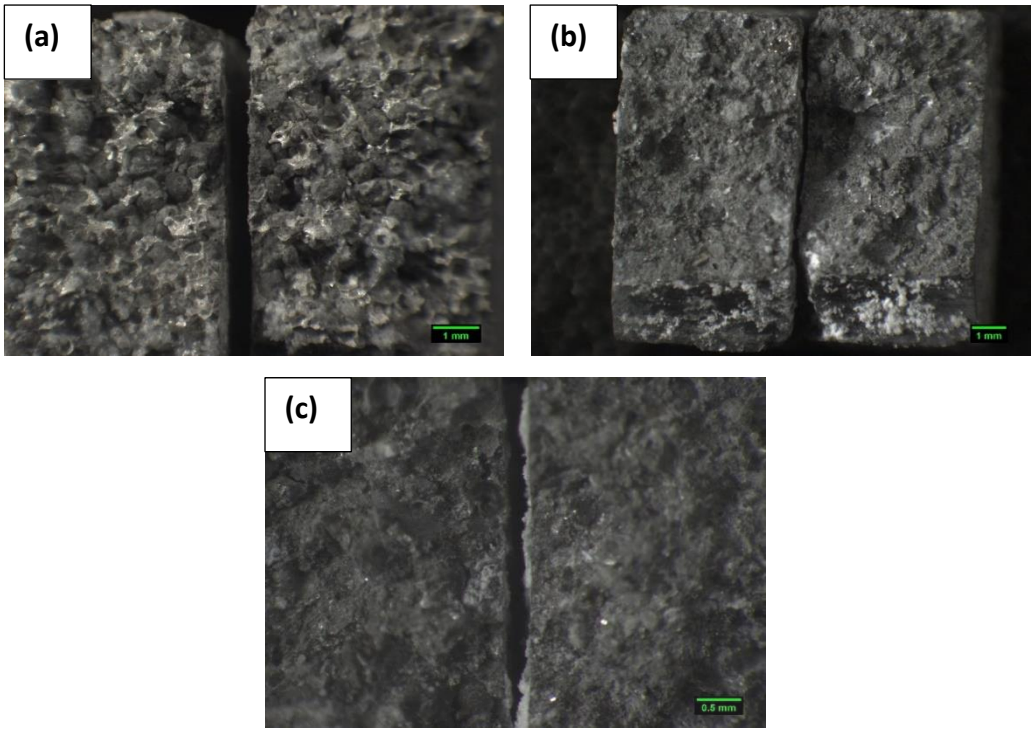

Figure 4-46: Micrographs of fracture surfaces for (a) L-ASF-T6, (b) M-ASF-T6 and (c) S-ASF-T6 samples

4.6.4 **Comparison with E-sphere syntactic foams**

Figure 4-47 shows the crack in the sample surface and a micrograph of the fracture surface of the E-sphere syntactic foam after the Charpy impact test. The crack is formed perpendicular to the length of the sample and propagates in a relatively straight line from the notch. The micrograph shows several broken E-sphere particles within the sample. This behaviour is somewhat different from that observed in the ASW particle syntactic foams. It is due to the stronger interfacial bonding and more porous E-sphere particles.

Table 4-26 compares the Charpy impact test properties of the ASW particle syntactic foam samples to the E-sphere syntactic foam sample. The impact toughness and energy absorbed of the E-sphere syntactic foam is higher than any of the ASW particle syntactic foams, with the closest being the Large ASW particle syntactic foam. The irregular structure and the varied composition of the ASW particles compared to the E-sphere particles is one of the reasons for this difference. The other is that the higher porosity in the E-sphere particles allows for a higher ductility, leading to an increase in impact energy and impact toughness.

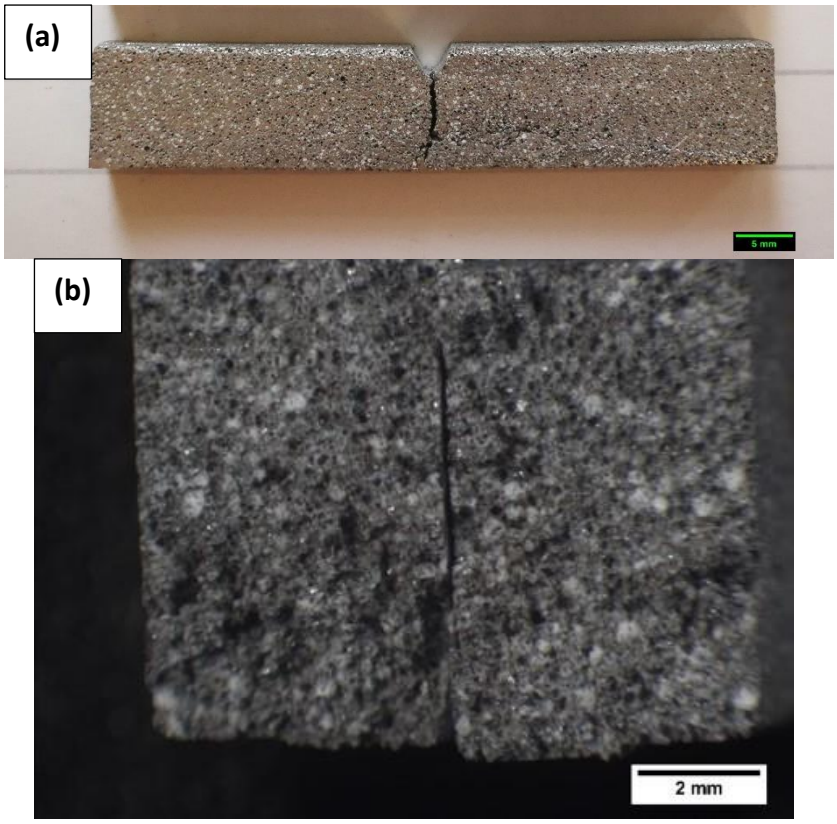

Figure 4-47: (a) Image of the cross-sectional surface showing the location of crack and (b) micrograph of fractured sample surface of the E-sphere syntactic foam sample

Table 4-26: Comparison of Charpy impact properties of the ASW particle and E-sphere syntactic foams

Sample ID	Charpy Angle (^{o})	Energy Absorbed (J)	Toughness A^k (kJ m^{-2})
L-ASF	132	2.48	9.02
M-ASF	135	2.00	7.28
S-ASF	136	1.85	6.72
E-sphere	130	2.81	10.22

4.6.5 **Summary**

This section investigates the properties of the ASW syntactic foams under Charpy impact test conditions. The energy absorbed and impact toughness decreases with decreasing particle size. The inhomogeneous particle distribution and the decrease in porosity as particle size decreases are the main reason for the decrease in energy absorbed. There are also some debris lost on impact for the M-ASF and S-ASF samples. The fracture surface shows that the deformation behaviour is similar to that observed for three-point bending tests, where the crack propagates largely through the interface between the metal and the particles. Furthermore, the dynamic loading conditions in the Charpy test compared to the static loading conditions in the three-point bending tests change the deformation from a ductile to a brittle failure mode.

Heating the ASW particles has little effect on the Medium and Small particle samples, whereas it leads to a decrease in impact toughness and energy absorbed for the Large particle sample. This is attributed to the decrease in particle strength and hardness upon heating, as described in Section 4.1. The LH-ASF sample also cracks in two places, one crack closer to the centre and the other close to the anvil. T6 treatment of the syntactic foam samples leads to an overall increase in impact toughness and strength due to the increase in the hardness of the Al matrix.

The ASW particle syntactic foam samples behave differently to the E-sphere syntactic foam sample. For the E-sphere syntactic foam sample, the crack propagates from the notch to the point of contact and runs straight through the sample, breaking the E-sphere particles. The impact toughness and energy absorbed of the E-sphere syntactic foam are higher than any of the ASW particle syntactic foam samples due

to the increased strength of the particle-matrix interface and the higher porosity in the E-sphere particles, which leads to a more ductile material.

4.7 Friction and Wear Behaviour of Syntactic Foams

This section presents and discusses the dry and lubricating sliding wear behaviour of ASW syntactic foam samples. More results are provided in Appendix C.

4.7.1 Dry sliding wear behaviour

4.7.1.1 *Coefficient of friction*

Figure 4-48 shows the development of the COF in dry sliding wear conditions as a function of sliding distance. The sliding distance for all tested samples in this section was 2000m. However, the COF showed very little variability as sliding distance increased above 500m. Therefore, only the data for sliding distance up to 500m is presented for convenience. Table 4-27 provides average values of the COF for the L-ASF, M-ASF and S-ASF samples. The COF decreases with decreasing particle size, with the L-ASF sample having the largest COF and the S-ASF with the smallest.

The COF vs sliding distance curves show three clear regions. At first, there is the initial sharp increase in COF in the first 50m of sliding distance. This occurs because the initial contact area is small and increases rapidly as the track is continuously worn, resulting in the first indents and grooves on the wear track. As sliding distance increases beyond 50m to 200m, the grooves become more pronounced on the wear track. Both the static partner and the syntactic foam are continuously worn, leading to a decrease in the slope of the curve. Beyond 200m, the contact area becomes nearly constant. The surface keeps getting worn continuously, leading to the flattening, and levelling out of the COF.

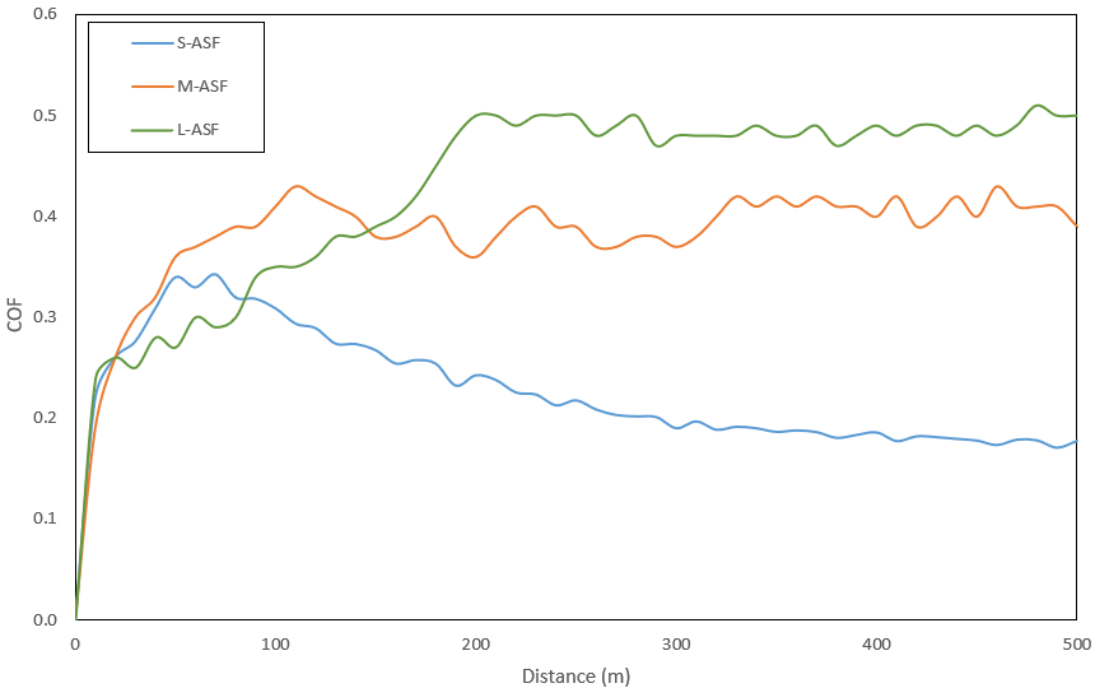

Figure 4-48: Development of COF vs sliding distance for ASW syntactic foam samples under dry sliding wear conditions

Table 4-27: Average COF for ASW syntactic foam samples under dry sliding wear conditions

Sample ID	COF
L-ASF	0.48
M-ASF	0.39
S-ASF	0.19

4.7.1.2 *Wear track analysis*

Wear track analysis was conducted on the ASW syntactic foam samples using Vision 3.0 and a section of the wear track was analysed to estimate the difference in surface roughness. The track analysis maps are shown in Figure 4-49 which were obtained using the profilometer. Table 4-28 summarizes the dry sliding wear parameters, including track depth, track width, differences in average surface roughness (ΔRa) and mean roughness depth (ΔRz), weight loss and specific wear. The specific wear, which is the amount of surface wear per unit sliding distance, was calculated using the weight loss and the sliding distance with the following formula:

$$Specific\ wear = \frac{\Delta Weight}{\rho \times 2000\ m}, where\ \rho\ is\ the\ density\ of\ the\ sample \qquad (4.1)$$

Before the sliding wear tests were conducted, the surfaces of all samples were perfectly flat and differences in surface roughness were as a result of the sliding.

There is a clear relationship between the wear parameters and ASW particle size. The track depth and specific wear of the samples decrease, while the difference in surface roughness increases, as particle size decreases. This is because smaller particles lead to a more uneven surface i.e. a high surface roughness. The resultant lower contact area creates high localised pressures at points of contact. This reduces the ability of contact points to carry any additional load before sliding. As the contact area increases, the frictional force and COF increase (Brizmer, 2018).

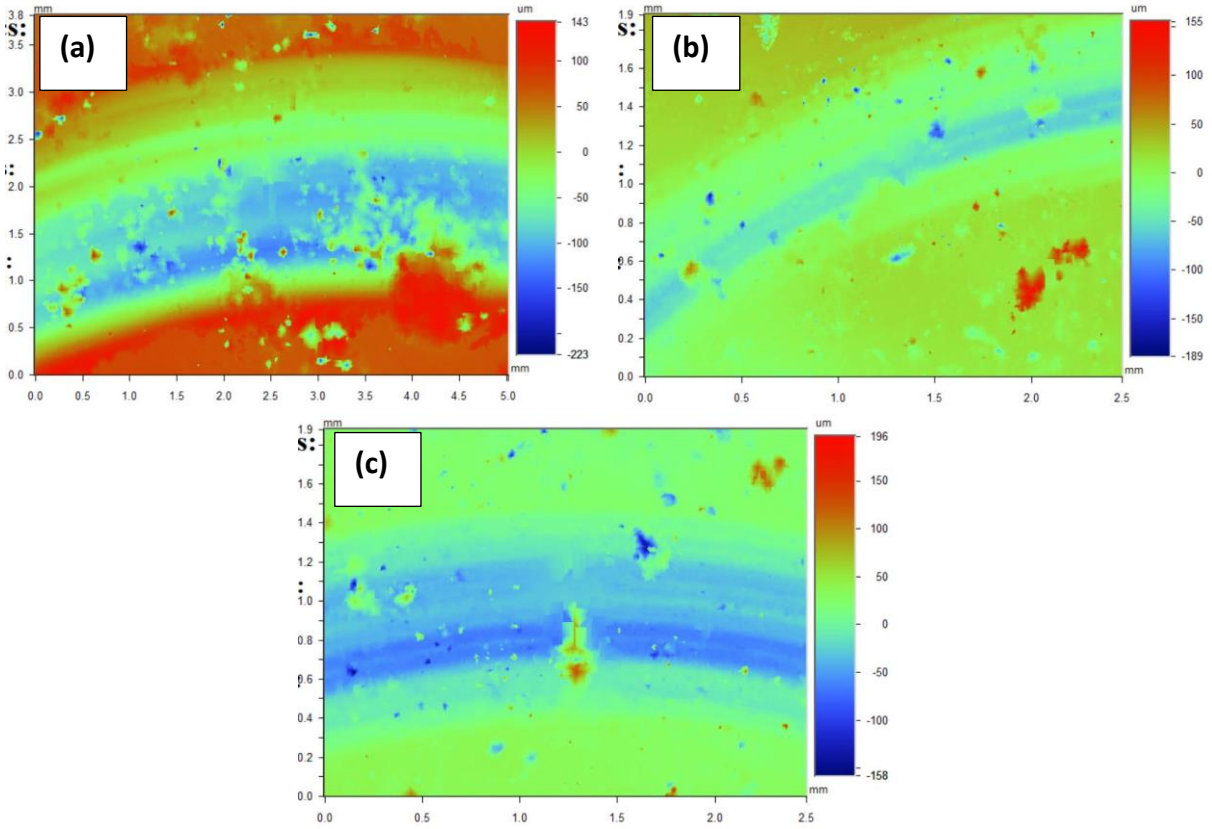

Figure 4-49: Wear track maps for (a) L-ASF, (b) M-ASF and (c) S-ASF samples under dry sliding wear conditions

Table 4-28: Summary of dry sliding wear parameters of ASW syntactic foam samples

Sample ID	Track depth (mm)	Track width (mm)	ΔRa ($x10^{-3}$) mm)	ΔRz ($x10^{-3}$) mm)	Weight loss (g)	Specific wear ($mm^3\ m^{-1}$)
L-ASF	0.143-0.161	5.84	19.57	52.52	0.08	0.020
M-ASF	0.061-0.125	5.70	23.54	68.08	0.06	0.015
S-ASF	0.058-0.118	5.34	28.85	78.55	0.06	0.014

Figure 4-50 displays micrographs of the worn surfaces of the ASW syntactic foam samples after dry sliding wear tests. All the samples have a relatively even wear track. The progression of wear as seen by the track surfaces is also similar. As the samples are porous, the ASW particles tend to be chipped off the surface and fall into the pores within the particles or the SF sample. As this happens, the surface becomes worn evenly and the COF levels out, as seen in Figure 4-48. This is seen on the worn surfaces in Figure 4-50 as the regions where the sliding direction is not evident and is indicated using red arrows. The L-ASF sample shows this behaviour to a greater extent than the M-ASF and the S-ASF samples, leading to the higher average COF value as seen in Table 4-27.

There are some darker patches observed on the worn tracks of all samples, which are characteristic of oxidative wear and are indicated on Figure 4-49 with blue arrows. Oxidative wear occurs when heating due to friction during sliding causes surface oxidation, leading to wear through the removal of oxide fragments (M. Ramachandra and Radhakrishna, 2007). Furthermore, there is evidence of fatigue-related wear known as delamination, where repeated sliding induces subsurface cracks that gradually grow and eventually shear to the surface, forming long thin wear sheets (M. Ramachandra and Radhakrishna, 2007; J. Zhang and Alpas, 1997). Delaminated sections are circled on Figure 4-50.

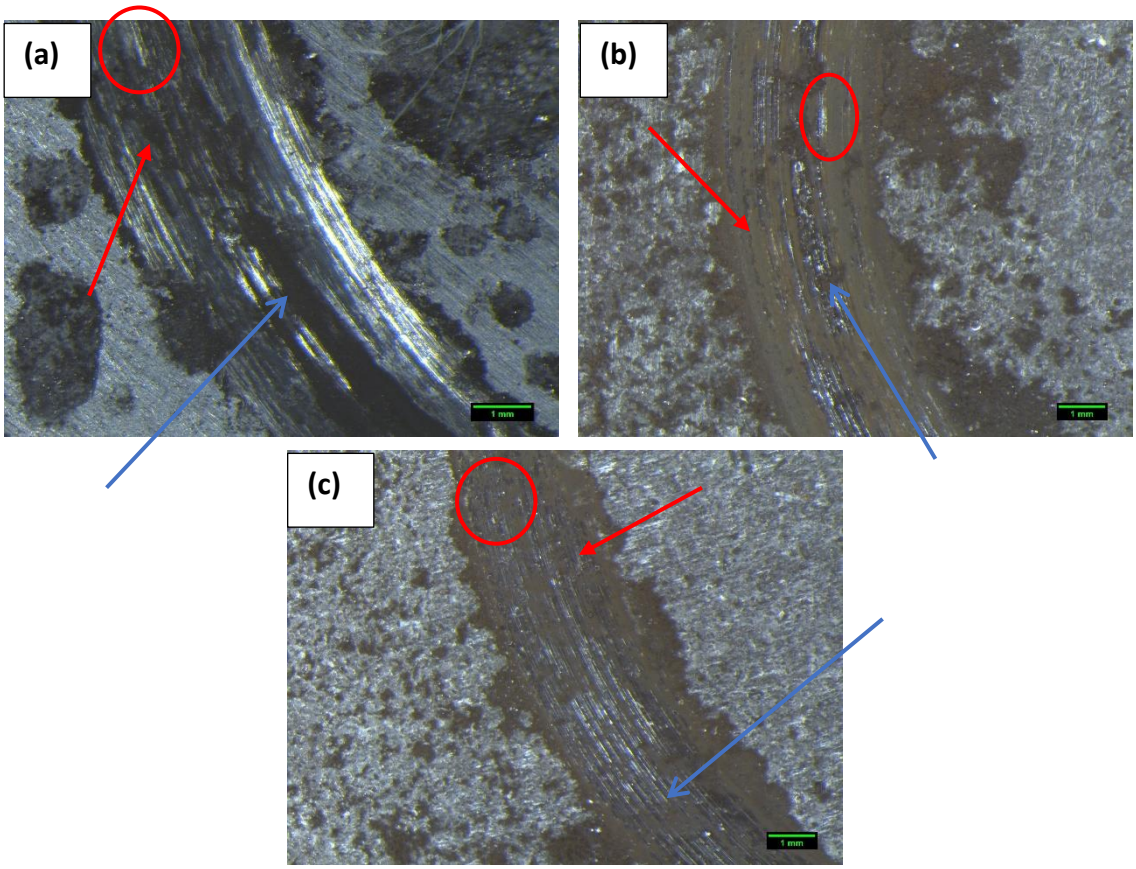

Figure 4-50: Micrographs of worn surfaces for (a) L-ASF, (b) M-ASF and (c) S-ASF samples under dry sliding wear conditions

The micrographs of the static partners to the respective ASW syntactic foam samples are shown in Figure 4-51. The static partner for the L-ASF sample has an even wear surface for the static partner, with a clear indication for the direction of wear and a symmetrical wear profile. There is no ceramic material or piece of SF seen on the static partner, so the wear is predominantly adhesive.

The static partner for the M-ASF sample also displays an even wear profile, however there is a section of the surface that looks to have been worn outside of the circular space. This may be due to an initial uneven surface or a higher surface roughness of the sample. Some regions of the static partner show the presence of ASW particles,

as indicated on Figure 4-51 with red arrows. The wear in this case displays certain features characteristic of abrasive wear.

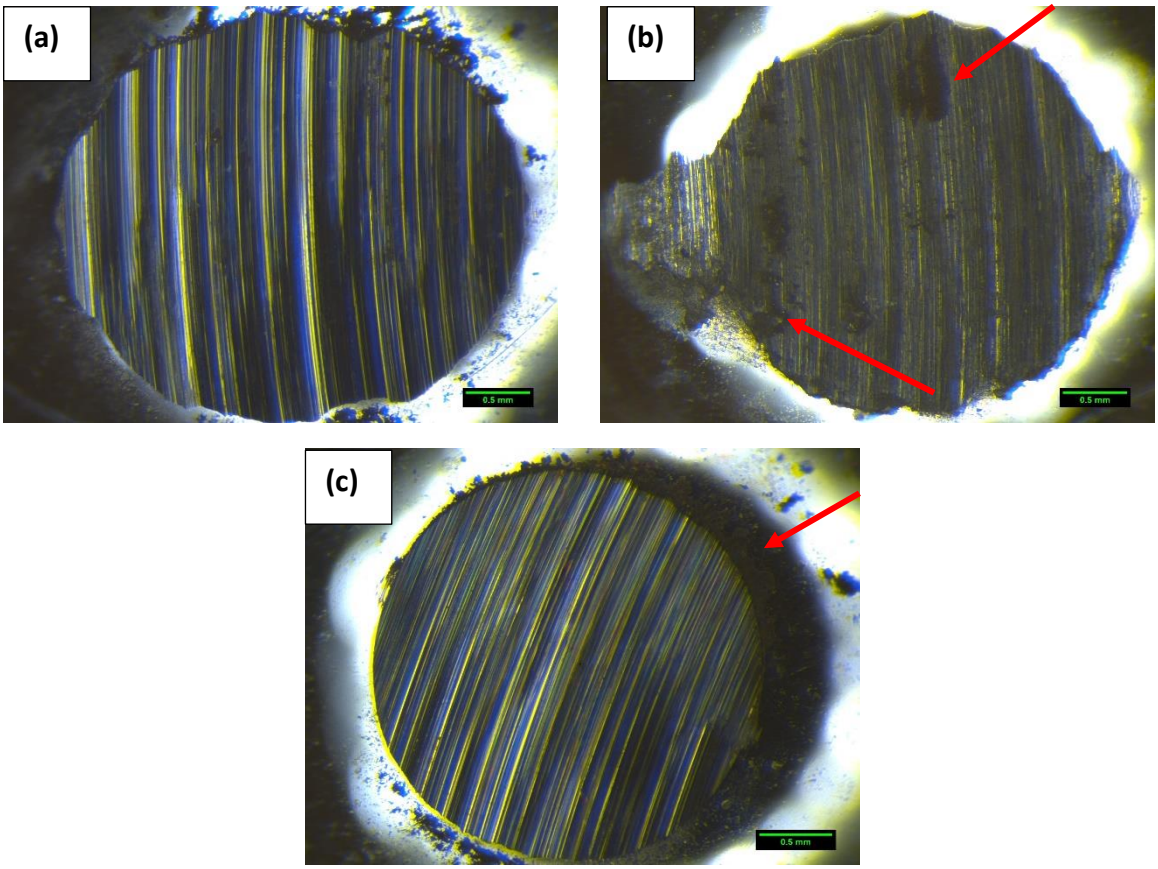

Figure 4-51: Micrographs of static partners for (a) L-ASF, (b) M-ASF and (c) S-ASF samples under dry sliding wear conditions

The static partner for the S-ASF sample also has an evenly worn surface, with the direction of wear evident. Like the static partner for the M-ASF sample, there are regions where the ASW particles have been embedded onto the surface of the static partner. This is indicative of adhesive wear. The ASW particles on the surface of the static partner then slide against the syntactic foam, which has ASW particles on its surface. This leads to the lower COF value and the decreasing COF development curve seen in Table 4-27 and Figure 4-48 respectively.

4.7.1.3 *Effect of heating ASW particles*

Figure 4-52 compares the development of COF for the syntactic foam samples with heated and non-heated ASW particles in dry sliding wear conditions as a function of sliding distance. Table 4-29 provides average COF values for the syntactic foam samples with heated ASW particles. Using heated ASW particles results in little change in wear behaviour for the Small and Medium ASW particle samples, but a significant change in behaviour for the Large ASW particle samples is seen, which is similar to what was observed in previous sections of this chapter.

The COF vs sliding distance curves for the SH-ASF and MH-ASF samples show the same three regions as their respective syntactic foam counterparts with non-heated ASW particles. There is an initial sharp increase in COF, followed by a decrease in gradient and a final steady state as the curve levels out with increasing sliding distance. The LH-ASF sample on the other hand remains on a low COF as sliding distance increases with minimal variations. This could be due to the decrease in strength of the ASW particles upon heating, as observed in Section 4.1.

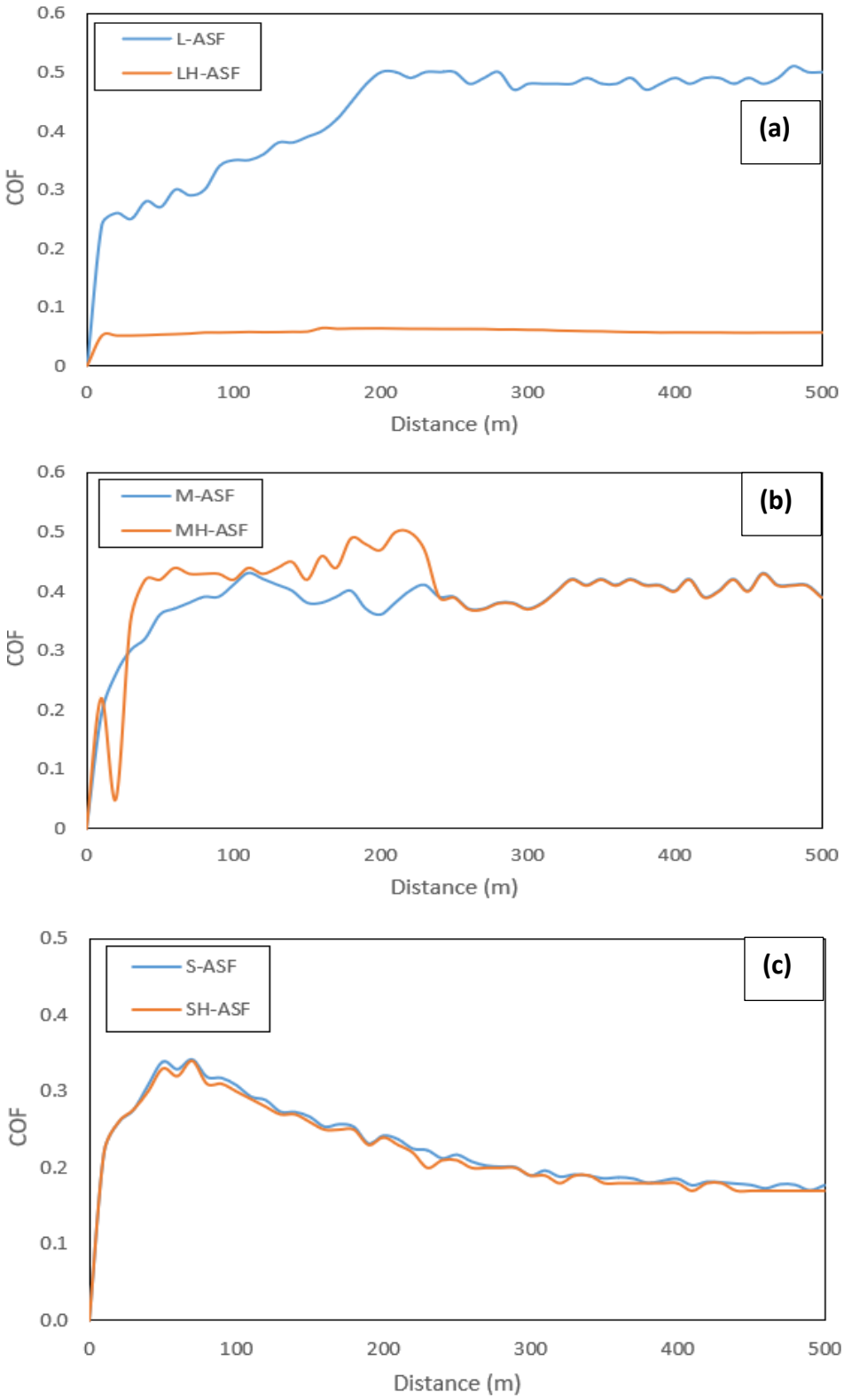

Figure 4-52: Comparison of COF development for syntactic foam samples with heated and non-heated ASW particles under dry sliding wear conditions

Table 4-29: Average COF for syntactic foam samples with heated ASW particles under dry sliding wear conditions

Sample ID	COF
LH-ASF	0.06
MH-ASF	0.41
SH-ASF	0.18

The wear track maps of the syntactic foams with heated ASW particles are shown in Figure 4-53. Table 4-30 summarizes the dry sliding wear parameters of the syntactic foam samples with heated ASW particles. The samples show an increase in surface roughness differences as particle size decreases, which is similar to what was observed for the syntactic foams with non-heated ASW particles. However, there is little correlation for the rest of the properties. Heating of the ASW particles does not lead to any significant change in properties for the Small and Medium samples, but there is a clear change in properties for the Large samples. This is because heating the ASW particles causes a change in particle properties, a similar effect as observed in results from previous sections in this chapter.

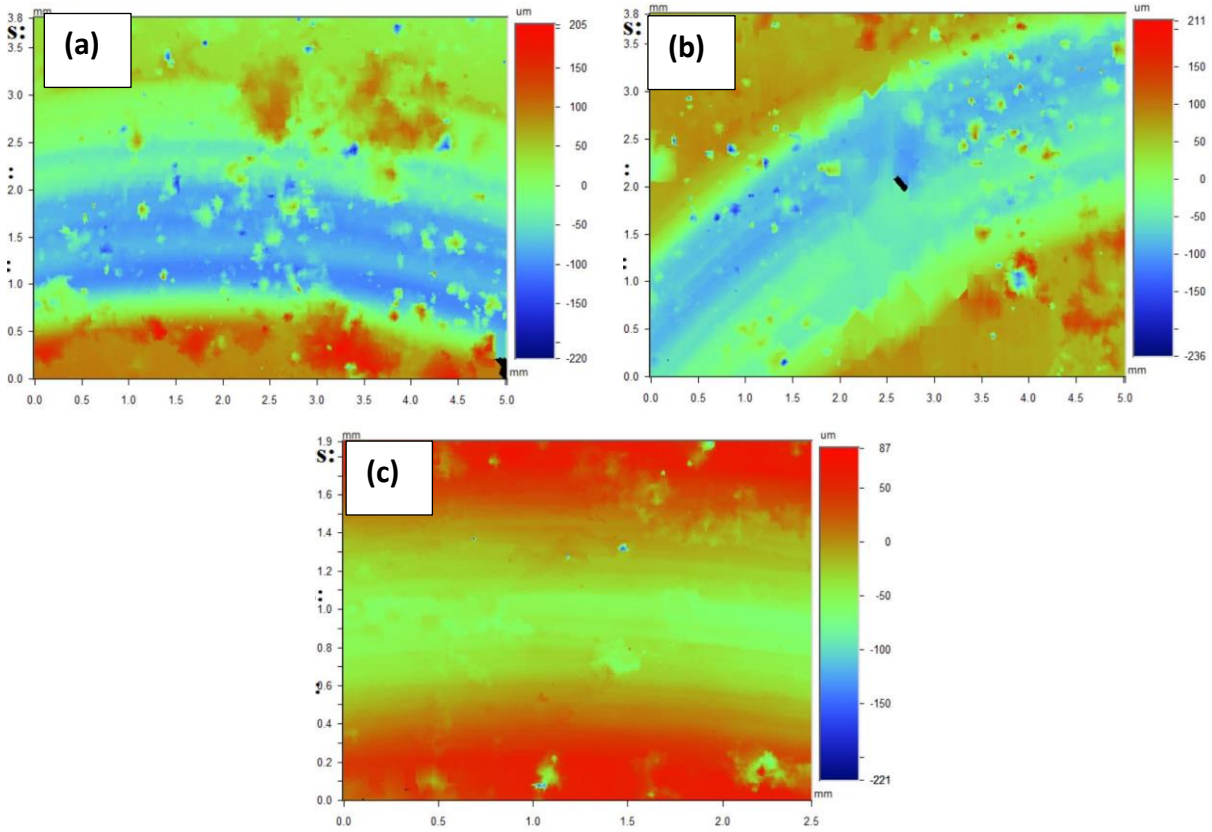

Figure 4-53: Wear track maps for (a) LH-ASF, (b) MH-ASF and (c) SH-ASF samples under dry sliding wear conditions

Table 4-30: Summary of dry sliding wear parameters of syntactic foam samples with heated ASW particles

Sample ID	Track depth (mm)	Track width (mm)	ΔRa ($x10^{-3}$) mm)	ΔRz ($x10^{-3}$) mm)	Weight loss (g)	Specific wear ($mm^3\ m^{-1}$)
LH-ASF	0.027-0.092	6.00	8.97	13.41	0.10	0.008
MH-ASF	0.054-0.159	5.86	22.10	72.65	0.07	0.020
SH-ASF	0.050-0.111	5.54	30.10	77.74	0.07	0.017

The micrographs of the worn surfaces of the syntactic foam samples with heated ASW particles are shown in Figure 4-54. Figure 4-55 displays micrographs of their static partners after dry sliding wear tests. These figures show that there is nearly no change in wear behaviour for the Small and Medium samples when the ASW particles are heated before infiltration as opposed to not, with adhesive wear being dominant for both, abrasive wear observed to some extent, and indications of oxidative wear and delamination as well. The LH-ASF sample shows a change in wear behaviour, where pieces of the ASW particles end up getting attached to the static partner, leading to abrasive wear and a resultant increase in weight loss, indicating an increase in amount of wear. The micrograph of the static partner (Figure 4-55a) also shows irregular wear on its surface.

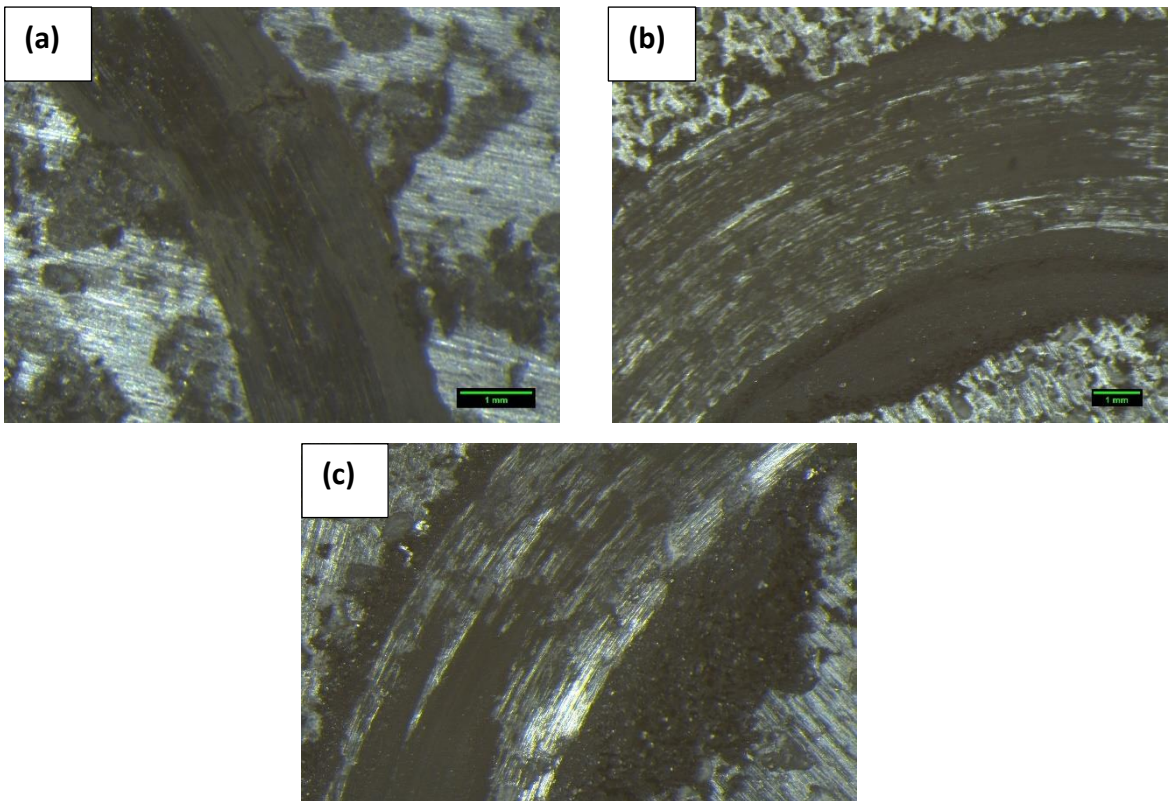

Figure 4-54: Micrographs of worn surfaces for (a) LH-ASF, (b) MH-ASF and (c) SH-ASF samples under dry sliding wear conditions

The change in properties of the LH-ASF sample to the L-ASF sample can be due to the change in mechanical properties of the ASW particles, as discussed in Section 4.1. When the Large ASW particles are heated, the hardness of the particles decreases. This leads to a lower force, friction or otherwise, required to break the particles down. The particles on the surface of the sample are therefore more easily broken off and are abrasively worn onto the surface of the static partner as well as filling the porosities present within the sample itself. The easier removal of ASW particles leads to the reduction in COF. Abrasive wear, which leads to two like materials sliding against each other, can also decrease the COF.

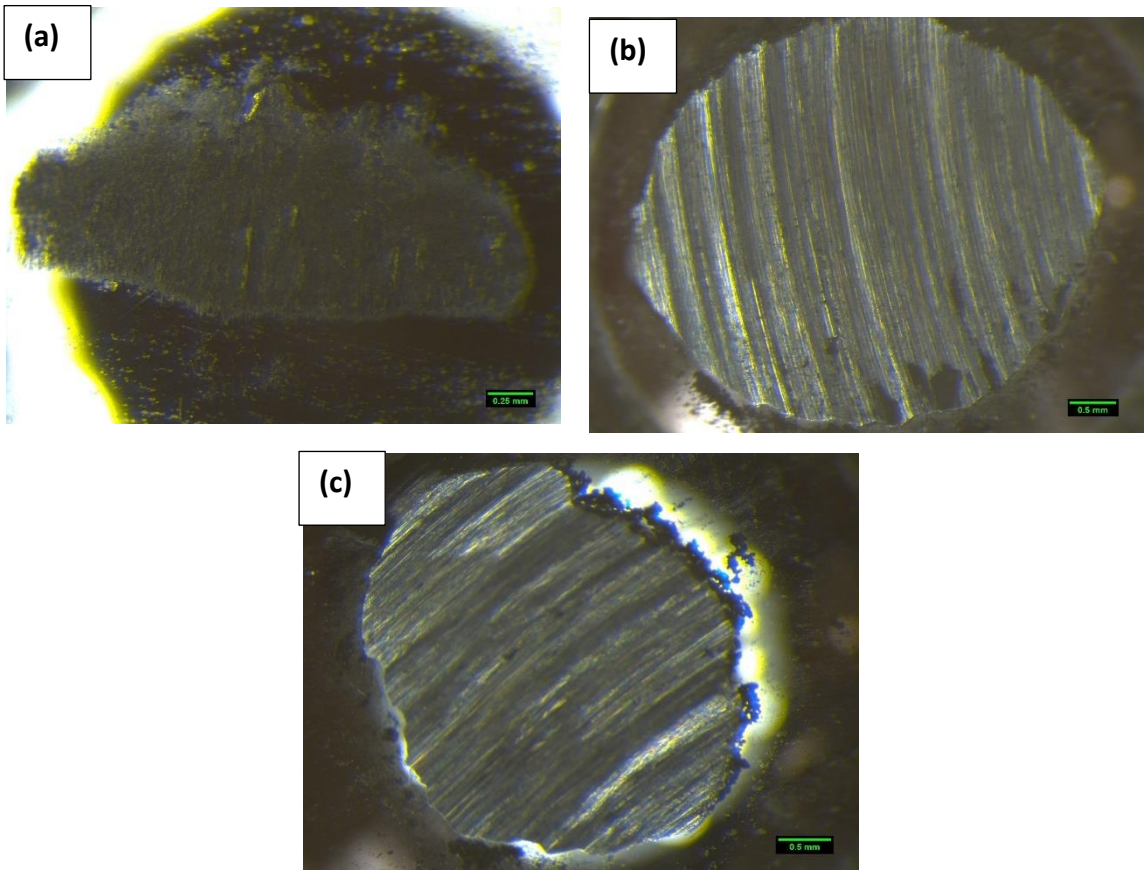

Figure 4-55: Micrographs of static partners for (a) LH-ASF, (b) MH-ASF and (c) SH-ASF samples under dry sliding wear conditions

4.7.1.4 *Effect of T6 treatment*

Figure 4-56 compares the development of COF as a function of sliding distance for the T6 treated and non-T6 treated ASW syntactic foam samples in dry sliding wear conditions. Table 4-31 provides average COF values for the T6 treated samples. The average COF results indicate a similar trend as to what was observed for the non-T6 treated syntactic foams, where the samples with larger ASW particles have a higher COF. However, the development of the COF is significantly different primarily due to the hardened Al matrix. For all samples, there is an initial sharp increase in COF at sliding distances of less than 50m, followed by a sudden drop and a low constant beyond 50m of sliding distance.

The change in behaviour from non-T6 treated to the T6 treated samples, i.e. the decrease beyond the initial sharp increase in COF is due to the hardening of the Al alloy, which results in a decrease in specific wear and COF (Sondur, Mallapur and Udupa, 2018). The development of other refined phases due to the presence of Si in the sample because of reactions in the interface can also lead to an enhanced wear performance and a decrease in COF (Sharma, Nanda and Pandey, 2019).

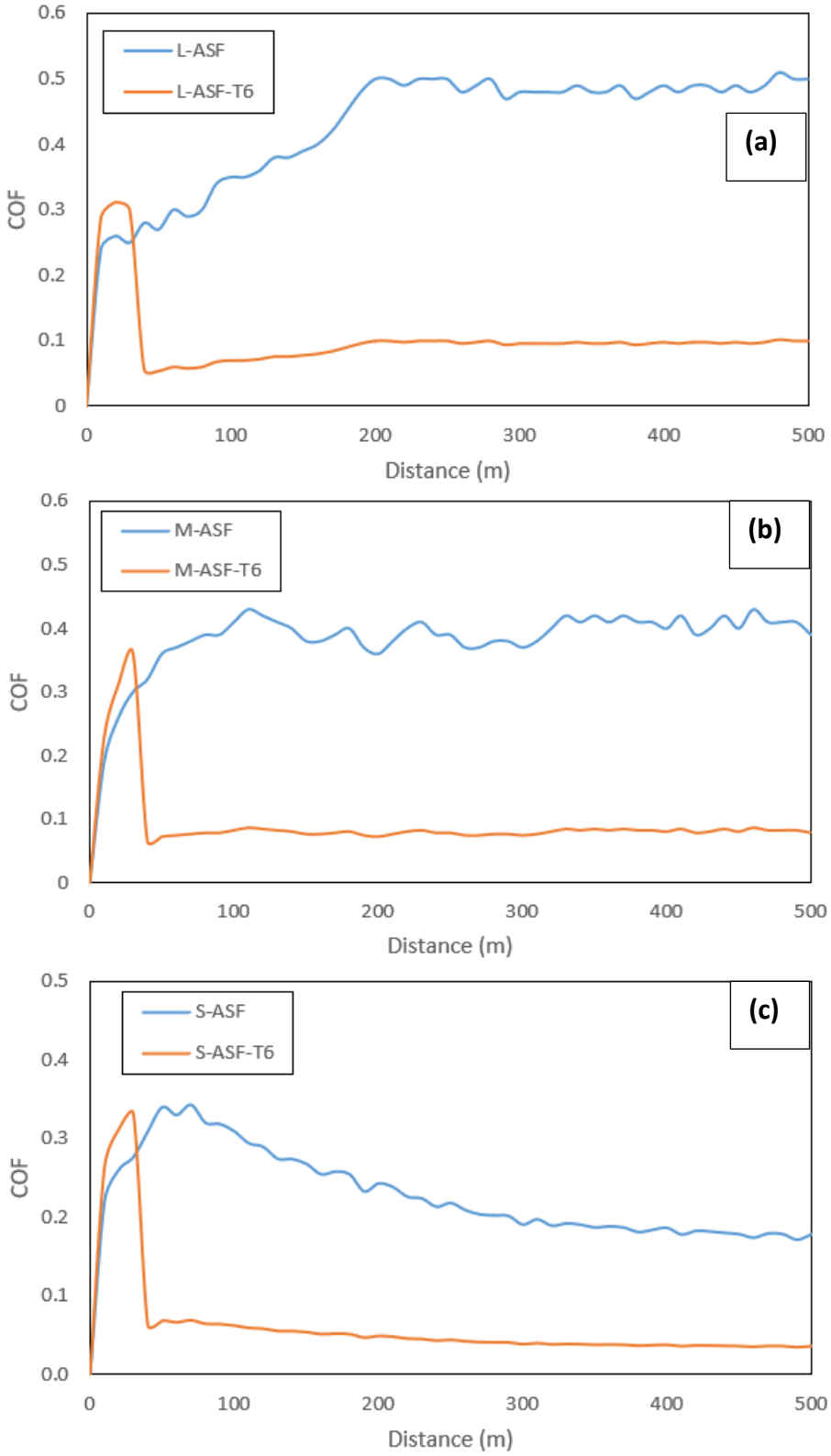

Figure 4-56: Comparison of COF development for T6 treated and non-T6 treated syntactic foam samples under dry sliding wear conditions

Table 4-31: Average COF for T6 treated ASW syntactic foam samples under dry sliding wear conditions

Sample ID	COF
L-ASF-T6	0.10
M-ASF-T6	0.09
S-ASF-T6	0.06

The wear track maps of the T6 treated ASW syntactic foam samples are shown in Figure 4-57. Table 4-32 summarizes the dry sliding wear parameters of the T6 treated samples. Each wear track shows an evenly worn surface, with less variability in height loss as the surface is worn when compared to the non-T6 treated samples.

The wear parameters show a similar correlation with particle size to the non-T6 treated syntactic foam samples, where the samples with larger ASW particles have lower wear resistance. Compared to the non-T6 treated syntactic foam samples, T6 treatment causes the Al matrix in the syntactic foam to harden, which results in an overall enhancement of wear resistance.

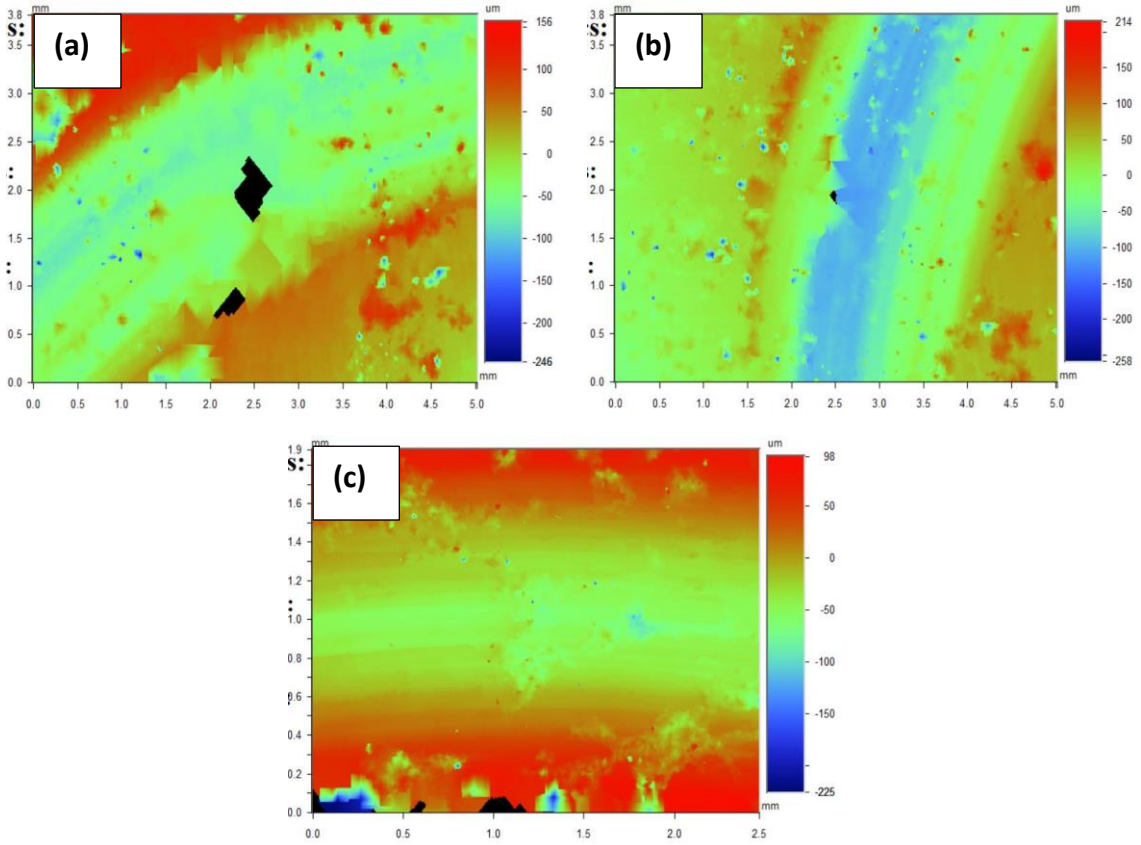

Figure 4-57: Wear track maps for (a) L-ASF-T6, (b) M-ASF-T6 and (c) S-ASF-T6 samples under dry sliding wear conditions

Table 4-32: Summary of dry sliding wear parameters of T6 treated ASW syntactic foam samples

Sample ID	Track depth (mm)	Track width (mm)	ΔRa ($x10^{-3}$) mm)	ΔRz ($x10^{-3}$) mm)	Weight loss (g)	Specific wear ($mm^3\ m^{-1}$)
LH-ASF-T6	0.055-0.177	5.94	2.02	15.00	0.05	0.012
MH-ASF-T6	0.035-0.164	5.60	8.45	19.53	0.04	0.008
SH-ASF-T6	0.048-0.115	5.30	15.22	25.20	0.03	0.006

The micrographs of the worn surfaces of the T6 treated ASW syntactic foam samples are shown in Figure 4-58. The wear track for all the samples is worn evenly throughout the surface. The main difference between the samples is in the amount of delamination and oxidative wear visible on the surface, with the larger particle size samples show features indicative of greater delamination and oxidative wear. All track surfaces are effectively covered with ASW particles and a very small and decreasing presence of delamination is visible on the surface as particle size decreases. The hardening of the Al matrix in the syntactic foam causes an initial increase in the frictional force, which is high enough to cause plastic deformation on the surface and allows debris to break off (Sondur, Mallapur and Udupa, 2018).

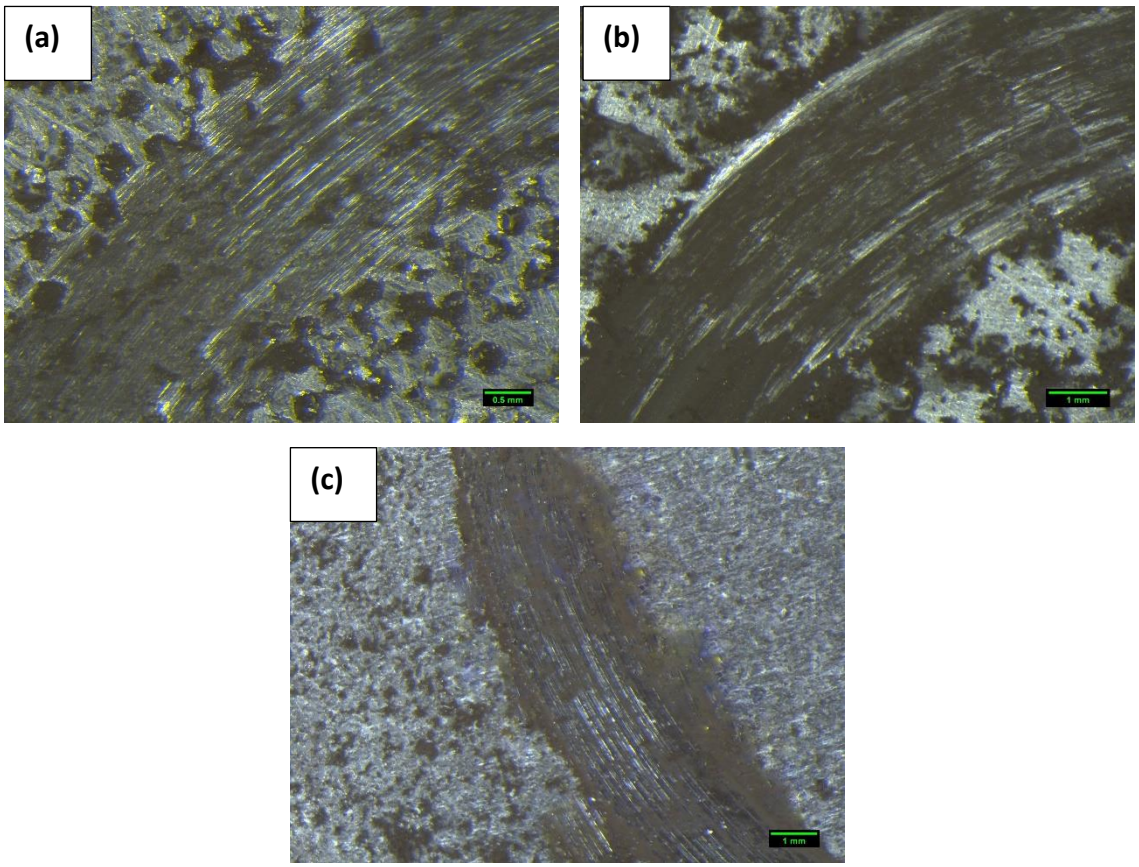

Figure 4-58: Micrographs of worn surfaces for (a) L-ASF-T6, (b) M-ASF-T6 and (c) S-ASF-T6 samples under dry sliding wear conditions

Figure 4-59 displays micrographs of their static partners after dry sliding wear tests. They show evenly worn surfaces with circular cross-sections. Some areas of the static partners show the presence of particles that have broken off from the surface of the syntactic foam samples, indicative of abrasive wear for all samples. The debris attached to the surface of the steel ball lead to slipping action, and some get deposited further along on the track. This also leads to a further reduction in the COF. These areas are more evident as the particle size decreases, which explains the larger decrease in COF in the S- and M- samples.

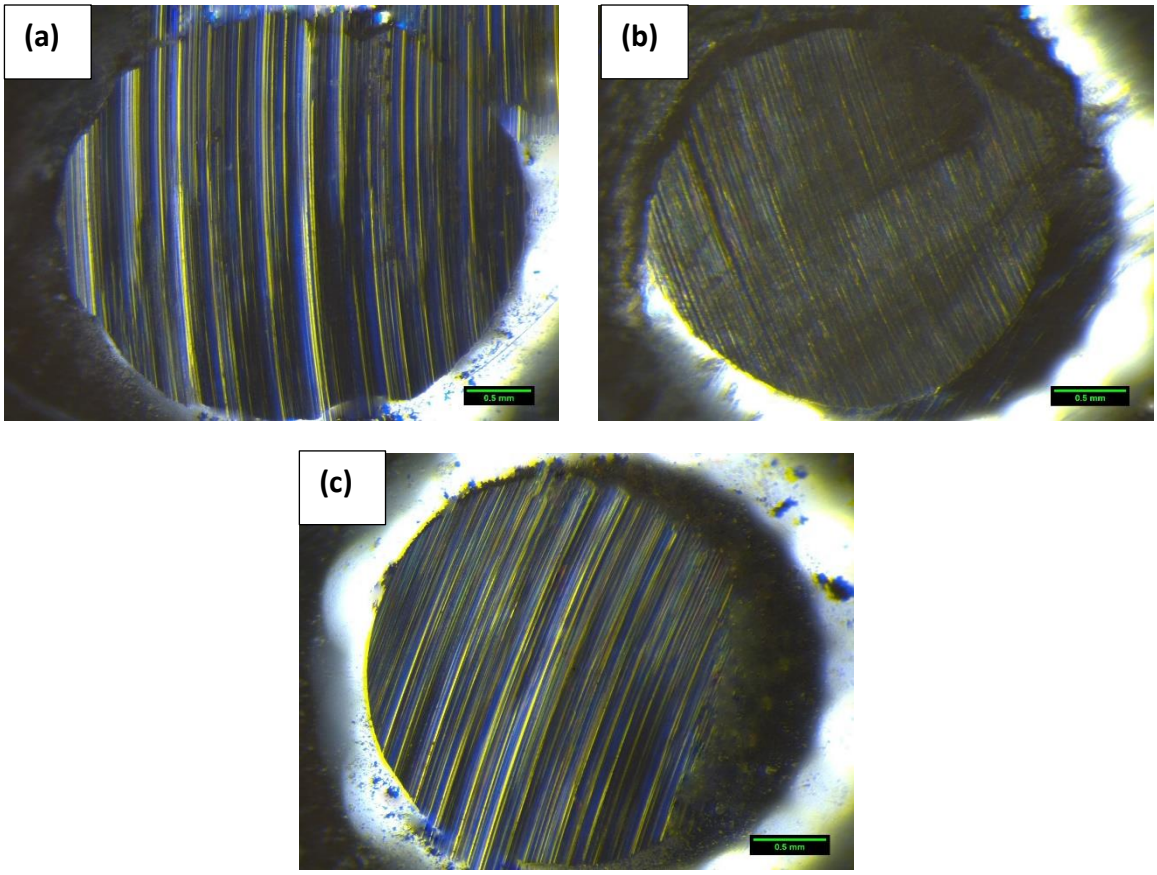

Figure 4-59: Micrographs of static partners for (a) L-ASF-T6, (b) M-ASF-T6 and (c) S-ASF -T6 samples under dry sliding wear conditions

4.7.1.5 *Comparison with E-sphere syntactic foam*

Figure 4-60 compares the development of COF as a function of sliding distance under dry sliding wear conditions for the ASW and E-sphere syntactic foam samples. The curve of the E-sphere syntactic foam sample shows three distinct regions: an initial sharp increase in COF as sliding distance increases, followed by a rapid decrease and finally a very slow gradual decrease as sliding distance increases. The initial sharp increase is also observed in the ASW syntactic foam samples, however the other two regions are different. The weaker E-sphere particles, compared to the ASW particles, on the surface of the syntactic foam sample get more easily plastically deformed. This leaves the static partner to slide against largely open pores, reducing the contact area and decreasing the COF. The gradual decrease in COF is due to continuous deformation of E-sphere particles and reductions in contact area.

Table 4-33 provides the average COF values of the ASW and E-sphere syntactic foam samples. The ASW syntactic foam samples have a higher COF than the E-sphere syntactic foam sample. The lower value for the E-sphere syntactic foam can be attributed to the increased porosity, which allows for a lower contact area as the surface as worn.

Table 4-33: Comparison of average COF for ASW and E-sphere syntactic foam samples under dry sliding wear conditions

Sample ID	COF
L-ASF	0.48
M-ASF	0.39
S-ASF	0.19
E-Sphere	0.04

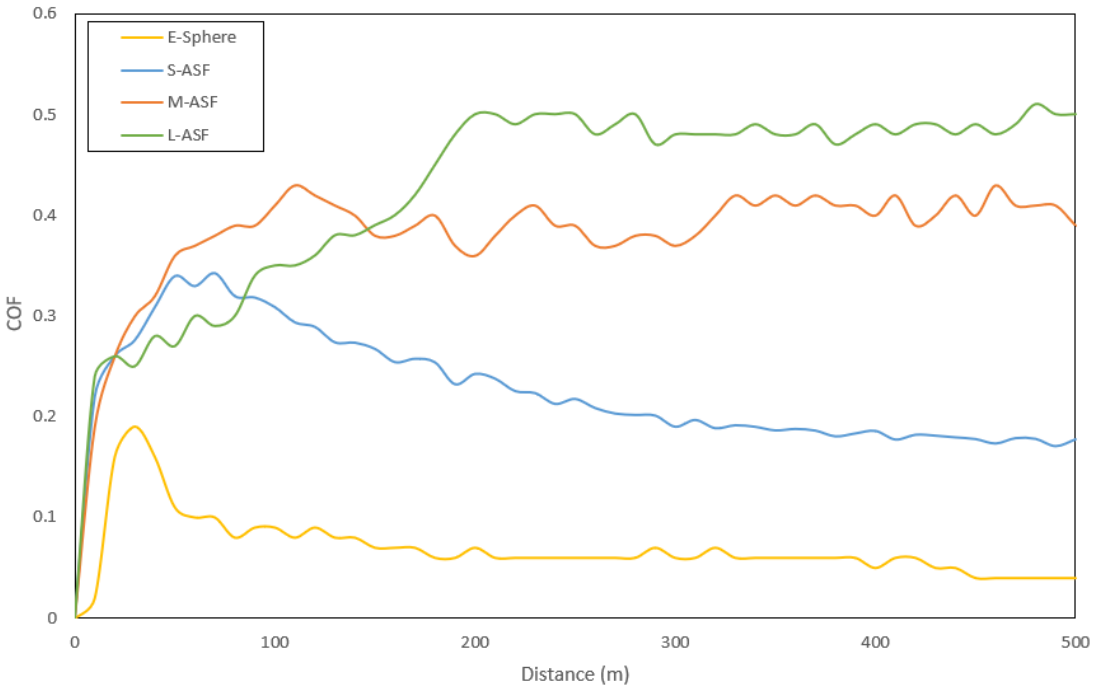

Figure 4-60: Comparison of COF development vs sliding distance for ASW and E-sphere syntactic foam samples under dry sliding wear conditions

Figure 4-61 displays the wear track map, a micrograph of the worn surface and a micrograph of the static partner for the E-sphere syntactic foam sample after dry sliding wear tests. The track is worn evenly throughout the surface of the sample. It is similar to the worn tracks of the ASW syntactic foam samples. The static partner is unevenly worn, with an irregular wear surface and a significant amount of abrasive wear. As sliding distance increases, some pieces of the E-sphere particles are broken off and are carried by the static partner due to the applied sliding force. Some of these are later deposited in the open pores on the surface of the syntactic foam sample, while others stay attached on the static partner. This leads to the lower COF values observed and recorded during the run of the experiment.

Table 4-34 summarizes the dry sliding wear parameters of the ASW and E-sphere syntactic foam samples. The E-sphere syntactic foam has a superior wear resistance than the L-ASF sample, but is inferior to the M-ASF and S-ASF samples, as seen in the differences in track depth and specific wear. It also has a higher ΔRa but a lower ΔRz. This shows that the surface of the E-sphere syntactic foam sample is overall rougher (higher ΔRa) but is also more even (lower ΔRz) than those of the ASW syntactic foam samples. The E-sphere syntactic foam sample loses more weight during the run of the experiment. This may be due to broken particles coming out as debris, which is not observed for the ASW syntactic foam samples. There is also a difference in densities between the E-sphere particles and the ASW particles, as shown in Section 4.1, which results in the lower specific wear.

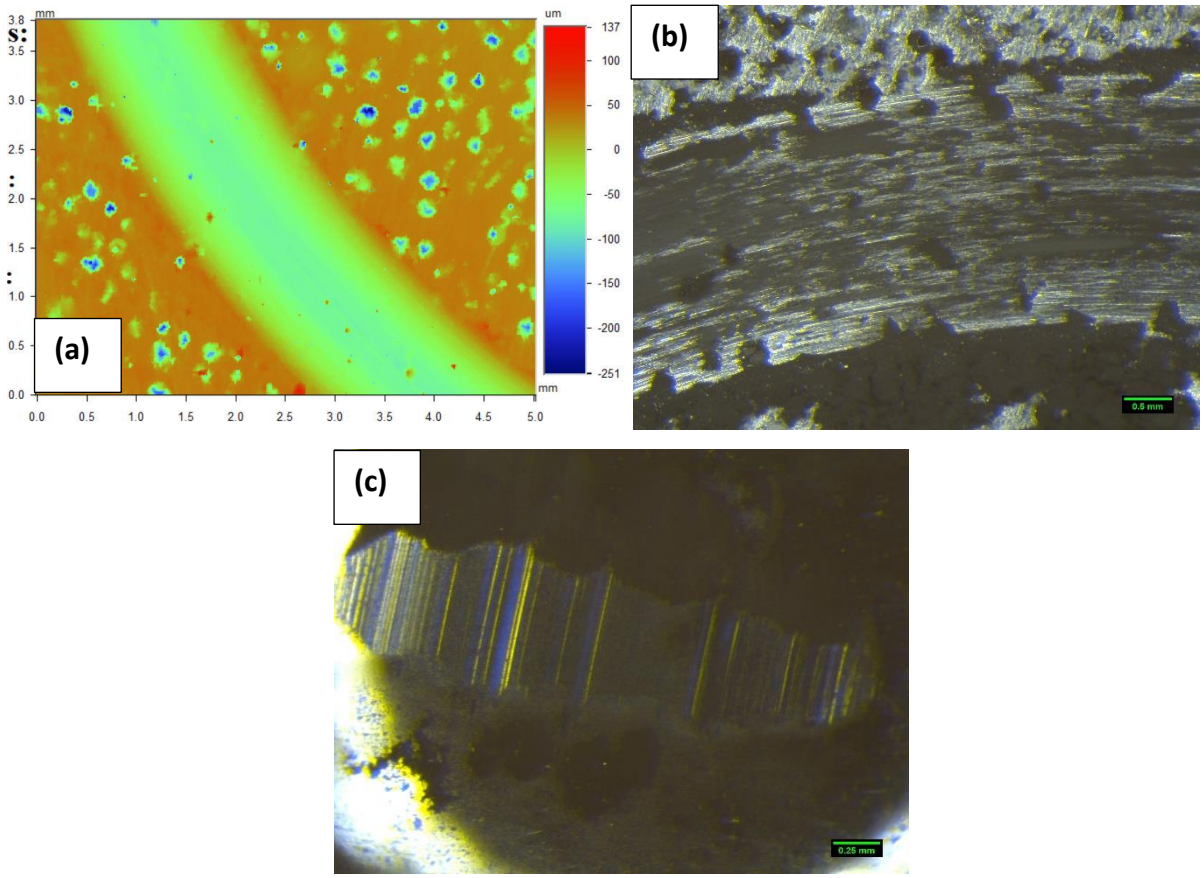

Figure 4-61: Micrographs of (a) wear track analysis map, (b) worn surface, and (c) static partner for E-sphere syntactic foam samples under dry sliding wear conditions

Table 4-34: Summary of dry sliding wear parameters of ASW and E-sphere syntactic foam samples

Sample ID	Track depth (mm)	Track width (mm)	ΔRa ($x10^{-3}$ mm)	ΔRz ($x10^{-3}$ mm)	Weight loss (g)	Specific wear ($mm^3\ m^{-1}$)
L-ASF	0.143-0.161	5.84	19.57	52.52	0.08	0.020
M-ASF	0.061-0.125	5.70	23.54	68.08	0.06	0.015
S-ASF	0.058-0.118	5.34	28.85	78.55	0.06	0.014
E-Sphere	0.120-0.197	5.08	31.55	28.99	0.10	0.018

4.7.2 **Lubricated sliding wear behaviour**

4.7.2.1 *Coefficient of friction*

Figure 4-62 compares the development of COF for the ASW syntactic foam samples as a function of sliding distance under dry and lubricated conditions. Table 4-35 provides average COF values under lubricated sliding wear conditions. During lubricated sliding wear, each curve shows an initial increase in COF as the track is worn, followed by a slight drop and then almost immediately a steady COF with increasing sliding distance. Steady state is achieved sooner than in the dry sliding tests, due to the lubricant film present causing a slipping action on the surface of the sample, leading to a faster settling of COF. There is a significant decrease in COF when compared to the dry sliding tests. The values for different particle sizes are fairly close together as opposed to being evidently different from one another when compared to the dry sliding tests. This is because the lubricant effectively dictates the wear behaviour under these conditions and therefore negates the magnitude of the particle size effect on the COF. The marginal difference in the COF as particle size changes can be attributed to the contact surfaces, where there are more ASW particles present in the smaller particle size sample.

The film thickness was estimated using the following equation (Gohar and Rahnejat, 2008):

$$h_0 = 4\frac{\eta_0 UR}{P'} \tag{4.2}$$

Where h_0, η_0, U, R and P' are the minimum film thickness, fluid viscosity (75 Pa.s), speed (0.5 m/s), radius of static partner (0.0015m) and the load per unit length (3.3 N/m), respectively. h_0 was found to be 0.45 mm.

Table 4-35: Average COF for ASW syntactic foam samples under lubricated sliding wear conditions

Sample ID	COF
L-ASF	0.04
M-ASF	0.05
S-ASF	0.07

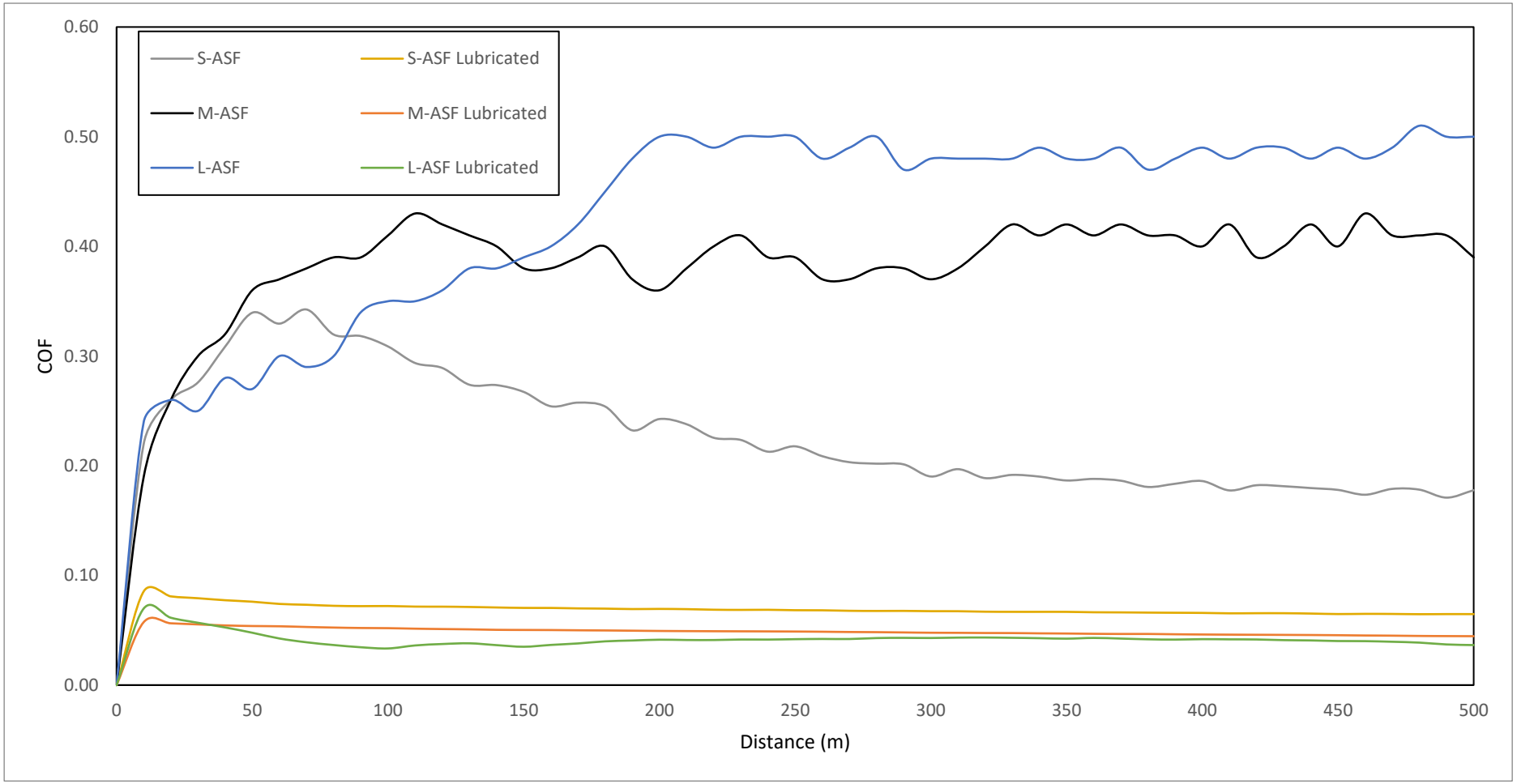

Figure 4-62: Comparison of COF development for ASW syntactic foam samples under dry and lubricated sliding wear conditions

4.7.2.2 *Wear track analysis*

The wear track maps of the ASW syntactic foam samples after lubricated wear tests are shown in Figure 4-63, with lines drawn to indicate the wear track. Table 4-36 summarizes the lubricated sliding wear parameters of the samples. The track depths are small under the lubricated sliding wear conditions when compared to the dry sliding wear conditions. The weight loss was not measurable using a scale. It was estimated from the specific wear value and therefore indicated with an asterix.

The track depths and weight losses observed in the samples are very similar to one another, with minute differences observed. The specific wear and differences in surface roughness increase with decreasing particle size. This is similar to what was observed under the dry sliding wear conditions, where the differences in surface roughness increased with decreasing particle size. This shows that regardless of the sliding wear test conditions, the wear behaviour is the same.

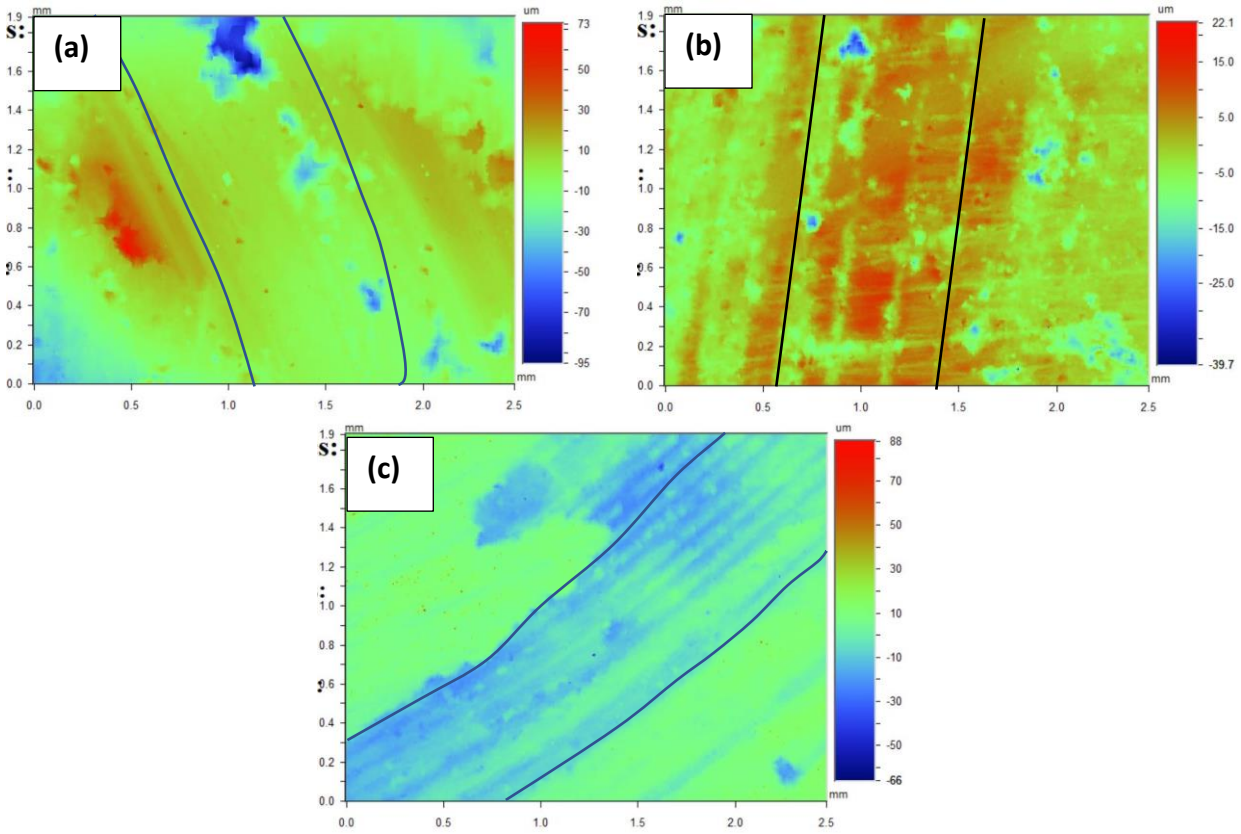

Figure 4-63: Wear track maps for (a) L-ASF, (b) M-ASF and (c) S-ASF samples under lubricated sliding wear conditions

Table 4-36: Summary of lubricated sliding wear parameters of ASW syntactic foam samples

Sample ID	Track depth (mm)	Track width (mm)	ΔRa ($x10^{-3}$ mm)	ΔRz ($x10^{-3}$ mm)	Weight loss (g)	Specific wear ($mm^3\ m^{-1}$)
L-ASF	0.001-0.045	3.36	1.92	4.94	0.006*	0.0011
M-ASF	0.012-0.034	2.86	2.74	12.53	0.010*	0.0018
S-ASF	0.018-0.037	2.48	8.78	12.56	0.014*	0.0026

The micrographs of the worn surfaces of the ASW syntactic foam samples after lubricated sliding wear tests are shown in Figure 4-64. The wear track for all samples is thinner than that seen under the dry sliding wear conditions. This is because the lubrication on the surface of the sample causes a slipping action that reduces the amount of wear occurring. The surface of the wear track is also more even and shows little presence of metal. The wear tracks of the L-ASF and M-ASF samples show some unbroken porous particles on the surface, indicated by arrows on the micrograph, which act as reservoirs and provide constant distribution of the lubricant. Along with the abrasive wear behaviour seen on the respective static partners, these factors contribute to the lower COF and specific wear compared to the dry sliding wear conditions.

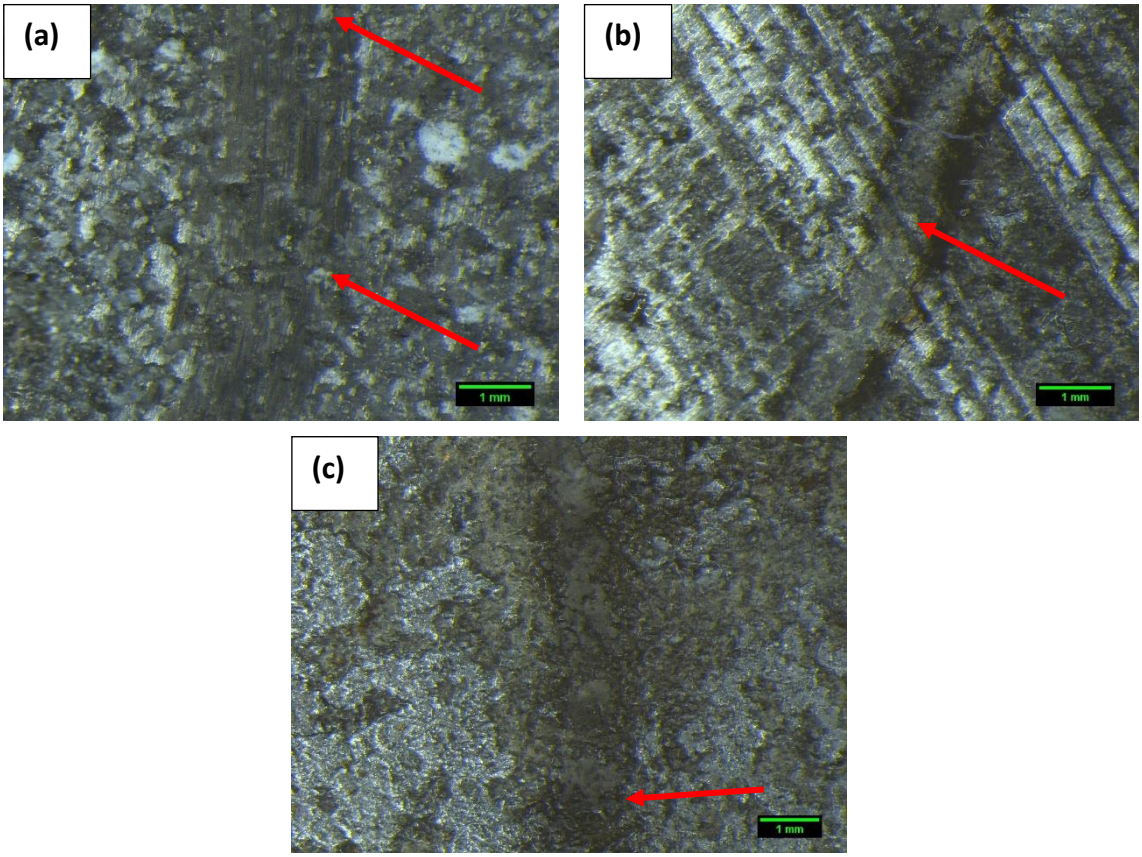

Figure 4-64: Micrographs of worn surfaces for (a) L-ASF, (b) M-ASF and (c) S-ASF samples under lubricated sliding wear conditions

Figure 4-64 displays micrographs of the static partners of the ASW/Al syntactic foam samples after the lubricated sliding wear tests. The micrographs for the S-ASF and M-ASF samples show a significant presence of abrasive wear. This is different from the dominant adhesive wear during dry sliding wear tests. There is also no evidence of delamination or oxidative wear. The change in wear type can be attributed partly to the lubricating effect and partly to the different testing conditions. The lubricant prevents excessive wear due to its slipping action, however it does carry debris lost from the surface of the sample. This debris can deposit onto the surface of the static

partner (Jha *et al.,* 2011; Májlinger *et al.,* 2016; Sondur, Mallapur and Udupa, 2018; Mofidi and Prakash, 2011). The high rotation speed and high applied force allow for the surface of the static partner to be worn more effectively.

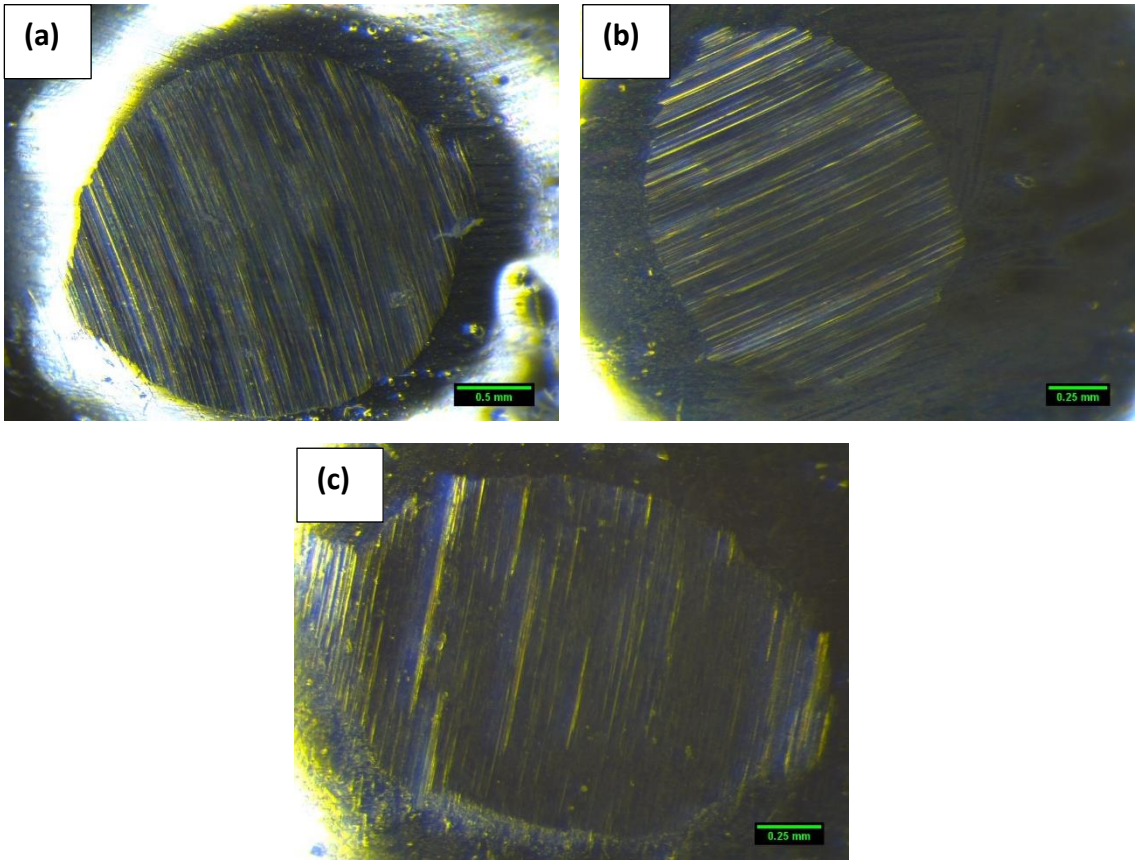

Figure 4-65: Micrographs of static partners for (a) L-ASF, (b) M-ASF and (c) S-ASF samples under lubricated sliding wear conditions

4.7.2.3 *Effect of heating ASW particles*

Figure 4-66 compares the development of COF as a function of sliding distance for the syntactic foam samples with heated and non-heated ASW particles under the lubricated sliding wear conditions. Like what was observed in dry sliding wear tests, there is little variation seen for the Small and Medium ASW particle size group samples and there is a small change in behaviour for the Large ASW particle size group sample. Table 4-37 provides average COF values for the syntactic foam samples with heated ASW particles. The COF averages are close to one another due to the lubrication used during the sliding wear tests.

The COF curves for all the samples show the same regions as their respective syntactic foam counterparts with non-heated ASW particles. There is an initial sharp increase in COF, followed by a steady state as the curve levels out with increasing sliding distance. The LH-ASF sample remains on a low COF as sliding distance increases, with minimal variations when compared to the development of COF for the L-ASF sample. This may be because of the decrease in strength upon heating of the ASW particles, leading to a decrease in frictional force required to cause surface deformation.

Table 4-37: Average COF for syntactic foam samples with heated ASW particles under lubricated sliding wear conditions

Sample ID	COF
LH-ASF	0.02
MH-ASF	0.04
SH-ASF	0.05

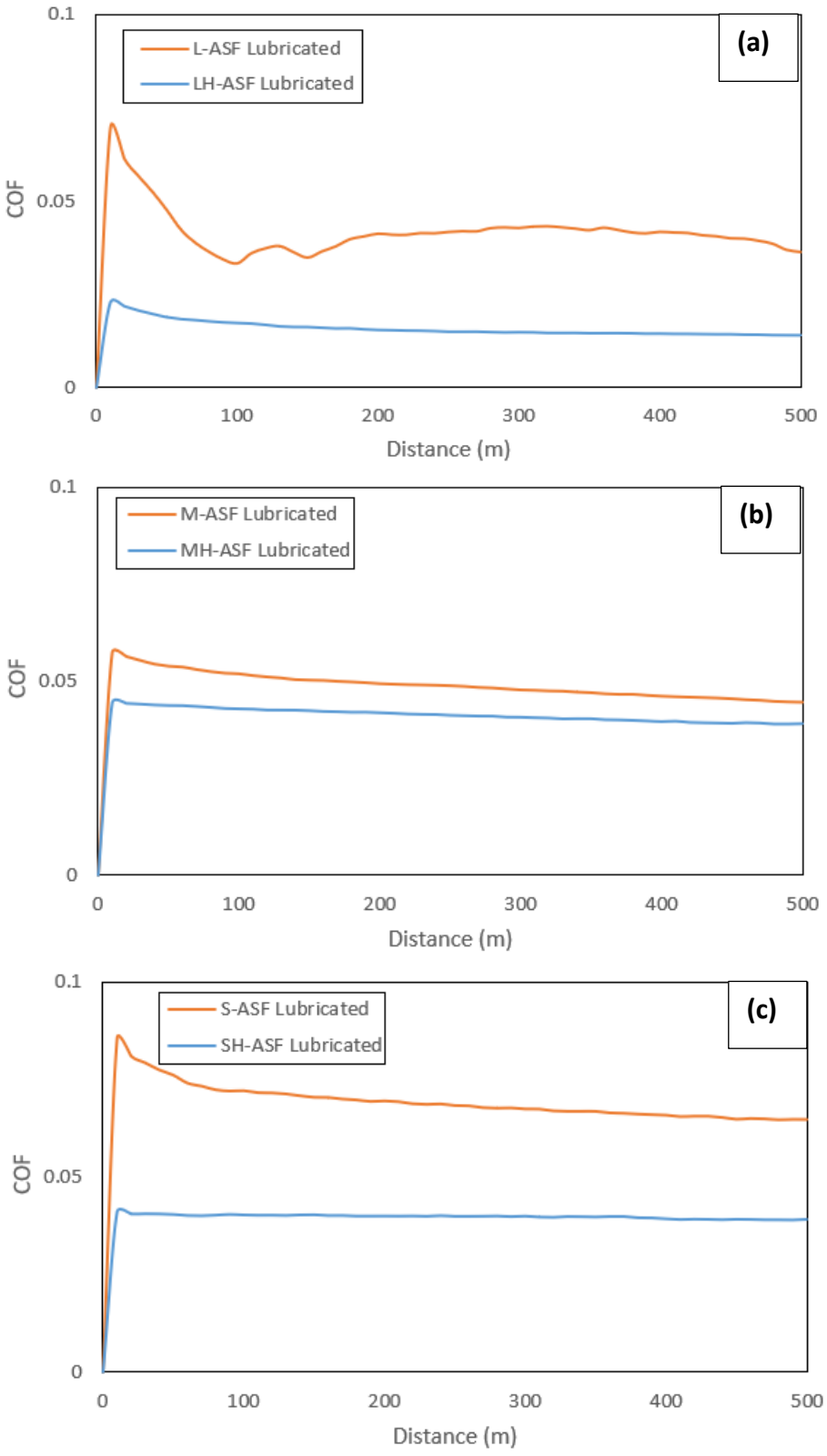

Figure 4-66: Comparison of COF development for syntactic foam samples with heated and non-heated ASW particles under lubricated sliding wear conditions

The wear track maps of the syntactic foam samples with heated ASW particles are shown in Figure 4-67. Table 4-38 summarizes their lubricated sliding wear parameters. The wear track depth and width are smaller than those of the same samples under the dry sliding test conditions. Lubrication of surfaces leads to an overall enhancement of wear properties, with lower specific wear values and smaller differences in surface roughness values regardless of ASW particle size.

The specific wear and surface roughness are sensitive to the particle size, with larger particle size group samples having lower specific wear and smaller differences in surface roughness. This is similar to what was observed under the dry sliding wear conditions, showing that regardless of the sliding wear test conditions, the wear behaviour is the same.

The LH-ASF sample shows lower track width, lower track depth and weight loss, lower surface roughness and a more enhanced specific wear than the L-ASF sample. There is very little change in the properties of Small and Medium syntactic foam samples with heated or non-heated ASW particles between lubricating and dry sliding wear test conditions. This behaviour is similar to what was observed in previous sections.

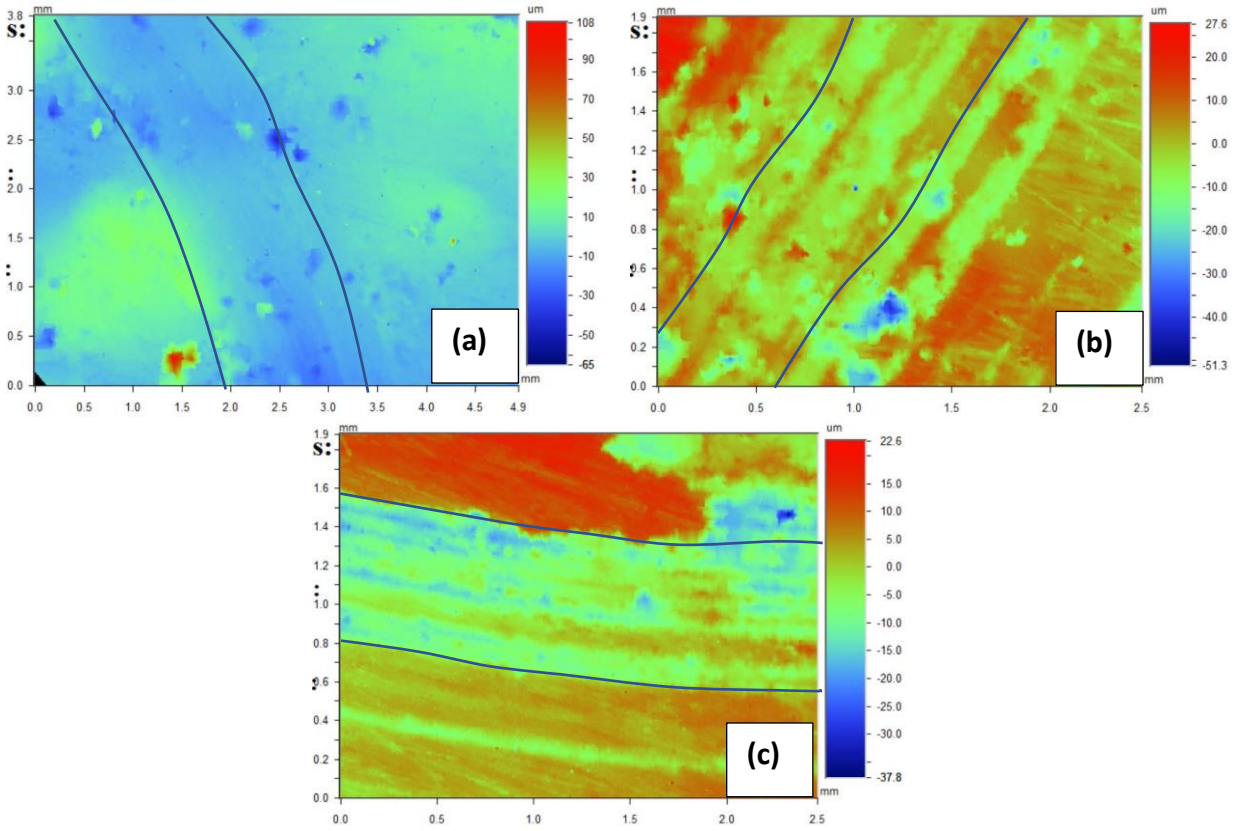

Figure 4-67: Wear track maps for (a) LH-ASF, (b) MH-ASF and (c) SH-ASF samples under lubricated sliding wear conditions

Table 4-38: Summary of lubricated sliding wear parameters of syntactic foam samples with heated ASW particles

Sample ID	Track depth (mm)	Track width (mm)	ΔRa ($x10^{-3}$) mm)	ΔRz ($x10^{-3}$) mm)	Weight loss (g)	Specific wear ($mm^3\ m^{-1}$)
LH-ASF	0.004-0.005	2.40	1.07	1.01	0.003*	0.0002
MH-ASF	0.002-0.016	2.80	1.10	11.74	0.008*	0.0016
SH-ASF	0.001-0.041	2.40	8.68	14.93	0.014*	0.0023

The micrographs of the worn surfaces of the syntactic foam samples with heated ASW particles after lubricated sliding wear tests are shown in Figure 4-68. Figure 4-69 displays micrographs of the respective static partners. There is minimal variability between syntactic foams with heated and non-heated ASW particles for the Medium and Small samples, as was also observed under dry sliding wear conditions. The wear type for the L-ASF sample is however more adhesive than abrasive with heated ASW particles. This transition explains the enhanced wear properties of the LH-ASF sample compared to the L-ASF sample under the lubricated sliding wear conditions.

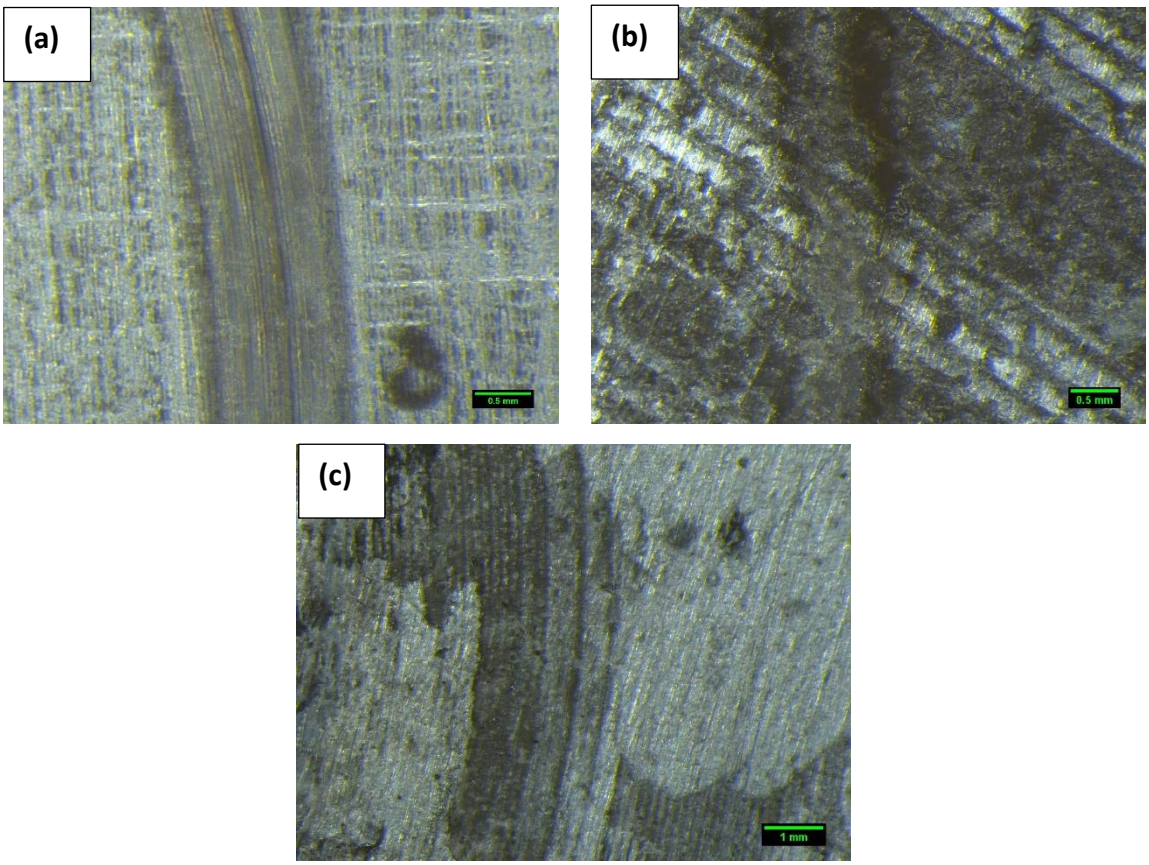

Figure 4-68: Micrographs of worn surfaces for (a) LH-ASF, (b) MH-ASF and (c) SH-ASF samples under lubricated sliding wear conditions

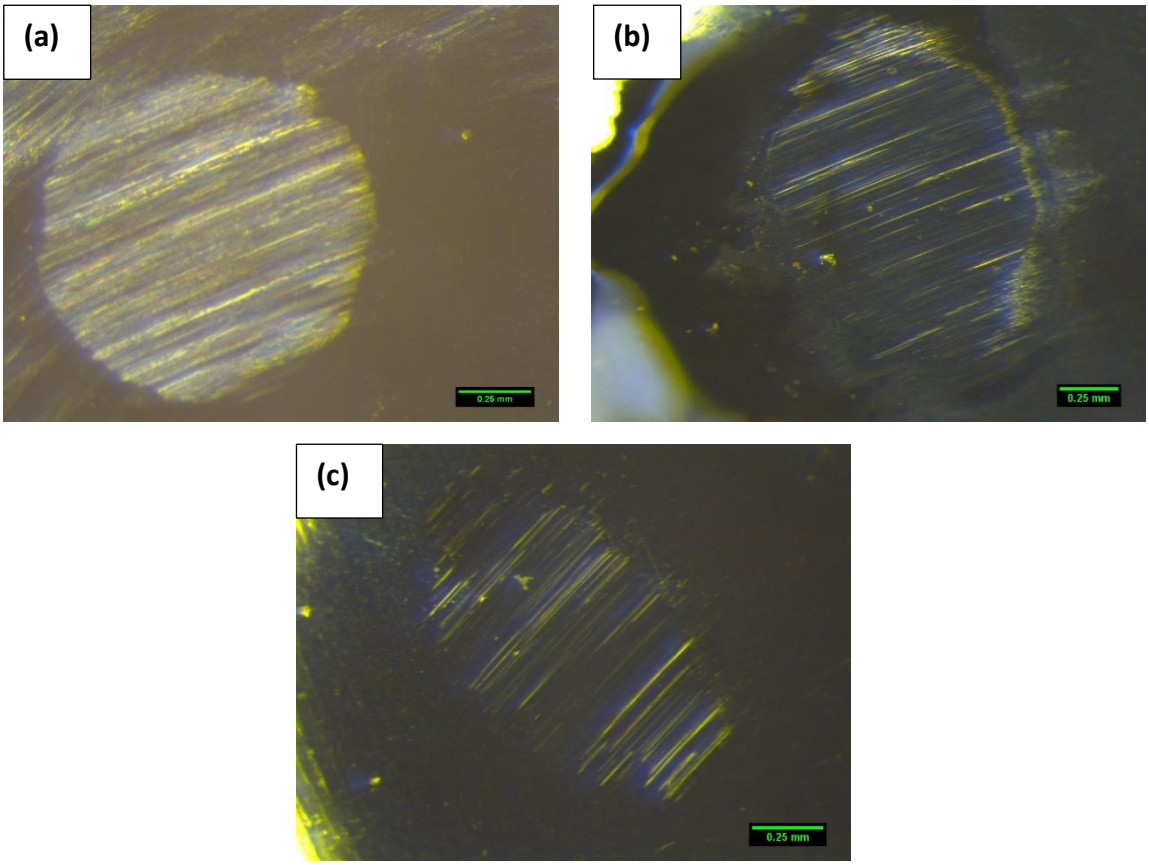

Figure 4-69: Micrographs of static partners for (a) LH-ASF, (b) MH-ASF and (c) SH-ASF samples under lubricated sliding wear conditions

4.7.2.4 *Effect of T6 treatment*

Figure 4-70 compares the development of COF as a function of sliding distance for the T6 treated and non-T6 treated ASW syntactic foam samples in lubricated sliding wear conditions. The curves for the T6 treated samples show three distinct regions: an initial sharp increase in COF as sliding distance increases, followed by a sudden decrease in COF and a final steady state achieved as sliding distance keeps increasing. These regions are largely similar to what was observed on the curves for the non-T6 treated syntactic foam samples under the dry conditions. The sharper increase and decrease in COF before achieving steady state for the T6 treated samples is due to the increase in hardness of the Al matrix.

Table 4-39 provides the average COF values for the T6 treated ASW syntactic foam samples. Overall, the same trend is observed as with non-T6 treated syntactic foam samples under the lubricated conditions, where the larger the particles, the lower the COF. T6 treatment also leads to a lower overall COF under the lubricated conditions, which is similar to what was observed under the dry sliding wear conditions. For any given sample, lubrication leads to an overall decrease in the average COF, which is the same as for other samples discussed above.

Table 4-39: Average COF for T6 treated ASW syntactic foam samples under lubricated sliding wear conditions

Sample ID	COF
L-ASF-T6	0.010
M-ASF-T6	0.012
S-ASF-T6	0.015

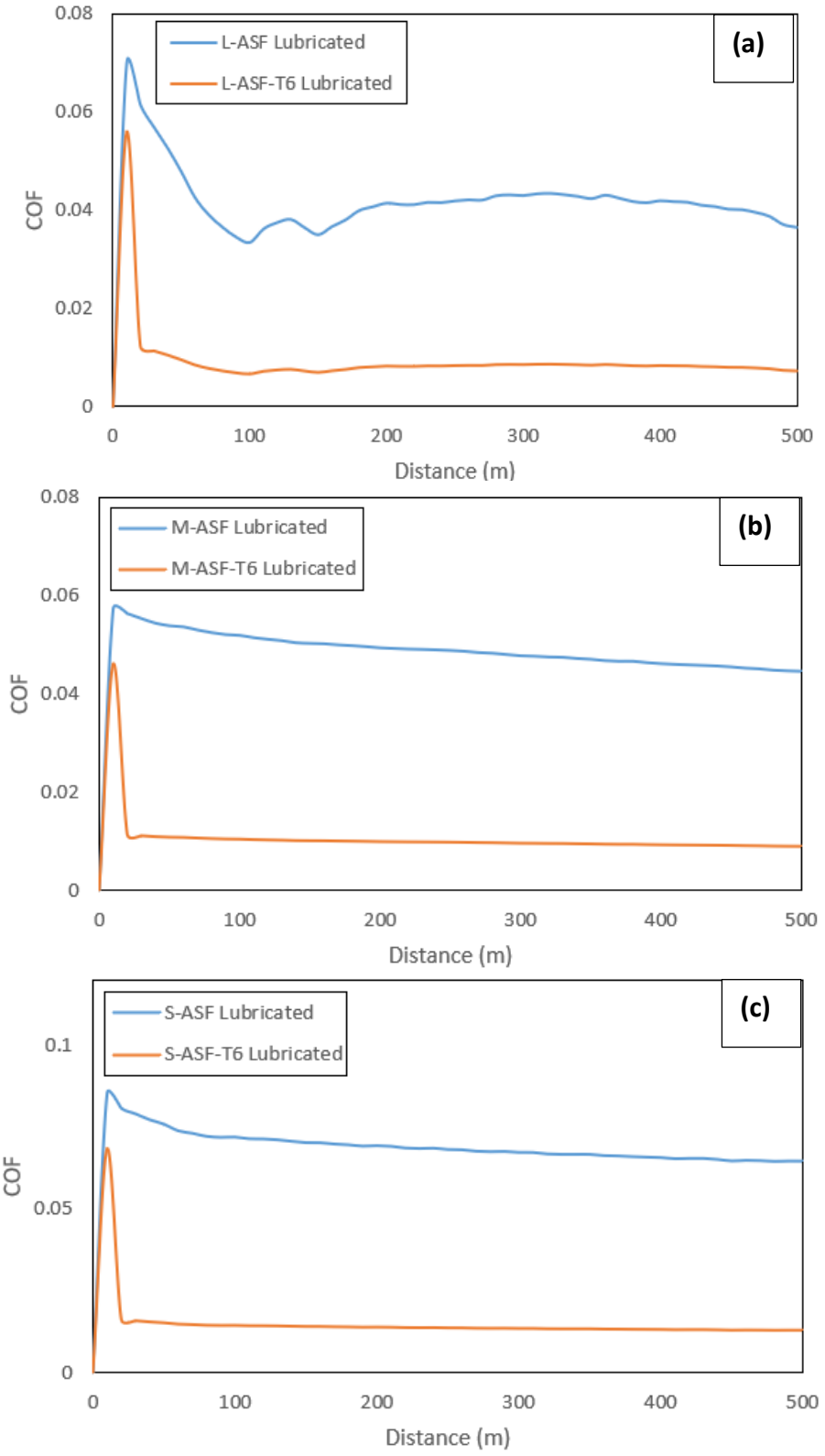

Figure 4-70: Comparison of COF development for T6 treated and non-T6 treated ASW syntactic foams under lubricated sliding wear conditions

The wear track maps of the T6 treated ASW syntactic foam samples are shown in Figure 4-71. Table 4-40 summarizes the lubricated sliding wear parameters of these samples. The wear track depth and width are smaller than those of the same samples under the dry sliding test condition. The wear parameters show that, like the non-T6 treated syntactic foam samples under the lubricated condition, the samples with larger ASW particles have an enhanced wear resistance. T6 treatment causes the Al metal to harden in the syntactic foam and results in an overall enhancement of wear resistance compared to the non T6-treated samples.

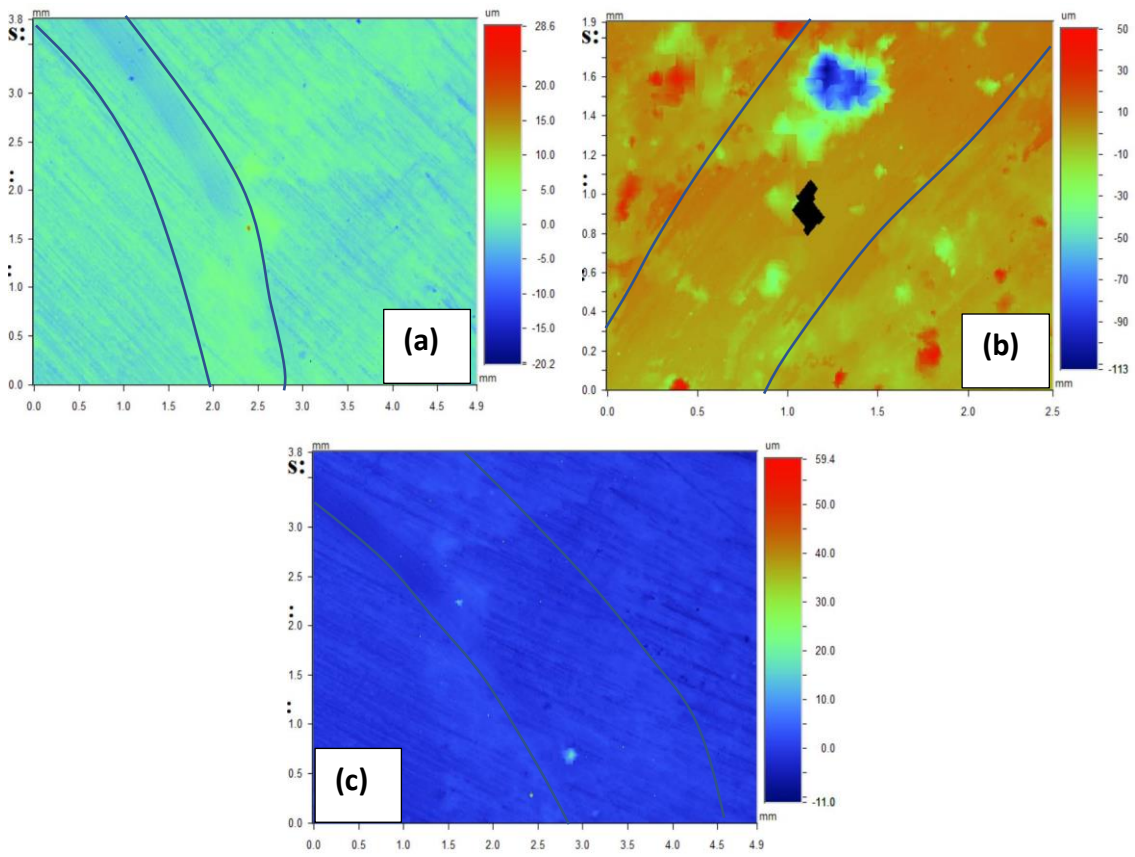

Figure 4-71: Wear track maps for (a) L-ASF-T6, (b) M-ASF-T6 and (c) S-ASF-T6 samples under lubricated sliding wear conditions

Table 4-40: Summary of lubricated sliding wear parameters of T6 treated ASW syntactic foam samples

Sample ID	Track depth (mm)	Track width (mm)	ΔRa ($x10^{-3}$) mm)	ΔRz ($x10^{-3}$) mm)	Weight loss (g)	Specific wear ($mm^3\ m^{-1}$)
L-ASF-T6	0.005-0.025	5.04	1.25	2.25	0.003*	0.0002
M-ASF-T6	0.012-0.034	3.12	4.87	5.25	0.004*	0.0005
S-ASF-T6	0.018-0.045	2.06	12.22	15.52	0.005*	0.0009

The micrographs of the worn surfaces of the T6 treated ASW syntactic foam samples are shown in Figure 4-72. The wear track for all the samples is even and worn equally throughout the surface and gets less evident as the particle size decreases. The T6 treated samples show significant presence of oxidative wear, which decreases as particle size decreases. The track surface is effectively covered with ASW particles, with a very small presence of metal on the surface, which is similar to the observations made for these samples after dry sliding wear tests. The hardening of the Al present in the syntactic foam causes a significant increase in the frictional force, which causes more wear on the surface when compared to the non-T6 treated samples. The debris gets attached to the surface of the steel ball, leading to slipping action. Some of it gets deposited further along on the track, leading to a further reduction in the COF.

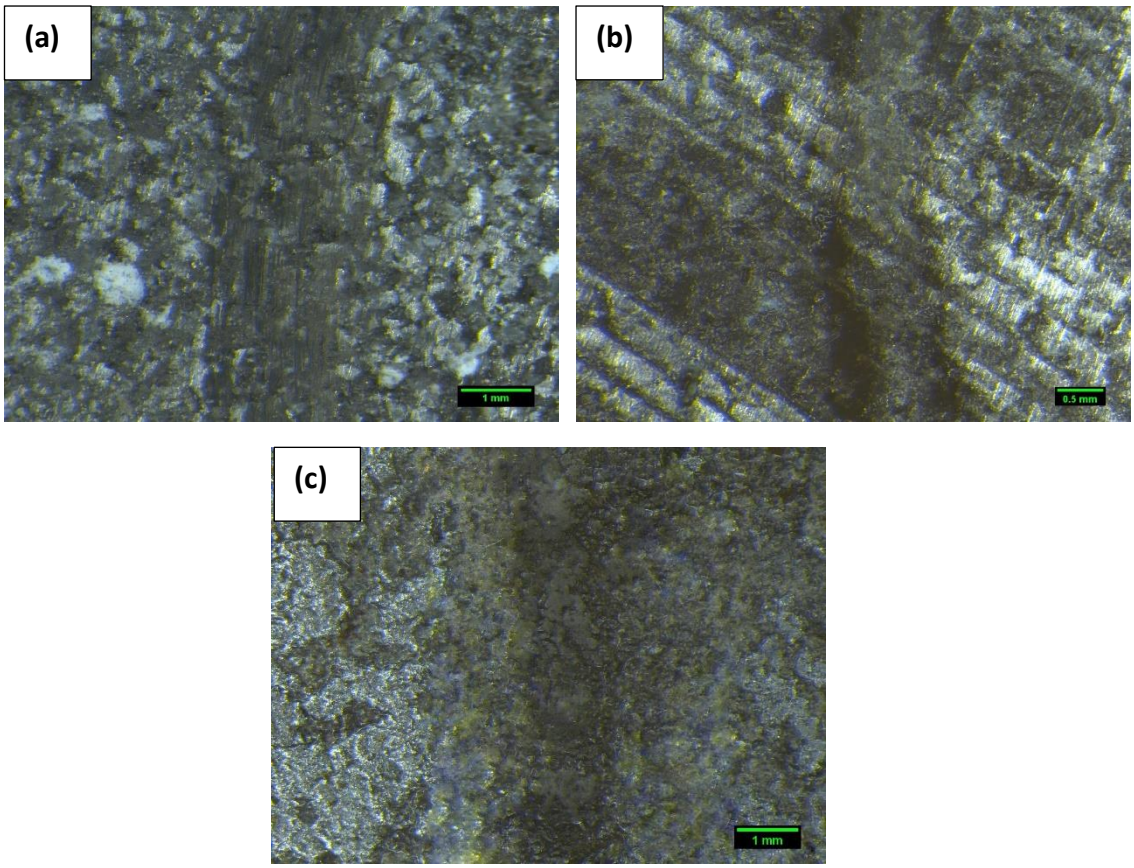

Figure 4-72: Micrographs of worn surfaces for (a) L-ASF-T6, (b) M-ASF-T6 and (c) S-ASF-T6 samples under lubricated sliding wear conditions

Figure 4-73 displays micrographs of their static partners after lubricated sliding wear tests. The micrographs show an unevenly worn surface with a relatively circular cross section. There is a significant presence of debris, indicating the abrasive nature of the wear. The abrasive wear behaviour is due to the lubrication effect, as observed in the non-T6 treated syntactic foam samples.

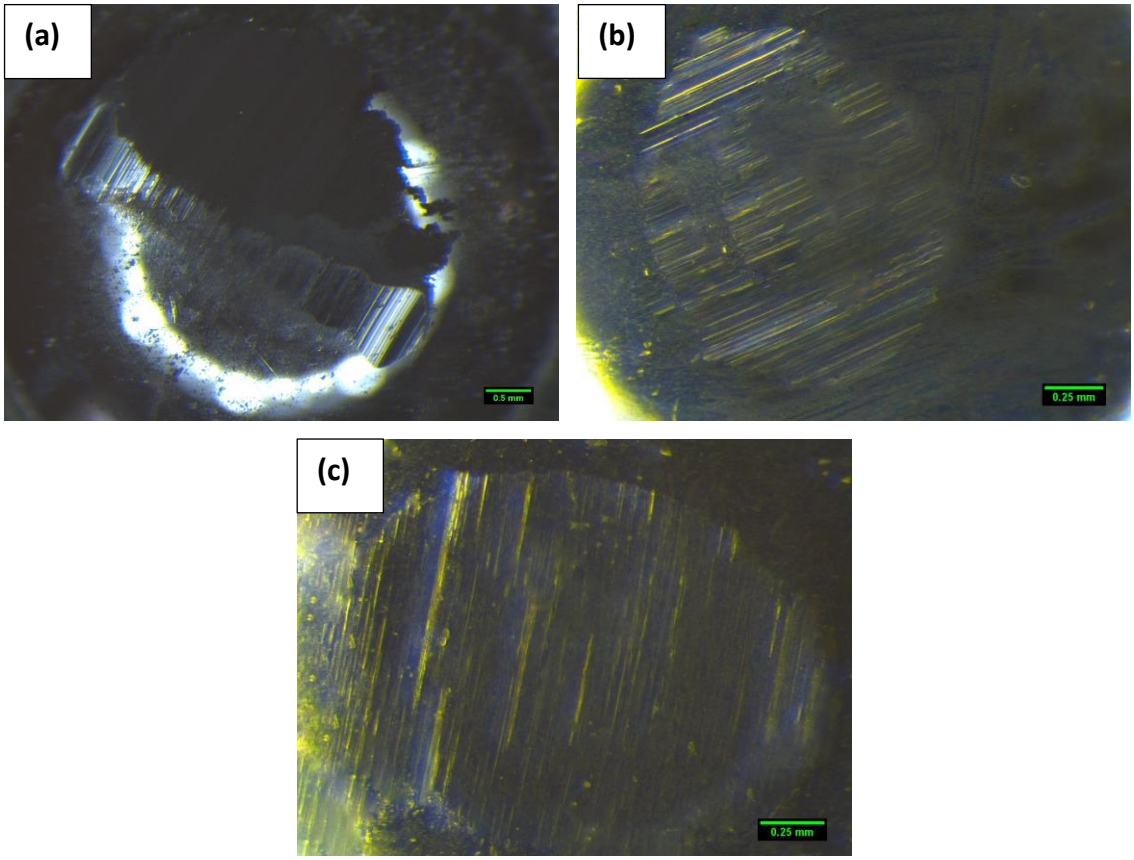

Figure 4-73: Micrographs of static partners for (a) L-ASF-T6, (b) M-ASF-T6 and (c) S-ASF-T6 samples under lubricated sliding wear conditions

4.7.2.5 *Comparison with E-sphere syntactic foams*

Figure 4-74 compares the development of COF as a function of sliding distance for the ASW and E-sphere syntactic foam samples under the lubricated condition. The E-sphere syntactic foam sample shows the same regions as the ASW syntactic foam samples, where an initial sharp increase in COF is followed by a steady state with lower variability as the sliding distance increases. The steady state is achieved much sooner than for the ASW syntactic foam samples and much sooner than for the E-sphere syntactic foam sample under the dry sliding wear condition.

Table 4-41 provides average COF values for all samples. In dry sliding wear condition, the E-sphere syntactic foam sample showed a significantly different average COF from those of the ASW syntactic foam samples. Under the lubricated condition, however, the difference is less evident. It seems lubrication dictates the wear behaviour and levels out many of the differences in morphology and composition, resulting in very similar properties between the E-sphere and ASW syntactic foam samples.

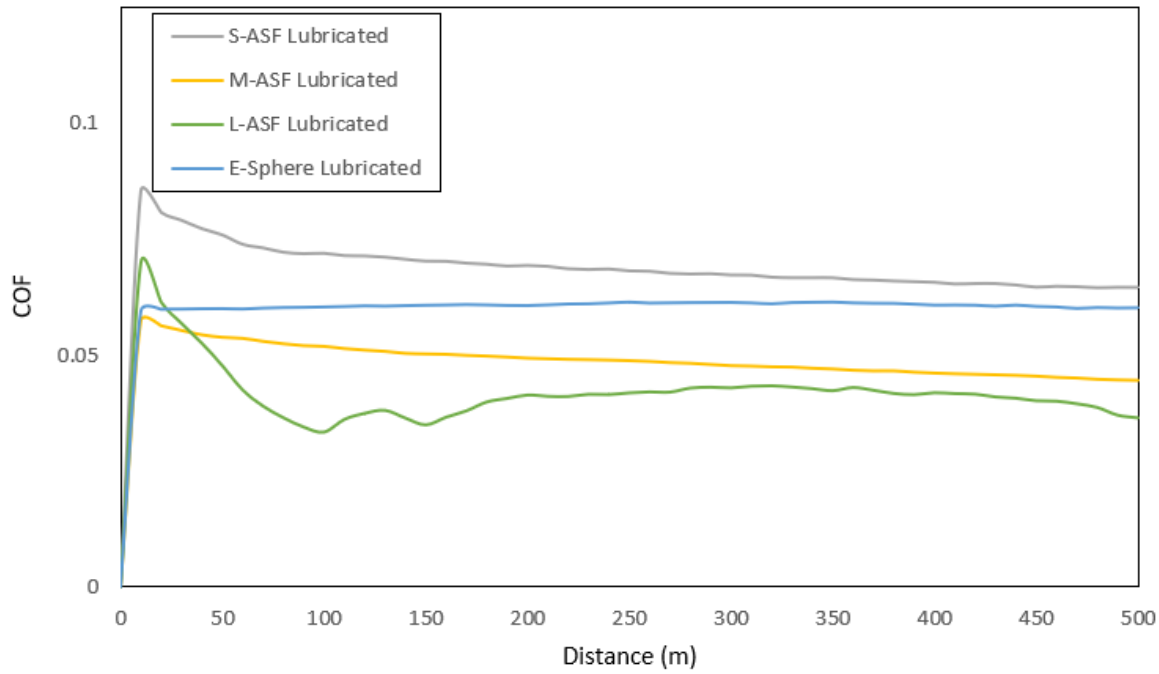

Figure 4-74: Comparison of COF development vs sliding distance for ASW and E-sphere syntactic foam samples under lubricated sliding wear conditions

Table 4-41: Comparison of average COF for ASW and E-sphere syntactic foam samples under lubricated sliding wear conditions

Sample ID	COF
L-ASF	0.04
M-ASF	0.05
S-ASF	0.07
E-Sphere	0.05

Figure 4-75 displays the wear track map, a micrograph of the worn surface and a micrograph of the static partner for the E-sphere syntactic foam sample after the lubricated sliding wear test. Table 4-42 summarizes the lubricated sliding wear parameters of the ASW and E-sphere syntactic foam samples. The wear track depth and width are smaller than those of the same samples under the dry sliding test condition.

The wear track is very small, with the presence of open particles on the surface. These particles act as lubricant reservoirs and allow for the even distribution of the lubricant during sliding wear tests. This phenomenon was also observed in ASW syntactic foam samples in the lubricated sliding wear tests.

The static partner shows an unevenly worn surface, with indications of abrasive wear. The extent of abrasive wear is lower than for the static partner under the dry sliding wear condition. This is due to both the slipping action of the lubricant and the lower amount of material in direct contact with the static partner. The porous particles in the E-sphere sample behave in the same way as those in the ASW/Al syntactic foam samples. However, since there are some hollow particles in the E-sphere syntactic foam sample as described in Chapter 3, there is minimal contact left for these particles once the outer shell is broken.

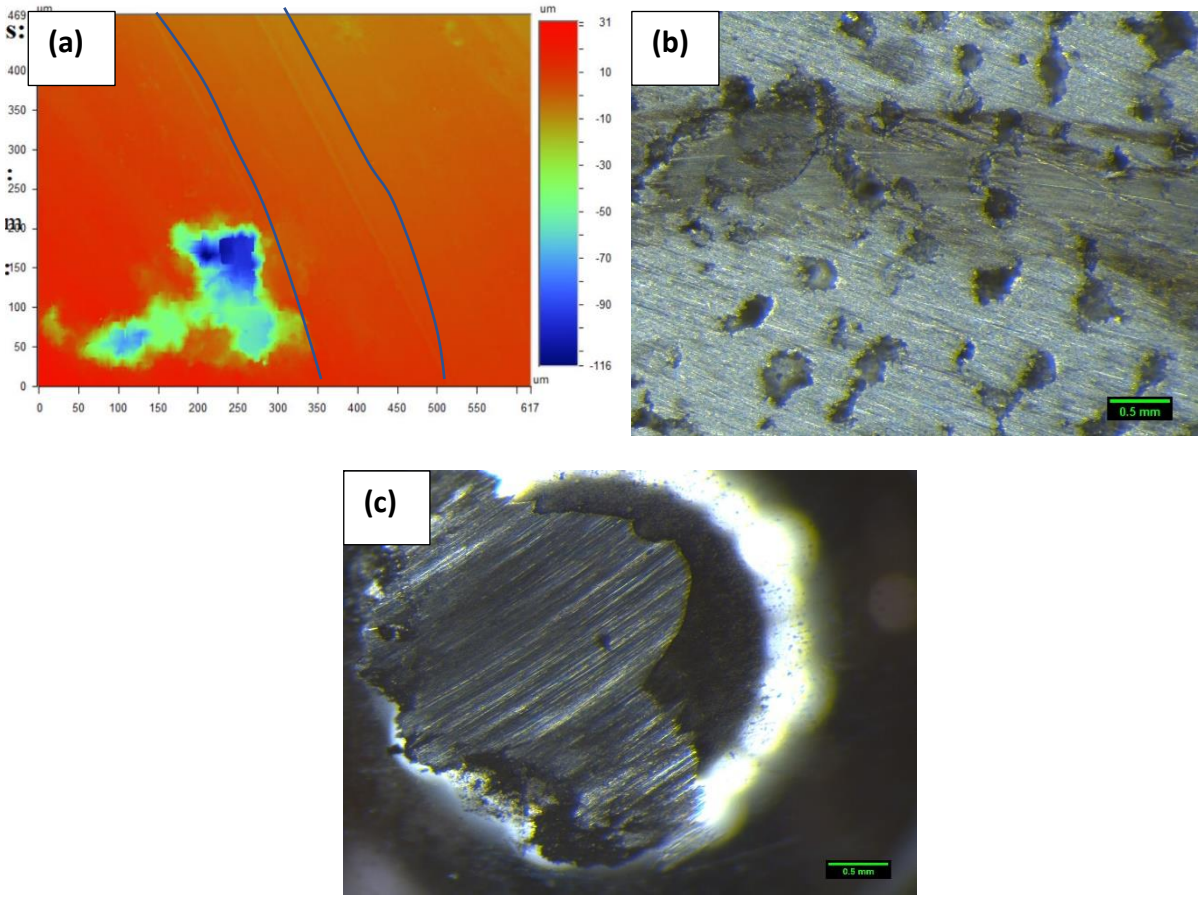

Figure 4-75: Micrographs of (a) wear track analysis map, (b) worn surface, and (c) static partner for E-sphere syntactic foam samples under lubricating sliding wear conditions

Like the ASW syntactic foam samples, the E-sphere syntactic foam sample has a lower track width, lower surface roughness and enhanced wear performance under the lubricating sliding wear condition when compared to the dry sliding wear behaviour. This is primarily due to the lubricating effect, as explained earlier.

Same as observed during the dry sliding tests, the E-sphere syntactic foam sample has superior wear resistance than the L-ASF sample, but is inferior to the M-ASF and S-ASF samples, as seen in the differences in track depth and specific wear. It has a lower ΔRa and a higher ΔRz than the ASW syntactic foam samples, showing that the

surface of the E-sphere syntactic foam sample is less rough on average but more uneven. However, the difference between the E-sphere and ASW syntactic foam samples is less evident under the lubricated sliding wear condition because the lubricant effectively dictates the wear behaviour.

Table 4-42: Summary of lubricated sliding wear parameters of ASW and E-sphere syntactic foam samples

Sample ID	Track depth (mm)	Track width (mm)	ΔRa ($x10^{-3}$) mm)	ΔRz ($x10^{-3}$) mm)	Weight loss (g)	Specific wear ($mm^3\ m^{-1}$)
L-ASF	0.001-0.045	3.36	8.78	12.56	0.014*	0.0026
M-ASF	0.012-0.034	2.86	2.74	12.53	0.010*	0.0018
S-ASF	0.018-0.037	2.44	1.92	4.94	0.006*	0.0011
E-Sphere	0.008-0.054	1.84	3.06	36.72	0.010*	0.0016

4.7.3 **Summary**

The properties of the ASW and E-sphere syntactic foam samples under dry and lubricated sliding wear conditions are presented and discussed in this section.

Under dry sliding wear conditions, the COF vs sliding distance curves of the ASW syntactic foam samples show three distinct regions: an initial sharp increase in COF as sliding distance increases up to 50m, followed by a gradual decrease in COF until 200m sliding distance, followed by a final steady state of COF as sliding distance increases further. The average COF is observed to decrease as particle size decreases. The lower COF in smaller particle sizes is due to the higher surface roughness, which leads to smaller contact area, and the presence of abrasive wear, which results in the same material sliding against one another. The samples also show behaviour indicative of delamination and oxidative wear. The wear profile indicates a decrease in specific wear as particle size decreases.

Heating of ASW particles leads to no change in properties for the Small and Medium size group samples, but it does lead to a reduction in COF, a change in COF development over the sliding distance and an enhancement of specific wear in the Large size group sample. The LH-ASF sample also shows a change in wear type from adhesive to abrasive. The abrasive nature of the wear is one of the reasons for the lower COF and the enhanced wear properties, along with the change in mechanical properties upon heating of the Large ASW particles.

T6 treatment leads to a significant reduction in COF as well as a change in COF development over the sliding distance. There exist the same three regions, however the steady state is reached sooner. While the wear type is the same as per the non-

T6 treated syntactic foam samples, an enhancement of wear properties is observed due to the hardening of the Al matrix in the syntactic foam samples.

The E-sphere syntactic foam sample curves show two regions: an initial sharp increase in COF followed by a steady COF as sliding distance increases. The average COF is also lower than that for the ASW syntactic foams. The E-sphere syntactic foam sample has predominantly abrasive wear, with some oxidative wear and delamination, which results in the lower COF. The weight lost for the E-sphere syntactic foam sample is higher than that for the ASW syntactic foams, with the specific wear also being higher than the S-ASF and M-ASF samples.

Under the lubricated sliding wear conditions, the COF vs sliding distance curves of the ASW syntactic foam samples show two distinct regions: a sharp initial increase in COF, followed by a steady state as sliding distance increases. The steady-state is achieved much sooner under the lubricated conditions than under the dry conditions. The average COF values are also close to one another regardless of particle size group. The wear type shows a change from adhesive to abrasive, with minimal delamination and oxidative wear, due to the lubricating effect, which also leads to a lowering of the surface roughness and an enhancement of the wear properties. The porous particles tend to act as lubricant reservoirs, which allow for a continuous presence of lubrication on the surface of the sample. Similar trends are observed as in the dry conditions, where the specific wear decreases as particle size decreases.

Heating of ASW particles leads to no change in properties for the Small and Medium size group samples. The LH-ASF sample however shows a lower COF, faster reach of

steady state and a lower specific wear than the L-ASF sample. This is due more to the change in mechanical properties of the heated Large ASW particles.

T6 treatment leads to a change in COF development, where three regions are observed. There is an initial sharp increase in COF, followed by a sudden drop in COF and a final steady state. The hardening of the Al matrix leads to a sharp spike and a lower steady-state in COF when compared to the non-T6 treated samples. The wear surfaces of the T6 treated samples showed behaviour indicative of oxidative wear and delamination. T6 treatment led to an enhancement of wear properties, with a lower weight lost and a lower specific wear.

The performance of the E-sphere syntactic foam sample is similar to that of the ASW-SFs under the lubricated conditions, except that the COF steady state is achieved sooner in the E-sphere syntactic foam sample than in the ASW syntactic foams. The E-sphere particles act as lubricant reservoirs, allowing for a continuous distribution of lubricant on the surface of the sample. The specific wear and surface roughness properties are very similar among all syntactic foam samples, showing that lubrication has a dominant effect, regardless of the sample characteristics.

Chapter 5 CONCLUSIONS AND FUTURE WORK

5.1 Conclusions

5.1.1 Characteristics of ASW particles

The ASW particles were observed to be irregular in shape, with pores present within the particles. The measured densities of the ASW particles were in the range of 1.05-1.40 gcm^{-3}, with the larger particles having a lower density due to the higher porosity. The composition of ASW varies with particle size group, with the Small and Medium particle size groups having more impurities. The larger the particles, the stronger and harder they are. Heating of ASW particles led to a significant increase in hardness and strength for the Small and Medium ASW particle size groups, but had the opposite effect on the Large ASW particle size group.

5.1.2 Structural Properties of Syntactic Foams

The manufactured syntactic foam samples had a good structural quality, with less than 1% of samples observed showing any presence of defects, such as infiltrated ASW particles with molten Al and cracks or air pockets due to incomplete infiltration. The measured densities of the samples ranged from 1.45 gcm^{-3} to 1.90 gcm^{-3} depending on particle size and heating of particles.

5.1.3 Quasi-Static Compressive Behaviour

The compressive stress-strain curve of the L-ASF sample showed a linear region, followed by a plateau region and finally a densification region, indicating a superior energy absorption capability The sample showed small cracks developed in the mid-section and a barrelling effect with the sample pushed outwards on its sides. The M-ASF and S-ASF samples, on the other hand, showed a brittle failure mode with a large drop in stress after the yield strength was reached and no apparent plateau region. Large cracks ran through the samples, reducing the strength and leading to catastrophic failure with minimal energy absorption capability. Under confined compressive loading, all samples showed a small increase in yield strength and a decrease in densification strain due to the limited possibility of barrelling and fragmentation.

Compared to the L-ASF sample, the LH-ASF sample showed a transition from ductile to brittle failure, where the large cracks developed in the sample led to a drop in strength, ultimate catastrophic failure, and a reduction in energy absorption capability. Compared to the M-ASF and S-ASF samples, the MH-ASF and SH-ASF samples showed no significant changes in behaviour, which suggests that the particles are adequately heated during infiltration. T6 treatment of the syntactic foam samples increased the yield strength of the samples, but showed no significant changes in deformation behaviour or failure modes.

ASW syntactic foams had a significantly higher strength and energy absorption capacity than the E-sphere syntactic foam, although the latter had a higher densification strain due to the higher porosity of the E-sphere particles.

5.1.4 **Drop Weight Impact Behaviour**

The ASW syntactic foam samples showed a significant increase in strength when compared to quasi-static loading. All samples developed large cracks that resulted in large stress drops and led to catastrophic failure. Since the impact behaviour of the L-ASF sample was different from what was observed under quasi-static loading, this indicated strain-rate sensitivity.

Heating the ASW particles before infiltration had no significant effect on the impact behaviour. T6 treatment of the syntactic foam samples resulted in an increase in strength and energy absorption. However, the samples also failed catastrophically. The M-ASF-T6 and S-ASF-T6 samples were reduced to debris, while the L-ASF-T6 sample showed some barrelling in its mid-section.

ASW syntactic foams showed a similar behaviour to E-sphere syntactic foams, but without the evident densification region. The E-sphere sample had superior energy absorption capabilities with significant barrelling in the mid-section and minimal debris and fragmentation.

5.1.5 Three-Point Bending Behaviour

The load-displacement curves for all ASW syntactic foam samples showed three distinct regions. There was an initial linear elastic region with a sharp increase in load, followed by plastic deformation region with a decreased gradient up to the critical load, and finally a region with a gradual decline in load until ultimate failure. The L-ASF sample shows behaviour resembling this, however the M-ASF and S-ASF samples displayed sharp drops in load due to crack propagation. The flexural strength and the flexural energy absorption decreased with decreasing particle size. The initial phase of the development of load over displacement was governed by the ASW particle properties and the extended plateau region was dependent on the properties of the metal matrix.

The LH-ASF sample showed a significant reduction in flexural strength and energy absorption due to the change in particle properties upon heating, while the MH-ASF and SH-ASF samples did not show significant changes in flexural properties. T6 treatment led to an increase in flexural strength and energy absorption, due to the increase in hardness of the Al matrix.

The ASW syntactic foam samples showed the same regions in the load-displacement curves as the E-sphere syntactic foam sample. The E-sphere syntactic foam sample had a more distinct decreasing gradient because the hollow spheres were more easily crushed, absorbing more energy before leading onto the extended region.

5.1.6 **Charpy Impact Behaviour**

Charpy impact energy and toughness decreased with decreasing particle size due to the decrease in porosity as well as due to the weak particle-matrix interfacial bonds. The crack propagated around the particles and through the matrix-particle interface. Heating of ASW particles led to no change in the MH-ASF and SH-ASF samples. The LH-ASF sample showed a decrease in impact energy and toughness, due to the change in particle properties upon heating. T6 treatment led to an overall increase in impact energy and toughness.

5.1.7 **Friction and Wear Behaviour**

Under dry sliding wear conditions, the COF vs sliding distance curves showed three regions. There was an initial sharp increase in COF, followed by a gradual decrease in COF and a final steady state as sliding distance continually increased. The average COF and specific wear decreased as particle size decreased, because the nature of wear became more abrasive. There was also evidence of oxidative wear and delamination on sample surfaces.

The LH-ASF sample had a reduced average COF and more enhanced wear properties than the L-ASF sample due to the transition from adhesive to abrasive wear and improved mechanical properties upon heating of ASW particles. The MH-ASF and SH-ASF samples showed no change when compared to their respective non-heated counterparts. In T6 treated samples, steady state of COF was achieved sooner, and the specific wear was lower than the non-T6 treated samples, due to the hardening of the Al matrix.

The average COF and ΔRz of the ASW syntactic foam samples were higher than those of the E-sphere syntactic foam sample, while ΔRa was lower. The E-sphere syntactic foam sample had a largely abrasive wear behaviour and its specific wear was higher than the S-ASF and M-ASF samples.

Under lubricated sliding conditions, the development of COF over the sliding distance showed two regions: a sharp increase in COF followed by a steady state, which was achieved much sooner than under the dry sliding conditions. The wear type changed from predominantly adhesive in dry sliding conditions to predominantly abrasive due to the lubricating effect. The lubricating effect led to a lowering of average COF,

surface roughness and an enhancement of the wear properties. The porosity present within the particles acted as lubricant reservoirs, ensuring a constant supply of lubricant during the wear test. The specific wear was observed to decrease as particle size decreased.

Heated ASW particles showed no change in wear properties for the MH-ASF and SH-ASF samples. The LH-ASF showed a lower average COF and more enhanced wear properties than the L-ASF sample due to improved mechanical properties of the Large ASW particles upon heating.

T6 treated samples showed a sharp increase in COF, followed by a sudden drop and a lower steady-state COF than the non-T6 treated sample. T6 treated samples had a lower specific wear and surface roughness than the non-T6 treated samples because of the harder Al matrix.

The ASW syntactic foam samples performed similar to the E-sphere syntactic foam sample under lubricated conditions, except that a steady-state COF was achieved sooner in the E-sphere syntactic foam sample. The lubrication had a significant effect on the sliding wear behaviour regardless of sample characteristics.

5.2 Future Work

5.2.1 Properties of ASW/Al syntactic foam samples manufactured by powder metallurgy

There are several routes to fabricating syntactic foams, as described in Chapter 2. One of these is powder metallurgy, or liquid sintering, where there is more control over the ratio of metal to filler material and therefore more control over the properties of the syntactic foams. As an extension to the current body of work, the properties of ASW/Al syntactic foam samples manufactured by powder metallurgy route can be studied to understand the flexibility available when manufacturing ASW/Al syntactic foams as well as to investigate the change in properties as the metal-filler material ratio is changed.

5.2.2 Fabrication and properties of bimodal ASW/Al syntactic foams

The results in this study showed that each ASW particle size group has certain beneficial properties. For instance, the Small ASW particle size group is stronger and harder than the Large ASW particle size group in a syntactic foam, whereas the L-ASF sample has a significantly improved energy absorption capability when compared to the M-ASF and S-ASF samples. Bimodal syntactic foam contains different particle size groups in a single syntactic foam sample. Manufacturing bimodal syntactic foams will allow for achievements of a wider range of and possibly better properties. To further this study, Al particles can be incorporated into the final mix to alter the Al-filler material ratio and investigate how the Al particles may improve the ductility of the ASW/Al syntactic foams.

5.2.3 **Numerical modelling of ASW/Al syntactic foams**

Developing numerical models is a useful way to cost-effectively predict the properties of several materials without the need to perform lab experiments, provided the models are validated against the corresponding experimental results. If the models are accurate and comparable to experimental results, they can be extrapolated for experiments that may be difficult to conduct in a lab-based environment. Therefore, an extension of this work would be to develop numerical models for predicting various properties of ASW/Al syntactic foams and compare the model predictions to the obtained experimental results.

References

A to Z of Materials (2004) *Bayer and Adidas Produce High Tech Soccer Ball for EUFA EURO 2004 Championship.* Available at: https://www.azom.com/article.aspx?ArticleID=2408 (Accessed: 14th May, 2020).

Abd El-Aty, A., Xu, Y., Zhang, S., Ha, S., Ma, Y. and Chen, D. (2019) 'Impact of high strain rate deformation on the mechanical behavior, fracture mechanisms and anisotropic response of 2060 Al-Cu-Li alloy', *Journal of Advanced Research,* 18, pp. 19-37. doi: https://doi.org/10.1016/j.jare.2019.01.012.

Ahmadi, H., Liaghat, G.H., Shokrieh, M.M., Hadavinia, H., Ordys, A. and Aboutorabi, A. (2015) 'Quasi-static and dynamic compressive properties of ceramic microballoon filled syntactic foam', *Journal of Composite Materials,* 49(10), pp. 1255-1266. doi: 10.1177/0021998314533362.

Ahmaruzzaman, M. (2010) 'A review on the utilization of fly ash', *Progress in Energy and Combustion Science,* 36(3), pp. 327-363. doi: 10.1016/j.pecs.2009.11.003.

Altenaiji, M. (2014) *Characterisation of Aluminium Matrix Syntactic Foams under Static and Dynamic Loading.* PhD. University of Liverpool.

An, Y., Yang, S., Zhao, E. and Wang, Z. (2017) 'Characterization of metal grid-structure reinforced aluminum foam under quasi-static bending loads', *Composite Structures,* 178, pp. 288-296. doi: https://doi.org/10.1016/j.compstruct.2017.07.031.

Antunes, F.V., Ferreira, J.A.M. and Capela, C. (2011) 'Numerical modelling of the Young's modulus of syntactic foams', *Finite Elements in Analysis and Design,* 47(2), pp. 78-84. doi: https://doi.org/10.1016/j.finel.2010.09.007.

Ashby, M.F. (2000) *Metal foams: a design guide.* Boston: Butterworth-Heinemann.

ASM (1991) *ASM Handbook Volume 4.*

ASTM (2018a) *ASTM C1341 - 13(2018): Standard Test Method for Flexural Properties of Continuous Fiber-Reinforced Advanced Ceramic Composites.* 5th edn.American Society for Testing and Materials.

ASTM (2018b) *ASTM E23 - 18: Standard Test Methods for Notched Bar Impact Testing of Metallic Materials.* 20th edn.American Society for Testing and Materials.

Banhart, J. (2001) 'Manufacture, Characterisation and Application of Cellular Metals and Metal Foams', *Progress in Materials Science,* 46(6), pp. 559-632. doi: 10.1016/S0079-6425(00)00002-5.

Blackman, B.R.K., Kinloch, A.J., Sohn Lee, J., Taylor, A.C., Agarwal, R., Schueneman, G. and Sprenger, S. (2007) 'The fracture and fatigue behaviour of nano-modified epoxy polymers', *Journal of Materials Science,* 42(16), pp. 7049-7051. doi: 10.1007/s10853-007-1768-6.

Brizmer, V. (2018) *Surface roughness Vs Coefficient of friction.* Available at: https://www.researchgate.net/post/Surface_roughness_Vs_Coefficient_of_friction (Accessed: 1st June, 2020).

Broxtermann, S., Vesenjak, M., Krstulović-Opara, L. and Fiedler, T. (2018) 'Quasi static and dynamic compression of zinc syntactic foams', *Journal of Alloys and Compounds,* 768, pp. 962-969. doi: https://doi.org/10.1016/j.jallcom.2018.07.215.

BSI (2019) *BS EN 573-3: 2019 - Aluminium and aluminium alloys. Chemical composition and form of wrought products. Chemical composition and form of products.* 6th edn.British Standards Institution.

Capek, J. and Vojtech, D. (2011) *Preparation and Properties of Magnesium Porous Materials for Medical Applications.* Brno, Czech Republic: .

Carton, E. (2016) *Can ceramics be chemically hardened (tempered)?* Available at: https://www.researchgate.net/post/Can_ceramics_be_chemically_hardened_tempered (Accessed: 31st March, 2020).

CenoStar (2020) *Cenospheres.* Available at: https://www.cenostar.com/pages/cenospheres (Accessed: 14th May 2020).

Chaitanya, C.S. and Rao, R.N. (2019) 'Effect of addition of reinforcements on the tribological behaviour of the polymer based syntactic foams', *Materials Today: Proceedings,* 26(2), pp. 415-418. doi: https://doi.org/10.1016/j.matpr.2019.12.070.

Chauhan, S.R. and Thakur, S. (2013) 'Effects of particle size, particle loading and sliding distance on the friction and wear properties of cenosphere particulate filled vinylester composites', *Materials & Design,* 51, pp. 398-408. doi: https://doi.org/10.1016/j.matdes.2013.03.071.

Chawla, K.K. and Chawla, N. (2013) *Metal Matrix Composites*, 2nd edn, New York: Springer-Verlag New York.

Colloca, M., Gupta, N. and Porfiri, M. (2013) 'Tensile properties of carbon nanofiber reinforced multiscale syntactic foams', *Composites Part B: Engineering,* 44(1), pp. 584-591. doi: https://doi.org/10.1016/j.compositesb.2012.02.030.

Das, D., Roy, D.K., Satpathy, M.P., Nanda, B.K. and Nayak, R.K. (2019) 'Compressive, impact and flexural behaviour of Al based metal matrix composites', *Materials Today: Proceedings,* 18, pp. 3080-3086. doi: https://doi.org/10.1016/j.matpr.2019.07.180.

Degischer, H. and Kriszt, B. (2002) *Handbook of cellular metals: production, processing, applications.* Weinheim: Wiley-VCH.

Demir, A. and Altinkok, N. (2004) 'Effect of gas pressure infiltration on microstructure and bending strength of porous Al2O3/SiC-reinforced aluminium matrix composites', *Composites Science and Technology,* 64(13-14), pp. 2067-2074. doi: 10.1016/j.compscitech.2004.02.015.

Dercz, G., Prusik, K., Pająk, L., Pielaszek, R., Jmalinowski, J.J. and Pudło, W. (2009) *Structure studies on nanocrystalline powder of MgO xerogel prepared by sol-gel method.*

Deuis, R.L., Subramanian, C. and Yellup, J.M. (1996) *Abrasive wear of aluminium composites—a review*.

Diao, K.K., Xiao, Z. and Zhao, Y.Y. (2015) 'Specific surface areas of porous Cu manufactured by Lost Carbonate Sintering: Measurements by quantitative stereology and cyclic voltammetry', *Materials Chemistry and Physics,* 162, pp. 571-579. doi: 10.1016/j.matchemphys.2015.06.031.

Dou, Z.Y., Jiang, L.T., Wu, G.H., Zhang, Q., Xiu, Z.Y. and Chen, G.Q. (2007) 'High strain rate compression of cenosphere-pure aluminum syntactic foams', *Scripta Materialia,* 57(10), pp. 945-948. doi: 10.1016/j.scriptamat.2007.07.024.

Du, H., Qi, J., Du, S., Xiong, T., Li, T. and Lee, S.W. (2010) 'Structure and oil retaining capacity of gasar copper fabricated by radial solidification with a combined crystallizer', *Journal of Materials Processing Technology,* 210(11), pp. 1523-1528. doi: https://doi.org/10.1016/j.jmatprotec.2010.04.011.

Du, H., Qi, J., Lao, Y. and Xiong, T. (2012) 'Oil retaining capability and sliding friction behaviour of porous copper with elongated cylindrical pores', *Journal of Materials Processing Technology,* 212(8), pp. 1796-1801. doi: https://doi.org/10.1016/j.jmatprotec.2012.03.024.

Duarte, I. (2012) 'Aluminium Alloy Foams: Production and Properties'*Powder Metallurgy* Rijeka: IntechOpen, pp. Ch. 3.

Duarte, I., Vesenjak, M. and Krstulović-Opara, L. (2014) 'Dynamic and quasi-static bending behaviour of thin-walled aluminium tubes filled with aluminium foam', *Composite Structures,* 109, pp. 48-56. doi: https://doi.org/10.1016/j.compstruct.2013.10.040.

Duarte, I., Vesenjak, M., Krstulović-Opara, L., Anžel, I. and Ferreira, J.M.F. (2015) 'Manufacturing and bending behaviour of in situ foam-filled aluminium alloy tubes', *Materials & Design,* 66, pp. 532-544. doi: https://doi.org/10.1016/j.matdes.2014.04.082.

Envirospheres Pty Ltd (2018) *E-SPHERES ® SL Series – High Performance, White Hollow Ceramic Microspheres – Envirospheres.* Available at: https://envirospheres.com.au/products/e-spheres-sl-series/ (Accessed: 20th January, 2020).

Fadhil, M.C. and Ravikiran, B.S. (2016) 'Characterization of aluminium alloy/SiC metal matrix composites', *International Journal of Engineering Research and Advanced Technology,* 2(9), pp. 1-5.

Fan, Z., Miao, Y., Wang, Z., Zhang, B. and Ma, H. (2019) 'Effect of the cenospheres size and internally lateral constraints on dynamic compressive behavior of fly ash cenospheres polyurethane syntactic foams', *Composites Part B: Engineering,* 171, pp. 329-338. doi: https://doi.org/10.1016/j.compositesb.2019.05.008.

Ferreira, J.A.M., Capela, C. and Costa, J.D. (2010) 'A study of the mechanical behaviour on fibre reinforced hollow microspheres hybrid composites', *Composites Part A: Applied Science and Manufacturing,* 41(3), pp. 345-352. doi: https://doi.org/10.1016/j.compositesa.2009.10.018.

Goel, M.D., Peroni, M., Solomos, G., Mondal, D.P., Matsagar, V.A., Gupta, A.K., Larcher, M. and Marburg, S. (2012) 'Dynamic compression behavior of cenosphere aluminum alloy syntactic foam', *Materials & Design,* 42, pp. 418-423. doi: 10.1016/j.matdes.2012.06.013.

Gohar, R. and Rahnejat, H. (2008) *Fundamentals of tribology.* London: Imperial College Press.

Gupta, N., Kishore, Woldesenbet, E. and Sankaran, S. (2001) 'Studies on compressive failure features in syntactic foam material', *Journal of Materials Science,* 36(18), pp. 4485-4491. doi: 10.1023/A:1017986820603.

Gupta, N., Karthikeyan, C.S., Sankaran, S. and Kishore, (1999) 'Correlation of Processing Methodology to the Physical and Mechanical Properties of Syntactic Foams With and Without Fibers', *Materials Characterization,* 43(4), pp. 271-277. doi: https://doi.org/10.1016/S1044-5803(99)00039-X.

Gupta, N., Luong, D.D. and Cho, K. (2012) 'Magnesium Matrix Composite Foams - Density, Mechanical Properties, and Applications', *Metals,* 2(4), pp. 238-252. doi: 10.3390/met2030238.

Gupta, N., Pinisetty, D. and Shunmugasamy, V.C. (2013) *Reinforced polymer matrix syntactic foams.* Cham: Springer.

Gupta, N. and Rohatgi, P.K. (2015) *Metal matrix syntactic foams: processing, microstructure, properties and applications.* 1st edn. Lancaster, PA: DEStech Publications, Inc.

Hanssen, A.G., Enstock, L. and Langseth, M. (2002) 'Close-range blast loading of aluminium foam panels', *International Journal of Impact Engineering,* 27(6), pp. 593-618. doi: 10.1016/S0734-743X(01)00155-5.

Hartmann, M., Crössmann, I., Reindel, K. and Singer, R. (1999) 'Microstructure and mechanical properties of cellular magnesium matrix composites', in Banhart, J., Ashby, M.F. and Fleck, N.A. (eds.) *Metal Foams and Porous Metal Structures* Germany: International Conference on Metal Foams and Porous Metal Structures, pp. 331-336.

Hossain, T.S., Johra, T.F. and Jung, W. (2018) 'Fabrication of Silicon Carbide from Recycled Silicon Wafer Cutting Sludge and Its Purification', *Applied Sciences,* 8(10), pp. 1841. doi: 10.3390/app8101841.

Huang, Y.J., Wang, C.-., Huang, Y.-., Guo, G. and Nutt, S.R. (2010) 'Enhancing specific strength and stiffness of phenolic microsphere syntactic foams through carbon fiber reinforcement', *Polymer Composites,* 31(2), pp. 256-262. doi: 10.1002/pc.20795.

Jang, W., Hsieh, W., Miao, C. and Yen, Y. (2015) 'Microstructure and mechanical properties of ALPORAS closed-cell aluminium foam', *Materials Characterization,* 107, pp. 228-238. doi: 10.1016/j.matchar.2015.07.012.

Jha, N., Badkul, A., Mondal, D.P., Das, S. and Singh, M. (2011) 'Sliding wear behaviour of aluminum syntactic foam: A comparison with Al-10wt% SiC composites', *Tribology International,* 44(3), pp. 220-231. doi: 10.1016/j.triboint.2010.10.004.

Jing-hong Song, Guang-lin Zhi, Zhang, Y. and Bing-chu Mei (2011) 'Synthesis and Characterization of CaF2 Nanoparticles with Different Doping Concentrations of Er3+', *Nano-Micro Letters,* 3(2), pp. 73-78. doi: 10.5101/nml.v3i2.p73-78.

John, B. and Nair, R. (2010) *Update on syntactic foams.* Shawbury, Shropshire: iSmithers.

Kalhapure, M.G. and Dighe, P.M. (2015) 'Impact of silicon content on mechanical properties of aluminum alloys', *Int. J. Sci. Res,* (4), pp. 38-40.

Kalkanli, A. and Yilmaz, S. (2008) 'Synthesis and characterization of aluminum alloy 7075 reinforced with silicon carbide particulates', *Materials & Design,* 29(4), pp. 775-780. doi: https://doi.org/10.1016/j.matdes.2007.01.007.

Karthikeyan, C., Sankaran, S. and Kumar, J. (2001) 'Processing and compressive strengths of syntactic foams with and without fibrous reinforcements', *Journal of Applied Polymer Science,* 81(2), pp. 405-411.

Karthikeyan, C.S., Sankaran, S. and Kishore (2000) 'Influence of chopped strand fibres on the flexural behaviour of a syntactic foam core system', *Polymer International,* 49(2), pp. 158-162. doi: 10.1002/(SICI)1097-0126(200002)49:23.0.CO;2-8.

Kirchner, H.P. (1979) *Strengthening of ceramics: treatments, tests and design applications.* New York: Dekker.

Kiser, M., He, M.Y. and Zok, F.W. (1999) 'The mechanical response of ceramic microballoon reinforced aluminum matrix composites under compressive loading', *Acta Materialia,* 47(9), pp. 2685-2694. doi: 10.1016/S1359-6454(99)00129-9.

Kishi, A. and Toraya, H. (2004) 'Simultaneous Measurements of X-Ray Diffraction (XRD) and Differential Scanning Calorimetry (DSC) Data Under Controlled Humidity Condition: Instrumentation and Application to Studies on Hydration, Dehydration, and Re-Hydration Processes of Pharmaceutical Compounds', *Advances in X-ray Analysis,* 47, pp. 240-248.

Klempner, D. and Sendijarevic, V. (2004) *Handbook of polymeric foams and foam technology.* Munich; Cincinnati: Hanser Publishers; Hanser Gardener i.e. Gardner Publications.

Kumar, D.V.R., Seenappa, Asha, P.B. and Rao, C.R.P. (2018) 'Influence Of Percent Filler On Tensile Strength, Impact Strength And Wear Properties Of The Al7075-Cenosphere Composite', *Materials Today: Proceedings,* 5(5, Part 2), pp. 11697-11708. doi: https://doi.org/10.1016/j.matpr.2018.02.139.

Kumar, P.R.S., Kumaran, S., Rao, T.S. and Natarajan, S. (2010) 'High temperature sliding wear behavior of press-extruded AA6061/fly ash composite', *Materials Science and Engineering: A,* 527(6), pp. 1501-1509. doi: 10.1016/j.msea.2009.10.016.

Kwok, J.K.M. and Lim, S.C. (1999) 'High-speed tribological properties of some Al/SiCp composites: II. Wear mechanisms', *Composites Science and Technology,* 59(1), pp. 65-75. doi: https://doi.org/10.1016/S0266-3538(98)00067-0.

Lin, Y., Zhang, Q., Ma, X. and Wu, G. (2016) 'Mechanical behavior of pure Al and Al–Mg syntactic foam composites containing glass cenospheres', *Composites Part A: Applied Science and Manufacturing,* 87, pp. 194-202. doi: https://doi.org/10.1016/j.compositesa.2016.05.001.

Lin, Y., Zhang, Q., Zhang, F., Chang, J. and Wu, G. (2017) 'Microstructure and strength correlation of pure Al and Al-Mg syntactic foam composites subject to uniaxial compression', *Materials Science and Engineering: A,* 696, pp. 236-247. doi: 10.1016/j.msea.2017.04.060.

Linggawati, A. (2016) 'Preparation and Characterization of Calcium Oxide Heterogeneous Catalyst Derived from Anadara Granosa Shell for Biodiesel Synthesis', *KnE Engineering,* 1(1). doi: 10.18502/keg.v1i1.494.

Liu, H., Cao, Z.K., Luo, H.J., Shi, J.C. and Yao, G.C. (2013) 'Performance of closed-cell aluminum foams subjected to impact loading', *Materials Science and Engineering: A,* 570, pp. 27-31. doi: https://doi.org/10.1016/j.msea.2012.11.094.

Lokesh, K.S., Chethan, I.C., Kumar, K.R., Kannantha, V. and Kumar, J.R., Naveen (2018) 'Determination of compressive strength of graphene reinforced with aluminium-7075 metal matrix composites', *International Journal of Mechanical Engineering and Technology,* 9, pp. 327-335.

Luong, D.D., Strbik, O.M., Hammond, V.H., Gupta, N. and Cho, K. (2013) 'Development of high performance lightweight aluminum alloy/SiC hollow sphere syntactic foams and compressive characterization at quasi-static and high strain rates', *Journal of Alloys and Compounds,* 550, pp. 412-422. doi: 10.1016/j.jallcom.2012.10.171.

Mahadev, Sreenivasa, C.G. and Shivakumar, K.M. (2018) 'A Review on Prodution of Aluminium Metal Foams', *IOP Conference Series: Materials Science and Engineering,* 376, pp. 012081. doi: 10.1088/1757-899x/376/1/012081.

Mahajan, S.M. and Jadhav, G.A. (2015) 'Aluminum Foaming For Lighter Structure', *International Journal of Computational Engineering Research (IJCER),* 5(1), pp. 70-74.

Maharsia, R.R. (2005) *Development of high performance hybrid syntactic foams: structure and material property characterization.* PhD. Louisiana State University.

Májlinger, K., Bozóki, B., Kalácska, G., Keresztes, R. and Zsidai, L. (2016) 'Tribological properties of hybrid aluminum matrix syntactic foams', *Tribology International,* 99, pp. 211-223. doi: 10.1016/j.triboint.2016.03.032.

Manakari, V., Parande, G., Doddamani, M., Gaitonde, V.N., Siddhalingeshwar, I.G., Kishore, Shunmugasamy, V.C. and Gupta, N. (2015) 'Dry sliding wear of epoxy/cenosphere syntactic foams', *Tribology International,* 92, pp. 425-438. doi: https://doi.org/10.1016/j.triboint.2015.07.026.

Manohar, A., Malkhandi, S., Yang, B., Yang, C., Prakash, G. and Narayan, S. (2012) 'A High-Performance Rechargeable Iron Electrode for Large-Scale Battery-Based Energy Storage', *Journal of the Electrochemical Society,* 159, pp. A1209-A1214. doi: 10.1149/2.034208jes.

McClusky, M. (2005) *Fuming over the World Cup's Foam Ball.* Available at: https://www.wired.com/2002/05/fuming-over-world-cups-foam-ball/ (Accessed: 14th May, 2020).

Menzie, W.D., Barry, J.J., Bleiwas, D.I., Bray, E.L., Goonan, T.G. and Matos, G. (2010) *OECD Global Forum on Environment Focusing on Sustainable Materials Development.* Mechelen, Belgium: OECD Environment Directorate. Available at: https://www.oecd.org/environment/waste/46133561.pdf (Accessed: 15th October, 2017).

Miyoshi, T., Itoh, M., Akiyama, S. and Kitahara, A. (2000) 'ALPORAS aluminum foam: Production process, properties, and applications', *Advanced Engineering Materials,* 2(4), pp. 179-183. doi: 10.1002/(SICI)1527-2648(200004)2:43.0.CO;2-G.

Mofidi, M. and Prakash, B. (2011) 'The Influence of Lubrication on Two-body Abrasive Wear of Sealing Elastomers Under Reciprocating Sliding Conditions', *Journal of Elastomers & Plastics,* 43(1), pp. 19-31. doi: 10.1177/0095244310385435.

Mohanty, S. and Chugh, Y.P. (2007) 'Development of fly ash-based automotive brake lining', *Tribology International,* 40(7), pp. 1217-1224. doi: 10.1016/j.triboint.2007.01.005.

Mondal, D.P., Das, S. and Jha, N. (2009) 'Dry sliding wear behaviour of aluminum syntactic foam', *Materials & Design,* 30(7), pp. 2563-2568. doi: 10.1016/j.matdes.2008.09.034.

Mondal, D.P., Datta Majumder, J., Jha, N., Badkul, A., Das, S., Patel, A. and Gupta, G. (2012) 'Titanium-cenosphere syntactic foam made through powder metallurgy route', *Materials & Design,* 34, pp. 82-89. doi: 10.1016/j.matdes.2011.07.055.

Mondal, D.P., Goel, M.D. and Das, S. (2009) 'Compressive deformation and energy absorption characteristics of closed cell aluminum-fly ash particle composite foam', *Materials Science and Engineering: A,* 507(1-2), pp. 102-109. doi: 10.1016/j.msea.2009.01.019.

Mondal, D.P., Jha, N., Badkul, A., Das, S. and Khedle, R. (2012) 'High temperature compressive deformation behaviour of aluminum syntactic foam', *Materials Science and Engineering: A,* 534, pp. 521-529. doi: 10.1016/j.msea.2011.12.002.

Murali, M., Suganthi, P., Athif, P., Sadiq Bukhari, A., Syed Mohamed, H.E., Basu, H. and Singhal, R.K. (2017) 'Histological alterations in the hepatic tissues of Al2O3 nanoparticles exposed freshwater fish Oreochromis mossambicus', *Journal of trace elements in medicine and biology : organ of the Society for Minerals and Trace Elements (GMS),* 44, pp. 125-131. doi: S0946-672X(17)30014-7 [pii].

Neville, B.P. and Rabiei, A. (2008) 'Composite metal foams processed through powder metallurgy', *Materials & Design,* 29(2), pp. 388-396. doi: 10.1016/j.matdes.2007.01.026.

Newsome, D.B., Schultz, B.F., Ferguson, J.B. and Rohatgi, P.K. (2015) 'PMC5512899; Synthesis and Quasi-Static Compressive Properties of Mg-AZ91D-Al(2)O(3) Syntactic Foams', *Materials (Basel),* 8(9), pp. 6085-6095. doi: 10.3390/ma8095292.

Nishida, Y. (2013) *Introduction to Metal Matrix Composites: Fabrication and Recycling*, Japan: Springer, Japan.

Nturanabo, F., Masu, L. and Kirabira, J.B. (2020) 'Novel Applications of Aluminium Metal Matrix Composites', in Leonard Masu (ed.) *Aluminium Alloys and Composites* Rijeka: IntechOpen, pp. Ch. 5.

Omar, M.Y., Xiang, C., Gupta, N., Strbik, O.M. and Cho, K. (2015) 'Syntactic foam core metal matrix sandwich composite under bending conditions', *Materials & Design,* 86, pp. 536-544. doi: https://doi.org/10.1016/j.matdes.2015.07.127.

Orbulov, I.N., Dobranszky, J. and Nemeth, A. (2009) 'Microstructural characterisation of syntactic foams', *Journal of Materials Science,* 44(15), pp. 4013-4019. doi: 10.1007/s10853-009-3552-2.

PCE Instruments (2020) *Roughness Tester.* Available at: https://www.pce-instruments.com/english/measuring-instruments/test-meters/roughness-tester-kat_40601.htm (Accessed: 20th January 2020).

Peroni, M., Solomos, G. and Pizzinato, V. (2013) 'Impact behaviour testing of aluminium foam', *International Journal of Impact Engineering,* 53, pp. 74-83. doi: https://doi.org/10.1016/j.ijimpeng.2012.07.002.

Purohit, R., Rana, R.S. and Verma, C.S. (2012) 'Fabrication of Al-SiCp composites through powder metallurgy process and testing of properties', *International Journal of Engineering Research and Applications (IJERA),* 2(3), pp. 420-437.

Rajan, T.P.D., Pillai, R.M., Pai, B.C., Satyanarayana, K.G. and Rohatgi, P.K. (2007) 'Fabrication and characterisation of Al-7Si-0.35Mg/fly ash metal matrix composites processed by different stir casting routes', *Composites Science and Technology,* 67(15-16), pp. 3369-3377. doi: 10.1016/j.compscitech.2007.03.028.

Ramachandra, M. and Radhakrishna, K. (2007) 'Effect of reinforcement of flyash on sliding wear, slurry erosive wear and corrosive behavior of aluminium matrix composite', *Wear,* 262(11), pp. 1450-1462. doi: https://doi.org/10.1016/j.wear.2007.01.026.

Ramachandra, S., Sudheer Kumar, P. and Ramamurty, U. (2003) 'Impact energy absorption in an Al foam at low velocities', *Scripta Materialia,* 49(8), pp. 741-745. doi: https://doi.org/10.1016/S1359-6462(03)00431-7.

Richerson, D.W. (1992) *Modern ceramic engineering: properties, processing, and use in design.* , rev and expand edn. New York: M. Dekker.

Rohatgi, P., Gupta, N., Schultz, B.F. and Luong, D.D. (2011) 'The Synthesis, Compressive Properties, and Applications of Metal Matrix Syntactic Foams', *JOM,* 63(2), pp. 36-42. doi: 10.1007/s11837-011-0026-1.

Rohatgi, P.K., Kim, J.K., Gupta, N., Alaraj, S. and Daoud, A. (2006) 'Compressive characteristics of A356/fly ash cenosphere composites synthesized by pressure infiltration technique', *Composites Part A: Applied Science and Manufacturing,* 37(3), pp. 430-437. doi: 10.1016/j.compositesa.2005.05.047.

Rohatgi, P.K., Weiss, D. and Gupta, N. (2006) 'Applications of fly ash in synthesizing low-cost MMCs for automotive and other applications', *JOM,* 58(11), pp. 71-76. doi: 10.1007/s11837-006-0232-4.

Schlesinger, M.E. (2017) *Aluminum Recycling.* London: Taylor & Francis Ltd.

Senden, T., Geitenbeek, R.G. and Meijerink, A. (2017) 'Co-precipitation Synthesis and Optical Properties of Mn(4+)-doped Hexafluoroaluminate w-LED Phosphors', *Materials (Basel, Switzerland),* 10(11), pp. 10.3390/ma10111322. doi: E1322 [pii].

Sharma, S., Nanda, T. and Pandey, O.P. (2019) 'Investigation of T4 and T6 heat treatment on the wear properties of sillimanite reinforced LM30 aluminium alloy composites', *Wear,* 426-427, pp. 27-36. doi: https://doi.org/10.1016/j.wear.2018.12.065.

Singh, A.K. and Siddhartha (2015) 'Leverage of cenosphere filler size on mechanical and dry sliding wear peculiarity of polyester composites', *Journal of Composite Materials,* 49(22), pp. 2789-2802. doi: 10.1177/0021998314554436.

Sondur, D.G., Mallapur, D.G. and Udupa, K.R. (2018) 'Effect of T6 treatment on the coefficient of friction of Al25Mg2Si2Cu4Fe alloy', *AIP Conference Proceedings,* 1943(1), pp. 020080. doi: 10.1063/1.5029656.

Song, B., Chen, W., Yanagita, T. and Frew, D.J. (2005) 'Confinement effects on the dynamic compressive properties of an epoxy syntactic foam', *Composite Structures,* 67(3), pp. 279-287. doi: https://doi.org/10.1016/j.compstruct.2004.07.011.

Stachowiak, G.W. (2017) 'How tribology has been helping us to advance and to survive', *Friction,* 5(3), pp. 233-247. doi: https://doi.org/10.1007/s40544-017-0173-7.

Sudarshan and Surappa, M.K. (2008) 'Synthesis of fly ash particle reinforced A356 Al composites and their characterization', *Materials Science and Engineering: A,* 480(1-2), pp. 117-124. doi: 10.1016/j.msea.2007.06.068.

Suresh, S., Karthikeyan, S. and Jayamoorthy, K. (2016) 'Effect of bulk and nano-Fe2O3 particles on peanut plant leaves studied by Fourier transform infrared spectral studies', *Journal of Advanced Research,* 7(5), pp. 739-747. doi: https://doi.org/10.1016/j.jare.2015.10.002.

Swetha, C. and Kumar, R. (2011) 'Quasi-static uni-axial compression behaviour of hollow glass microspheres/epoxy based syntactic foams', *Materials & Design,* 32(8), pp. 4152-4163. doi: https://doi.org/10.1016/j.matdes.2011.04.058.

Tagliavia, G., Porfiri, M. and Gupta, N. (2010) 'Analysis of flexural properties of hollow-particle filled composites', *Composites Part B: Engineering,* 41(1), pp. 86-93. doi: https://doi.org/10.1016/j.compositesb.2009.03.004.

Taherishargh, M., Vesenjak, M., Belova, I.V., Krstulović-Opara, L., Murch, G.E. and Fiedler, T. (2016) 'In situ manufacturing and mechanical properties of syntactic foam filled tubes', *Materials & Design,* 99, pp. 356-368. doi: https://doi.org/10.1016/j.matdes.2016.03.077.

Tao, X.F. and Zhao, Y.Y. (2012) 'Compressive failure of Al alloy matrix syntactic foams manufactured by melt infiltration', *Materials Science and Engineering: A,* 549, pp. 228-232. doi: 10.1016/j.msea.2012.04.047.

Tao, X.F. and Zhao, Y.Y. (2009) 'Compressive behavior of Al matrix syntactic foams toughened with Al particles', *Scripta Materialia,* 61(5), pp. 461-464. doi: 10.1016/j.scriptamat.2009.04.045.

The Air Brake Association (1924) *The Principles and Design of Foundation Brake Rigging.* 1st edn. New York: The Air Brake Association.

Tressaud, A. (2019) *1 - History and milestones of fluorine and fluorinated products through the centuries* Elsevier.

Tsakiridis, P.E. (2012) 'Aluminium salt slag characterization and utilization - A review', *Journal of hazardous materials,* 217-218, pp. 1-10. doi: 10.1016/j.jhazmat.2012.03.052.

Vogiatzis, C.A., Tsouknidas, A., Kountouras, D.T. and Skolianos, S. (2015) 'Aluminum-ceramic cenospheres syntactic foams produced by powder metallurgy route', *Materials & Design,* 85, pp. 444-454. doi: 10.1016/j.matdes.2015.06.154.

Wang, L., Zhang, J., Yang, X., Zhang, C., Gong, W. and Yu, J. (2014) 'Flexural properties of epoxy syntactic foams reinforced by fiberglass mesh and/or short glass fiber', *Materials & Design,* 55, pp. 929-936. doi: https://doi.org/10.1016/j.matdes.2013.10.065.

Wang, N., Chen, X., Li, A., Li, Y., Zhang, H. and Liu, Y. (2016) 'Three-point bending performance of a new aluminum foam composite structure', *Transactions of Nonferrous Metals Society of China,* 26(2), pp. 359-368. doi: https://doi.org/10.1016/S1003-6326(16)64088-8.

Wouterson, E.M., Boey, F.Y.C., Hu, X. and Wong, S. (2005) 'Specific properties and fracture toughness of syntactic foam: Effect of foam microstructures', *Composites Science and Technology,* 65(11), pp. 1840-1850. doi: https://doi.org/10.1016/j.compscitech.2005.03.012.

Wu, G.H., Dou, Z.Y., Jiang, L.T. and Cao, J.H. (2006) 'Damping properties of aluminum matrix-fly ash composites', *Materials Letters,* 60(24), pp. 2945-2948. doi: 10.1016/j.matlet.2006.02.018.

Wu, G.H., Dou, Z.Y., Sun, D.L., Jiang, L.T., Ding, B.S. and He, B.F. (2007) 'Compression behaviors of cenosphere–pure aluminum syntactic foams', *Scripta Materialia,* 56(3), pp. 221-224. doi: https://doi.org/10.1016/j.scriptamat.2006.10.008.

Xia, X., Chen, X., Zhang, Z., Chen, X., Zhao, W., Liao, B. and Hur, B. (2014) 'Compressive properties of closed-cell aluminum foams with different contents of ceramic microspheres', *Materials & Design (1980-2015),* 56, pp. 353-358. doi: https://doi.org/10.1016/j.matdes.2013.11.040.

Xie, J.W., Zhao, Y.Y. and Dunkley, J.J. (2013) 'Effects of processing conditions on powder particle size and morphology in centrifugal atomisation of tin', *Powder Metallurgy,* 47(2), pp. 168-172. doi: 10.1179/003258904225015482.

Xue, X. and Zhao, Y.Y. (2011) 'Ti Matrix Syntactic Foam Fabricated by Powder Metallurgy: Particle Breakage and Elastic Modulus', *JOM,* 63(2), pp. 43-47.

Xue, X.B., Zhao, Y.Y., Kearns, V., Williams, R.L. and TMS (2010) *Mechanical and Biological Properties of Titanium Syntactic Foams* TMS.

Yue, Z. (2019) *Mechanical Properties of Metal Matrix Syntactic Foam.* PhD. University of Liverpool.

Zhang, B., Lin, Y., Li, S., Zhai, D. and Wu, G. (2016) 'Quasi-static and high strain rates compressive behavior of aluminum matrix syntactic foams', *Composites Part B: Engineering,* 98, pp. 288-296. doi: https://doi.org/10.1016/j.compositesb.2016.05.034.

Zhang, J. and Alpas, A.T. (1997) 'Transition between mild and severe wear in aluminium alloys', *Acta Materialia,* 45(2), pp. 513-528. doi: https://doi.org/10.1016/S1359-6454(96)00191-7.

Zhang, J., Liu, S., Lu, Y., Dong, Y. and Li, T. (2016) 'Fabrication process and bending properties of carbon fibers reinforced Al-alloy matrix composites', *Journal of Materials Processing Technology,* 231, pp. 366-373. doi: https://doi.org/10.1016/j.jmatprotec.2016.01.007.

Zhang, L.P. and Zhao, Y.Y. (2007) 'Mechanical Response of Al Matrix Syntactic Foams Produced by Pressure Infiltration Casting', *Journal of Composite Materials,* 41(17), pp. 2105-2117. doi: 10.1177/0021998307074132.

APPENDIX A: COMPRESSIVE BEHAVIOUR OF ASW SYNTACTIC FOAMS

This appendix presents additional stress-strain curves for quasi-static and drop hammer impact compressive loading.

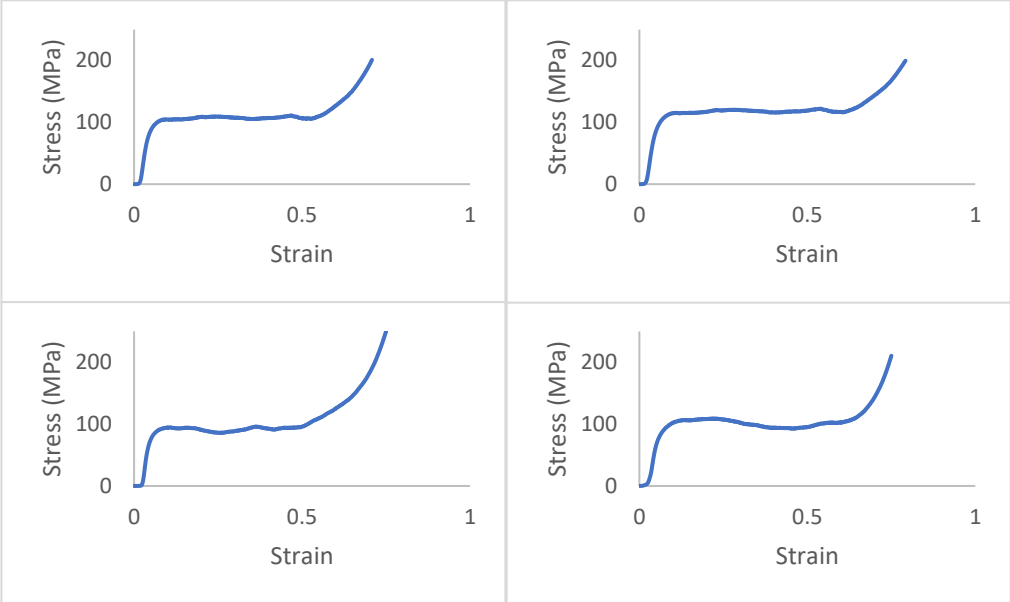

Figure A – 1: Stress-strain curves for L-ASF samples under quasi-static compressive loading

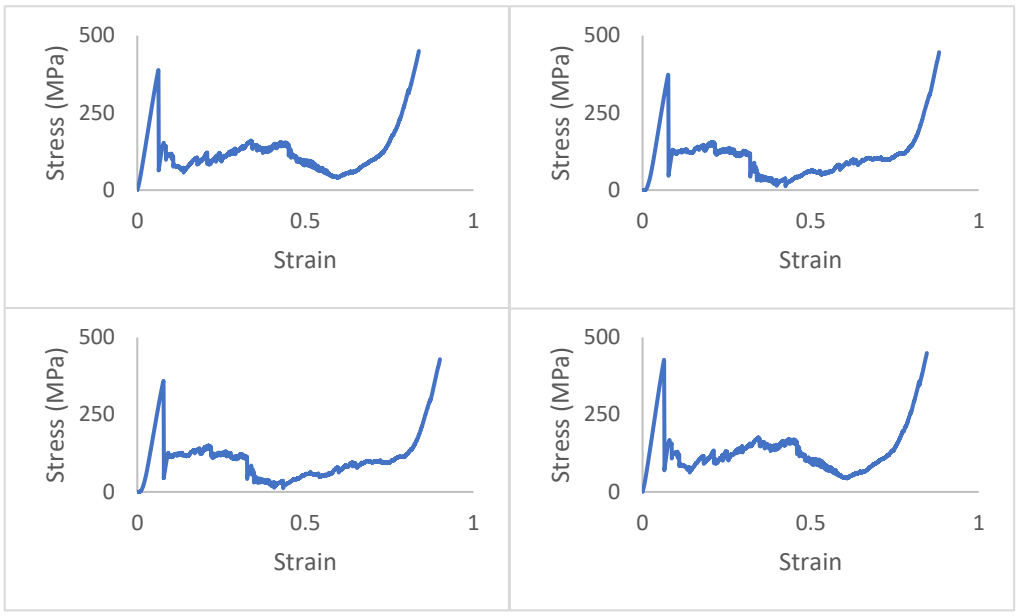

Figure A – 2: Stress-strain curves for M-ASF samples under quasi-static compressive loading

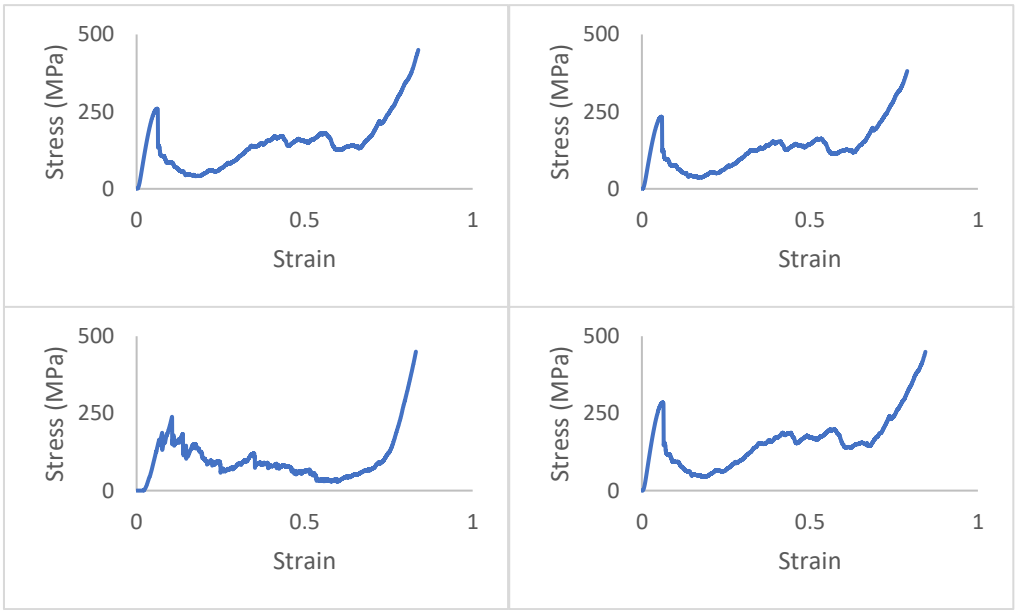

Figure A – 3: Stress-strain curves for S-ASF samples under quasi-static compressive loading

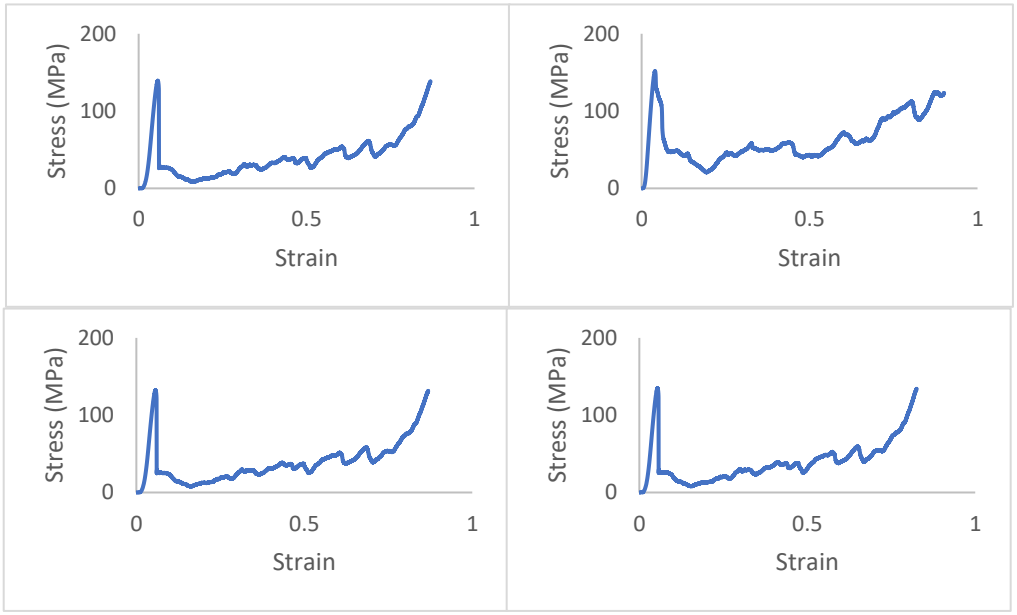

Figure A – 4: Stress-strain curves for LH-ASF samples under quasi-static compressive loading

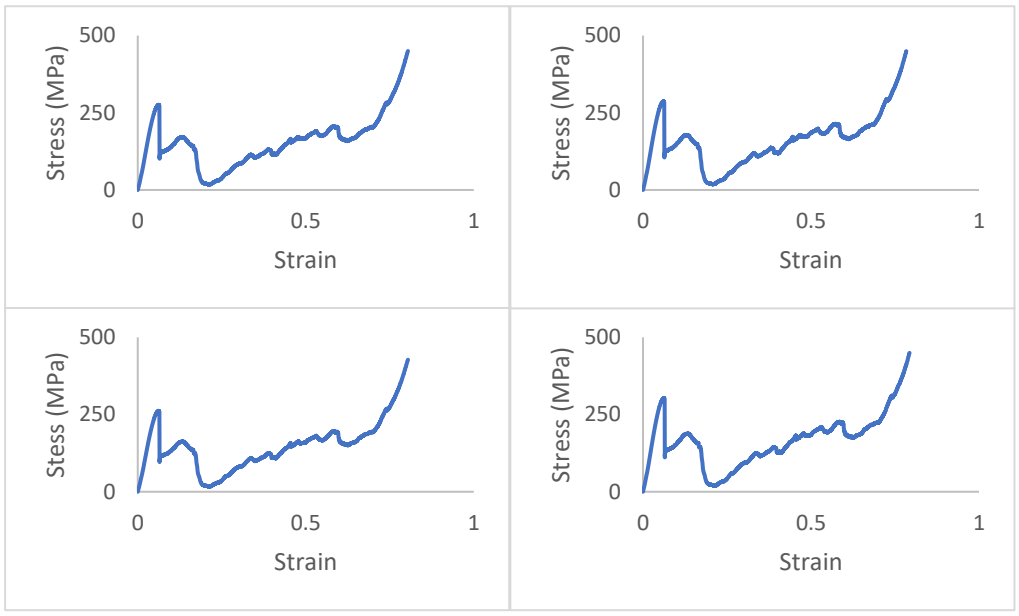

Figure A – 5: Stress-strain curves for MH-ASF samples under quasi-static compressive loading

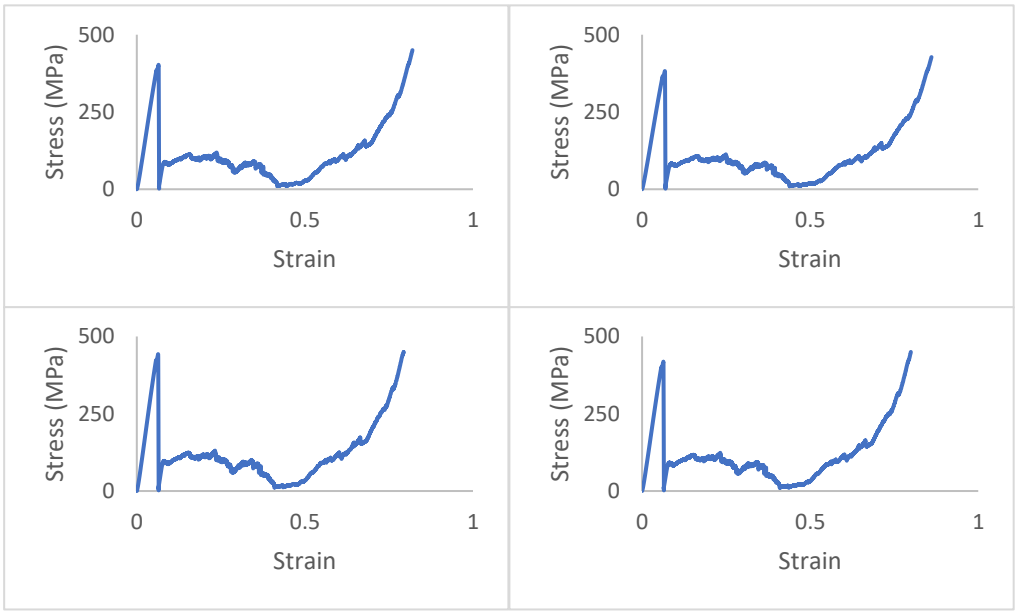

Figure A – 6: Stress-strain curves for SH-ASF samples under quasi-static compressive loading

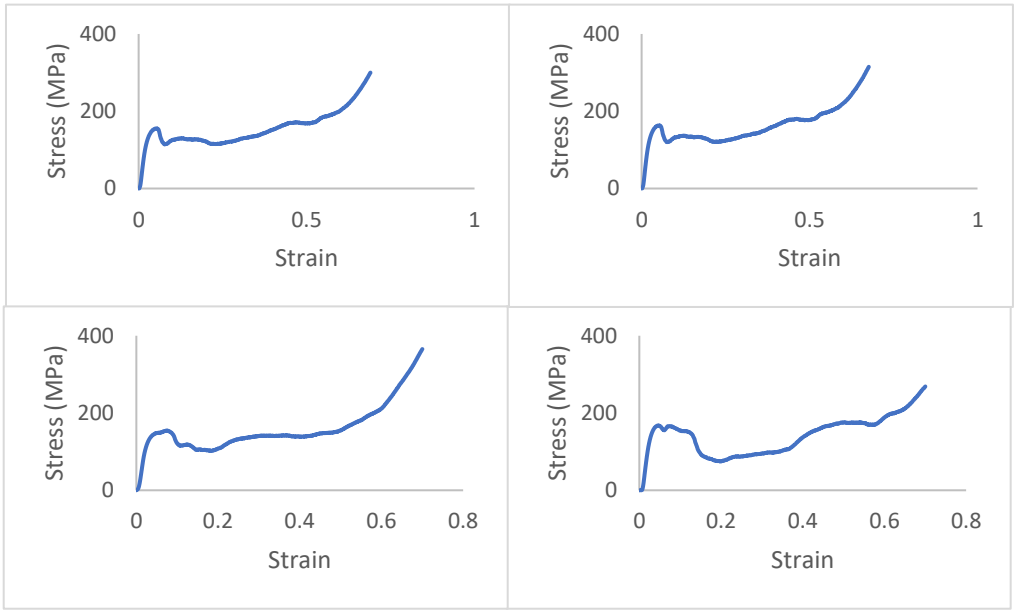

Figure A – 7: Stress-strain curves for L-ASF-T6 samples under quasi-static compressive loading

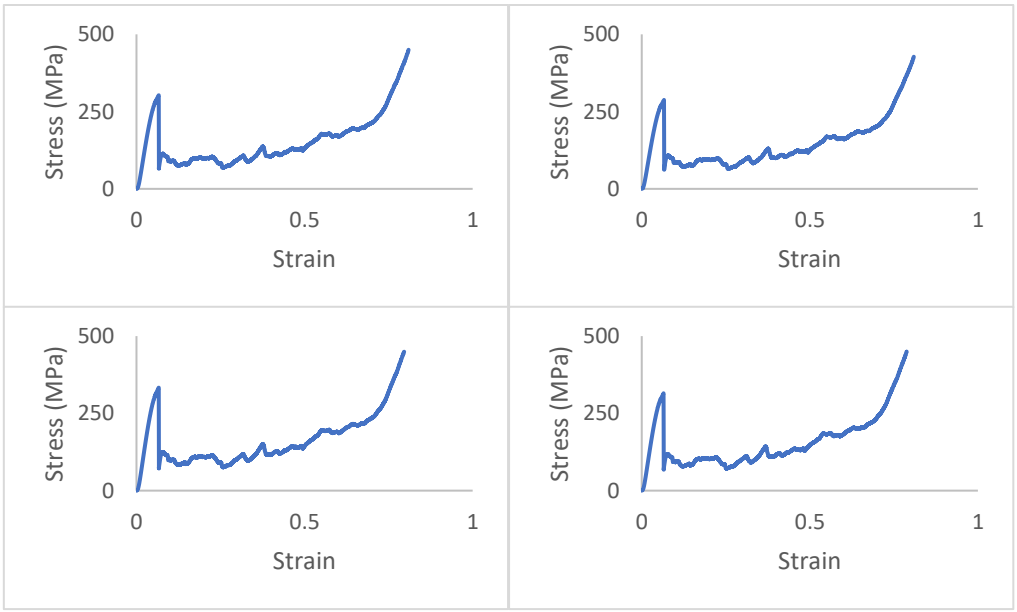

Figure A – 8: Stress-strain curves for M-ASF-T6 samples under quasi-static compressive loading

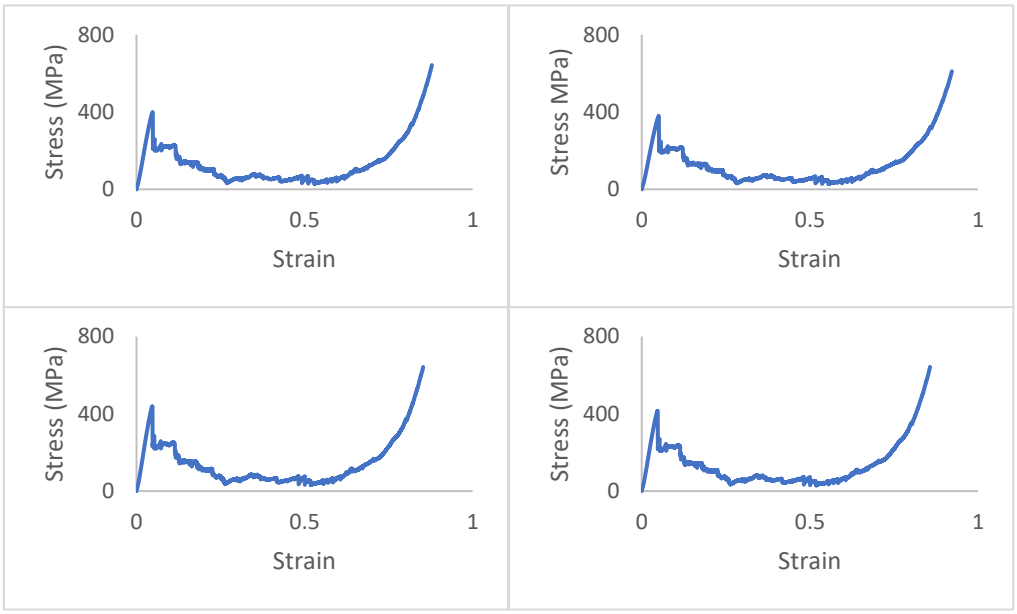

Figure A – 9: Stress-strain curves for S-ASF-T6 samples under quasi-static compressive loading

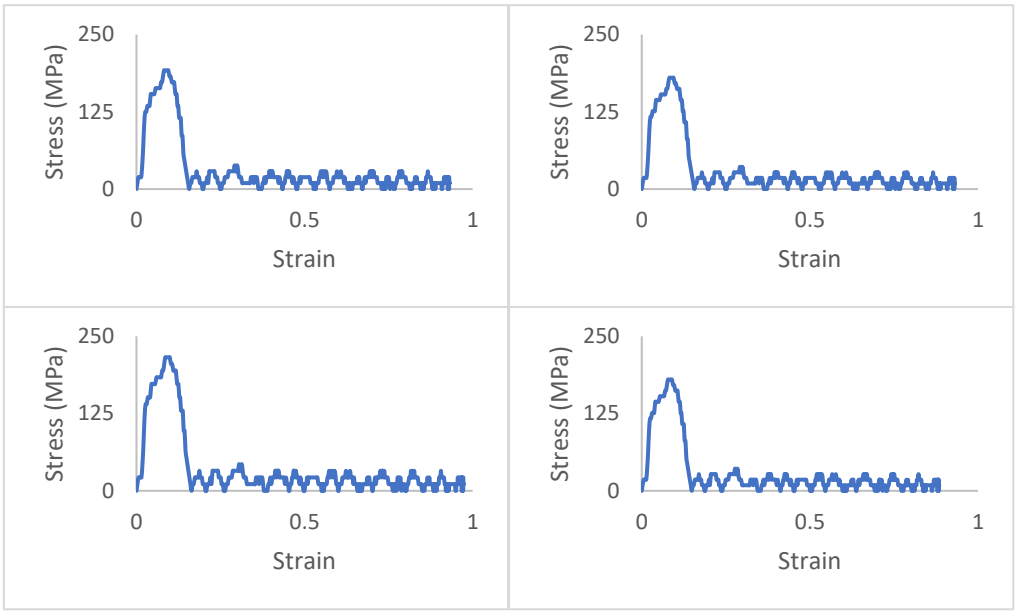

Figure A – 10: Stress-strain curves for L-ASF samples under drop weight impact

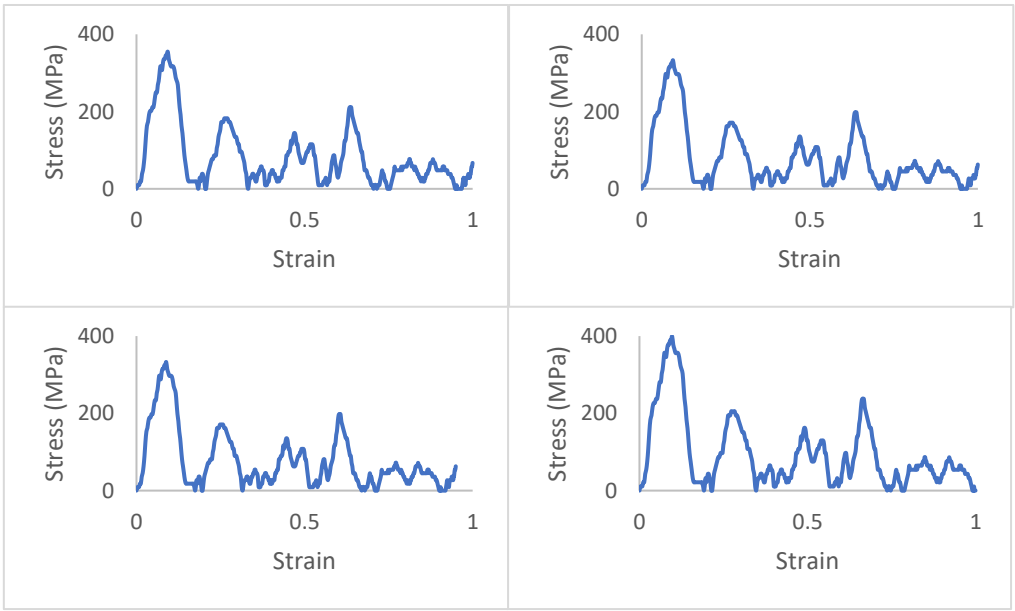

Figure A – 11: Stress-strain curves for M-ASF samples under drop weight impact

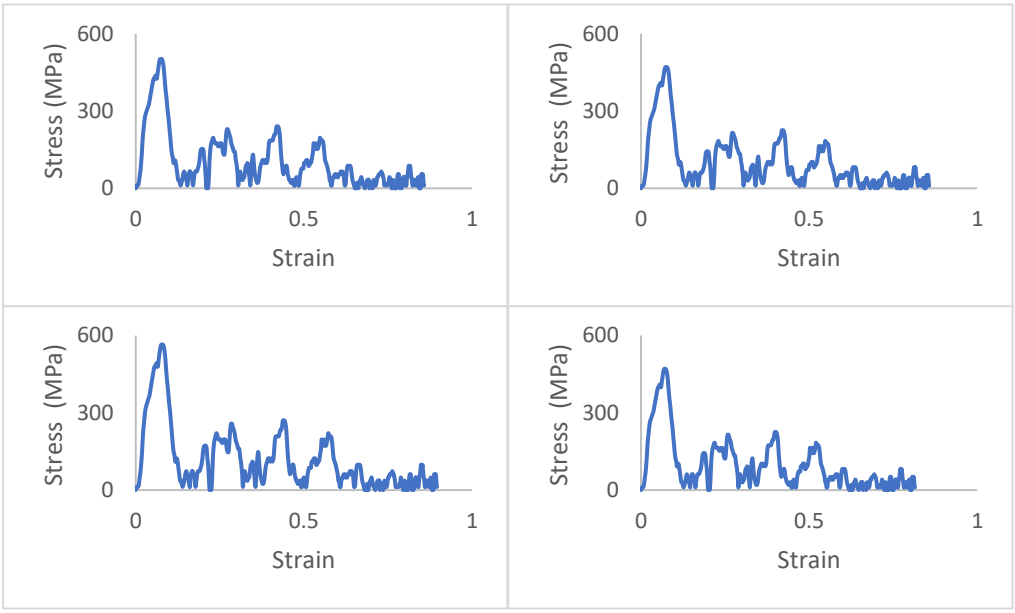

Figure A – 12: Stress-strain curves for S-ASF samples under drop weight impact

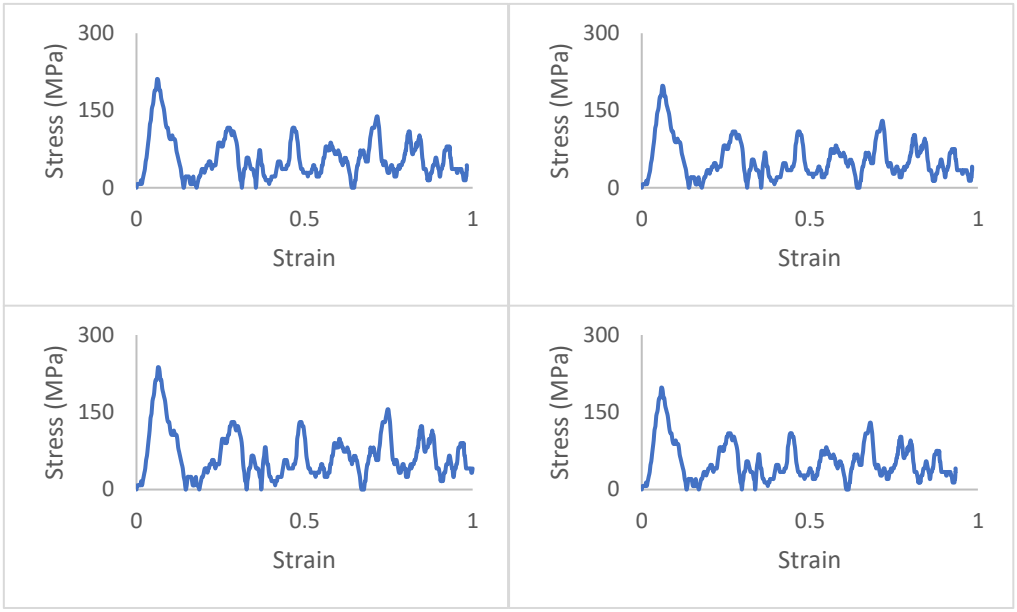

Figure A – 13: Stress-strain curves for LH-ASF samples under drop weight impact

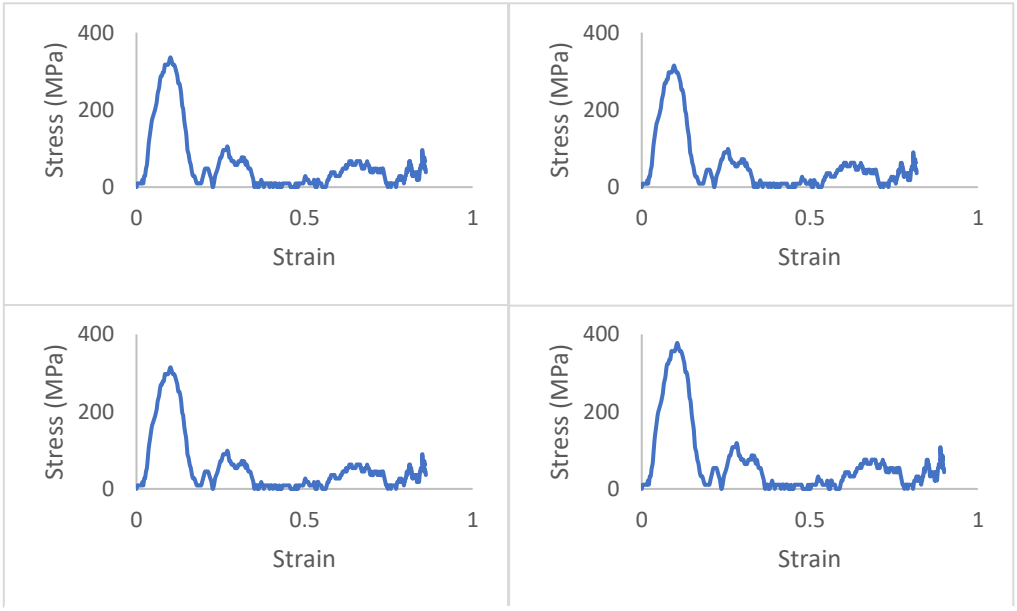

Figure A – 14: Stress-strain curves for MH-ASF samples under drop weight impact

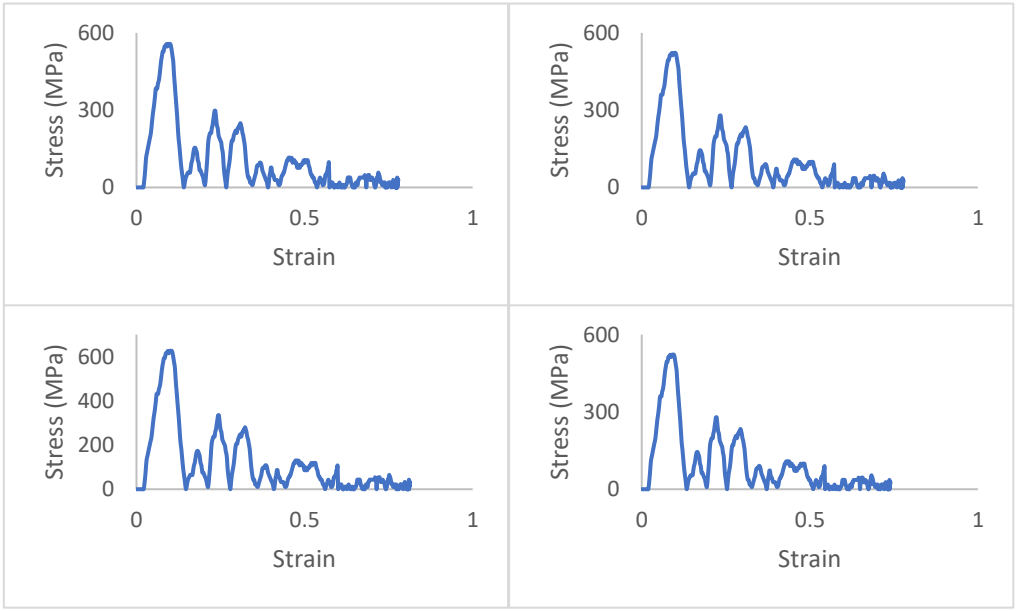

Figure A – 15: Stress-strain curves for SH-ASF samples under drop weight impact

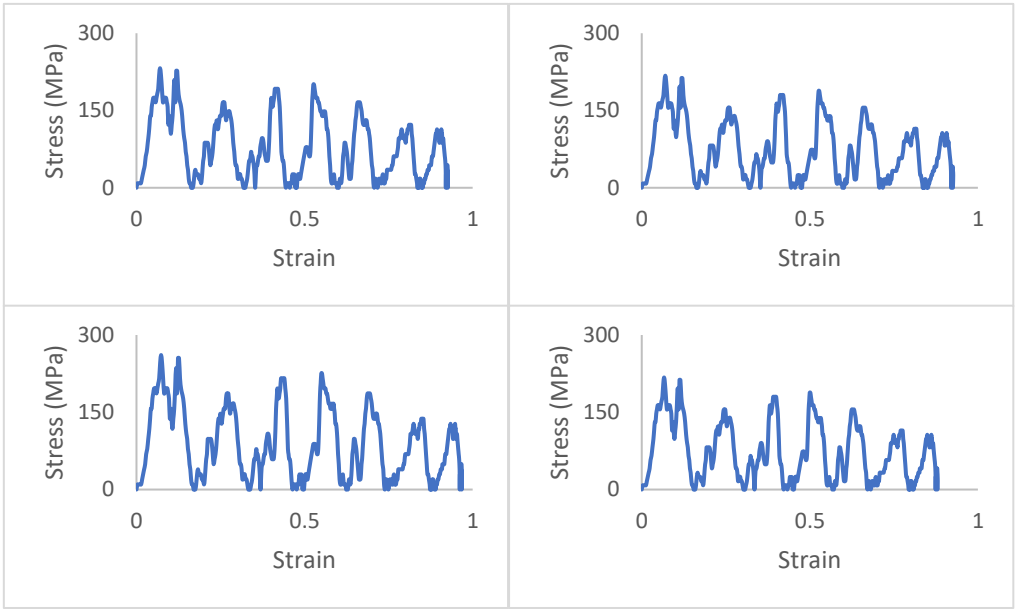

Figure A – 16: Stress-strain curves for L-ASF-T6 samples under drop weight impact

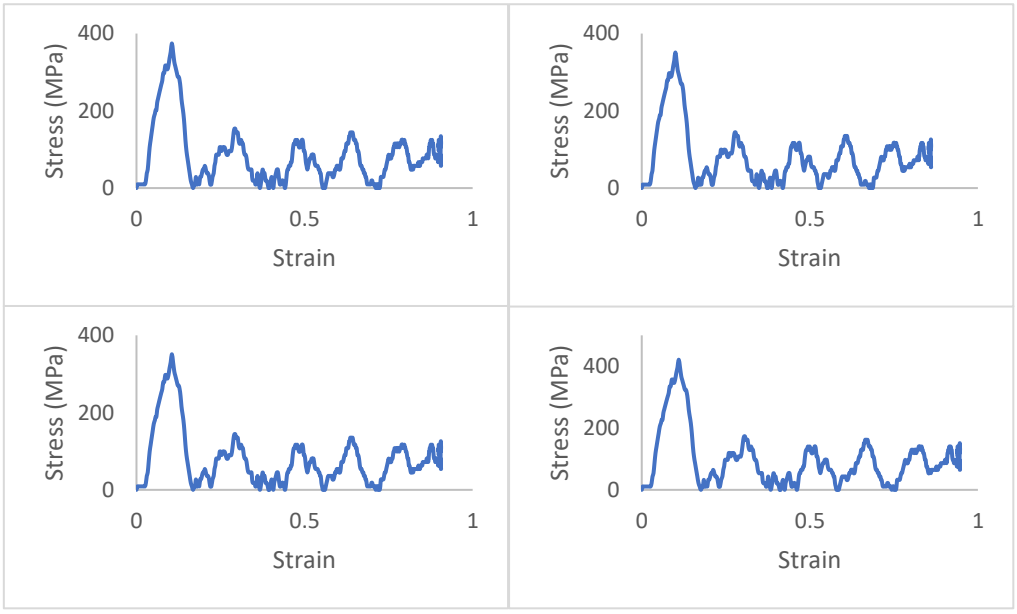

Figure A – 17: Stress-strain curves for M-ASF-T6 samples under drop weight impact

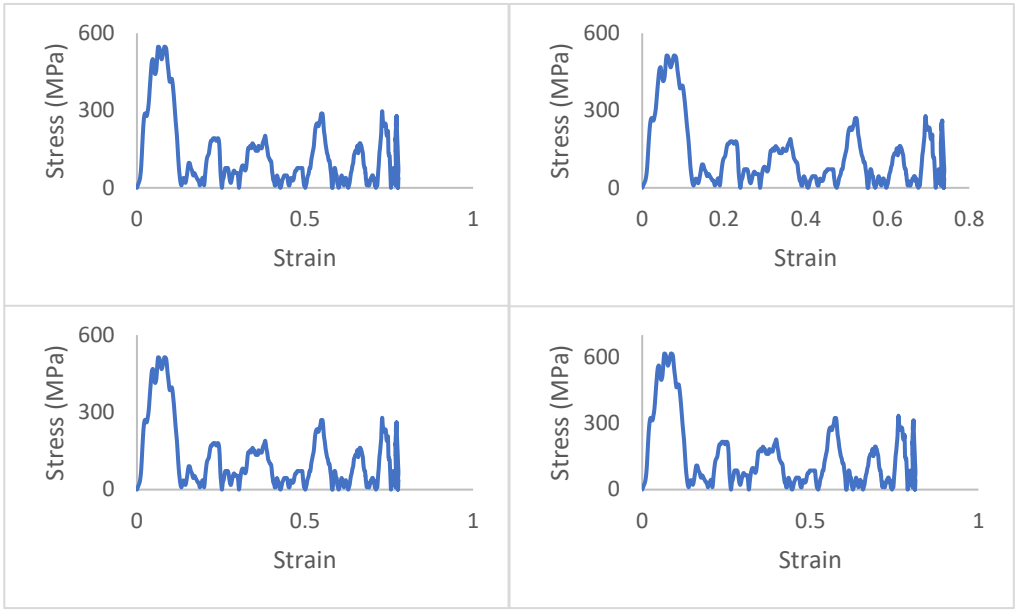

Figure A – 18: Stress-strain curves for S-ASF-T6 samples under drop weight impact

APPENDIX B: FLEXURAL BEHAVIOUR OF ASW SYNTACTIC FOAMS

This appendix presents additional load-displacement curves for three-point bending.

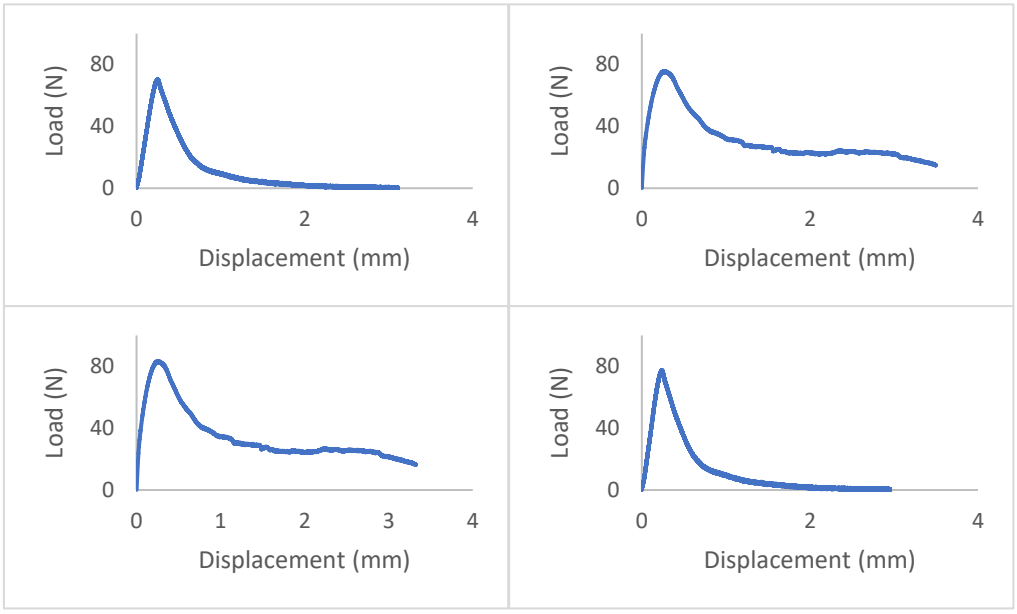

Figure B – 1: Load-displacement curves for L-ASF samples under three-point bending

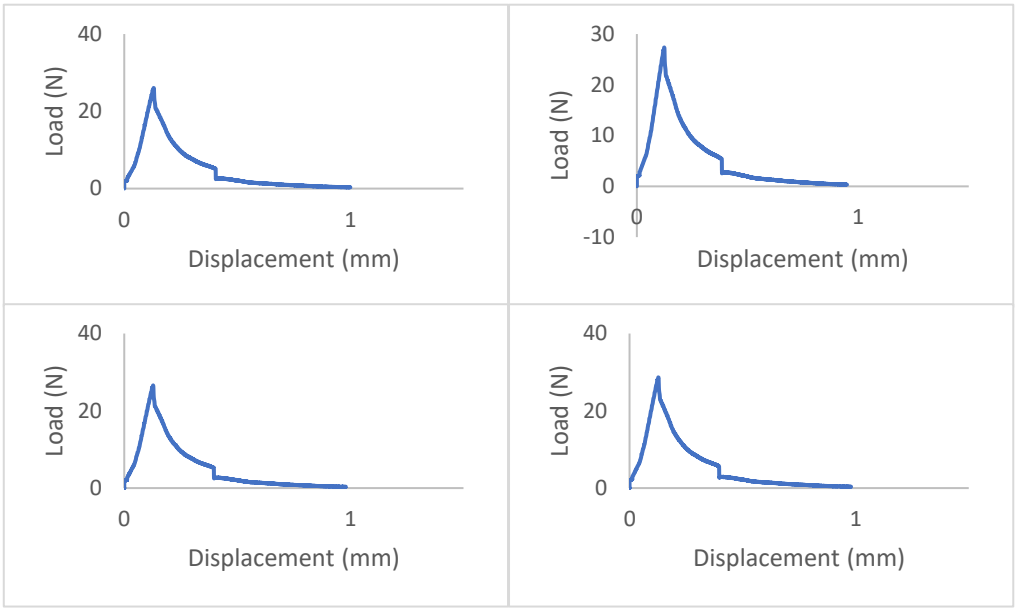

Figure B – 2: Load-displacement curves for M-ASF samples under three-point bending

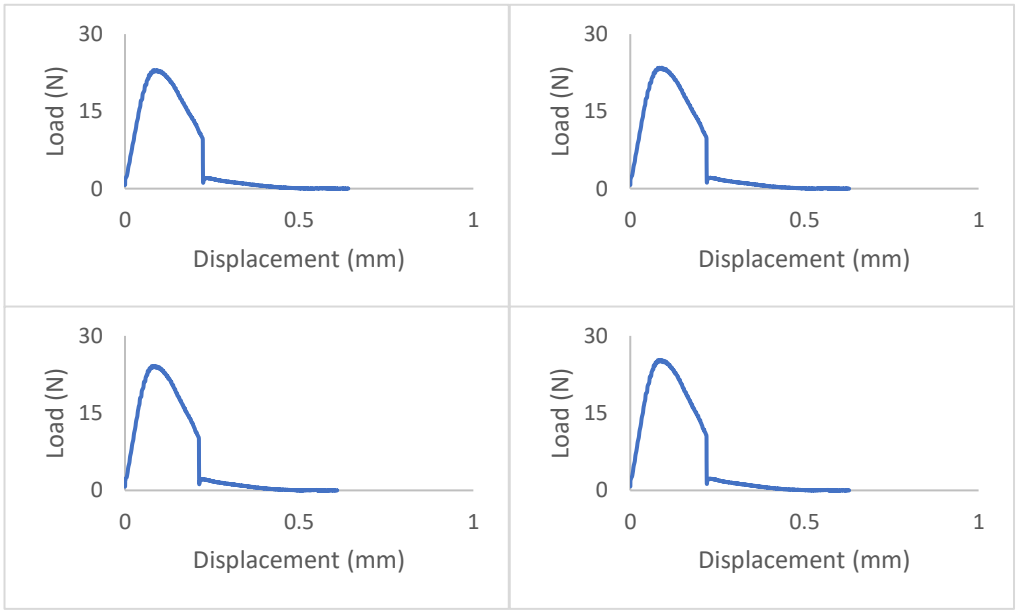

Figure B – 3: Load-displacement curves for S-ASF samples under three-point bending

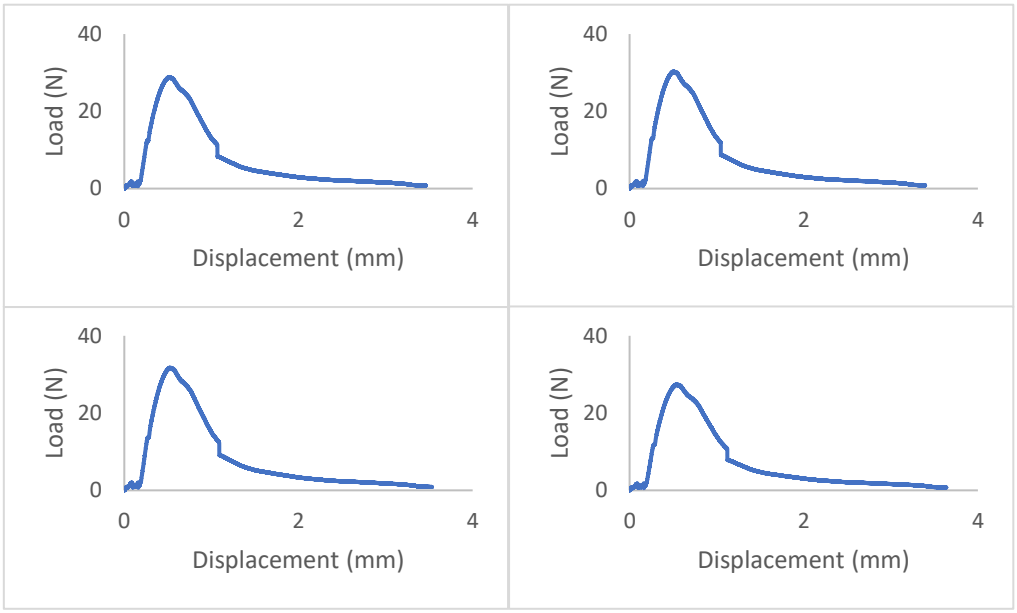

Figure B – 4: Load-displacement curves for LH-ASF samples under three-point bending

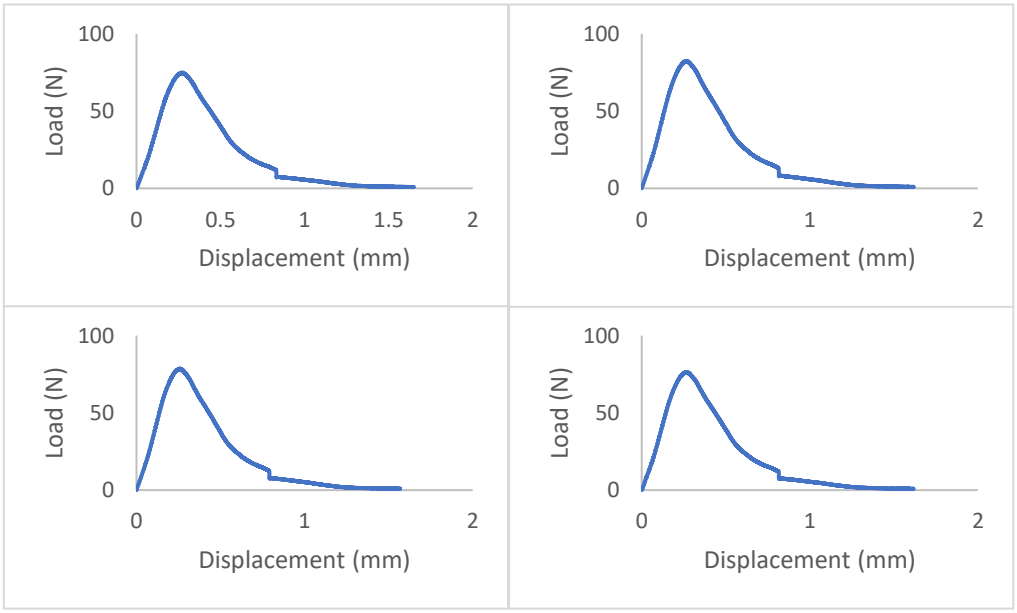

Figure B – 5: Load-displacement curves for MH-ASF samples under three-point bending

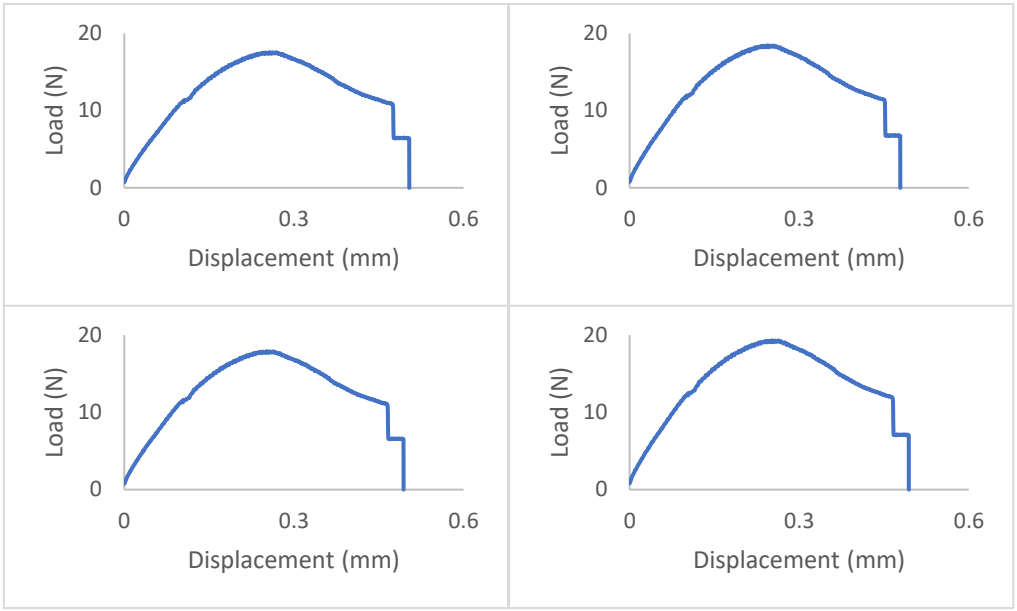

Figure B – 6: Load-displacement curves for SH-ASF samples under three-point bending

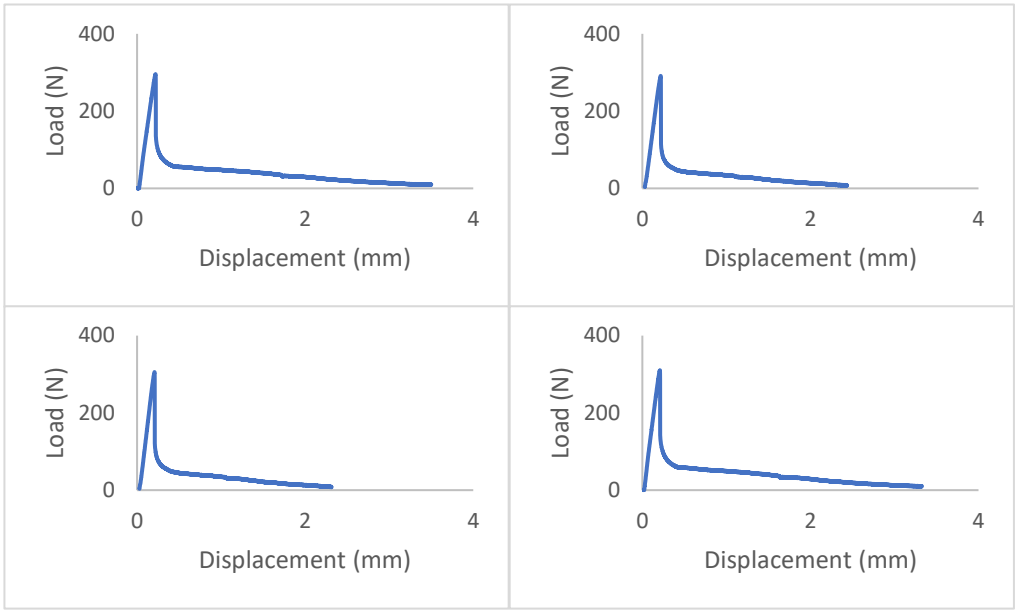

Figure B – 7: Load-displacement curves for L-ASF-T6 samples under three-point bending

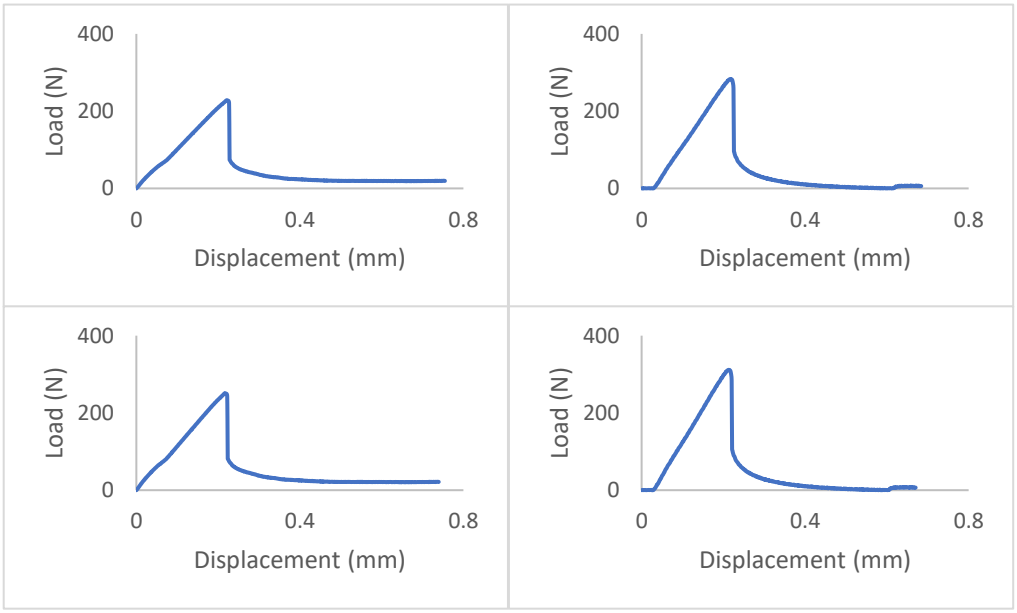

Figure B – 8: Load-displacement curves for M-ASF-T6 samples under three-point bending

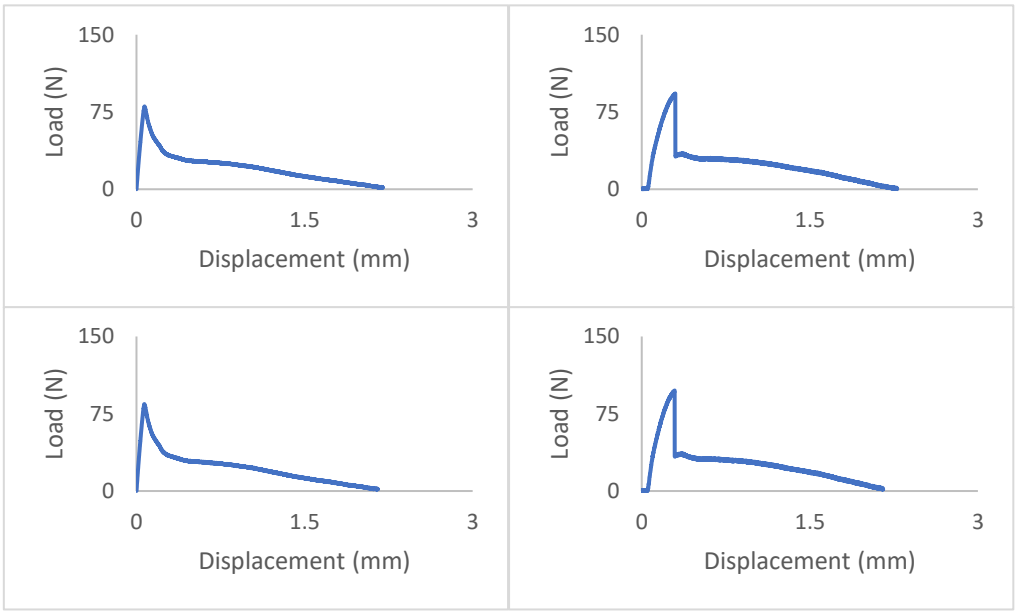

Figure B – 9: Load-displacement curves for S-ASF-T6 samples under three-point bending

APPENDIX C: TRIBOLOGICAL BEHAVIOUR OF ASW SYNTACTIC FOAMS

This appendix presents additional COF vs sliding distance curves for ASW syntactic foams under dry and lubricated sliding wear conditions.

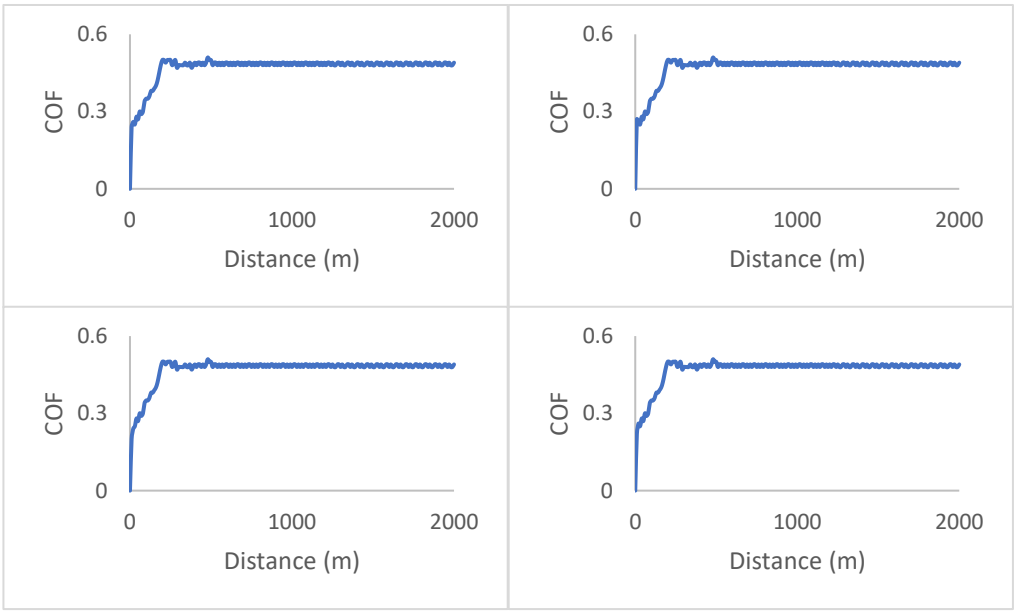

Figure C – 1: Development of COF vs sliding distance for L-ASF samples under dry sliding conditions

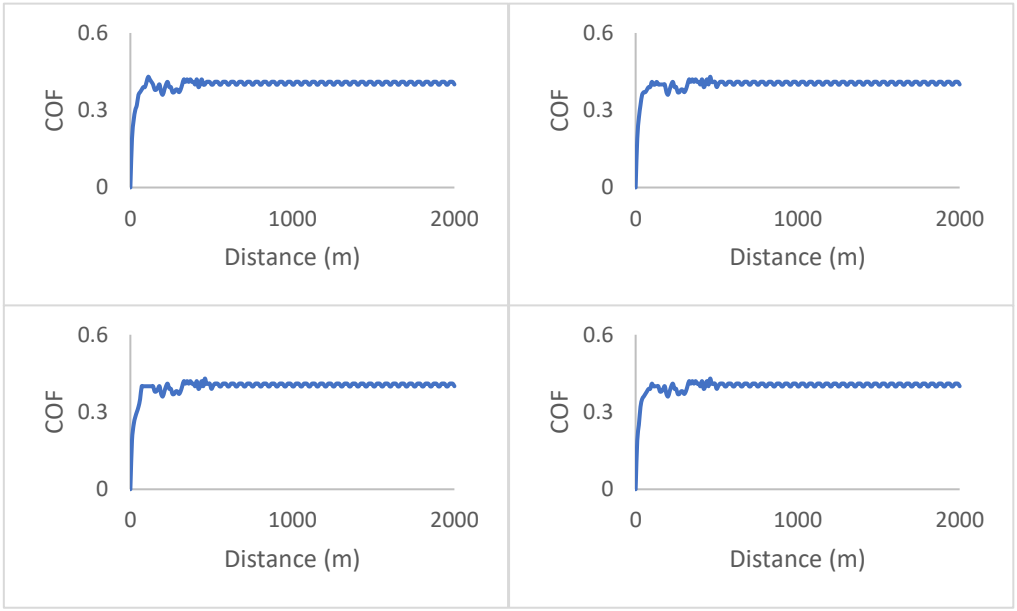

Figure C – 2: Development of COF vs sliding distance for M-ASF samples under dry sliding conditions

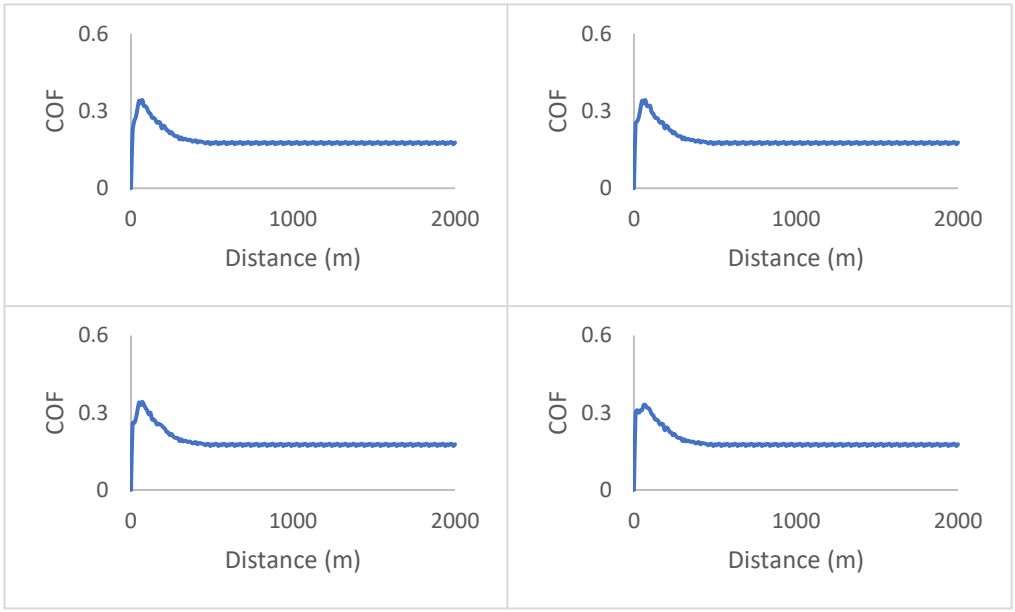

Figure C – 3: Development of COF vs sliding distance for S-ASF samples under dry sliding conditions

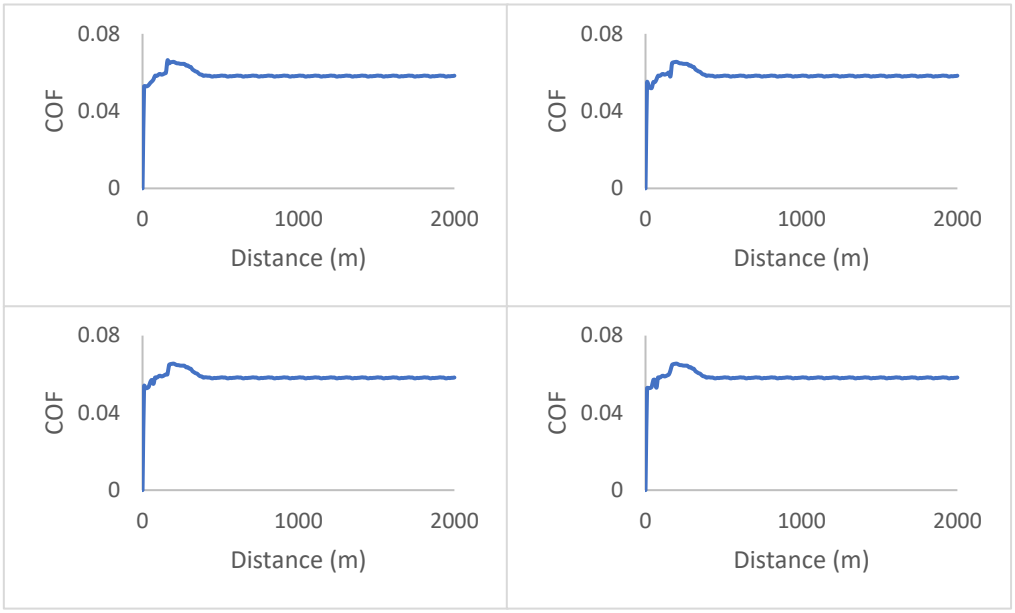

Figure C – 4: Development of COF vs sliding distance for LH-ASF samples under dry sliding conditions

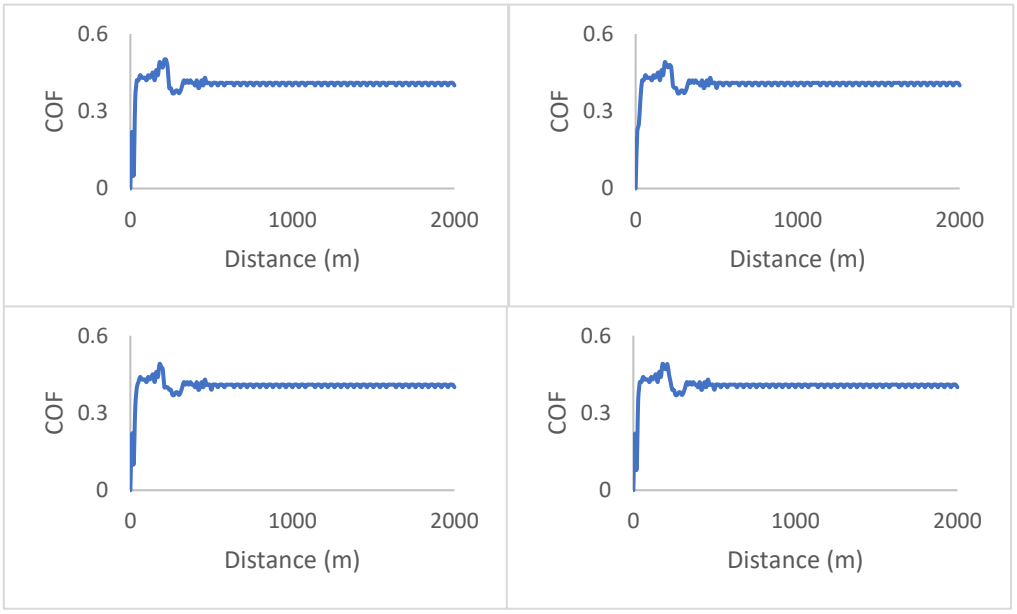

Figure C – 5: Development of COF vs sliding distance for MH-ASF samples under dry sliding conditions

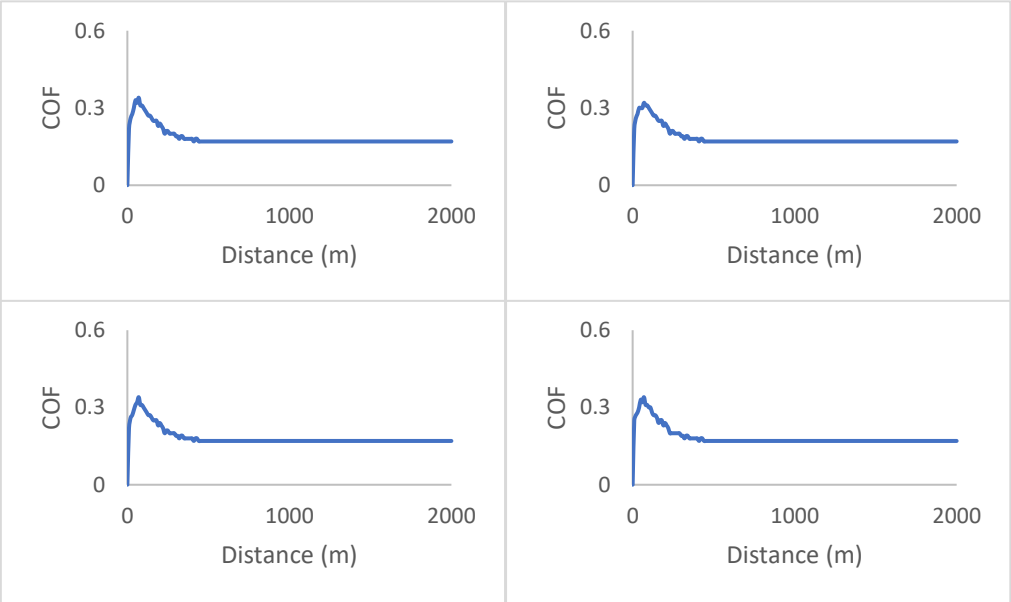

Figure C – 6: Development of COF vs sliding distance for SH-ASF samples under dry sliding conditions

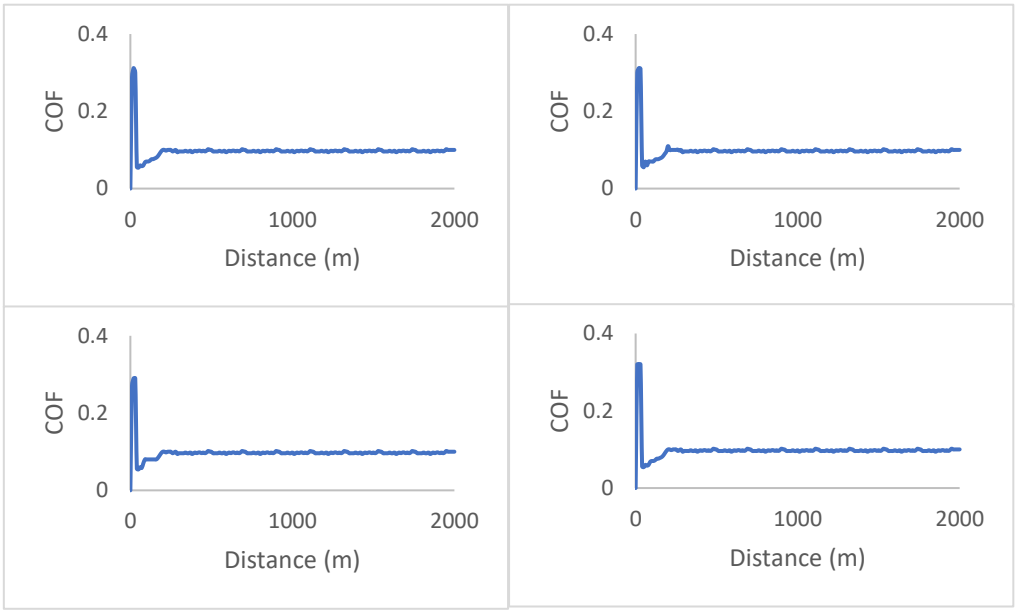

Figure C – 7: Development of COF vs sliding distance for L-ASF-T6 samples under dry sliding conditions

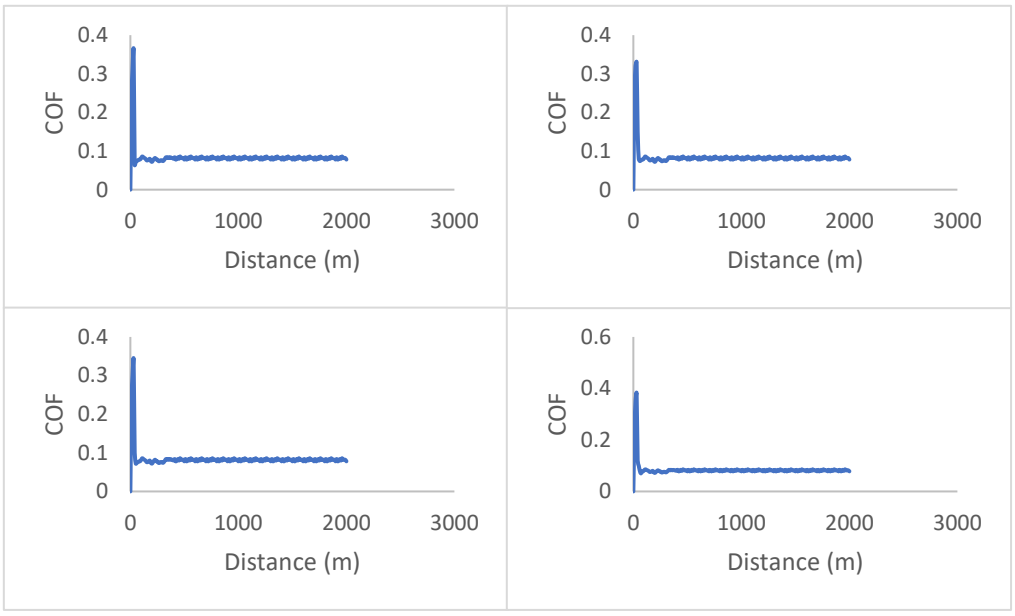

Figure C – 8: Development of COF vs sliding distance for M-ASF-T6 samples under dry sliding conditions

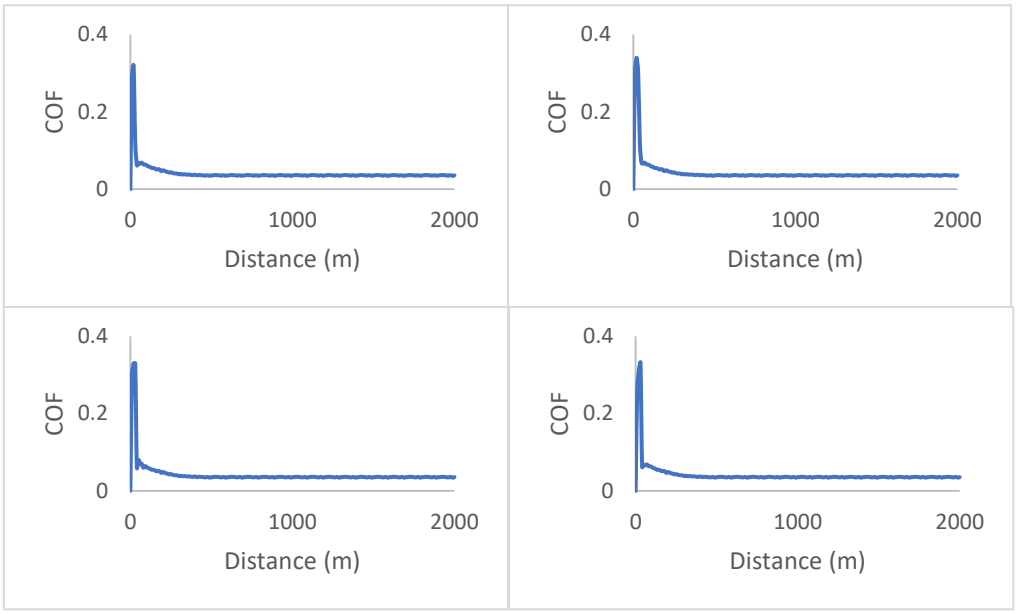

Figure C – 9: Development of COF vs sliding distance for M-ASF-T6 samples under dry sliding conditions

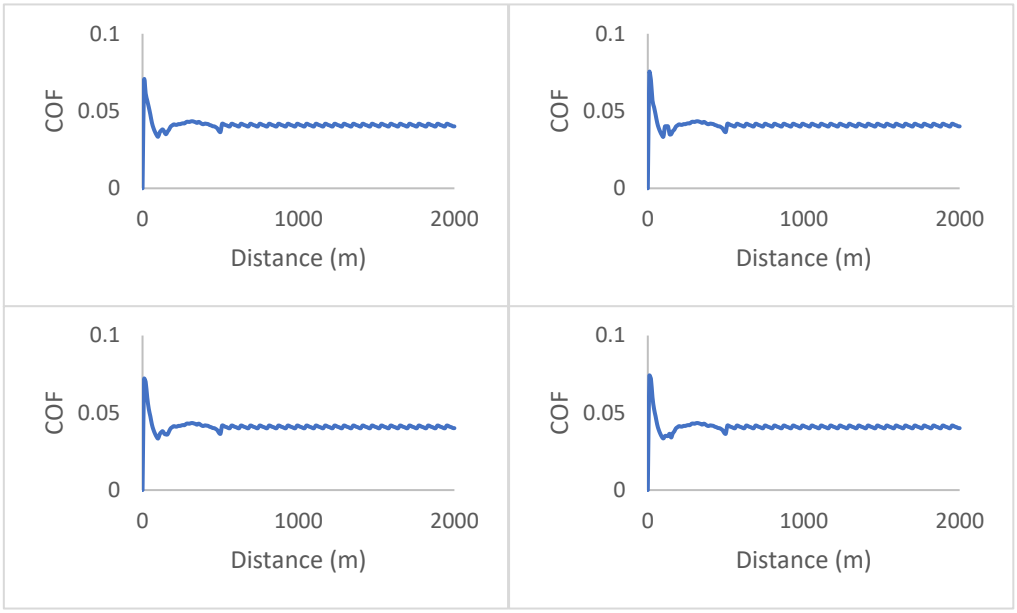

Figure C – 10: Development of COF vs sliding distance for L-ASF samples under lubricated sliding conditions

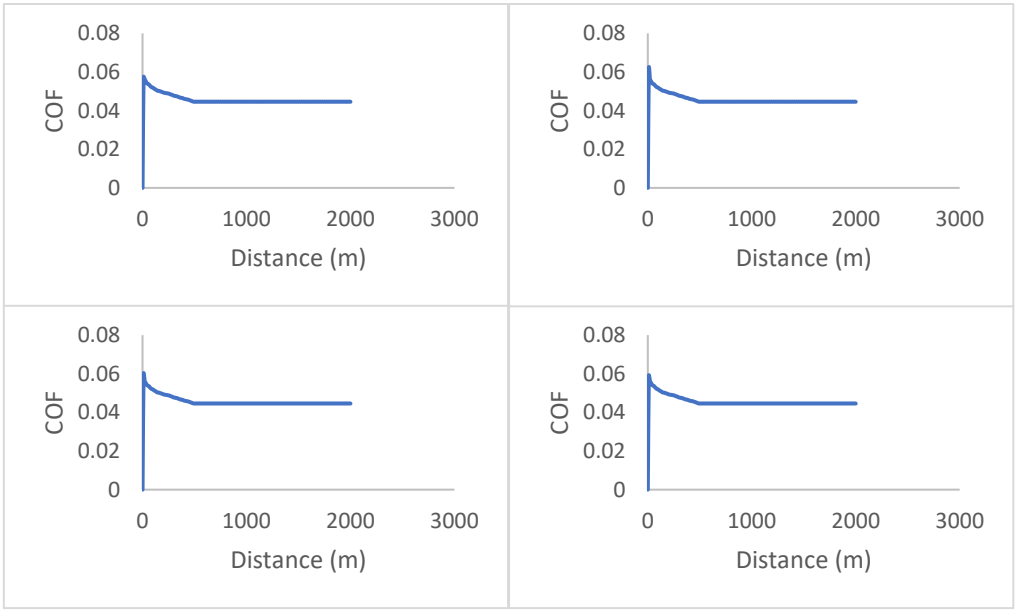

Figure C – 11: Development of COF vs sliding distance for M-ASF samples under lubricated sliding conditions

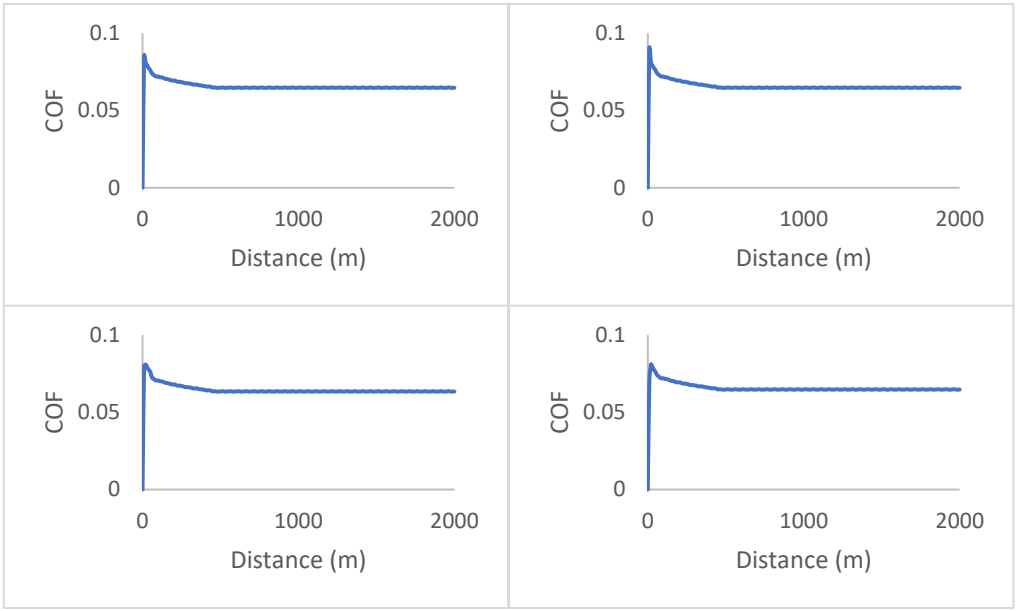

Figure C – 12: Development of COF vs sliding distance for S-ASF samples under lubricated sliding conditions

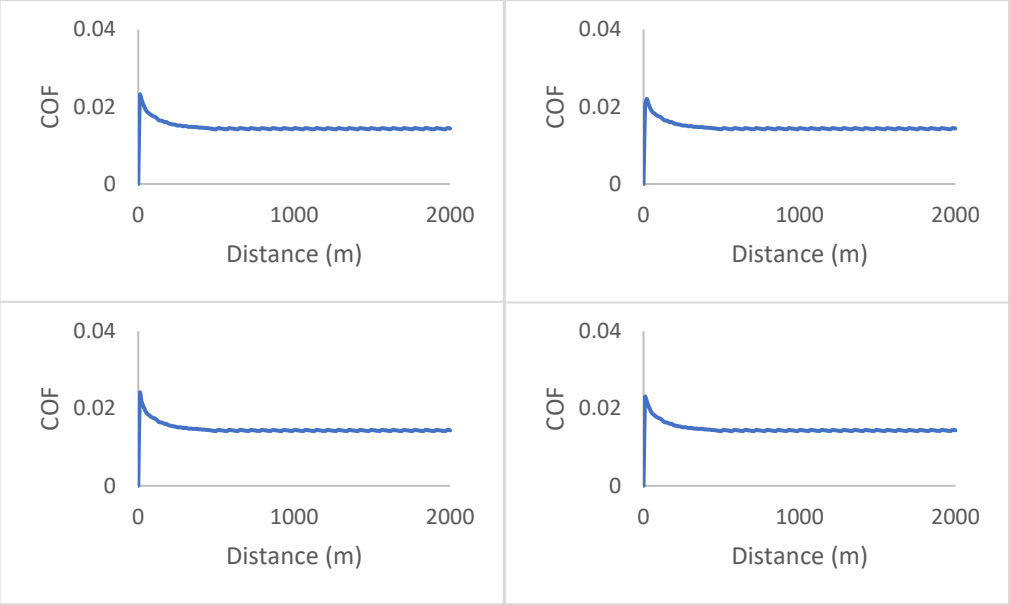

Figure C – 13: Development of COF vs sliding distance for LH-ASF samples under lubricated sliding conditions

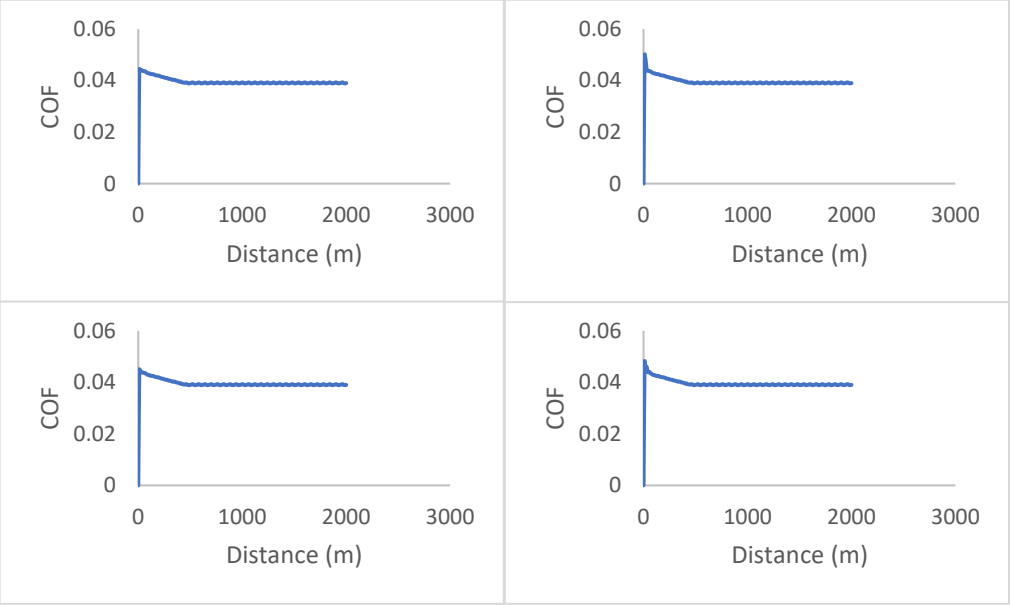

Figure C – 14: Development of COF vs sliding distance for MH-ASF samples under lubricated sliding conditions

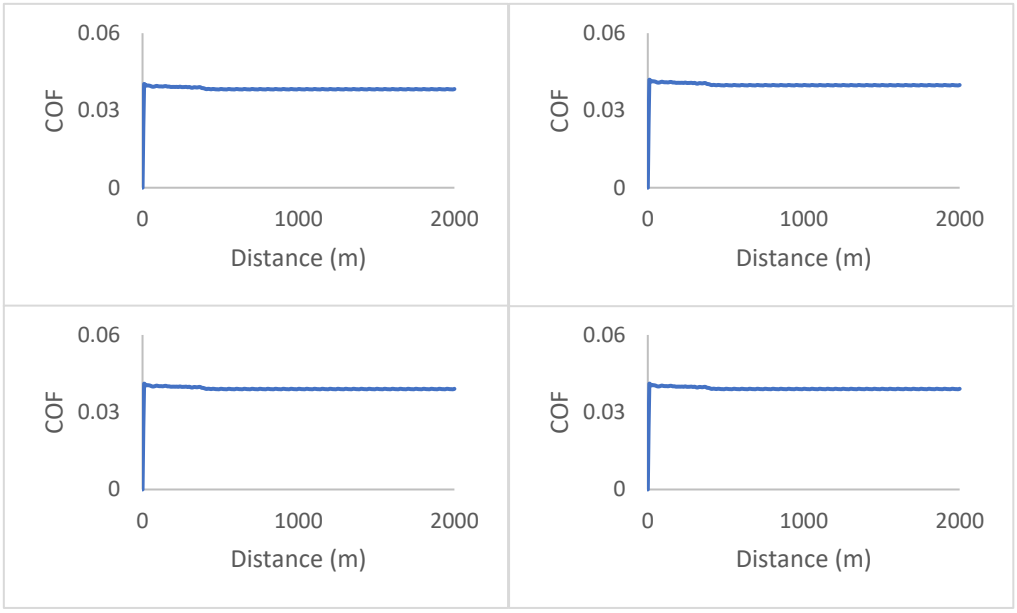

Figure C – 15: Development of COF vs sliding distance for SH-ASF samples under lubricated sliding conditions

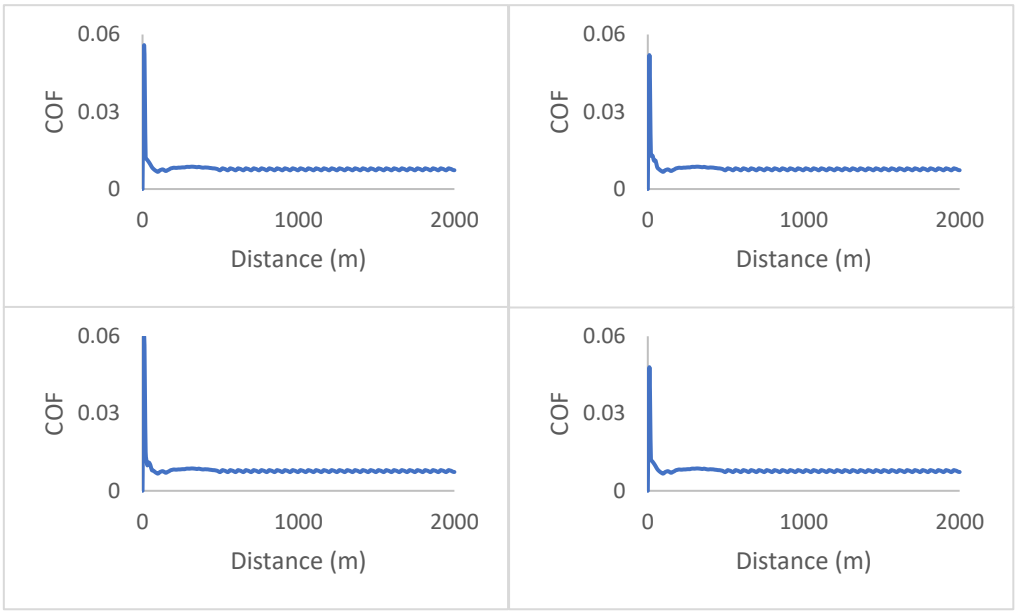

Figure C – 16: Development of COF vs sliding distance for L-ASF-T6 samples under lubricated sliding conditions

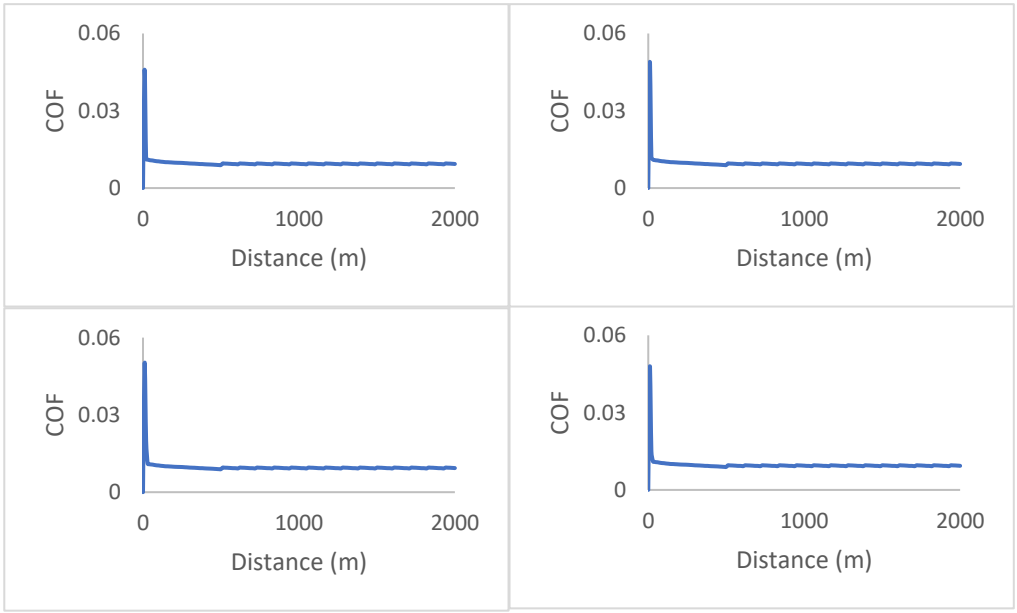

Figure C – 17: Development of COF vs sliding distance for M-ASF-T6 samples under lubricated sliding conditions

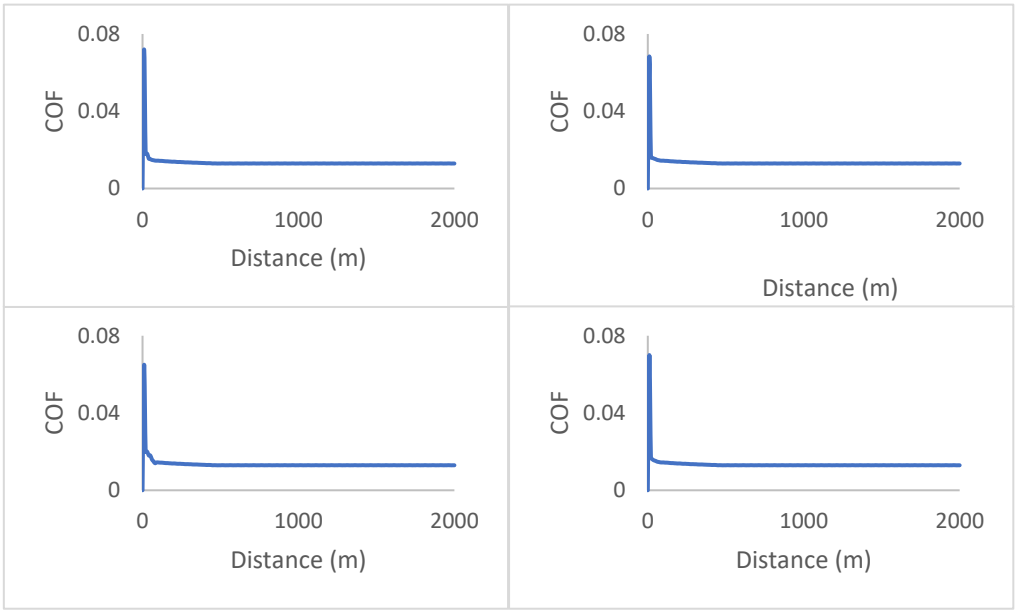

Figure C – 18: Development of COF vs sliding distance for S-ASF-T6 samples under lubricated sliding conditions